AALBORG UNIVERSITET

Low frequency directivity control

Authors:
Olivier Le Bot

Supervisor:
Christian Sejer Pedersen

Aalborg University
Acoustics
Department of Electronic Systems
Frederik Bajers Vej 7
9220 Aalborg Ø
Telephone 96 35 86 00
http://acoustics.es.aau.dk/

Title: Subwoofer directivity control

Theme: Low frequency

Project term:
P10, spring semester 2010

Project group:
10gr1064

Group members:
Olivier Le Bot

Supervisor:
Christian Sejer Pedersen

Copies: 3

Pages: 189

Appendices: 1 CD

Finished 01/06/2010

Synopsis:

The directivity of loudspeakers is an important factor for the sound field production and perception. If controlling the directivity at high frequencies is easy with waveguides, it becomes much harder as long as the frequency decreases and the wavelength becomes bigger than the size of the sound source. An analytical study of traditional setups for controlling the low frequency directivity is made, completed by Finite-Difference Time-Domain simulations. Two solutions to improve the directivity control are proposed. One based on an all pass filter delaying the signal by different amounts at different frequencies and another base on the difference of gain of the signal applied on the different subwoofers. The different solutions have been simulated with FDTD methods and tested through measurements of a real setup. Improvements have been noted with the proposed solutions.

This report is made by:

Olivier Le Bot

Contents

Part I

Introduction

1
Project Description

The directivity of a loudspeaker is a parameter describing how a sound source radiates in its environment and which sound field it produces.

For a long time loudspeaker manufacturers have tried to control the directivity of their loudspeakers using different mounting arrangements to obtain a specific sound field. From the first horns invented in the 17^{th} century to the most advanced wave guide technologies used today on the line source systems, the focus of manufacturers has mostly been on controlling the directivity at mid and high frequencies.

One of the reason to that is also that the size of the wavelength at low frequencies makes impossible the realization of waveguides of reasonable size for controlling the directivity of low frequencies. Indeed, as long as the wavelength becomes higher than the size of the source, the control of the directivity becomes harder and the source behavior becomes more and more omnidirectional.

However low frequency directivity control would be beneficial in different applications. In live-music applications, it would help to reduce the amount of low frequency sent back to the stage or to the technicians working in backstage nearby the subwoofers. In room acoustics Ferekidis has shown in [12] the advantages of using cardioid subwoofers to limit the formation of modes in small rooms even when the loudspeaker is positioned in a critical place (for example a corner).

Therefore the need of a directivity control at low frequency is real.

This project aims to propose and study different solutions for controlling the directivity of subwoofers. These solutions are studied through three different points of view: analytical, simulations and measurements. One will mainly focus on the obtention of a cardioid pattern directivity as it is the most common pattern desired in the audio industry.

After an analytical description of basic setups providing a control of the directivity at low frequencies, one develops two solutions to improve the directivity control. A simulation tool based on finite-difference time-domain is developed to simulate the behavior of the different proposed solutions. Finally measurements are made to validate these solutions on a real setup.

Part II

Analysis

2

Fundamentals of gradient loudspeakers

2.1 Introduction

In 1973, Harry F. Olson introduced the term of gradient-loudspeaker as a reciprocal of the gradient microphone [16]. According to Olson, and still by reciprocity to the different types of microphone, loudspeakers can be divided in two categories: the wave-type loudspeakers and the gradient-type loudspeakers.

Wave-type loudspeakers are the most common. Their directivity depends in some way upon wave interference. With these loudspeakers a certain directivity can be obtained for frequencies whose wavelengths are comparable to the dimensions of the radiators. So it is easy to understand that achieving a good directivity at low-frequencies without using very large systems is difficult.

The term gradient-loudspeaker designates a loudspeaker consisting of two or more loudspeakers separated in space and operating with a difference in phase. The dimension of gradient loudspeakers are small compared to the wavelength, but combining them in certain way can lead to achieve a good directivity at low-frequencies.

This chapter aims to introduce the fundamental principles of gradient-loudspeakers by presenting the theoretical considerations of the performances of simple sound sources operating under various orders of the gradient. For each order of the gradient, different MATLAB simulations are presented and discussed in order to show the positive and negative points of such systems.

2.2 Zero-order gradient sound source: omnidirectional

The Zero-Order Gradient sound source-omnidirectional is the basis of all the other orders of gradient sound source. So this section aims to find the proper expression that describes the sound pressure produced by a Zero-Order Gradient sound source-omnidirectional.

Fundamentals of the wave equation

Under some assumptions relative to the properties of the fluid where the acoustic wave propagates and depicted more precisely in [9], a system of equations describing the state of the fluid when submitted to an acoustic wave can be fund. The analysis is limited to waves of relatively small amplitude so the acoustic pressure p is small compared to the atmospheric pressure. The changes in the density of the medium ρ_0 are small compared to its equilibrium value so the condensation s is also very small ($s << 1$). The acoustic processes are nearly isentropic (adiabatic and reversible). The first fundamental equation is the linear continuity equation:

$$\frac{\partial s}{\partial t} + \nabla.\vec{u} = 0 \tag{2.1}$$

with

- s: the condensation at (x,y,z)
- u: the particle velocity

The second fundamental equation is the Euler equation:

$$\rho_0 \frac{\partial \vec{u}}{\partial t} = -\nabla p \tag{2.2}$$

with

- ρ_0 the equilibrium density at (x, y, z)
- u the particle velocity of a fluid element
- p the acoustic pressure at (x,y,z)

The third equation is the equation of state:

$$p = \rho_0 c^2 s \tag{2.3}$$

with

- p the acoustic pressure at (x,y,z)
- ρ_0 the equilibrium density at (x,y,z)
- c the thermodynamic speed of sound of the fluid
- s the condensation at (x,y,z)

Combining these three equations 2.1, 2.2, 2.3 and respecting the approximations stated before leads to the linear wave equation:

$$\nabla^2 p - \frac{1}{c^2}\frac{\partial^2 p}{\partial t^2} = 0 \tag{2.4}$$

Velocity potential

While calculating the rotational of equation 2.2, it can be found that

$$\rho_0 \frac{\partial(\nabla \times \vec{u})}{\partial t} = \nabla \times (-\nabla p) \tag{2.5}$$

By definition

$$\nabla \times (\nabla p) = 0 \tag{2.6}$$

So the particle velocity $\vec{u}$ is irrotational $\nabla \times \vec{u} = 0$. Moreover, using the definition 2.6, the particle velocity can be expressed as the gradient of a scalar function ϕ, where ϕ is called the velocity potential.

$$\vec{u} = \nabla \phi \tag{2.7}$$

The Euler equation 2.2 can then be written:

$$\rho_0 \frac{\partial \phi}{\partial t} + p = 0 \tag{2.8}$$

And ϕ satisfies also the wave equation:

$$\nabla^2 \phi - \frac{1}{c^2} \frac{\partial^2 \phi}{\partial t^2} = 0 \tag{2.9}$$

Solution in spherical coordinates

When expressing the wave equation in spherical coordinates the laplacian operator ∇^2 becomes $\nabla^2 = \frac{\partial^2}{\partial r^2} + \frac{2}{r}\frac{\partial}{\partial r}$. Therefore the wave equation in spherical coordinates is:

$$\nabla^2 (r\phi) - \frac{1}{c^2} \frac{\partial^2 (r\phi)}{\partial t^2} = 0 \tag{2.10}$$

The solution of the wave equation is $r\phi$ and so:

$$\phi = \frac{\alpha}{r} \exp j(\omega t - kr) \tag{2.11}$$

with α the amplitude of ϕ.

In order to find the expression of the pressure, equation 2.8 is used. It can thus be fund that:

$$p = -\frac{j\rho_0 \alpha \omega}{r} \exp j(\omega t - kr) \tag{2.12}$$

Acoustic reciprocity

In equation 2.12, α is still defined as the amplitude of ϕ 2.11. It is possible to determine an expression of α by using the concept of acoustic reciprocity.

As explained in details in [], if a region of the space containing two irregularly shaped sources A and B is considered, then if p_1 is the pressure at B when source A is active with a velocity $\vec{u_1}$ (see figure 2.1)and p_2 is the pressure at A when source B is active with a velocity $\vec{u_2}$ (see figure 2.2), then the concept of acoustic reciprocity gives:

$$\int_{S_A} p_2 \vec{u_1} \,.\, \hat{n} \, dS = \int_{S_B} p_1 \vec{u_2} \,.\, \hat{n} \, dS \tag{2.13}$$

If the pressure is uniform over each source:

$$\frac{1}{p_1} \int_{S_A} \vec{u_1} \,.\, \hat{n} \, dS = \frac{1}{p_2} \int_{S_B} \vec{u_2} \,.\, \hat{n} \, dS \tag{2.14}$$

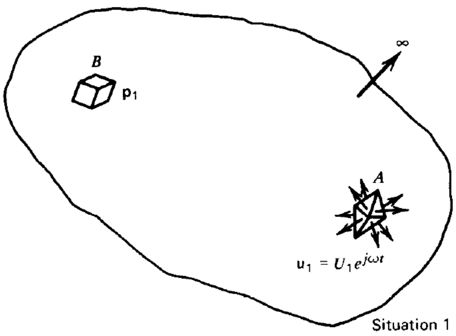

Figure 2.1: p_1 is the pressure at B when source A is active with a velocity $\vec{u_1}$(page 174 [9])

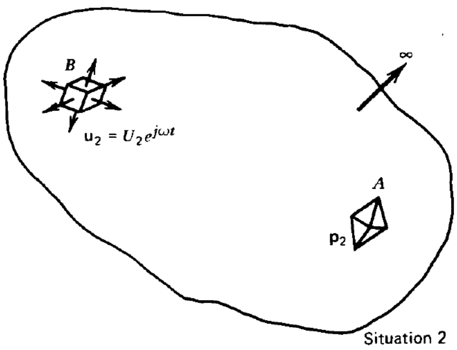

Figure 2.2: p_2 is the pressure at A when source B is active with a velocity $\vec{u_2}$ (page 174 [9])

The complex source strength Q is defined as:

$$Q \exp{(j\omega t)} = \int_S \vec{u} \,.\, \hat{n} \, dS \tag{2.15}$$

Therefore, substituting 2.15 and 2.12 into 2.14 gives:

$$\frac{Q_1}{P_1(r)} = \frac{Q_2}{P_2(r)} \tag{2.16}$$

with

$$p(r) = P(r) \exp j(\omega t - kr) \tag{2.17}$$

If the example of a pulsating sphere of radius a and amplitude velocity U_0 vibrating in an infinite, homogenous and isotropic medium is taken, it is possible to find that the source strength Q of this pulsating sphere is a real number such that:

$$Q = 4\pi a^2 U_0 \tag{2.18}$$

and that the pressure generated at a distance r is

$$p = \frac{j\rho_0 \omega U_0 a^2}{r} \exp j(\omega t - kr) \tag{2.19}$$

Therefore, if a simple source is in free space, 2.18 and 2.19 show that the ratio 2.16 is always:

$$\frac{Q}{P(r)} = -j \frac{2\lambda r}{\rho_0 c} \tag{2.20}$$

Introducing in 2.20 the expression of P(r) found for 2.12 , the expression of Q becomes

$$Q = -j\frac{2\lambda r}{\rho_0 c} \times -j\frac{\rho_0 \alpha \omega}{r} \tag{2.21}$$

$$Q = -4\pi\alpha \tag{2.22}$$

As Q is also equal to the complex volume velocity $\frac{\partial V}{\partial t} = \int_S \vec{u} \,.\, \hat{n} \, dS$, thus

$$Q = S \times U_0 \tag{2.23}$$

with S the area of the source and U_0 the maximum velocity over the surface S.

Finally the expression for α is obtained with 2.22 and 2.23:

$$\alpha = \frac{S \times U_0}{4\pi} \tag{2.24}$$

Pressure and polar directivity pattern of a monopole sound source

The expressions 2.12 and 2.24 give the pressure generated by a Zero-Order Gradient sound source-omnidirectional:

$$p(r) = -\frac{j\rho_0 U_0 Skc}{4\pi r} \exp j(\omega t - kr) \tag{2.25}$$

Extracting the real part gives:

$$p(r) = \frac{\rho_0 U_0 Skc}{4\pi r} \sin(\omega t - kr) \tag{2.26}$$

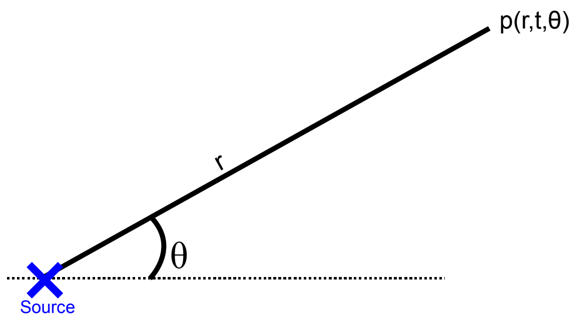

Figure 2.3: Schematic diagram of a Zero-Order gradient sound source

Since the expression 2.26 is independent of θ the angle between the line joining the sound source and the observation point and some reference line as shown on figure 2.3, it is proven that the Zero-Order Gradient sound source radiates equally in all the directions and the polar directional pattern R_θ is constant (see Figure 2.4):

$$R_\theta = K \tag{2.27}$$

Thus the expression 2.26 is a good analytical model to simulate the behavior of an omnidirectional sound source like subwoofers.
The next sections of this chapter aims to present the analytical models of different First and Second-Order Gradient sound sources that use different combinations of Zero-Order Gradient sound sources.

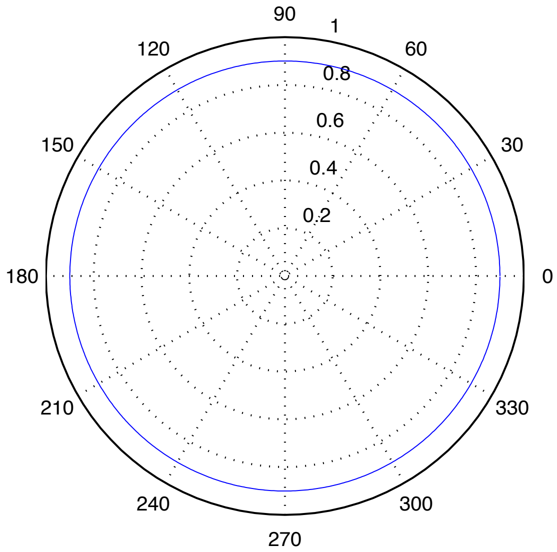

Figure 2.4: Polar directivity pattern of a Zero-Order gradient sound source

2.3 First-order gradient sound source: Bidirectional

The First-Order gradient sound radiator with bidirectional characteristics consists of two Zero-Order Gradient sound sources separated by a small distance D and operating with $180\,^\circ$ difference in phase as shown in Figure .

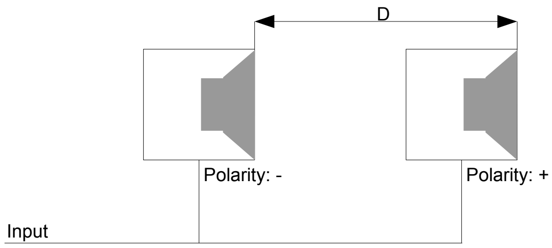

Figure 2.5: Schematic diagram of a First-Order gradient sound source-bidirectional

The goal of this section is to calculate the pressure generated by this setup in far field and its polar directivity pattern.

Approximations

Figure 2.6 shows the setup for a First-order gradient sound source-bidirectional with a geometrical point of view.
The far field approximation gives:

- $D << r$
- $\Delta r << r$
- $\Delta r_1 \approx \Delta r_2 \approx \frac{D}{2} \cos \theta = \Delta r$

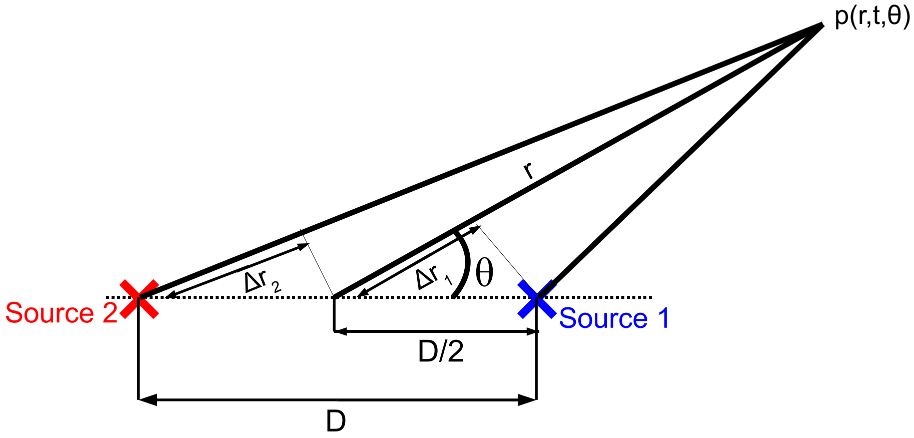

Figure 2.6: Geometrical diagram of a First-Order gradient sound source-bidirectional

Pressure radiated by a First-Order gradient sound source-bidirectional

According to equation 2.25, the pressures generated by sources 1 and 2 at a distance r are respectively:

$$p_1(r) = -\frac{j\rho_0 U_0 Skc}{4\pi(r - \Delta r_1)} \exp j(\omega t - k(r - \Delta r_1)) \tag{2.28}$$

$$p_2(r) = -\frac{j\rho_0 U_0 Skc}{4\pi(r + \Delta r_2)} \exp j(\omega t - k(r + \Delta r_2)) \tag{2.29}$$

The resulting pressure at a distance r is the sum of p_1 2.28 and p_2 2.29 with a coefficient of multiplication of -1 for p_2 in order to model the 180 ° difference of phase between both sources.

$$\begin{aligned} p(r) &= p_1(r) + (-1) \times p_2(r) \\ &= -\tfrac{j\rho_0 U_0 Skc}{4\pi(r-\Delta r_1)} \exp j(\omega t - k(r - \Delta r_1)) + \tfrac{j\rho_0 U_0 Skc}{4\pi(r+\Delta r_2)} \exp j(\omega t - k(r + \Delta r_2)) \\ &= -\tfrac{j\rho_0 U_0 Skc}{4\pi r}[\tfrac{\exp(jk\Delta r)}{1-\frac{\Delta r}{r}} - \tfrac{\exp(-jk\Delta r)}{1+\frac{\Delta r}{r}}] \exp j(\omega t - kr) \\ &= -\tfrac{j\rho_0 U_0 Skc}{4\pi r}[\exp(jk\Delta r) - \exp(-jk\Delta r)] \exp j(\omega t - kr) \\ &= -\tfrac{j\rho_0 U_0 Skc}{4\pi r} \times 2j \sin(k\Delta r) \exp j(\omega t - kr) \end{aligned}$$

So finally, the pressure generated by a First-Order gradient sound source-bidirectional is:

$$p(r) = 2\frac{\rho_0 U_0 Skc}{4\pi r} \times \sin(k\frac{D}{2}\cos\theta) \exp j(\omega t - kr) \tag{2.30}$$

Extracting the real part from 2.36 gives:

$$p(r) = 2\frac{\rho_0 U_0 Skc}{4\pi r} \times \sin(k\frac{D}{2}\cos\theta) \cos(\omega t - kr) \tag{2.31}$$

The polar directivity pattern of a First-Order gradient sound source-bidirectional is:

$$R_\theta = \sin(k\frac{D}{2}\cos\theta) \tag{2.32}$$

2.4 First-order gradient sound source: Unidirectional

The First-order gradient sound source with unidirectional characteristic consists of two Zero-Order gradient sound sources separated by a small distance $\frac{D}{2}$ operating with 180° difference in phase and with a delay to one of the source as shown on Figure 2.7

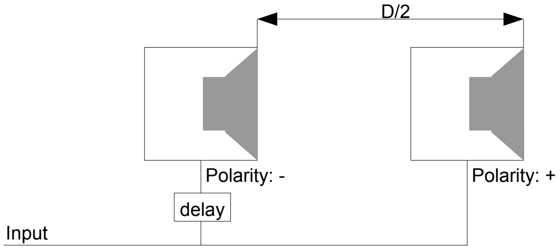

Figure 2.7: Schematic diagram of a First-Order gradient sound source-unidirectional

Delay

The action of delaying can be thought in time domain or in space. Delaying in the time domain a loudspeaker is equivalent to move it physically in the space. Let x be a sound signal such that $x(t) = f(\omega t)$. If a delay of Δt is applied to this signal, then x(t) becomes $x(t - \Delta t) = f(\omega(t - \Delta t))$. As $\omega = kc$, it is possible to write $\omega(t - \Delta t) = \omega t - kc\Delta t$. With c the celerity of the sound in the considered medium. By definition

$$c = \frac{distance}{\Delta t} \tag{2.33}$$

Therefore $\omega(t - \Delta t) = \omega t - k \times distance$.
For convenience in the way for expressing the polar directivity pattern, the delay will be applied in the space domain in the next part of this section.

Pressure radiated by a First-Order Gradient sound source-unidirectional

Figure 2.8 shows the setup for a First-Order Gradient sound source-unidirectional with a geometrical point of view. The approximations already discussed in 2.3 are still valid in this section.
In order to simplify the calculations, instead of applying a delay of $\frac{d}{2}$ meters to source 2, it is preferred to delay source 2 of only $\frac{d}{4}$ meters and advance source on of $\frac{d}{4}$ meters.
Therefore, using equation 2.25,the pressure generated by sources 1 and 2 at a distance r are respectively:

$$p_1(r) = -\frac{j\rho_0 U_0 Skc}{4\pi(r - \Delta r_1)} \exp j(\omega t - k(r - \Delta r_1 - \frac{d}{4})) \tag{2.34}$$

$$p_2(r) = -\frac{j\rho_0 U_0 Skc}{4\pi(r + \Delta r_2)} \exp j(\omega t - k(r + \Delta r_2 + \frac{d}{4})) \tag{2.35}$$

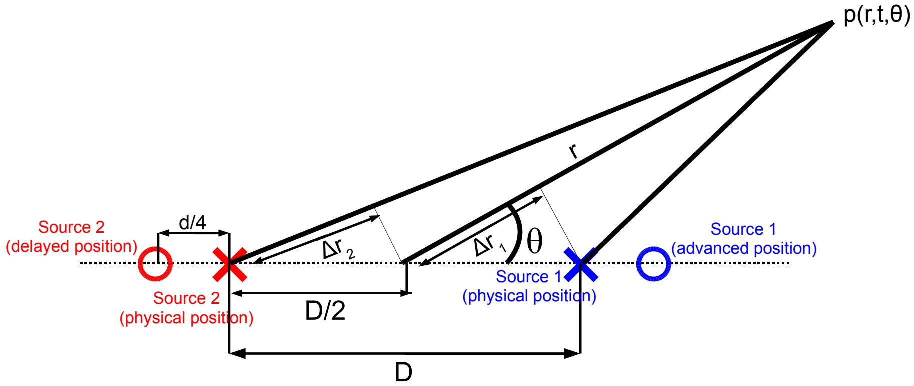

Figure 2.8: Geometrical diagram of a First-Order gradient sound source-unidirectional

The resulting pressure at a distance r is the sum of p_1 2.34and p_2 2.35 with a coefficient of multiplication of -1 for p_2 in order to model the 180 ° difference of phase between both sources.

$$\begin{aligned}
p(r) &= p_1(r) + (-1) \times p_2(r) \\
&= -\tfrac{j\rho_0 U_0 Skc}{4\pi(r-\Delta r_1)} \exp j(\omega t - k(r - \Delta r_1 - \tfrac{d}{4})) + \tfrac{j\rho_0 U_0 Skc}{4\pi(r+\Delta r_2)} \exp j(\omega t - k(r + \Delta r_2 + \tfrac{d}{4})) \\
&= -\tfrac{j\rho_0 U_0 Skc}{4\pi r} [\tfrac{\exp(jk\Delta r + j\frac{kd}{4})}{1-\frac{\Delta r}{r}} - \tfrac{\exp(-jk\Delta r - j\frac{kd}{4})}{1+\frac{\Delta r}{r}}] \exp j(\omega t - kr) \\
&= -\tfrac{j\rho_0 U_0 Skc}{4\pi r} [\exp(jk\Delta r + j\tfrac{kd}{4}) - \exp(-jk\Delta r - j\tfrac{kd}{4})] \exp j(\omega t - kr) \\
&= -\tfrac{j\rho_0 U_0 Skc}{4\pi r} \times 2j \sin(k\Delta r + \tfrac{kd}{4}) \exp j(\omega t - kr)
\end{aligned}$$

So finally, the pressure generated by a First-Order gradient sound source-unidirectional is:

$$p(r) = 2\frac{\rho_0 U_0 Skc}{4\pi r} \times \sin(k\frac{d}{4} + k\frac{D}{4}\cos\theta) \exp j(\omega t - kr) \tag{2.36}$$

Extracting the real part from 2.36 gives:

$$p(r) = 2\frac{\rho_0 U_0 Skc}{4\pi r} \times \sin(k\frac{d}{4} + k\frac{D}{4}\cos\theta) \cos j(\omega t - kr) \tag{2.37}$$

The polar directivity pattern of a First-Order gradient sound source-unidirectional is:

$$R_\theta = \sin(k\frac{d}{4} + k\frac{D}{4}\cos\theta) \tag{2.38}$$

2.5 Second-order gradient sound source: Unidirectional

The Second-Order gradient sound source with unidirectional characteristics consists of two First-Order gradient sound sources with bidirectional characteristics separated by a small distance $\frac{D}{2}$ operating with 180 ° difference of phase and with a delay to one of the First-Order units as shown on Figure 2.9.

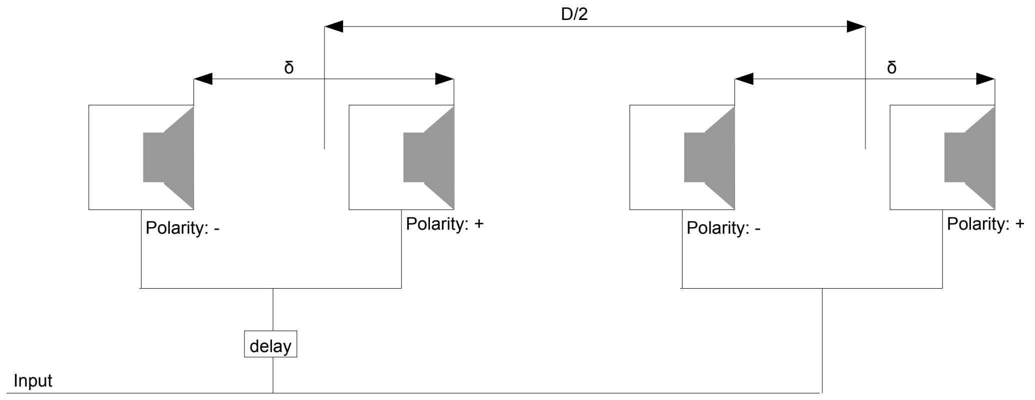

Figure 2.9: Schematic diagram of a Second-Order gradient sound source-unidirectional

Figure 2.10 shows the setup for a Second-order gradient sound source-unidirectional with a geometrical point of view. The approximations introduced in section 2.3 are still considered here

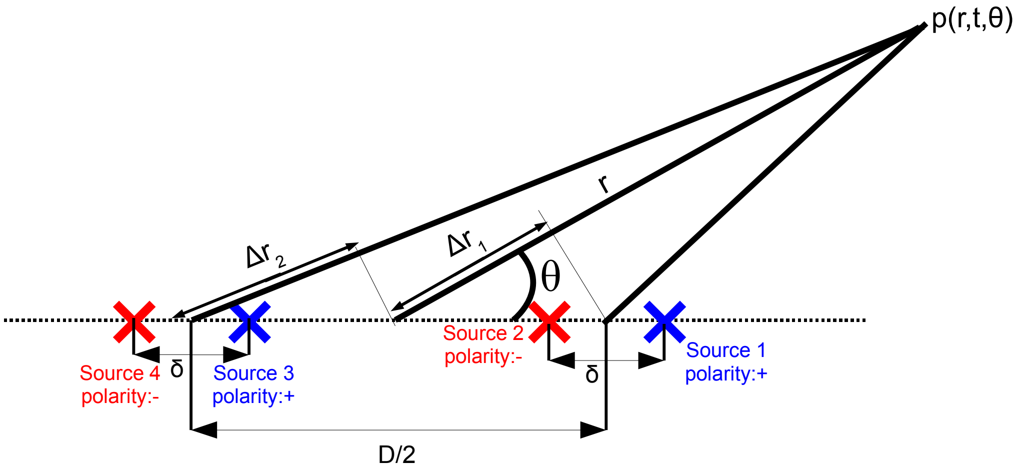

Figure 2.10: Geometrical diagram of a Second-Order gradient sound source-unidirectional

as well as the paragraph about delay in section 2.4. The pressure in far field generated by each units of First-Order gradient sound source-bidirectional is given by 2.36 from section 2.3. When including a delay of $\frac{d}{4}$ to units 2 and an advance of $\frac{d}{4}$ to unit 1, therefore the pressures produced by units 1 and unit 2 in far field are respectively:

$$p_1(r) = 2\frac{\rho_0 U_0 Skc}{4\pi r} \times \sin{(k\frac{\delta}{2}\cos\theta)} \exp j(\omega t - k(r - \Delta r - \frac{d}{4})) \tag{2.39}$$

$$p_2(r) = 2\frac{\rho_0 U_0 Skc}{4\pi r} \times \sin{(k\frac{\delta}{2}\cos\theta)} \exp j(\omega t - k(r + \Delta r + \frac{d}{4})) \tag{2.40}$$

The resulting pressure at a distance r is the sum of p_1 2.39and p_2 2.40 with a coefficient of multiplication of -1 for p_2 in order to model the 180$\,^\circ$ difference of phase between both sources.

$$
\begin{aligned}
p(r) &= p_1(r) + (-1) \times p_2(r) \\
&= 2\tfrac{\rho_0 U_0 Skc}{4\pi r} \times \sin(k\tfrac{\delta}{2}\cos\theta)\exp j(\omega t - k(r - \Delta r - \tfrac{d}{4})) \\
&\quad -2\tfrac{\rho_0 U_0 Skc}{4\pi r} \times \sin(k\tfrac{\delta}{2}\cos\theta)\exp j(\omega t - k(r + \Delta r + \tfrac{d}{4})) \\
&= 2\tfrac{\rho_0 U_0 Skc}{4\pi r} \times \sin(k\tfrac{\delta}{2}\cos\theta)[\tfrac{\exp(jk\Delta r + j\frac{kd}{4})}{1-\frac{\Delta r}{r}} - \tfrac{\exp(-jk\Delta r - j\frac{kd}{4})}{1+\frac{\Delta r}{r}}]\exp j(\omega t - kr) \\
&= 2\tfrac{\rho_0 U_0 Skc}{4\pi r} \times \sin(k\tfrac{\delta}{2}\cos\theta)[\exp(jk\Delta r + j\tfrac{kd}{4}) - \exp(-jk\Delta r - j\tfrac{kd}{4})]\exp j(\omega t - kr) \\
&= 2\tfrac{\rho_0 U_0 Skc}{4\pi r} \times \sin(k\tfrac{\delta}{2}\cos\theta) \times 2j\sin(k\Delta r + j\tfrac{kd}{4})\exp j(\omega t - kr)
\end{aligned}
$$

So finally the pressure generated by a Second-Order Gradient source- unidirectional is:

$$p(r) = 4j\frac{\rho_0 U_0 Skc}{4\pi r} \times \sin(k\frac{\delta}{2}\cos\theta) \times \sin(k\frac{D}{4}\cos\theta + \frac{kd}{4})\exp j(\omega t - kr) \quad (2.41)$$

Extracting the real part from 2.41 gives:

$$p(r) = -4\frac{\rho_0 U_0 Skc}{4\pi r} \times \sin(k\frac{\delta}{2}\cos\theta) \times \sin(k\frac{D}{4}\cos\theta + \frac{kd}{4})\sin(\omega t - kr) \quad (2.42)$$

The polar directivity pattern of a Second-Order gradient sound source-unidirectional is:

$$R_\theta = \sin(k\frac{\delta}{2}\cos\theta)\sin(k\frac{D}{4}\cos\theta + \frac{kd}{4}) \quad (2.43)$$

2.6 Simulations and analysis of the results

In sections 2.2, 2.3, 2.4 and 2.5, the expressions of the pressure and the directivity pattern have been determined for different orders of gradient sound sources. In this section, different simulations are carried out, in order to determine the influences of the frequency and the distance between the sound sources on the pressure emitted ”on-axis” and on the polar directivity pattern for each order of gradient.

2.6.1 Zero-Order Gradient sound source-omnidirectional

As already discussed in section 2.2, equation 2.26 shows that this order of gradient radiates equally in all the directions and thus has a constant polar directional pattern for all the frequencies as shown on figure 2.4.

The frequency response of the sound pressure delivered by a Zero-Order Gradient source following equation 2.26 - assuming that $\rho_0 U_0 Skc$ is independent of the frequency - is independent of the frequency as shown on figure 2.11.

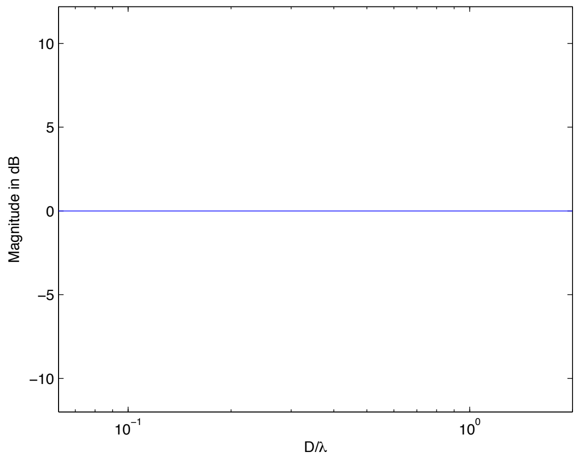

Figure 2.11: The frequency response of the sound pressure produced on-axis by a Zero-Order gradient source

2.6.2 First-Order Gradient sound source-bidirectional

The frequency response of the sound pressure produced on-axis (for $\theta = 0°$) by a bidirectional First-Order gradient sound source employing to simple sound sources is shown on figure 2.12.

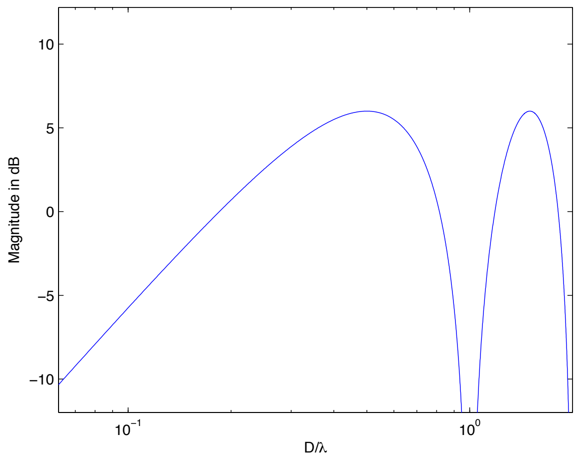

Figure 2.12: The frequency response of the sound pressure produced on-axis by a First-Order gradient source-bidirectional

The polar directional pattern for a First-Order Gradient sound source-bidirectional is given by the equation 2.32.
Changing k by $\frac{2\pi}{\lambda}$ in 2.32 leads to a new expression of the directional pattern 2.44:

$$R_\theta = \sin\left(\pi \frac{D}{\lambda} \cos\theta\right) \tag{2.44}$$

The polar directivity 2.44 is now expressed in function of the ratio between the distance separating the two simple sound sources and the wavelength.

Figure 2.13 shows the polar directional patterns for different values of $\frac{D}{\lambda}$.

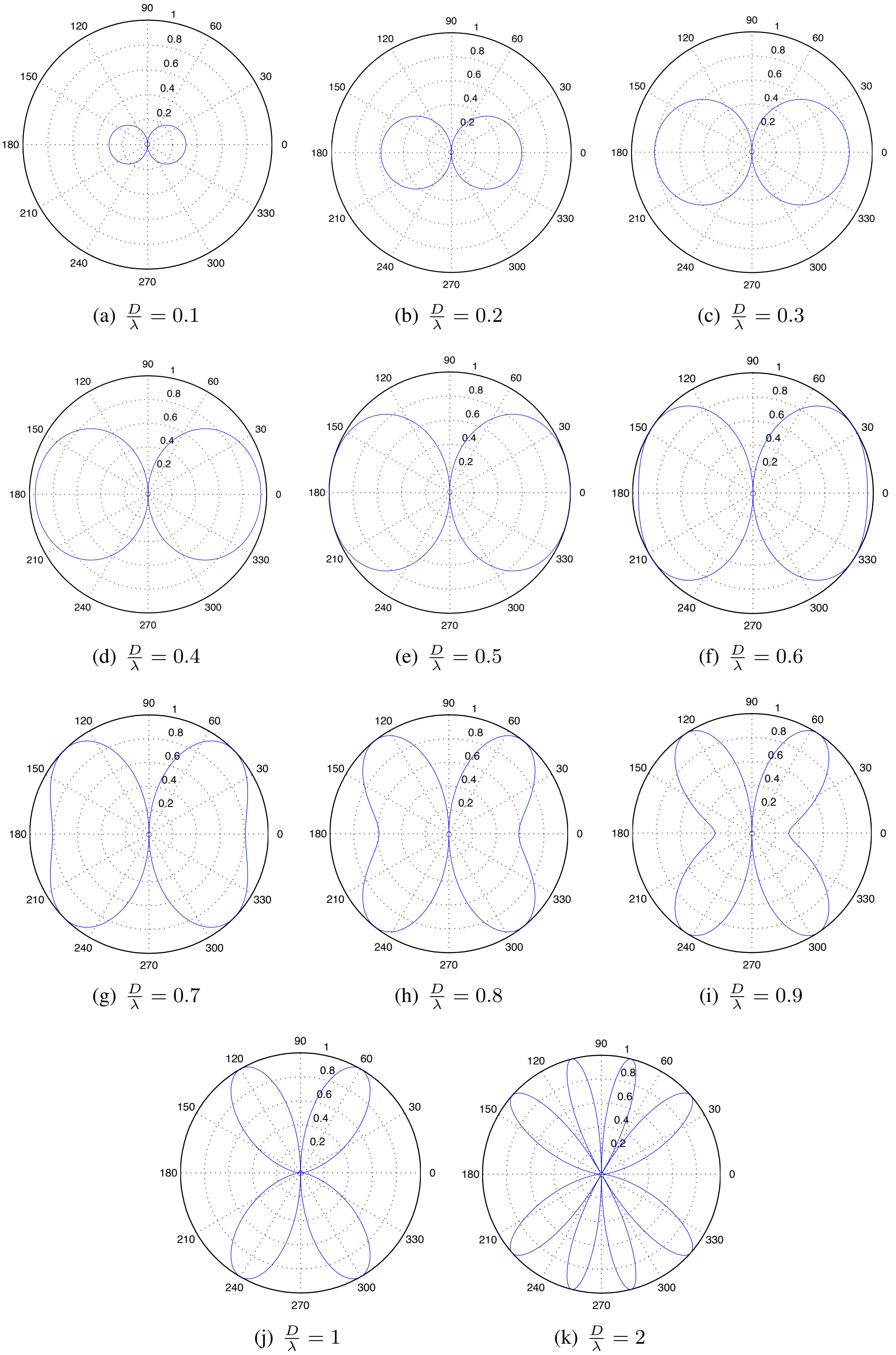

(a) $\frac{D}{\lambda} = 0.1$ (b) $\frac{D}{\lambda} = 0.2$ (c) $\frac{D}{\lambda} = 0.3$

(d) $\frac{D}{\lambda} = 0.4$ (e) $\frac{D}{\lambda} = 0.5$ (f) $\frac{D}{\lambda} = 0.6$

(g) $\frac{D}{\lambda} = 0.7$ (h) $\frac{D}{\lambda} = 0.8$ (i) $\frac{D}{\lambda} = 0.9$

(j) $\frac{D}{\lambda} = 1$ (k) $\frac{D}{\lambda} = 2$

Figure 2.13: Polar directivity pattern for a First-Order gradient sound source-bidirectional for different values of $\frac{D}{\lambda}$

For $\frac{D}{\lambda} < \frac{1}{4}$, the polar directivity is a cosine pattern as shown on subfigures G.8(g) and A.12(a). When $\frac{D}{\lambda} = \frac{1}{2}$ the polar directivity is broader than a cosine (see subfigure A.15(a)) and if the ratio $\frac{D}{\lambda}$ is higher than $\frac{1}{2}$ more lobes start to appear. With $\frac{D}{\lambda} = 1$ the polar directivity has four lobes and with $\frac{D}{\lambda} = 2$ the polar directivity has eight lobes.

2.6.3 First-Order Gradient sound source-unidirectional

The frequency response of the sound pressure produced on-axis (for $\theta = 0\,°$) by an unidirectional First-Order gradient sound source is shown on figure 2.14.

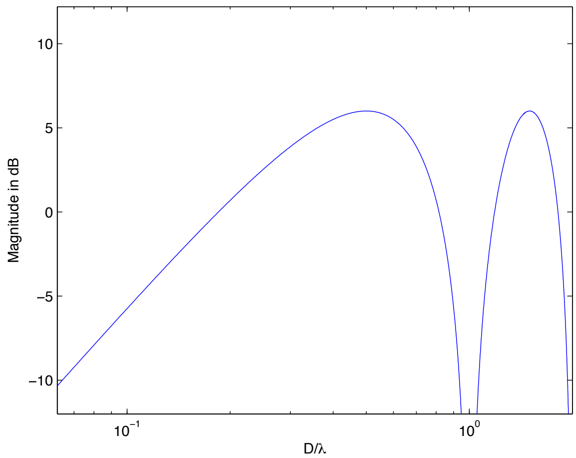

Figure 2.14: The frequency response of the sound pressure produced on-axis by a First-Order gradient source-unidirectional for d=D

The polar directional pattern expressed as a function of the ratio $\frac{D}{\lambda}$ and $\frac{d}{\lambda}$ is given by equation 2.45:

$$R_\theta = \sin\left(\pi \frac{d}{2\lambda} + \pi \frac{D}{2\lambda} \cos\theta\right) \tag{2.45}$$

If $d = D$, then equation 2.45 becomes:

$$R_\theta = \sin\left(\pi \frac{D}{2\lambda}(1 + \cos\theta)\right) \tag{2.46}$$

Equation 2.46 is the polar equation of a cardioid. Figure 2.15 shows the polar directional pattern modeled by equation 2.46 for different values of $\frac{D}{\lambda}$.

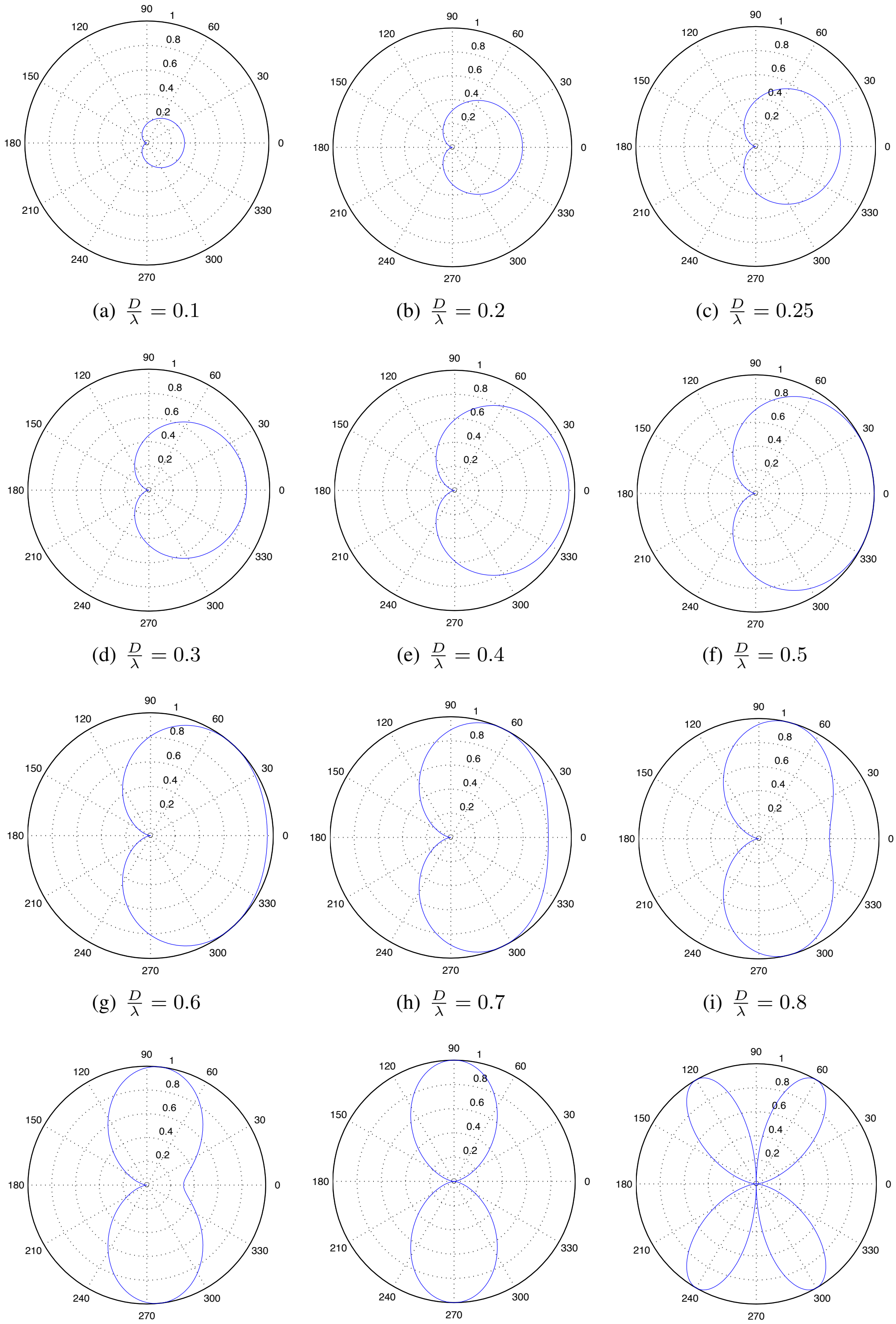

(a) $\frac{D}{\lambda} = 0.1$ (b) $\frac{D}{\lambda} = 0.2$ (c) $\frac{D}{\lambda} = 0.25$

(d) $\frac{D}{\lambda} = 0.3$ (e) $\frac{D}{\lambda} = 0.4$ (f) $\frac{D}{\lambda} = 0.5$

(g) $\frac{D}{\lambda} = 0.6$ (h) $\frac{D}{\lambda} = 0.7$ (i) $\frac{D}{\lambda} = 0.8$

(j) $\frac{D}{\lambda} = 0.9$ (k) $\frac{D}{\lambda} = 1$ (l) $\frac{D}{\lambda} = 2$

Figure 2.15: Polar directivity pattern for a First-Order gradient sound source-Unidirectional for different values of $\frac{D}{\lambda}$ and with D=d

The polar directivity for $\frac{D}{\lambda} < \frac{1}{4}$ is a cardioid (see figures 2.15(a), 2.15(b) and 2.15(c)). Then, the polar directivity is broader than a cardioid for $\frac{D}{\lambda} = \frac{1}{2}$ (see figures 2.15(f)). When $\frac{D}{\lambda}$ continues to increase until 1, the pressure on the front tends to diminish while on the sides it tends to increase, leading to two lateral lobes for $\frac{D}{\lambda} = 1$. For $\frac{D}{\lambda} = 2$ four lobes are obtained.

Figures 2.16 and 2.17 show more polar directional patterns based on equation 2.45.
Starting from the case of a perfect cardioid model with $\frac{D}{\lambda} = \frac{d}{\lambda} = \frac{1}{4}$, subfigures of 2.16 are obtained by keeping $\frac{D}{\lambda}$ constant equal to 0.25 and $\frac{d}{\lambda}$ varying from 0.1 to 1.

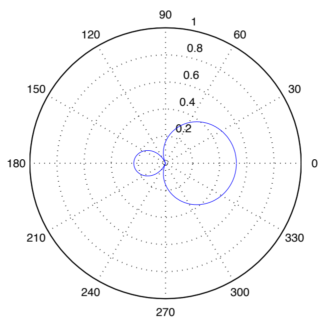

(a) $\frac{d}{\lambda} = 0.1$

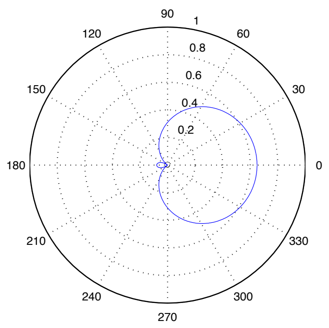

(b) $\frac{d}{\lambda} = 0.2$

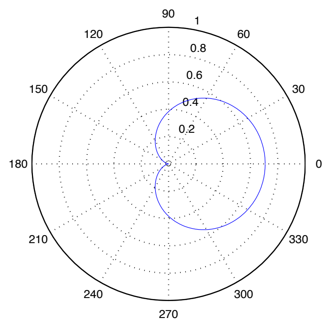

(c) $\frac{d}{\lambda} = 0.25$

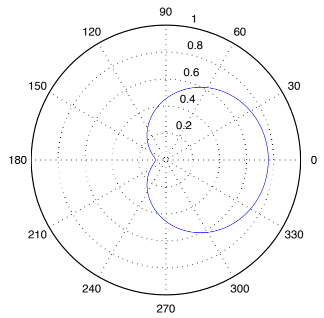

(d) $\frac{d}{\lambda} = 0.3$

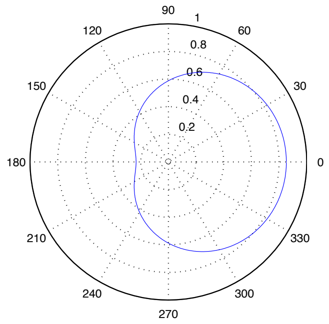

(e) $\frac{d}{\lambda} = 0.4$

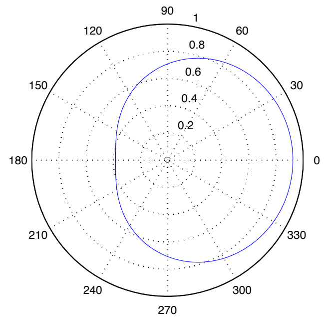

(f) $\frac{d}{\lambda} = 0.5$

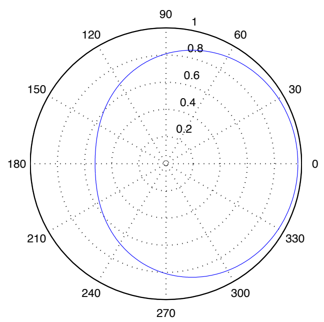

(g) $\frac{d}{\lambda} = 0.6$

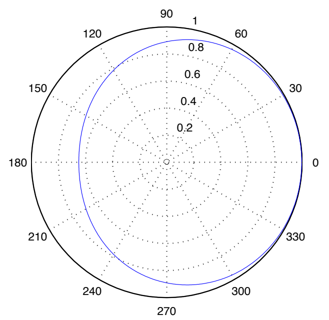

(h) $\frac{d}{\lambda} = 0.7$

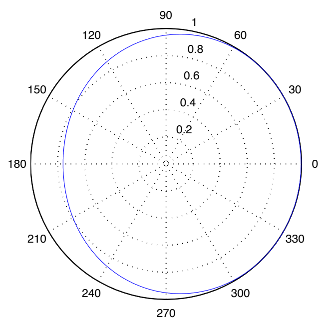

(i) $\frac{d}{\lambda} = 0.8$

Figure 2.16: Polar directivity pattern for a First-Order gradient sound source-Unidirectional for different values of $\frac{d}{\lambda}$ with $\frac{D}{\lambda} = 0.25$

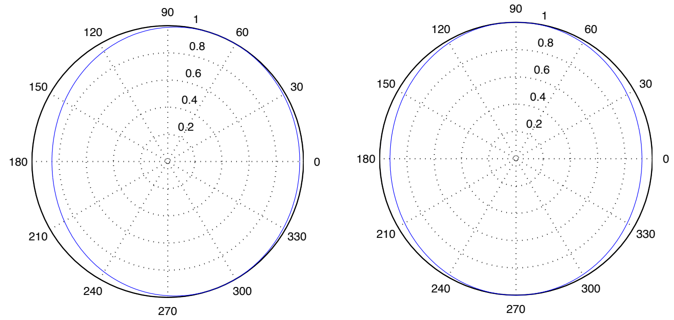

(j) $\frac{d}{\lambda} = 0.9$ (k) $\frac{d}{\lambda} = 1$

Figure 2.16: Polar directivity pattern for a First-Order gradient sound source-Unidirectional for different values of $\frac{d}{\lambda}$ with $\frac{D}{\lambda} = 0.25$

On figure 2.17 the delay d is kept constant so that $\frac{d}{\lambda} = \frac{1}{4}$ while $\frac{D}{\lambda}$ varies from 0.1 to 1.

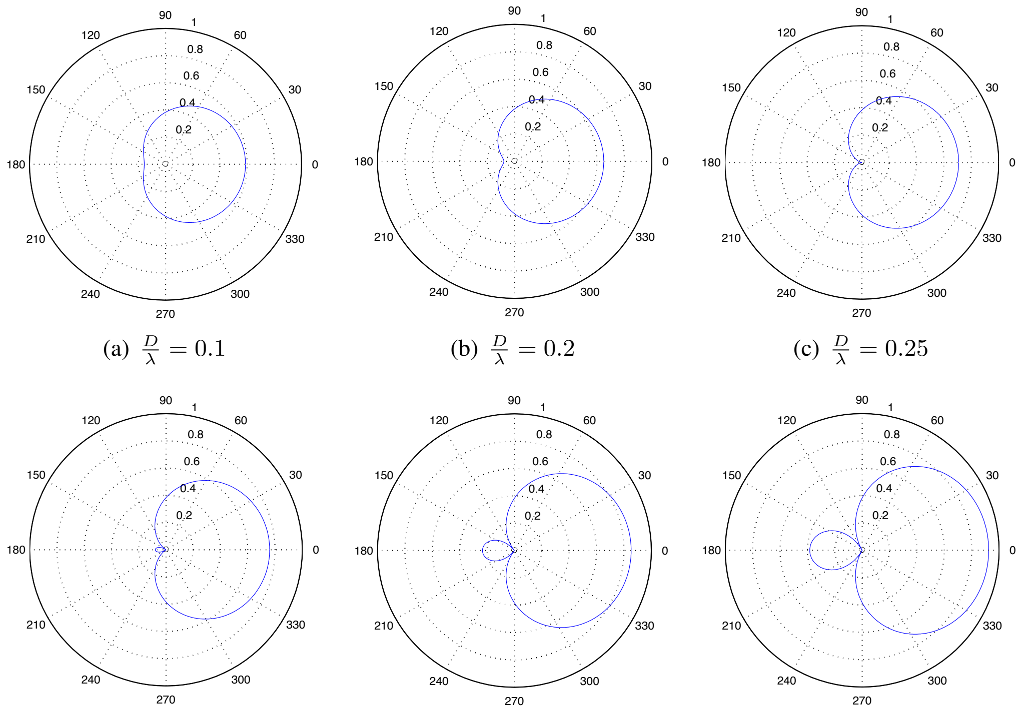

(a) $\frac{D}{\lambda} = 0.1$ (b) $\frac{D}{\lambda} = 0.2$ (c) $\frac{D}{\lambda} = 0.25$

(d) $\frac{D}{\lambda} = 0.3$ (e) $\frac{D}{\lambda} = 0.4$ (f) $\frac{D}{\lambda} = 0.5$

Figure 2.17: Polar directivity pattern for a First-Order gradient sound source-Unidirectional for different values of $\frac{D}{\lambda}$ with $\frac{d}{\lambda} = 0.25$

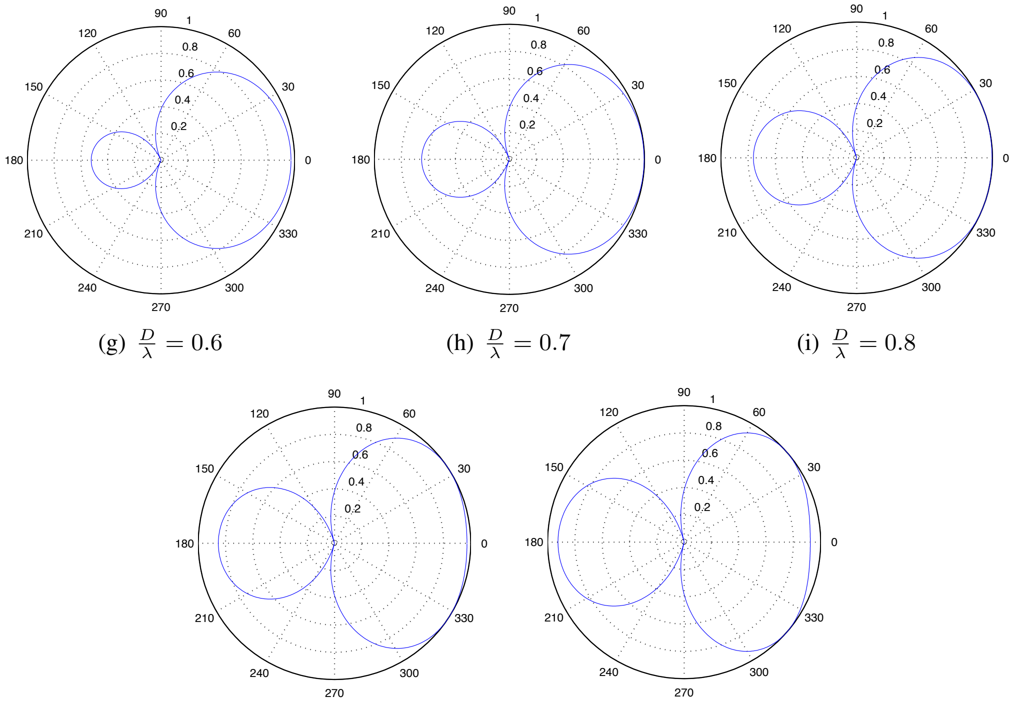

(g) $\frac{D}{\lambda} = 0.6$ (h) $\frac{D}{\lambda} = 0.7$ (i) $\frac{D}{\lambda} = 0.8$

(j) $\frac{D}{\lambda} = 0.9$ (k) $\frac{D}{\lambda} = 1$

Figure 2.17: Polar directivity pattern for a First-Order gradient sound source-Unidirectional for different values of $\frac{D}{\lambda}$ with $\frac{d}{\lambda} = 0.25$

2.6.4 Second-Order Gradient sound source-unidirectional

The frequency response of the sound pressure produced on-axis (for $\theta = 0\,°$) by an unidirectional Second-Order gradient sound source is shown on figure 2.18.

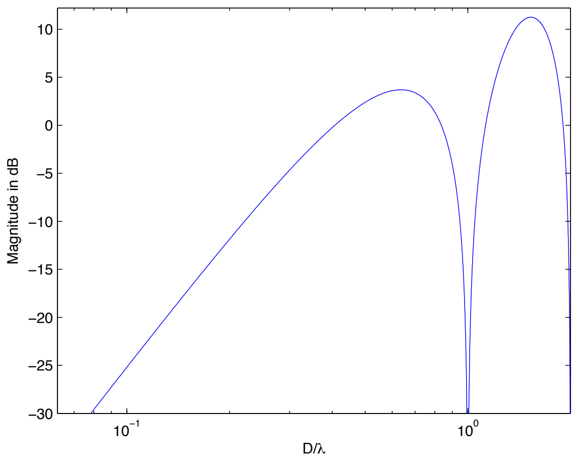

Figure 2.18: Schematic diagram of a First-Order gradient sound source-bidirectional

The polar directional pattern of a Second-Order gradient source is described by equation 2.43.

Assuming that $d = D$ and $\Delta = \frac{D}{4}$ equation 2.43 becomes:

$$R_\theta = \sin\left(\frac{\pi}{4}\frac{D}{\lambda}\cos\theta\right)\sin\left(\frac{\pi}{2}\frac{D}{\lambda}\cos\theta + \frac{\pi}{2}\frac{D}{\lambda}\right) \tag{2.47}$$

Figure 2.19 shows the polar directivity of a Second-Order gradient source modeled by equation 2.47 for different values of $\frac{D}{\lambda}$.

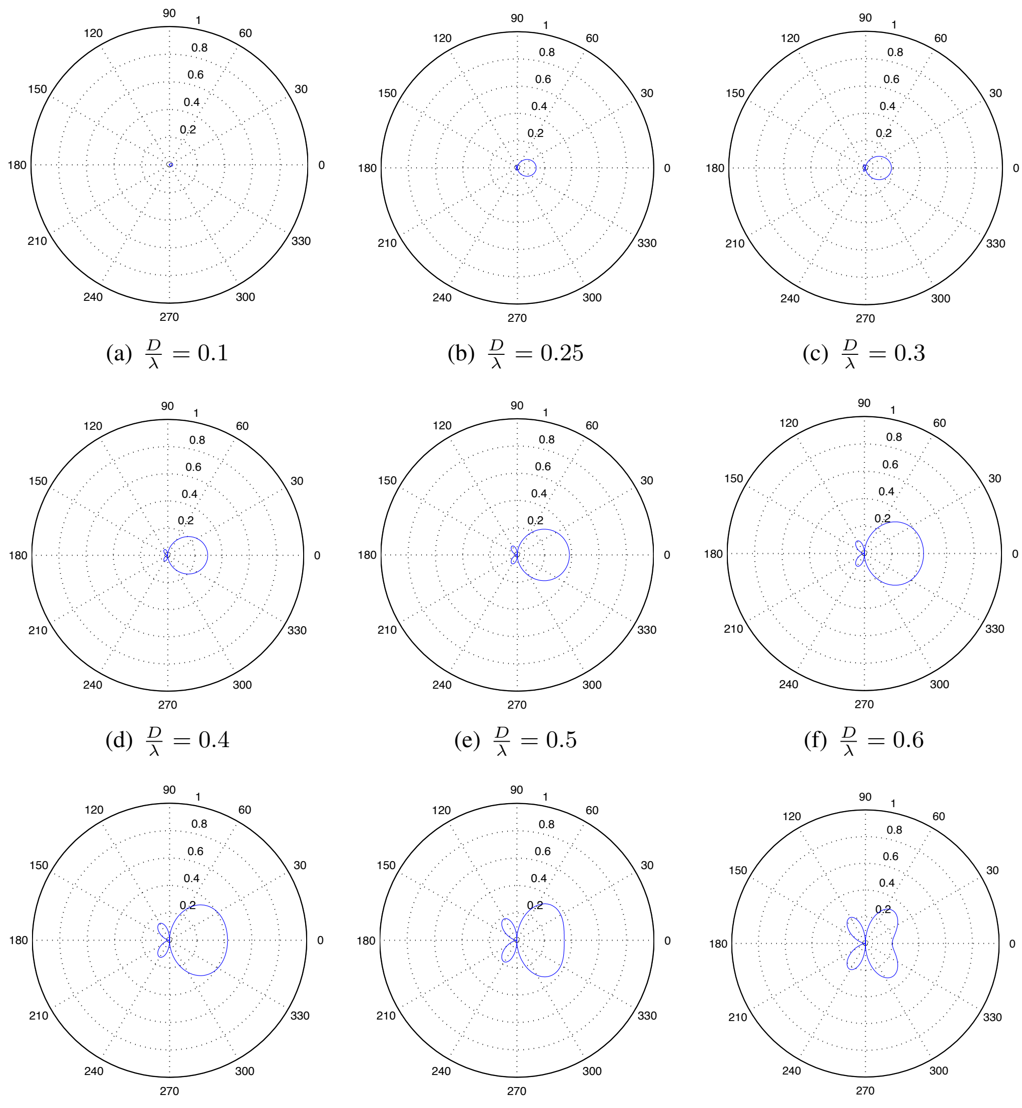

(a) $\frac{D}{\lambda} = 0.1$ (b) $\frac{D}{\lambda} = 0.25$ (c) $\frac{D}{\lambda} = 0.3$

(d) $\frac{D}{\lambda} = 0.4$ (e) $\frac{D}{\lambda} = 0.5$ (f) $\frac{D}{\lambda} = 0.6$

(g) $\frac{D}{\lambda} = 0.7$ (h) $\frac{D}{\lambda} = 0.8$ (i) $\frac{D}{\lambda} = 0.9$

Figure 2.19: Polar directivity pattern for a Second-Order gradient sound source-Unidirectional for different values of $\frac{D}{\lambda}$

The polar directivity pattern is a cosine multiply by a cardioid in the frequency region below $\frac{D}{\lambda} < \frac{1}{4}$. It is broader at $\frac{D}{\lambda} = \frac{1}{2}$. For $\frac{D}{\lambda} = 1$ and $\frac{D}{\lambda} = 2$, the directivity pattern has four lobes. For $1 < \frac{D}{\lambda} < 2$ the polar directivity has successively five, three and four lobes.

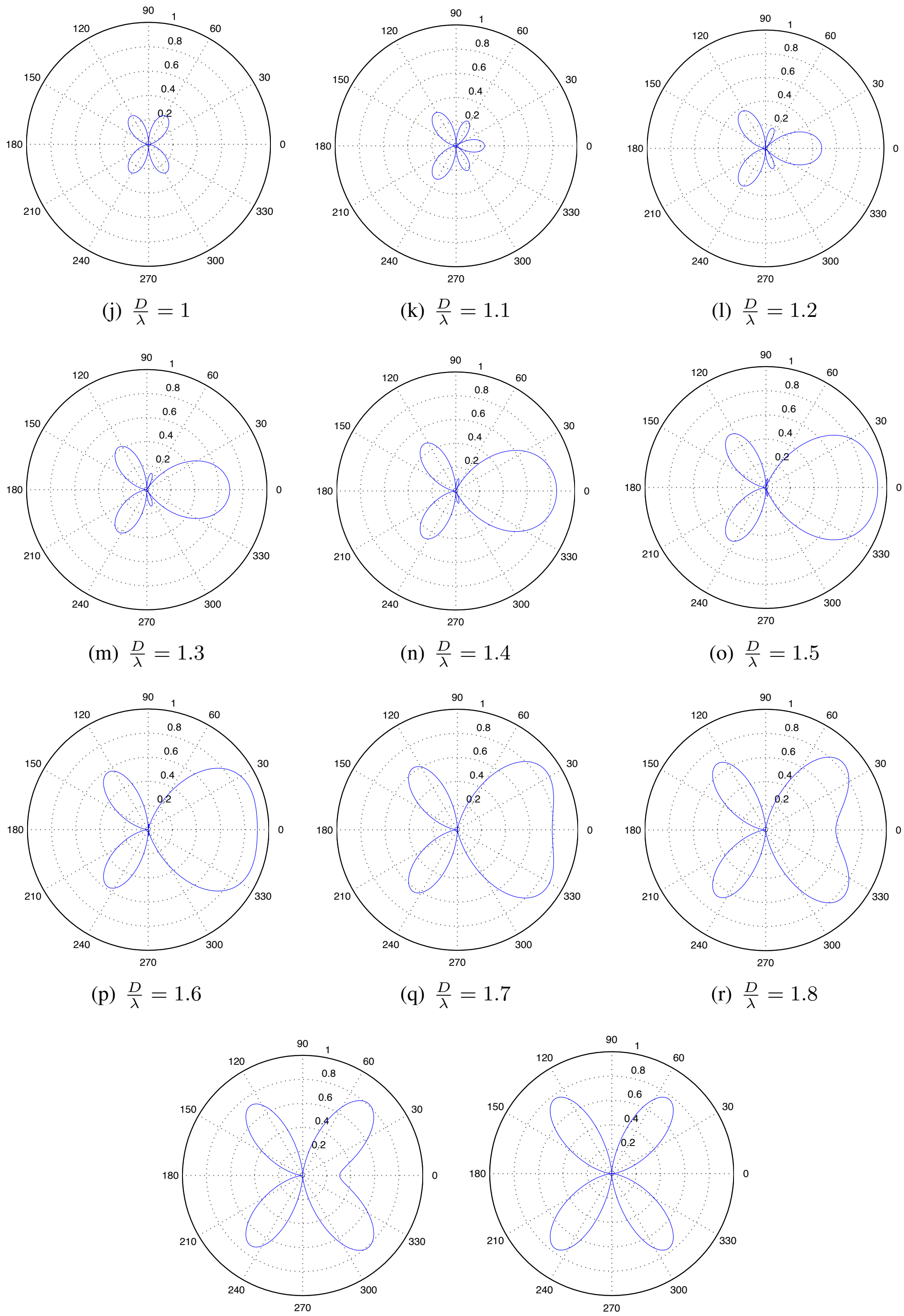

(j) $\frac{D}{\lambda} = 1$ (k) $\frac{D}{\lambda} = 1.1$ (l) $\frac{D}{\lambda} = 1.2$

(m) $\frac{D}{\lambda} = 1.3$ (n) $\frac{D}{\lambda} = 1.4$ (o) $\frac{D}{\lambda} = 1.5$

(p) $\frac{D}{\lambda} = 1.6$ (q) $\frac{D}{\lambda} = 1.7$ (r) $\frac{D}{\lambda} = 1.8$

(s) $\frac{D}{\lambda} = 1.9$ (t) $\frac{D}{\lambda} = 2$

Figure 2.19: Polar directivity pattern for a Second-Order gradient sound source-Unidirectional for different values of $\frac{D}{\lambda}$

2.6.5 Analysis

Magnitude on-axis

Figures 2.12, 2.14 and 2.18 shows that the magnitude depends of the ratio $\frac{D}{\lambda}$. In a concrete case, the distance D between two loudspeakers stays constant. So the ratio $\frac{D}{\lambda}$ changes when λ changes and so when the frequency changes.

For a First-Order gradient source-bidirectional and a First-Order gradient source-unidirectional (with D=d), the magnitude presents two deeps for $\frac{D}{\lambda} = 1$ and $\frac{D}{\lambda} = 2$ and two peaks for $\frac{D}{\lambda} = 0.5$ and $\frac{D}{\lambda} = 1.5$. For a Second-Order gradient source (with $\Delta = \frac{D}{4}$ and $D = d$), the magnitude is minimum for $\frac{D}{\lambda} = 1$ and $\frac{D}{\lambda} = 2$ and presents a relative maximum for $0.1 < \frac{D}{\lambda} < 1$ and an absolute maximum for $1 < \frac{D}{\lambda} < 2$.

So when choosing the distance D between both loudspeakers and the delay d, it must be aware that the deeps are not within the frequency range of interest.

Polar directional pattern

Figures 2.13, 2.15, 2.16, 2.17 and 2.19 shows the polar directivity for different orders of gradient and different values of the ratio $\frac{D}{\lambda}$ and $\frac{d}{\lambda}$.

The first observation concerning these figures is that when using two or more loudspeakers associated with pure delay and polarity shift, it is possible to get several kinds of polar directional pattern. So depending on the applications and the conditions where the loudspeakers have to be used lot of possibilities exist to adapt and control the polar directivity.

The second observation is that the polar directional patterns are very sensitive to the ratio $\frac{D}{\lambda}$, and so of the frequency. For a real setup with D constant, the polar pattern changes a lot with the frequency. Therefore when positioning loudspeakers in some way to get a desired pattern, this target pattern will be effectively obtained of a limited frequency range. For the other frequencies, the directional pattern will be more or less close to the desired pattern. So the expressions First-Order gradient source-unidirectional and Second-Order gradient source-unidirectional are only valid in a limited frequency range, for certain values of D and d, and seems to be inappropriate nouns for other frequencies. The main reason of these problems of frequency-dependence is that the delays and polarity shifts applied in this analytical part and then in the simulations are frequency-independent.

Thus, from these different observations it seems interesting to develops algorithms working in real-time and allowing to have delays or polarity shifts depend on the frequency.

Part III

Advanced program for acoustical wave field simulation

3

Review of the existing methods for sound field modelisation

In the previous chapter 2 analytical models of different orders of gradient loudspeakers have been studied. These models are ideal and purely theoretical. Therefore, a new method of sound field simulation closer to the reality should be considered. This simulation tool must be able to model the sound field generated by real loudspeakers working in free field conditions as well as in real room. This chapter aims to make a review of the different existing methods used for sound field modeling in architectural acoustics.

3.1 Geometrical method: Ray tracing and mirror image

Ray tracing and mirror image are two well established techniques for studying the acoustical quality of large closed space. Among the different advantages of these two techniques, the absorption coefficient of the walls can be taken into account and accurate loudspeaker models can be used. Nevertheless these both methods are limited to high frequencies. When the wavelength is comparable to the dimensions of the room their results are not accurate. Therefore ray tracing and mirror image are not appropriate for the low frequency simulations and so for this project.

3.2 Numerical methods

3.2.1 Finite Element Method

The finite element method is a numerical analysis method that gives an approximated solution to the partial differential equation (page 149 [6]). This method is very useful in case of non-linear problems, high sound pressure or when the acoustic domain is non-homogeneous. Allowing the use of accurate loudspeaker models this method helps to determine the acoustic field - and more particularly the complex sound pressure level - in spaces with complex geometry. It is a particularly adapted method to study the low frequency range. Unfortunately each frequency has to be calculated separately. Therefore it is time and memory consuming. Translation to a time domain formulation is possible but also computationally expensive. At last it is a time-independent method, which can be a problem for this project as time delay needs to be used. So the finite element method do not fulfill all the conditions required for this project.

3.2.2 Boundary Element Method

The boundary element method is also a numerical method that calculates the sound radiating by a vibrating body and lets to predict the sound field inside a cavity (car, room, etc...) or the sound scattered by an object. As output the BEM simulation gives the sound pressure distribution, the sound intensity and the sound power. The main advantage of this method is that only the boundary surface (e.g exterior of a vibrating body) needs to be modeled with a mesh (page 157 [6]). Accurate loudspeaker model can thus be used and reflecting surfaces can easily be described by their reflection coefficients and their acoustic impedance. Like the FEM it is a well adapted method for low frequency range. As disadvantage, this method has to calculate each discrete frequencies separately that is time consuming. Moreover it is restricted to linear and homogeneous problems (page 165 [6]). In the same way than for FEM, translation to a time domain formulation is possible but computationally consuming. Therefore, this simulation method is not fully adapted for this project.

3.2.3 Finite-Difference Time-Domain

The Finite-Difference Time-Domain is an other numerical method for solving the acoustic wave equation based on the finite difference approximation for both time and space derivative. The main advantage of this method is that all calculations are done directly in time domain. Therefore, it is possible to know the acoustic pressure and the particle velocity at any time during the simulation for analysis and simulation ([1]). At each position of the space post processing (e.g FFT analysis) are possible. Working in the time domain has also the advantage that the sound source and the signals used during the simulations can also be time dependent. Thus it is easy to model real loudspeaker using their impulse response and directivity pattern. It is a method adapted for low frequency analysis. Its main disadvantage is its problem for describing frequency-dependent material characteristics. This problem can be solved by studying narrow frequency range. At last the computational speed is higher than for the FEM and BEM methods. So regarding the advantages and disadvantages of the different methods presented in this chapter the finite-difference time-domain method will be chosen for the next simulations of this project.

4
Finite-Difference Time-Domain: theory

The finite-difference time-domain method (FDTD) for wave propagation problems is based on a finite-difference approximation for both time and space derivatives in the wave equation. This is a numerical method that lets to simulate the sound field produced by loudspeakers at low-frequency as already discussed in chapter 3. This chapter aims to present the theory supporting this method.

4.1 Equations

The FDTD method utilizes two coupled first-order differential equations [1]. The first equation is the linear continuity equation 2.1 already presented in section 2.2 and valid for acoustic processes of small amplitude:

$$\nabla.\vec{u} = -\frac{1}{\rho_0 c^2}\frac{\partial \vec{p}}{\partial t}$$

The second equation is the Euler equation 2.2 also presented in section 2.2:

$$\nabla p = -\rho_0 \frac{\partial \vec{u}}{\partial t}$$

Since the FDTD method works in the time-domain it calculates the derivative and linearized forms of these two equations in the time domain.

The typical formulation of the FDTD approximation uses a Cartesian staggered grid in which pressure and particle velocity are the unknown quantities. To solve these equations numerically the space and the time are discretized [5]. If the spacial discretization steps are δx, δy and δz and the time step is δt then the acoustical pressure is determined at the grid points ($i\delta x$,$j\delta y$,$k\delta z$) and at time $t = l\delta t$. The indices i, j, k mark the spacial points and index l marks the discrete time as shown on figure 4.1.

The three components of the particle velocity are determined at positions $(i \pm \frac{1}{2})\delta x$, $(j \pm \frac{1}{2})\delta y$, $(k \pm \frac{1}{2})\delta z$ and at intermediate time $t = (l \pm \frac{1}{2})\delta t$:

$$\vec{u} = \begin{cases} u^x[(i \pm \frac{1}{2})\delta x, j\delta y, k\delta z] \\ u^y[i\delta x, (j \pm \frac{1}{2})\delta y, k\delta z] \\ u^z[i\delta x, j\delta y, (k \pm \frac{1}{2})\delta z] \end{cases}$$

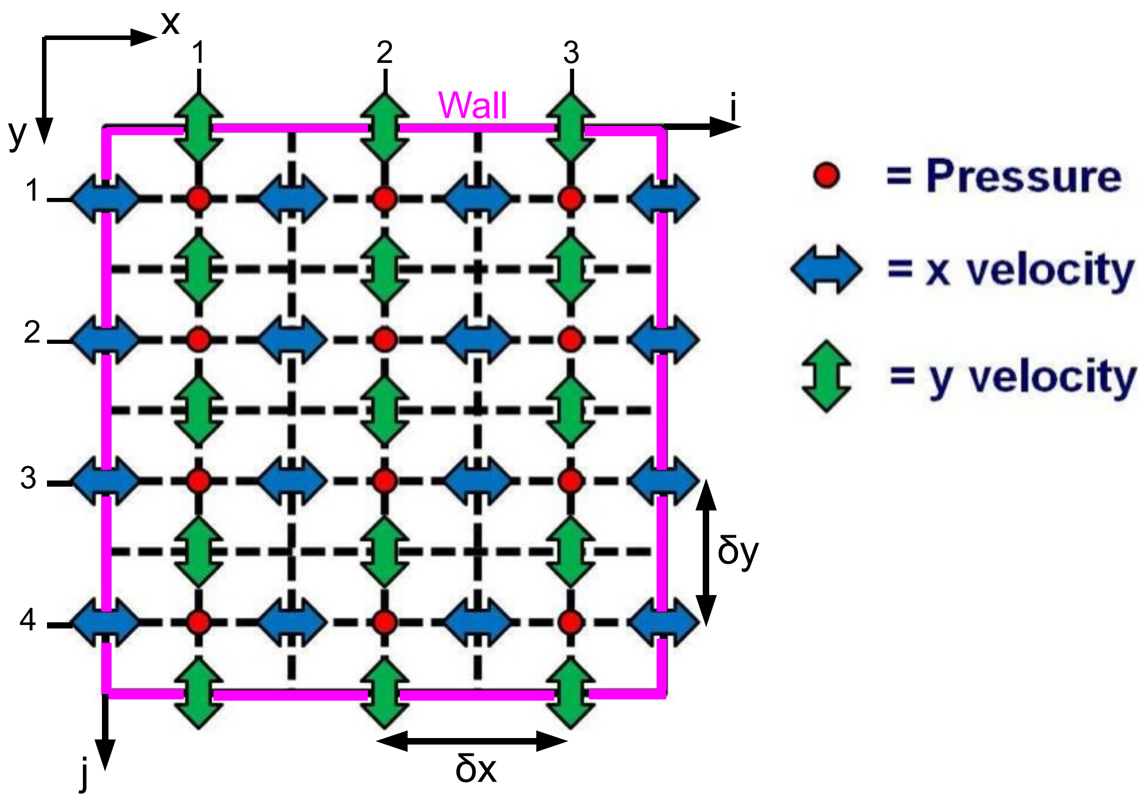

Figure 4.1: Example of a calculation grid in a 2D plan ([3])

Figure 4.1 shows an example of grid in an enclosure for calculating the components of the acoustic pressure and the particle velocity points.

Developping equations 2.1 and 2.2 gives:

$$\begin{cases} -\frac{1}{\rho_0 c^2}\frac{\partial p}{\partial t} = \frac{\partial u_x}{\partial x} + \frac{\partial u_y}{\partial y} + \frac{\partial u_z}{\partial z} \\ \frac{\partial p}{\partial x}\vec{x} + \frac{\partial p}{\partial y}\vec{y} + \frac{\partial p}{\partial z}\vec{z} = -\rho_0\frac{\partial \vec{u}}{\partial t} \end{cases} \tag{4.1}$$

The first linearized equation of system 4.1 is:

$$\begin{aligned} \frac{p_{(i,j,k)}(t+\delta t) - p_{(i,j,k)}(t)}{\delta t} &= -\rho_0 c^2 \Big(\frac{u^x_{(i+\frac{1}{2},j,k)}(t+\frac{\delta t}{2}) - u^x_{(i-\frac{1}{2},j,k)}(t+\frac{\delta t}{2})}{\delta x} \\ &\quad + \frac{u^y_{(i,j+\frac{1}{2},k)}(t+\frac{\delta t}{2}) - u^y_{(i,j-\frac{1}{2},k)}(t+\frac{\delta t}{2})}{\delta y} \\ &\quad + \frac{u^z_{(i,j,k+\frac{1}{2})}(t+\frac{\delta t}{2}) - u^z_{(i,j,k-\frac{1}{2})}(t+\frac{\delta t}{2})}{\delta z} \Big) \end{aligned}$$

So the evolution of acoustical pressure in the time and space is given by equation 4.2:

$$\begin{aligned} p_{(i,j,k)}(t+\delta t) &= p_{(i,j,k)}(t) - \rho_0 c^2 \delta t \Big(\frac{u^x_{(i+\frac{1}{2},j,k)}(t+\frac{\delta t}{2}) - u^x_{(i-\frac{1}{2},j,k)}(t+\frac{\delta t}{2})}{\delta x} \Big) \\ &\quad - \rho_0 c^2 \delta t \Big(\frac{u^y_{(i,j+\frac{1}{2},k)}(t+\frac{\delta t}{2}) - u^y_{(i,j-\frac{1}{2},k)}(t+\frac{\delta t}{2})}{\delta y} \Big) \\ &\quad - \rho_0 c^2 \delta t \Big(\frac{u^z_{(i,j,k+\frac{1}{2})}(t+\frac{\delta t}{2}) - u^z_{(i,j,k-\frac{1}{2})}(t+\frac{\delta t}{2})}{\delta z} \Big) \end{aligned} \tag{4.2}$$

The second equation of system 4.1 gives the following system:

$$\begin{cases} \frac{\partial p}{\partial x} = -\rho_0 \frac{\partial u_x}{\partial t} \\ \frac{\partial p}{\partial y} = -\rho_0 \frac{\partial u_y}{\partial t} \\ \frac{\partial p}{\partial z} = -\rho_0 \frac{\partial u_z}{\partial t} \end{cases} \tag{4.3}$$

Then the three linearized equations of system 4.3 are:

$$\begin{cases} \frac{p_{(i+1,j,k)}(t)-p_{(i,j,k)}(t)}{\delta x} = -\rho_0 \left(\frac{u^x_{(i+\frac{1}{2},j,k)}(t+\frac{\delta t}{2})-u^x_{(i+\frac{1}{2},j,k)}(t-\frac{\delta t}{2})}{\delta t} \right) \\ \frac{p_{(i,j+1,k)}(t)-p_{(i,j,k)}(t)}{\delta y} = -\rho_0 \left(\frac{u^y_{(i,j+\frac{1}{2},k)}(t+\frac{\delta t}{2})-u^y_{(i,j+\frac{1}{2},k)}(t-\frac{\delta t}{2})}{\delta t} \right) \\ \frac{p_{(i,j,k+1)}(t)-p_{(i,j,k)}(t)}{\delta z} = -\rho_0 \left(\frac{u^z_{(i,j,k+\frac{1}{2})}(t+\frac{\delta t}{2})-u^z_{(i,j,k+\frac{1}{2})}(t-\frac{\delta t}{2})}{\delta t} \right) \end{cases}$$

Finally the equations describing the evolution in time and space of the three components of the particle velocity are given by 4.4:

$$\begin{cases} u^x_{(i+\frac{1}{2},j,k)}(t+\frac{\delta t}{2}) = u^x_{(i+\frac{1}{2},j,k)}(t-\frac{\delta t}{2}) - \frac{\delta t}{\rho_0 \delta x}\Big(p_{(i+1,j,k)}(t) - p_{(i,j,k)}(t)\Big) \\ u^y_{(i+\frac{1}{2},j,k)}(t+\frac{\delta t}{2}) = u^y_{(i+\frac{1}{2},j,k)}(t-\frac{\delta t}{2}) - \frac{\delta t}{\rho_0 \delta y}\Big(p_{(i,j+1,k)}(t) - p_{(i,j,k)}(t)\Big) \\ u^z_{(i,j,k+\frac{1}{2})}(t+\frac{\delta t}{2}) = u^z_{(i,j,k+\frac{1}{2})}(t-\frac{\delta t}{2}) - \frac{\delta t}{\rho_0 \delta z}\Big(p_{(i,j,k+1)}(t) - p_{(i,j,k)}(t)\Big) \end{cases} \tag{4.4}$$

For the simulations made with Matlab and discussed in the next chapter equations 4.2 and 4.4 will be used. Now that equations describing the FDTD method have been determined the stability conditions of these equations have to be discussed. This is the purpose of the next section 4.2.

4.2 Stability conditions

The reliability of the results obtained with the FDTD method is conditioned by the respect of some rules that have to be followed in order to guaranty the stability. These stability conditions are directly linked with the choice of the cell size defined by δx, δy, δz and the time step δt.

4.2.1 Cell size

A fundamental constraint in the FDTD method is the choice of the cell size δx, δy, δz. The cell size must be much less than the smallest wavelength for which accurate results are desired. The question is how much less.

The Nyquist sampling theorem is: $2f_{max} \leq f_{sampling}$., with f_{max} the maximum frequency of interest and $f_{sampling}$ the sampling frequency for the FDTD simulation.

The frequency can be expressed in function of the wave celerity c and the wavelength λ so the Nyquist sampling theorem can also be written: $2\frac{c}{\lambda_{f_{max}}} \leq \frac{c}{\lambda_{f_{sampling}}}$, where $\lambda_{f_{max}}$ is the wavelength of the maximum frequency of interest and $\lambda_{f_{sampling}}$ is the wavelength of the sampling frequency.
Therefore, in term of spacial period the Nyquist theorem is: $2\lambda_{f_{sampling}} \leq \lambda_{f_{max}}$.

$\lambda_{f_{sampling}}$ is the length of the spacial period of the FDTD method and so in 3D is equal to δx, δy, δz. Thus the size of the cells must respect the following system:

$$\begin{cases} 2\delta x \leq \lambda_{f_{max}} \\ 2\delta y \leq \lambda_{f_{max}} \\ 2\delta z \leq \lambda_{f_{max}} \end{cases} \tag{4.5}$$

As the smallest wavelength is not precisely determined more than two spacial samples per wavelength are required to ensure the stability of the FDTD method. This leads to more restricted conditions for the maximum cell size allowed. A minimum of 5 cells per wavelength for the smallest wavelength is an acceptable boundary condition giving equations 4.6:

$$\begin{cases} \delta x \leq \frac{\lambda_{f_{max}}}{5} \\ \delta y \leq \frac{\lambda_{f_{max}}}{5} \\ \delta z \leq \frac{\lambda_{f_{max}}}{5} \end{cases} \tag{4.6}$$

It has to be aware that if some portion of the computational space is filled with permeable material the wavelength in the material has to be used to determined the maximum cell size.

The respect of equation 4.6 is necessary but other considerations should be taken into account for choosing the cell size. It is admitted that reasonable results can be obtained using from five to ten cells per wavelength (page 30-31 [10]). Moreover, the important characteristics of the problem geometry must be accurately modeled. This is normally met for $\delta x \leq \frac{\lambda_{f_{max}}}{10}$ (page 31 [10]). In some specific cases a thiner cell size can be used.

4.2.2 Time step size

When the cell size is determined the maximum size of the time step can be determined.
If a plane wave propagates through a FDTD grid, in one time step any point on this wave must not pass through more than one cell. During one time step the wave can propagate only from one cell to its nearest neighbors (page 32 [10]). So the time step δt can be expressed in function of the wave celerity c and of δx, δy, δz. For a 3D rectangular grid the relation is:

$$c\delta t \leq \frac{1}{\sqrt{\frac{1}{\delta x^2} + \frac{1}{\delta y^2} + \frac{1}{\delta z^2}}} \tag{4.7}$$

In case the equality is hold for 4.7 the discretized wave approximates most closely the actual wave propagation and grid dispersion errors are minimized. In most of the situations more accurate results will not be obtained by using a smaller value of δt.

4.3 Boundary conditions

In this section the boundary conditions when a sound wave hits a surface are discussed and introduced to the FDTD method.

Boundary conditions are mostly frequency dependent. Nevertheless it will be time consuming to do the calculation at all the frequencies. Thus some approximations are necessary.
In a room, at low frequencies, two typical absorbing boundary constructions are common:

- Thin boundary compared to the wavelength
- Light non-stiff walls

In the first case, the materials can be approximated by a complex frequency-dependent impedance (pages 177-183, [11]):

$$Z = Z_0 + \frac{Z_{-1}}{j\omega} \tag{4.8}$$

In the second case the behavior of the materials is quite accurately described by (page 164-165, [11]):

$$Z = Z_0 + j\omega Z_1 \tag{4.9}$$

Therefore in [5] it is proposed to approximate a general boundary impedance by :

$$Z = Z_0 + j\omega Z_1 + \frac{Z_{-1}}{j\omega} \tag{4.10}$$

with Z_0, Z_1, Z_{-1} real number that can be determined experimentally and ω is the pulsation.

In time domain the impedance defined by equation 4.10 leads to the boundary condition:

$$p(t) = Z_0 u_n(t) + Z_1 \frac{du_n(t)}{dt} + Z_{-1} \int_{-\infty}^{t} u_n(\tau) d\tau \tag{4.11}$$

with $p(t)$ the acoustic pressure and $u_n(t)$ the component of the particle velocity orthogonal to the boundary plane. As an example, let consider the boundary at plane $z = (k_0 + \frac{1}{2})\delta t$. The third equation of the equation system 4.4 can not be used to determine the particle velocity u^z at the boundary since $p(i, j, k_0 + 1)$ is not known. So an asymmetric finite-difference approximation is used instead:

$$\left.\frac{\partial p}{\partial z}\right|^{t}(i, j, k_0 + \frac{1}{2}) = \frac{p(i, j, k_0 + \frac{1}{2}) - p(i, j, k_0)}{\frac{\delta z}{2}} \tag{4.12}$$

Thus, the particle velocity at the boundary can be written:

$$u^z_{(i,j,k_0+\frac{1}{2})}(t + \frac{\delta t}{2}) = u^z_{(i,j,k_0+\frac{1}{2})}(t - \frac{\delta t}{2}) - \frac{2\delta t}{\rho_0 \delta z}\Big(p_{(i,j,k_0+\frac{1}{2})}(t) - p_{(i,j,k_0)}(t)\Big) \tag{4.13}$$

The value of $p_{(i,j,k_0+\frac{1}{2})}$ is not known but it can be found using equation 4.11 and $u^z_{(i,j,k_0+\frac{1}{2})}$. Therefore equation 4.13 becomes:

$$\begin{aligned} u^z_{(i,j,k_0+\frac{1}{2})}(t + \tfrac{\delta t}{2}) \;&=\; u^z_{(i,j,k_0+\frac{1}{2})}(t - \tfrac{\delta t}{2}) - \tfrac{2\delta t}{\rho_0 \delta z}\Big(- p_{(i,j,k_0)}(t) + Z_0 u^z_{(i,j,k_0+\frac{1}{2})}(t) \\ &\quad + Z_1 \tfrac{\partial u^z_{(i,j,k_0+\frac{1}{2})}(t)}{\partial t} + Z_{-1} \textstyle\int_{-\infty}^{t} u^z_{(i,j,k_0+\frac{1}{2})}(\tau) d\tau \Big) \end{aligned} \tag{4.14}$$

Introducing the finite-difference approximation for the derivative of $u^z_{(i,j,k_0+\frac{1}{2})}(t)$ and the summation to replace the integration, the results in a boundary cell FDTD equation is:

$$\begin{aligned} u^z_{(i,j,k_0+\frac{1}{2})}(t + \tfrac{\delta t}{2}) \;&=\; u^z_{(i,j,k_0+\frac{1}{2})}(t - \tfrac{\delta t}{2}) - \tfrac{2\delta t}{\rho_0 \delta z}\Big(- p_{(i,j,k_0)}(t) + Z_0 u^z_{(i,j,k_0+\frac{1}{2})}(t) \\ &\quad + Z_1 \tfrac{u^z_{(i,j,k_0+\frac{1}{2})}(t+\frac{\delta t}{2}) - u^z_{(i,j,k_0+\frac{1}{2})}(t-\frac{\delta t}{2})}{\delta t} + Z_{-1}\delta t \sum_{m=-\infty}^{t} u^z_{(i,j,k_0+\frac{1}{2})}(m - 0.5)\Big) \end{aligned} \tag{4.15}$$

A linear interpolation is used to express $u^z_{(i,j,k_0+\frac{1}{2})}(t)$ in function of $t-\frac{\delta t}{2}$ and $t+\frac{\delta t}{2}$.

Finally the equation expressing the evolution of the particle velocity at the boundary $k_0+\frac{1}{2}$ is:

$$u^z_{(i,j,k_0+\frac{1}{2})}(t+\tfrac{\delta t}{2}) = \alpha u^z_{(i,j,k_0+\frac{1}{2})}(t-\tfrac{\delta t}{2}) + \beta\frac{2\delta t}{\rho_0\delta z}\left(p_{(i,j,k_0)}(t) - Z_{-1}\delta t\sum_{m=-\infty}^{t} u^z_{(i,j,k_0+\frac{1}{2})}(m-0.5)\right) \tag{4.16}$$

with

- $\alpha = \frac{1-Z_0/Z_{FDTD}+2Z_1/Z_{FDTD}\delta t}{1+Z_0/Z_{FDTD}+2Z_1/Z_{FDTD}\delta t}$
- $\beta = \frac{1}{1+Z_0/Z_{FDTD}+2Z_1/Z_{FDTD}\delta t}$
- $Z_{FDTD} = \frac{\rho_0\delta z}{\delta t}$

Equation 4.16 is a general result which models and solves the problem of the boundary conditions in FDTD method. In the reality the knowledge of the complex impedance 4.10 is rare. Nevertheless in most of the cases the real part of the material impedance is the predominant part and it is therefore possible to make the assumption that the impedance is assumed to be real ($Z_1 = Z_{-1} = 0$) [15]. The relation 4.16 is simplified to:

$$u^z_{(i,j,k_0+\frac{1}{2})}(t+\tfrac{\delta t}{2}) = \frac{\frac{\rho_0\delta z}{\delta t}-Z_0}{\frac{\rho_0\delta z}{\delta t}+Z_0} u^z_{(i,j,k_0+\frac{1}{2})}(t-\tfrac{\delta t}{2}) + 2\frac{1}{\frac{\rho_0\delta z}{\delta t}+Z_0}p_{(i,j,k_0)}(t) \tag{4.17}$$

This last equation 4.17 is very interesting because the real part of a material impedance can be approximated by its real absorption coefficient as depicted in the equation 4.18.

$$Z_0 = \rho_0 c\frac{1+\sqrt{1-\alpha}}{1-\sqrt{1-\alpha}} \tag{4.18}$$

The knowledge of the absorption coefficient is in general easier to obtained (by measurement or as a manufacturer data) than the material impedance.

Two specific cases of absorption coefficient can be studied in details.

Case 1: $\alpha = 0$

If $\alpha = 0$ meaning that at the boundary there is a full reflection, then 4.18 gives an impedance Z_0 that tends to infinity. Therefore:

- $\lim\limits_{Z_0\to\infty} \frac{\frac{\rho_0\delta z}{\delta t}-Z_0}{\frac{\rho_0\delta z}{\delta t}+Z_0} = -1$
- $\lim\limits_{Z_0\to\infty} \frac{1}{\frac{\rho_0\delta z}{\delta t}+Z_0} = 0$

These two results lead to:

$$u^z_{(i,j,k_0+\frac{1}{2})}(t+\frac{\delta t}{2}) = -u^z_{(i,j,k_0+\frac{1}{2})}(t-\frac{\delta t}{2}) \tag{4.19}$$

4.19 is verified only if $u^z_{(i,j,k_0+\frac{1}{2})}$ is null all the time. So it demonstrates that when $\alpha = 0$ the particle velocity at the boundary is always null.

Case 2: $\alpha = 1$

If $\alpha = 1$ meaning that at the boundary there is a full absorption, then 4.18 gives $Z_0 = \rho_0 c$. Thus, the equation describing the evolution of $u^z_{(i,j,k_0+\frac{1}{2})}$ over the time is 4.20:

$$u^z_{(i,j,k_0+\frac{1}{2})}(t+\frac{\delta t}{2}) = \frac{\frac{\delta z}{\delta t}-c}{\frac{\delta z}{\delta t}+c} u^z_{(i,j,k_0+\frac{1}{2})}(t-\frac{\delta t}{2}) + 2\frac{1}{\frac{\rho_0 \delta z}{\delta t}-\rho_0 c} p_{(i,j,k_0)}(t) \tag{4.20}$$

4.4 Sound source model

One of the main advantage of the FDTD method is that it is a time-dependent algorithm. Therefore, an infinity of sound signals can be used during FDTD simulations. It is possible to cite the sinusoid, the gaussian pulse or the Maximum Length Sequence as example of signals commonly used for FDTD simulations. Moreover, it is possible to use the impulse response of real loudspeakers in order to get results as close as possible to the reality.

The sound source is usually defined as a pressure source. Thus it is positioned on a pressure-point of the FDTD-grid and excites this pressure point. Then, the acoustical wave propagates through the FDTD model by exciting successively the points of the particle velocity grids and those of the pressure grid. A such definition gives an omnidirectional behavior for the sound source.

When several pressure sources are used in the same simulation, the points of the FDTD-grid where the sound sources are located are forced by the signal feeding the sound sources. Therefore the sound sources are not transparent to the waves produced by the other sources.

Also, it has to be noticed that in some specific cases it is possible to model sound sources as particle velocity sources.

5

Finite-Difference Time-Domain: simulation

In the previous chapter 4 the theory describing all the aspects of the FDTD method has been presented. In this chapter 5 the FDTD method is simulated with Matlab. After introducing some practical considerations relative to the cell size, the time step size, the boundary limit, the sound source and the general algorithm, several simulations are conducted in order to re-find the different analytical results obtained in chapter 2 for the different orders of gradient sound source.

5.1 Cell size

As discussed in section 4.2.1 the choice of the cell size is directly linked to the maximum frequency of interest desired for the simulation of the FDTD method but not only.
All the simulations of this project are run in free field or in rectangular rooms. Therefore, the shape of the space where simulations are run is kept simple. So it is possible to take $\delta x = \delta y = \delta z = h$ to simplify the algorithm. To determine the value of h the maximum frequency of interest for the simulation has to be chosen.
This project aims to simulate, with a FDTD method, the behavior of subwoofers working in low frequency range. Depending on subwoofers and their utilizations (concert, studio, home-cinema) the maximum frequency of interest can change from 80 Hz for professional subwoofer used in concert until 200 Hz for home-cinema subwoofer. So for the first simulations, which only aims to re-find the results of chapter 2, the maximum frequency is chosen equal to 300 Hz. The wavelength for a frequency of 300 Hz is 1.1433 m (for a sound celerity $c = 343m.s^{-1}$).

Then, given this maximum frequency, h has to fit the condition defined by equation 4.6 as well as the other recommendations discussed in subsection 4.2.1

Therefore it is decided to choose $h = \frac{\lambda_{max}}{10}$ in this project, which gives $h = 0.1m$ for the maximum frequency chosen earlier: $f_{max} = 300Hz$.

5.2 Time step size

When the cell size is determined the time step size can then be calculated. According to equation 4.7 and for the value of h chosen in the previous section5.1, δt must be inferior or equal to $1,9245.10^{-4}s$. This value is equivalent to a sampling frequency of 5196.2 Hz. As some real loudspeaker impulse response will be used later with a sampling frequency of 8000 Hz, it is decided to take also a sampling frequency of 8000 Hz for the FDTD simulation. A such sampling frequency gives a time step size of $\delta t = 1.2500e - 04second$ which respects the stability condition of equation 4.7.

5.3 General algorithm

The main part of the algorithm simulating the FDTD method, excluding the case of the boundary cells, is modeled by equations 4.2 and 4.4. In 2D-simulations it is simple to related the spacial coordinates i, j used in equations 4.2 and 4.4 with the number of the line and the row of a matrix as shown on figure 5.1.

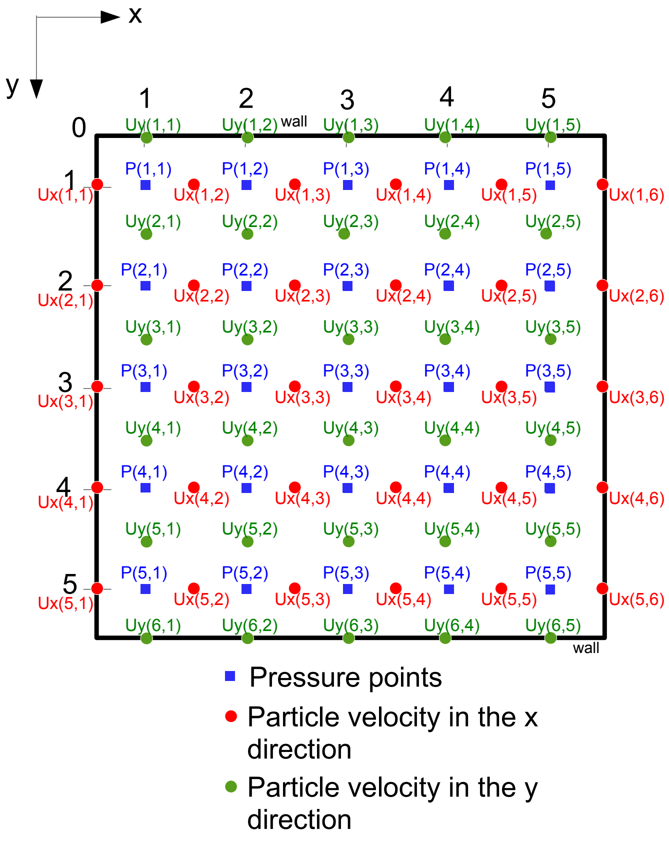

Figure 5.1: Example of coordinate-matrix correspondance in a 2D-simulation

Therefore, the corresponding matrixes for figure 5.1 are:

- P= $\begin{bmatrix} p(1,1) & p(1,2) & p(1,3) & p(1,4) & p(1,5) \\ p(2,1) & p(2,2) & p(2,3) & p(2,4) & p(2,5) \\ p(3,1) & p(3,2) & p(3,3) & p(3,4) & p(3,5) \\ p(4,1) & p(4,2) & p(4,3) & p(4,4) & p(4,5) \\ p(5,1) & p(5,2) & p(5,3) & p(5,4) & p(5,5) \end{bmatrix}$

- U_x= $\begin{bmatrix} u_x(1,1) & u_x(1,2) & u_x(1,3) & u_x(1,4) & u_x(1,5) & u_x(1,6) \\ u_x(2,1) & u_x(2,2) & u_x(2,3) & u_x(2,4) & u_x(2,5) & u_x(2,6) \\ u_x(3,1) & u_x(3,2) & u_x(3,3) & u_x(3,4) & u_x(3,5) & u_x(3,6) \\ u_x(4,1) & u_x(4,2) & u_x(4,3) & u_x(4,4) & u_x(4,5) & u_x(4,6) \\ u_x(5,1) & u_x(5,2) & u_x(5,3) & u_x(5,4) & u_x(5,5) & u_x(5,6) \end{bmatrix}$
- U_y= $\begin{bmatrix} u_y(1,1) & u_y(1,2) & u_y(1,3) & u_y(1,4) & u_y(1,5) \\ u_y(2,1) & u_y(2,2) & u_y(2,3) & u_y(2,4) & u_y(2,5) \\ u_y(3,1) & u_y(3,2) & u_y(3,3) & u_y(3,4) & u_y(3,5) \\ u_y(4,1) & u_y(4,2) & u_y(4,3) & u_y(4,4) & u_y(4,5) \\ u_y(5,1) & u_y(5,2) & u_y(5,3) & u_y(5,4) & u_y(5,5) \\ u_y(6,1) & u_y(6,2) & u_y(6,3) & u_y(6,4) & u_y(6,5) \end{bmatrix}$

Then, it can be seen that equations 4.2 and 4.4 are directly solved for most of the points by adding or subtracting these three matrixes weighted by some coefficients. The only exception is to calculate the different particle velocities at the boundaries. This point is discussed in section 5.4.

In 3D-simulations, the third spacial coordinate k can be integrated using 3D-matrix for the pressure. The z-component of the particle velocity is added using extra layers creating therefore the third dimension as shown on figure 5.2.

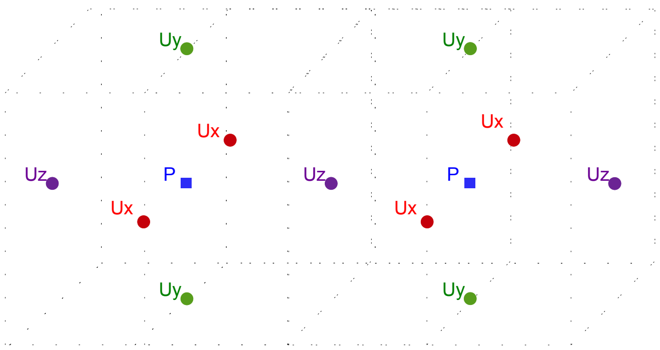

Figure 5.2: Grid for 3D simulation

5.4 Boundary limit

The boundary conditions are defined by equation 4.17. If this equation is limited to a 2D-simulation then four equations can be written for the left, right, top and bottom wall. For the wall on the left the equation (with a Matlab syntax) at the boundary is:

$$u^x_{(:,1)}(t+\frac{\delta t}{2}) \quad = \quad \frac{\frac{\rho_0 \delta z}{\delta t}-Z_0}{\frac{\rho_0 \delta z}{\delta t}+Z_0} u^x_{(:,1)}(t-\frac{\delta t}{2}) + 2\frac{1}{\frac{\rho_0 \delta z}{\delta t}+Z_0} p_{(:,1)}(t) \tag{5.1}$$

The corresponding plan is given on figure 5.3.

For the wall on the right the equation at the boundary is:

$$u^x_{(:,6)}(t+\frac{\delta t}{2}) \quad = \quad \frac{\frac{\rho_0 \delta z}{\delta t}-Z_0}{\frac{\rho_0 \delta z}{\delta t}+Z_0} u^x_{(:,5)}(t-\frac{\delta t}{2}) + 2\frac{1}{\frac{\rho_0 \delta z}{\delta t}+Z_0} p_{(:,5)}(t) \tag{5.2}$$

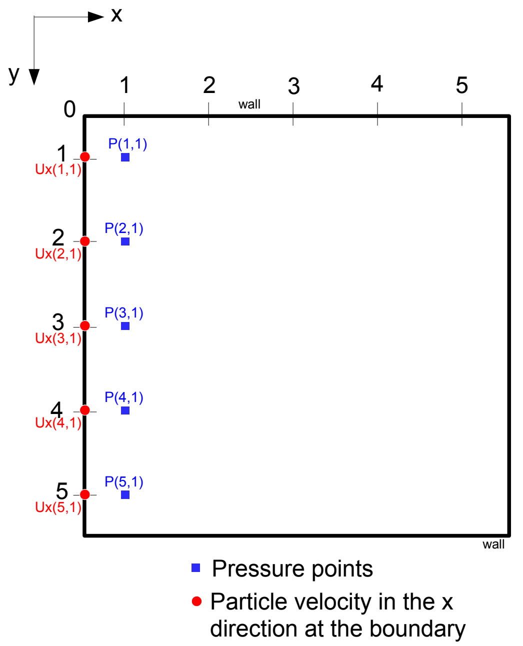

Figure 5.3: Example of a calculation grid in a 2D plane

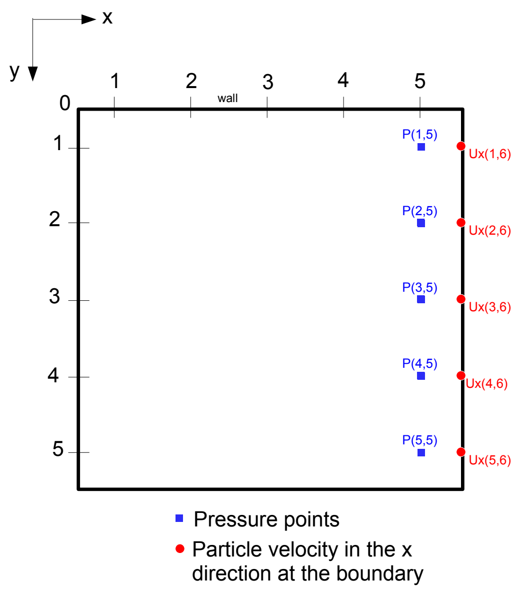

Figure 5.4: Example of a calculation grid in a 2D plane

The corresponding plan is given on figure 5.4.

For the wall on the top the equation at the boundary is:

$$u^y_{(1,:)}(t+\tfrac{\delta t}{2}) \;=\; \frac{\frac{\rho_0\delta z}{\delta t}-Z_0}{\frac{\rho_0\delta z}{\delta t}+Z_0}u^y_{(1,:)}(t-\tfrac{\delta t}{2})+2\frac{1}{\frac{\rho_0\delta z}{\delta t}+Z_0}p_{(1,:)}(t) \tag{5.3}$$

The corresponding plan is given on figure 5.5.

For the wall on the bottom the equation at the boundary is:

$$u^y_{(6,:)}(t+\tfrac{\delta t}{2}) \;=\; \frac{\frac{\rho_0\delta z}{\delta t}-Z_0}{\frac{\rho_0\delta z}{\delta t}+Z_0}u^y_{(5,:)}(t-\tfrac{\delta t}{2})+2\frac{1}{\frac{\rho_0\delta z}{\delta t}+Z_0}p_{(5,:)}(t) \tag{5.4}$$

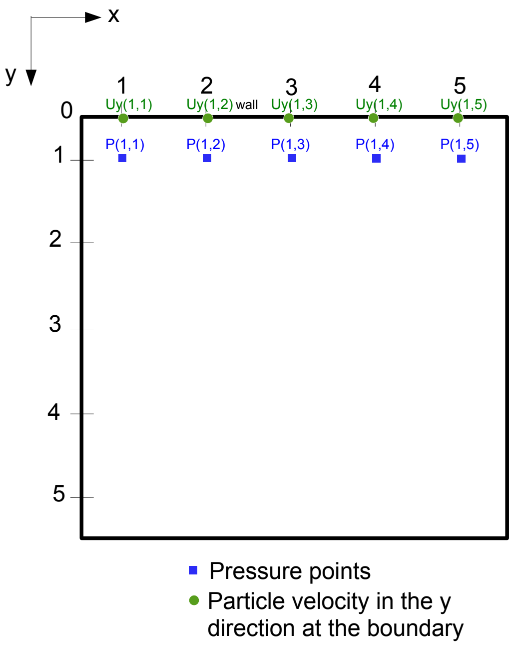

Figure 5.5: Example of a calculation grid in a 2D plane

The corresponding plan is given on figure 5.6.

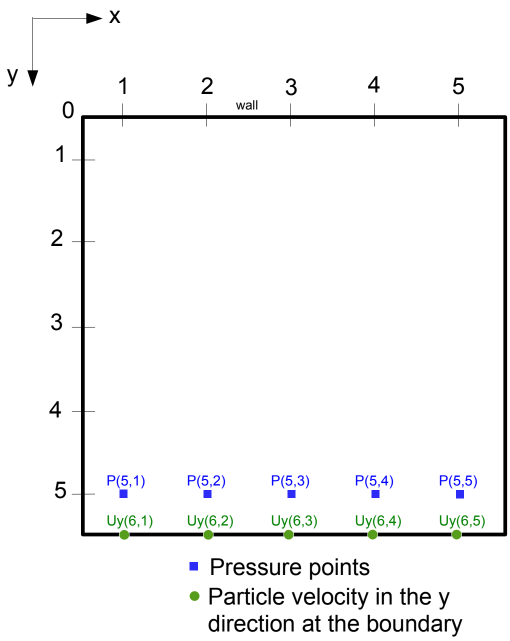

Figure 5.6: Example of a calculation grid in a 2D plane

When the particle velocities at the boundaries are known their values can be added as extra rows and lines in matrixes u_x and u_y defined in the previous section 5.3. Therefore, calculating the pressure next to the boundary $\big($p(1,1), p(1,2), ..., p(2,1), p(3,1)... $\big)$ becomes possible. For the simulations run in this chapter, the boundary are such that all the energy is absorbed by the walls simulating then a free field behavior in the space of interest.

5.5 Sound source

In the previous chapter 4 several kind of sound sources and signals have been mentioned. As the simulations here aim principally to study the acoustic field for specific values of the ratio D/λ (D the distance between the sound sources) and so for different frequencies, all the sound sources will be modeled by a point source fed with a sinusoidal signal of single frequency. Therefore the pressure at the input point varies according to the sinusoidal signal between -1 and +1 Pa.

5.6 Simulations

5.6.1 Characteristics of the plotting

When all the different practical aspects relative to the simulation of the FDTD method have been discussed and that choices for the cell size, time step size and the sound source have been made (sections 5.1, 5.2, 5.5 respectively), simulations can be run. This section presents the results of the different orders of gradient-loudspeakers presented in chapter 2 simulated with the FDTD method in free field.

The simulation is run over a time of $t = \frac{1}{f_{min}}$ so that for the lowest frequency f_{min} the period of the sinusoid signal is completed. It is chosen $f_{min} = 20$ Hz as most of the subwoofer have a such cut-off frequency. So it gives a simulation of 0.05 seconds.

Then for each time step the pressure is saved at each discrete position of the room. The RMS pressure at all the discrete positions is calculated according to formula 5.5:

$$P_{rms}(i,j) = \sqrt{\frac{(p^2_{t=\delta t}(i,j) + p^2_{t=2\delta t}(i,j) + p^2_{t=3\delta t}(i,j) + ... + p^2_{t=n\delta t}(i,j)}{n}} \tag{5.5}$$

In equation 5.5 *n* is the total number of time step, i and j are the indexes in the FDTD grid on the x and y-axis respectively .

For all the simulations three types of figures are presented. On the first one, the RMS pressure expressed in pascal is plotted in a linear scale. On the second figure the RMS pressure in dB SPL is plotted in logarithmic scale. On the third figure, the polar pattern extracted from the FDTD simulation is compared to the analytical polar pattern obtained in chapter 2. The polar pattern from the FDTD simulation is obtained by extracting the RMS pressures (in pascal) at discrete-positions situated on a circle of radius 10 meters and centered on the acoustical center of each gradient-loudspeaker as shown on figure 5.7. Despite a distance of 1 meter is usually used to measure the directivity pattern of loudspeakers it has been arbitrary decided to take 10 meters. The reasons for that are to limit the effects of the direct radiations induced by the source when being close to it and also to be in a situation that could resemble to a far-field measurement condition. It has to be reminded that the analytical part is made with far-field approximations which could then justify a directivity measurement in far-field.

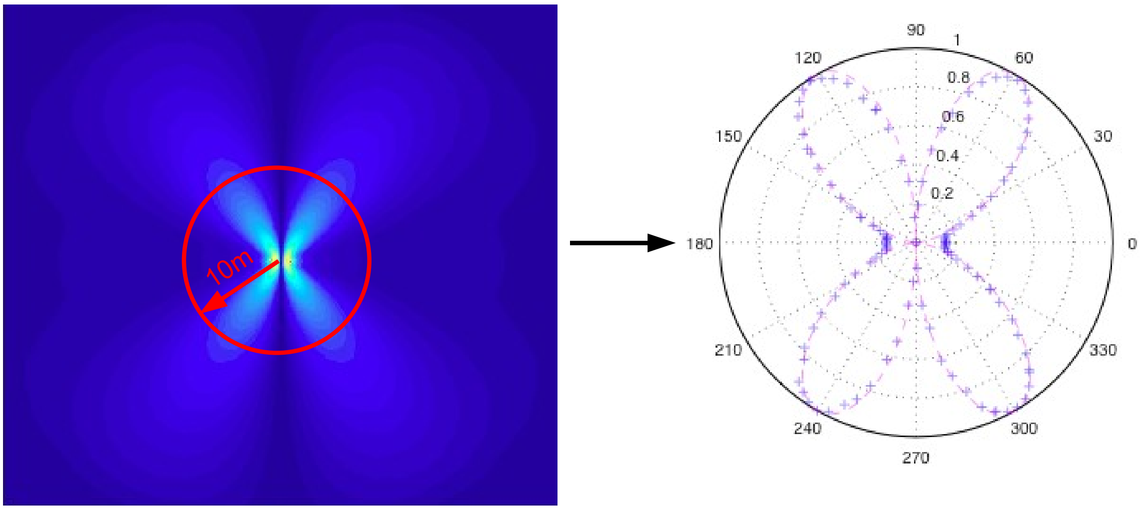

Figure 5.7: Example of polar directivity extraction. The figure on the left shows the pressure field in pascal. The figure on the right shows the polar directivity obtained analytically (purple line) and the one extracted from the pressure field (blue crosses) at 10 meters (on the red circle)

Before starting the analysis of the results it is important to remind that in the polar directivity figure, the analytical curve (in purple) obtained with the results of chapter 2 is independent of the distance. At the opposite the results extracted from the FDTD simulations (blue crosses) are measured at a specific distance distance (10 meters). Therefore the results of the FDTD simulations have to be compensated in gain to perfectly match the analytical results.

5.6.2 First Order Gradient sound source: Bidirectional

Figures 5.8, 5.9 and 5.10 show three examples of simulation results for ratios $\frac{D}{\lambda}$ equal to 0.2, 0.5 and 1 respectively. The whole results are visible in appendix A.1.

The graduations on the x-axis and y-axis of figures *a* and *b* represent the indexes in the FDTD grid used to calculate the pressure. As the cell size has been chosen equal to 0.1 meter (see section 5.1), it is possible to switch directly from index to distance (expressed in meter) by multiplying the index-scale of the figures by 0.1.

In these simulations, the distance between the sources is kept constant $D = 1.14m$, which corresponds to the wavelength of 300 Hz (see figure 2.6). Then the frequency of the sinusoidal signal is changed in order to obtain the different values $\frac{D}{\lambda}$.

For this type of gradient-source, the FDTD simulation gives results comparable to the analytical model described in section 2.3. The main deviation appears for $\frac{D}{\lambda} = 1$ where the notches of the FDTD model are not as sharp as the ones of the analytical model. This discrepancy will be discussed later in subsection 5.6.3 as it appears often in other setups of gradient sources.

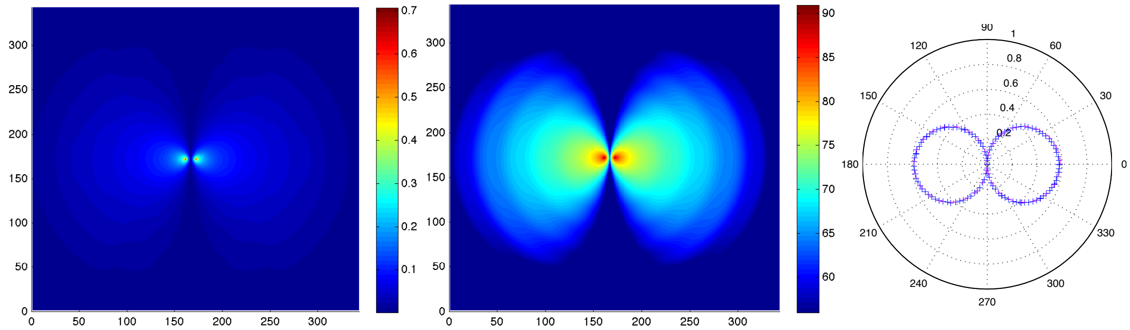

(a) RMS pressure field in pascal

(b) RMS pressure field in dB SPL

(c) Polar pattern at 10 m with scale in pascal

Figure 5.8: FDTD simulation for $\frac{D}{\lambda}$=0.2, f=60Hz

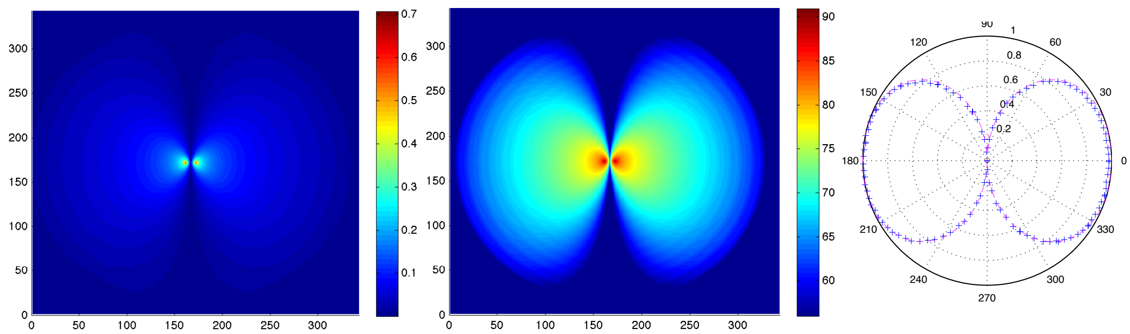

(a) RMS pressure field in pascal

(b) RMS pressure field in dB SPL

(c) Polar pattern at 10 m with scale in pascal

Figure 5.9: FDTD simulation for $\frac{D}{\lambda}$=0.5, f=150 Hz

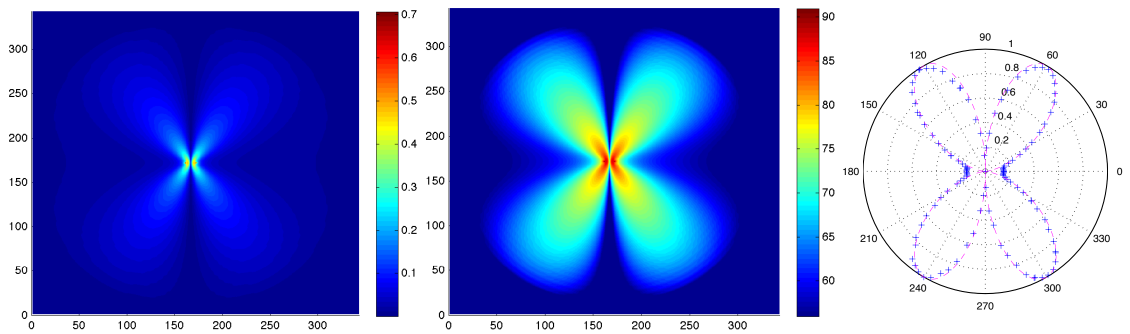

(a) RMS pressure field in pascal

(b) RMS pressure field in dB SPL

(c) Polar pattern at 10 m with scale in pascal

Figure 5.10: FDTD simulation for $\frac{D}{\lambda}$=1, f=300 Hz

5.6.3 First Order Gradient sound source: Unidirectional

Case 1: $D = d$

Figures 5.11, 5.12 and 5.13 show three examples of simulation results for a first order gradient sound source with $\frac{D}{\lambda} = \frac{d}{\lambda}$ equal to 0.2, 0.5 and 1 respectively. The whole results are visible in appendix A.2.1.

The graduations on the x-axis and y-axis of figures *a* and *b* represent the indexes in the FDTD grid used to calculate the pressure. As the cell size has been chosen equal to 0.1 meter (see section 5.1), it is possible to switch directly from index to distance (expressed in meter) by multiplying the index-scale of the figures by 0.1.

In these simulations $D = d = 1.14m$ which corresponds to the wavelength of 300 Hz. In order to respect the analytical study of chapter 2 and the works of Olson [16] the distance between the sources as well as the numerical delay applied on the back-source are kept constant and equal to $\frac{d}{2} = \frac{D}{2} = 0.57m$ in accordance to figure 2.8. Then the frequency of the sinusoidal signal is changed in order to obtain the different values $\frac{D}{\lambda}$ and $\frac{d}{\lambda}$.

Regarding the results of the simulations some observations can be made.
First, on the front side, the FDTD model suits the analytical model and from 270 °(-90 °) to 90 ° the directional patterns are similar.
Then on the rear side two discrepancies appear. When $\frac{D}{\lambda}$ is lower than 0.5, a rejection at $\theta = 180$ ° is observed with the FDTD model while the analytical model has a dip. Different hypothesis can explain this difference. The polar pattern of the analytical model is only dependent on the angle θ. The distance from the source is not included. Moreover, the analytical model is realized in far-field. With the FDTD model, errors could come from the approximations due to the space and time discretization. The polar pattern of the FDTD is computed at 10 meters so the far field conditions are not totally respected and the influence of the direct radiations of the source can still exist. When $\frac{D}{\lambda}$ becomes higher than 0.6 some notches present in the analytical models are not as much pronounced in the FDTD simulation. Here again, the influence of the direct radiation of the source could be an explanation.

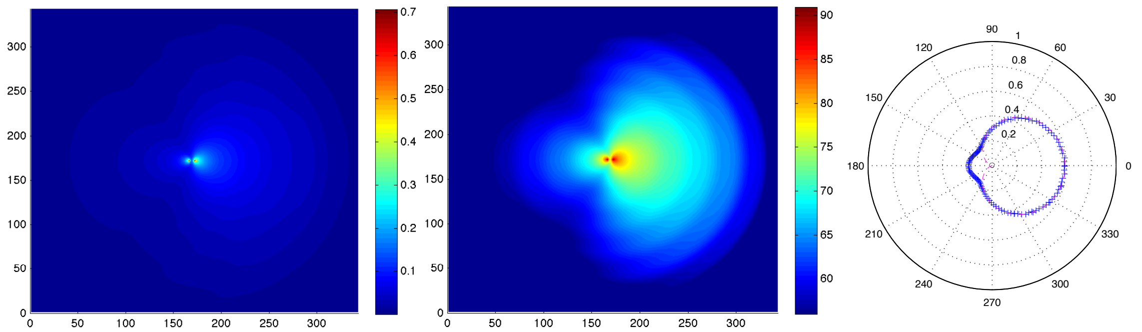

(a) RMS pressure field in pascal (b) RMS pressure field in dB SPL (c) Polar pattern at 10 m with scale in pascal

Figure 5.11: FDTD simulation for $\frac{D}{\lambda} = \frac{d}{\lambda}$=0.2, f=60 Hz

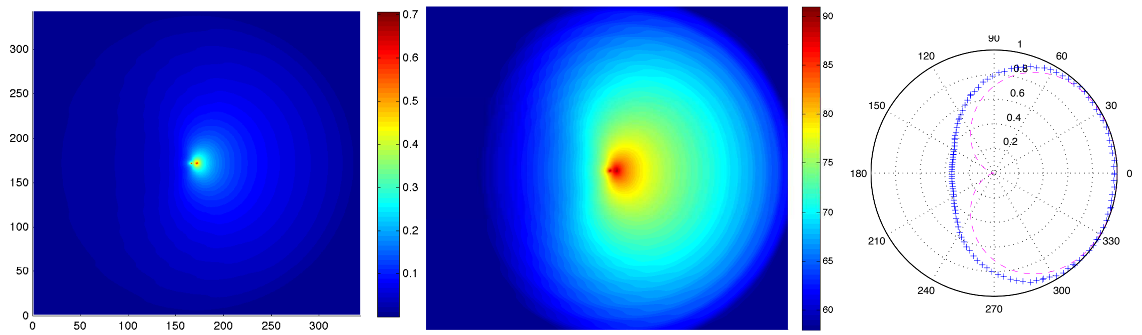

(a) RMS pressure field in pascal

(b) RMS pressure field in dB SPL

(c) Polar pattern at 10 m with a scale in pascal

Figure 5.12: FDTD simulation for $\frac{D}{\lambda} = \frac{d}{\lambda}$=0.5, f=150 Hz

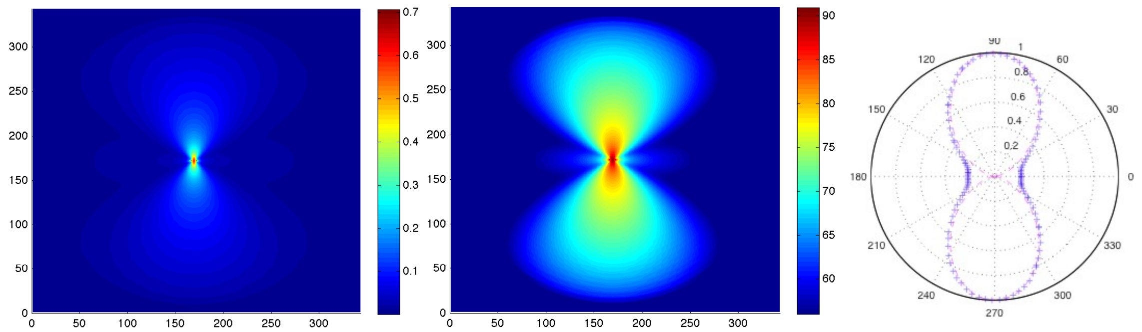

(a) RMS pressure field in pascal

(b) RMS pressure field in dB SPL

(c) Polar pattern at 10 m with scale in pascal

Figure 5.13: FDTD simulation for $\frac{D}{\lambda} = \frac{d}{\lambda}$=1, f=300

The same observations and conclusion can be made for the other setups of first-order gradient source-unidirectional whose figures are displayed in annex A.2.2 (for $\frac{D}{\lambda} = 0.25$ and $\frac{d}{\lambda} \in [0.1, 1]$) and A.2.3 (for $\frac{d}{\lambda} = 0.25$ and $\frac{D}{\lambda} \in [0.1, 1]$)

5.6.4 Second-Order gradient sound source-Unidirectional

This subsection displays some of the results obtained for a Second-order gradient sound source-unidirectional. The whole results are presented in annex A.3. In these simulations, very high differences exist between the analytical and the FDTD models for some of the values of $\frac{D}{\lambda}$. The closeness of the sound sources could lead to a combination of their radiations that is not fully described in the analytical model.

The graduations on the x-axis and y-axis of figures *a* and *b* represent the indexes in the FDTD grid used to calculate the pressure. As the cell size has been chosen equal to 0.1 meter (see section 5.1), it is possible to switch directly from index to distance (expressed in meter) by multiplying the index-scale of the figures by 0.1.

In these simulations $D = d = 1.14m$ which corresponds to the wavelength of 300 Hz. The distances between the sources and the delays are kept constant in accordance to figure 2.10. Then the frequency of the sinusoidal signal is changed in order to obtain the different values $\frac{D}{\lambda}$ and $\frac{d}{\lambda}$.

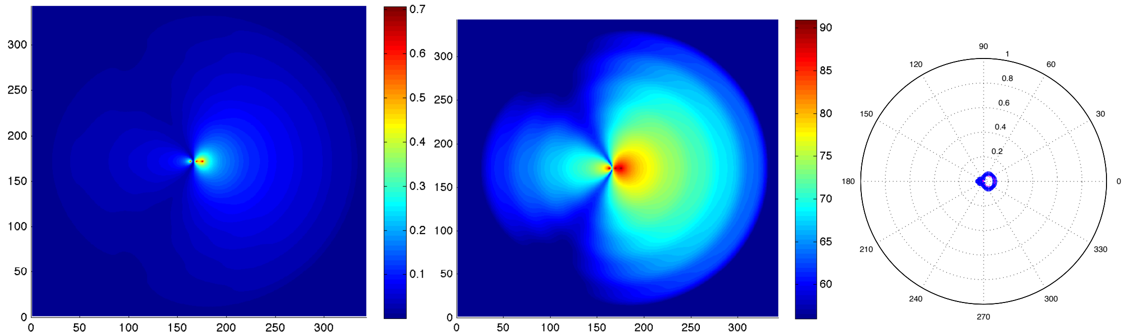

(a) RMS pressure field (b) RMS pressure field in dB SPL (c) Polar pattern at 10 m with scale in pascal

Figure 5.14: FDTD simulation for $\frac{d}{\lambda}=\frac{D}{\lambda}$=0.2, f=60 Hz

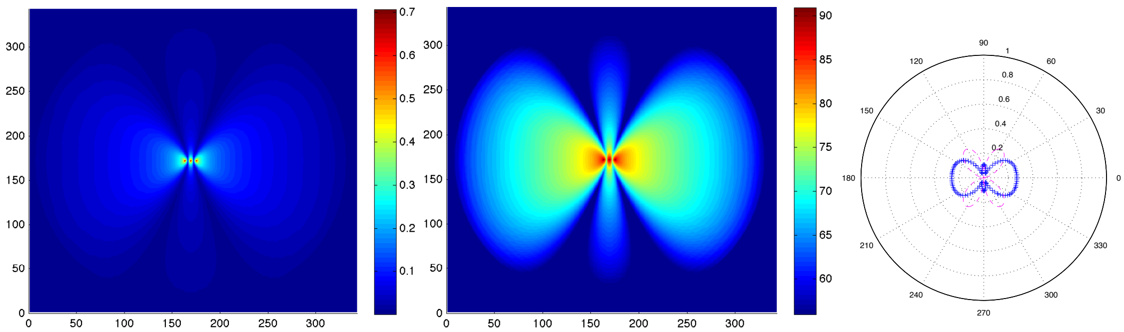

(a) RMS pressure field (b) RMS pressure field in dB SPL (c) Polar pattern at 10 m with scale in pascal

Figure 5.15: FDTD simulation for $\frac{d}{\lambda}=\frac{D}{\lambda}$=1, f=300 Hz

5.6.5 Conclusion

In this section different orders of gradient sound sources have been simulated with a FDTD algorithm. The results obtained have been compared with the ones of the analytical models from chapter 2. These results are satisfying and allow to validate the FDTD method. In the next section a more accurate model of subwoofer using real impulse responses will be implemented.

6

Finite-Difference Time-Domain: simulation using real subwoofer impulse response

6.1 Introduction

In the previous chapter 5 different orders of gradient sound sources have been simulated with a FDTD method. These simulations have been done with sinusoidal sources creating mono-frequency waves. The results obtained with the FDTD method appeared to be consistent with the analytic results of chapter 2.

It has been showed that when positioning omnidirectional sound sources in a certain way and applying specific delays and phase shifts to them different directivity patterns could be obtained. Nevertheless these directivity patterns are frequency dependent.

This chapter aims to present the results of simulations using the impulse response of a real subwoofer whose frequency response spreads on around 100 Hz. First-order gradient sound source setup with unidirectional directivity is privileged in these simulations as it is the most commonly used setup when a control of the low-frequency directivity is desired. Different distances between the sources as well as different values of delay are used in order to reveal the advantages and disadvantages of such setup when using real subwoofers. The analysis of the results will be focused on the directivity obtained at different frequencies.

6.2 Simulation parameters

6.2.1 Sound source

In the simulations realized in this chapter the impulse response of a real subwoofer is used.

The subwoofer used is a DALI SWA8. It is a closed-box type with a 8” woofer driver. This subwoofer is a direct-radiation type (to be distinguished from the manifold type or the bass reflex type). It has an integrated amplifier and an embedded active low pass filter whose cut-off frequency can vary from 50 Hz to 150 Hz.

Figure 6.1: Subwoofer DALI SWA 8

The impulse response used for the simulations is an average of impulse responses measured around the subwoofer. The procedure to obtain this averaged impulse response is detailed in appendix B. The cut-off frequency of the low pass filter of the subwoofer is chosen to be 150 Hz in order to have the wider frequency response allowed.

The impulse response of the subwoofer contains originally 65535 samples and has a sampling frequency of 8000 Hz. This number of samples is too high for the memory capacities allowed by Matlab in these FDTD simulations and would also be too much time consuming. Therefore the impulse response is truncated and only the first 8000 samples are conserved. Indeed after the first 8000 samples the impulse response is similar to noise. Moreover the magnitude obtained via the fft of the truncated impulse response is similar to the one obtained with the complete impulse response.

In the following simulations the sound source is assimilated to a pressure source so the impulse response excites a pressure point of the FDTD grid.

6.2.2 Cell size

The cell size is determined by the maximum frequency of interest desired in the FDTD simulation. The cut-off frequency (-3 dB) of the subwoofer is 150 Hz. Therefore to have a safety-margin the cell size is calculated for a maximum frequency of 250 Hz. With the respect of equation 4.6 the cell size is chosen equal to 0.2 meter.

6.2.3 Time step size

When the cell size is determined on can calculate the time step size according to equation 4.7. A cell size of 0.2 meter gives a maximum time step of 4.1×10^{-4} s which is equivalent to a minimum sampling frequency of 2425 Hz. The sampling frequency of the impulse response used in these simulations is 8000 Hz. Because 8000 Hz fulfills the conditions of stability described before it is decided to choose 8000 Hz as sampling frequency for the FDTD simulation. This choice will also avoid any resampling process.

With a sampling frequency of 8000 Hz and an impulse response of 8000 points the simulation lasts 1 second.

6.3 Simulation results

In the simulations made in this chapter one wants to reach a unidirectional behavior with a cardioid pattern. Therefore the only setup simulated is the first order gradient sound source-unidirectional.

For each simulation some pressure-maps are plotted at different discrete frequencies. To obtain such maps the pressure at each pressure-point of the FDTD grid is saved at each time step in order to be able to have the impulse response received by each pressure-point of the grid. Then the fft can be calculated at each pressure-point of the grid and the magnitude is obtained as the absolute value of the fft. Finally at each point of the grid one extracts the value of the magnitude at different discrete frequencies. The frequencies extracted are 40 Hz, 50 Hz, 60 Hz, 80 Hz, 100 Hz, 120 Hz and 150 Hz which correspond approximately to the usual center frequencies of a $\frac{1}{3}$ octave band analysis.

In the previous chapter 5 one has seen that the perfect cardioid behavior is only obtained at one specific value of $\frac{D}{\lambda}$ and approximated at the others frequencies around. In the simulations presented in this chapter one try to reason in a more practical way to be closer to real setups. Thus, in the next simulations one tests different frequencies giving a perfect cardioid directivity pattern and put the appropriate distance between the sources as well as the appropriate delay for the chosen frequency in order to see how it affects the directivity pattern of the others frequencies around.

Four different cases are tested.

Case 1:$f_{cardioid} = 150Hz$

In the first case, the frequency giving the ideal cardioid directivity is $f_{cardioid}$=150 Hz. For a such frequency, the distance between the sources is $D = \frac{\lambda_{f_{cardioid}}}{4} = 0.6m$ and the delay applied on the back subwoofer is $d = \frac{\lambda_{f_{cardioid}}}{4} = 0.6m$.

The results of a this setup simulated with the FDTD method are presented in C.1. For example, three pressure-maps corresponding to the frequencies $f = 50Hz$, $f = 100Hz$ and $f = 150Hz$ are presented bellow in figure 6.2. The scales on the x-axis and y-axis represent the indexes in the FDTD grid and can be converted into meter by multiplying them by 0.2 (the grid size).

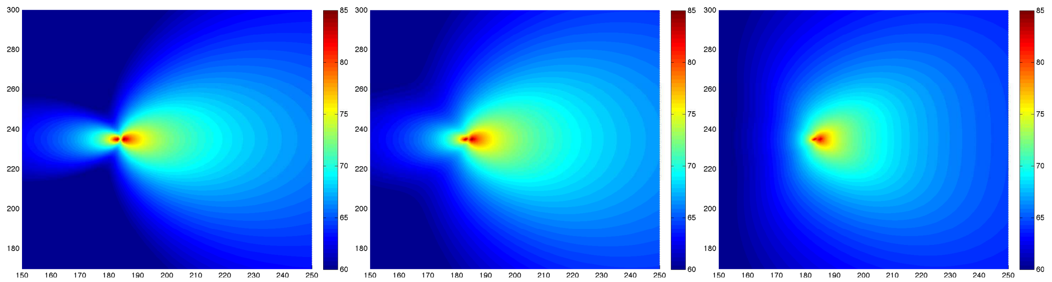

(a) $f = 50Hz$ (b) $f = 100Hz$ (c) $f = 150Hz$

Figure 6.2: Pressure in dB SPL for a first order gradient sound source-unidirectional setup simulated with a FDTD method and the impulse response of a subwoofer

In this first case, one can see that the pressure generated by the system at 150 Hz is different to the one generated at 100 Hz or 50 Hz. It can be observed that as long as the frequency decreases the rejection in the back of the subwoofer increases. The pressure in the front is also modified from frequency to another but no notches are introduced.

Case 2: $f_{cardioid} = 100Hz$

In the second case, the frequency giving the ideal cardioid directivity is $f_{cardioid}$=100 Hz. For a such frequency, the distance between the sources is $D = \frac{\lambda_{f_{cardioid}}}{4} = 0.85m$ and the delay applied on the back subwoofer is $d = \frac{\lambda_{f_{cardioid}}}{4} = 0.85m$.

The results of a this setup simulated with the FDTD method are presented in C.2. For example, three pressure-maps corresponding to the frequencies $f = 50Hz$, $f = 100Hz$ and $f = 150Hz$ are presented bellow in figure 6.3. The scales on the x-axis and y-axis represent the indexes in the FDTD grid and can be converted into meter by multiplying them by 0.2 (the grid size).

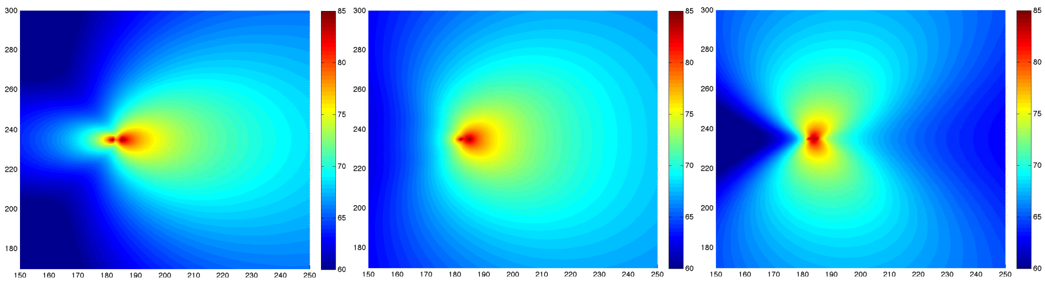

(a) $f = 50Hz$ (b) $f = 100Hz$ (c) $f = 150Hz$

Figure 6.3: Pressure in dB SPL for a first order gradient sound source-unidirectional setup simulated with a FDTD method and the impulse response of a subwoofer

In this second case the differences between each frequencies are more obvious. Below 100 Hz (the cardioid frequency) the rejection on the back of the system increases when the frequency decreases. On the front the pressure is also modified. The directivity seems to become more and more narrow when the frequency decreases. For frequencies up to 100 Hz on can see a notch appearing on the front of the system. This notch is a non-desired effect. So in such setup one should apply a low pass filter with a cutting frequency of 100 Hz to avoid this undesired effect at frequencies upper to the cardioid frequency.

Case 3: $f_{cardioid} = 80Hz$

In the third case, the frequency giving the ideal cardioid directivity is $f_{cardioid}$=80 Hz. For a such frequency, the distance between the sources is $D = \frac{\lambda_{f_{cardioid}}}{4} = 1.1m$ and the delay applied on the back subwoofer is $d = \frac{\lambda_{f_{cardioid}}}{4} = 1.1m$.

The results of a this setup simulated with the FDTD method are presented in C.3. For example, three pressure-maps corresponding to the frequencies $f = 50Hz$, $f = 100Hz$ and $f = 150Hz$ are presented bellow in figure 6.4. The scales on the x-axis and y-axis represent the indexes in the FDTD grid and can be converted into meter by multiplying them by 0.2 (the grid size). the FDTD grid and can be converted into meter by multiplying them by 0.2 (the grid size).

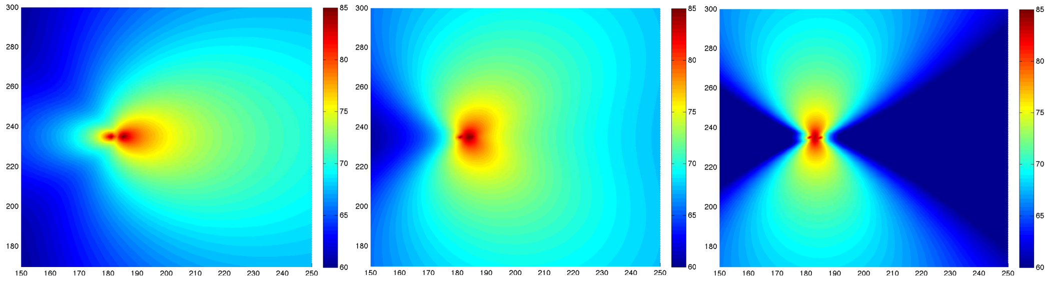

(a) $f = 50Hz$ (b) $f = 100Hz$ (c) $f = 150Hz$

Figure 6.4: Pressure in dB SPL for a first order gradient sound source-unidirectional setup simulated with a FDTD method and the impulse response of a subwoofer

In this setup the observations are the same than in case 2. Up to 80 Hz an undesired notch appears in front of the system.

Case 4:$f_{cardioid} = 50Hz$

In the fourth case, the frequency giving the ideal cardioid directivity is $f_{cardioid}$=50 Hz. For a such frequency, the distance between the sources is $D = \frac{\lambda_{f_{cardioid}}}{4} = 1.7m$ and the delay applied on the back subwoofer is $d = \frac{\lambda_{f_{cardioid}}}{4} = 1.7m$.

The results of a this setup simulated with the FDTD method are presented in C.4. For example, three pressure-maps corresponding to the frequencies $f = 50Hz$, $f = 100Hz$ and $f = 150Hz$ are presented bellow in figure 6.5. The scales on the x-axis and y-axis represent the indexes in the FDTD grid and can be converted into meter by multiplying them by 0.2 (the grid size).

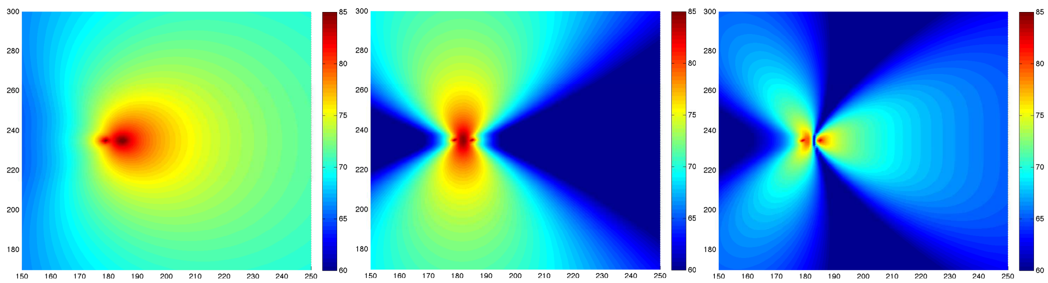

(a) $f = 50Hz$ (b) $f = 100Hz$ (c) $f = 150Hz$

Figure 6.5: Pressure in dB SPL for a first order gradient sound source-unidirectional setup simulated with a FDTD method and the impulse response of a subwoofer

In this fourth case the unidirectional behavior is met for frequencies down to 50 Hz. Up to 50 Hz notches appear on the front of the system. For 100 Hz, the frequency equal to twice the cardioid frequency, the directional pattern is a 8-figure with dips in the front and the back of the system. For 150 Hz, the frequency equal to three times the cardioid frequency, the system generates a main lobe on the front and two lobes on the side.

6.4 Conclusion

In this chapter the impulse response of a real subwoofer has been included in the FDTD simulations of a first order gradient source-unidirectional. It has been observed that depending which frequency was chosen for the ideal cardioid behavior, the pressure field obtained for other frequencies of the bandwidth could be very different.
In all the simulations, one has seen that down to the cardioid frequency a rejection appeared on the back of the system. This rejection is more and more important as long as the frequency decreases. For frequencies up to the cardioid frequency one has seen in cases 2, 3 and 4 that notches appeared on the front of the system. These notches are an undesired effect because they reduce considerably the bandwidth of the subwoofer.
Therefore the choice of the cardioid frequency seems an important parameter. Taking the cardioid frequency equal to the upper cutoff frequency of the subwoofer could be a judicious choice in order to avoid the presence of notches in the front of the system. This point will be demonstrated in the next chapter 7.

Part IV

Enhanced Low-frequency directivity control

7

Frequency dependent delay

7.1 Introduction

In the previous chapter 6 the impulse response of a real loudspeaker has been included in a first-order gradient setup and simulations with a FDTD method have been conducted. Results of this simulations showed that the directivity pattern could change sensibly at different frequencies. Particularly the perfect cardioid pattern is only achieved at one frequency.

It has been shown in chapter 5 that to achieve a desired polar pattern at a specific frequency, the distance between the sound sources and the delay applied on the back subwoofer were the parameters one can play with. If changing the distance between the sources in live is impossible, playing with the delay applied on the back subwoofer seems more realistic.

In order to keep the directivity pattern of a first order gradient sound source as constant as possible on a large frequency range one want to establish a mathematical relation between the delay applied on the back subwoofer and the frequency.

In this chapter a frequency dependent delay function is determined empirically to achieve a pre-determined polar pattern on a wide frequency range. FDTD simulations are done with this new delay function to demonstrate its advantages and disadvantages when a mono-frequency sinusoidal signal is used.

7.2 Analysis

The starting point of this study is the expression of the polar directivity for a first order gradient sound source-unidirectional determined analytically in section 2.4.

For recall if the distance between the sources is D and the delay applied on the back source is d (in meter) then the polar directivity of a first order gradient source-unidirectional is :

$$R_\theta = \sin\left(\pi\frac{d}{\lambda} + \pi\frac{D}{\lambda}\cos\theta\right) \tag{7.1}$$

where λ is the wavelength.

Frequency range of interest

From the results of subsection 2.6.3 it is known that the perfect cardioid pattern is obtained when $\frac{d}{\lambda} = \frac{D}{\lambda} = 0.25$ as shown on figure 7.1 and approximated when $\frac{d}{\lambda} = \frac{D}{\lambda} < 0.25$

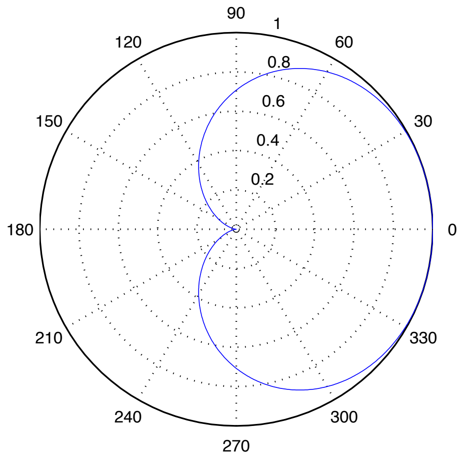

Figure 7.1: Cardioid pattern corresponding to equation 7.1 with $D = d = 0.25\lambda$ with $\lambda = c/f$, $c = 343 m.s^{-1}$ and $f = 150 Hz$

When $\frac{D}{\lambda}$ is higher than 0.25 one can observe a decrease of the pressure at $\theta = 0°$ as shown on figure 7.2.

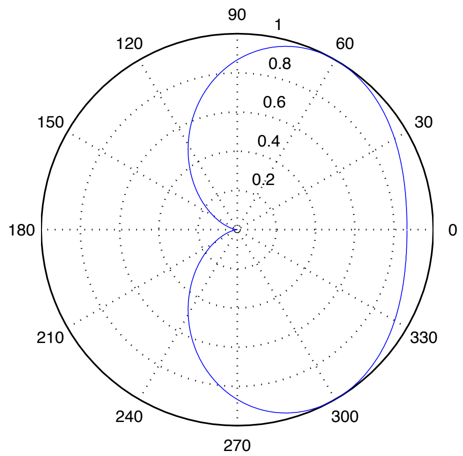

Figure 7.2: Cardioid pattern corresponding to equation 7.1 with $D = d = 0.25\lambda_c$ with $\lambda_c = c/f_{cardioid}$, $c = 343 m.s^{-1}$, $f_{cardioid} = 150 Hz$ and $\lambda = c/f$, $f = 200 Hz$

Taking a constant distance $D = D_0$ between two subwoofers, if two frequencies of wavelength λ_1 and λ_2 are chosen such that $\frac{D_0}{\lambda_1} = 0.25$ and $\frac{D_0}{\lambda_2} > 0.25$, then the inequality becomes $\frac{D_0}{\lambda_2} > \frac{D_0}{\lambda_1}$ giving $\lambda_2 < \lambda_1$. This shows that when the conditions to obtain a cardioid pattern are met for the frequency of wavelength λ_1 they are not met at higher frequencies (squeezing of the front pressure).

Therefore it demonstrates that when choosing the frequency for which the perfect cardioid pattern is desired one should take the maximum frequency produced by the subwoofer.

Empirical study

When the maximum frequency of interest f_{max} is known, one can calculate the distance D and the delay d that will give the perfect cardioid pattern for it with equation 7.2:

$$D = d = 0.25\lambda_{f_{max}} \tag{7.2}$$

Then the empirical study can start for frequencies lower than f_{max}. The aim of this study is to determine the best delay d for the lower frequencies using equation 7.1 and for $D = 0.25\lambda_{f_{max}}$ kept constant.

To evaluate if a delay $d(f_0)$ can be considered as the ideal one for a frequency f_0 different from f_{max}, the pressures at $\theta = 0°$, $\theta = 90°$ and $\theta = 180°$ given by equation 7.1 are compared with the ones obtained in the case of a constant delay $d = 0.25\lambda_{f_{Max}}$. For $\theta = 0°$ one want to keep the pressure as high as possible. At $\theta = 180°$ one want the pressure to be as low as possible and nearly constant for all the frequencies. At last, the pressure at $\theta = 90°$ should change in the same proportion than the one at $\theta = 0°$ meaning that the SPL(90°)-SPL(0°) should be nearly constant at all the frequencies. This would guaranty that the directivity pattern in the front of the system has the same shape for all the frequencies.

Practically equation 7.1 is simulated in Matlab at several different discrete frequencies. For each discrete frequencies different values of delay d are tested. The next figures 7.3 and 7.4 show some examples.

In these examples it is assumed that the frequency giving the ideal cardioid behavior is $f_{Max} = 150Hz$. Thus, in equation 7.1, $D = 0.25\lambda_{f_{Max}} = 0.57m$. If the ideal delay d wants to be found for the frequency 100 Hz one must take $\lambda = c/f$ with $f = 100$ Hz in equation 7.1. Then different values of d are tested as shown on figure 7.3. It is important to say that only few numbers of d are plotted there and do not represent the total number of tries made for each frequency.

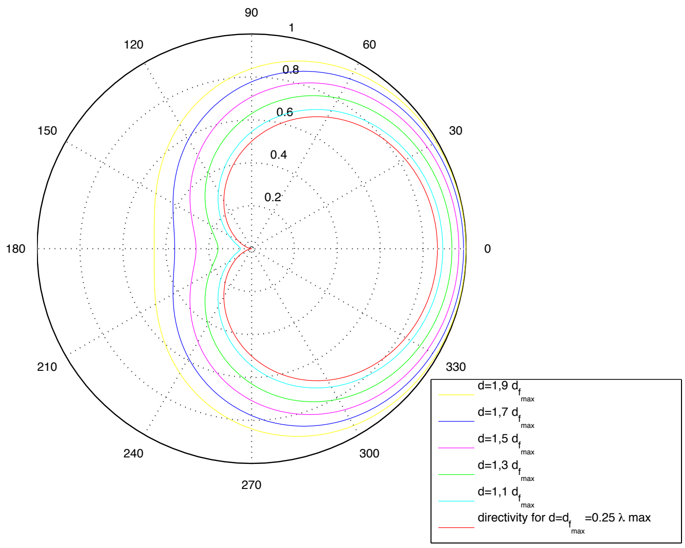

Figure 7.3: Cardioid pattern corresponding to equation 7.1 with $D = d = 0.25\lambda_c$ with $\lambda_c = c/f_{cardioid}$, $c = 343m.s^{-1}$, $f_{cardioid} = 150Hz$, $\lambda = c/f$, $f = 100Hz$ and d varying from 1 to 1.9

On figure 7.4 the same procedure is done for $f = 75Hz$

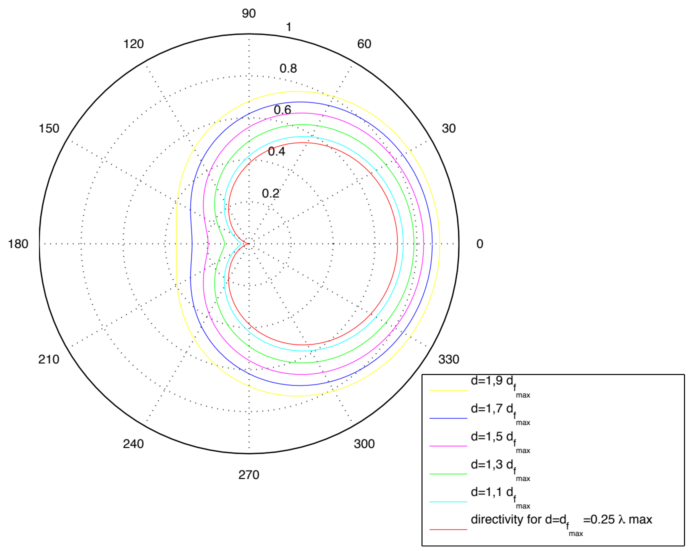

Figure 7.4: Cardioid pattern corresponding to equation 7.1 with $D = d = 0.25\lambda_c$ with $\lambda_c = c/f_{cardioid}$, $c = 343m.s^{-1}$, $f_{cardioid} = 150Hz$, $\lambda = c/f$, $f = 75Hz$ and d varying from 1 t0 1.9

What can be observed on these figures is that when the delay is kept constant equal to $d = 0.25\lambda_{f_{Max}}$ the pressure on the front decrease rapidly with the frequency decrease. Moreover the shape of the cardioid changes also. On the side ($\theta = 90°$) the pressure decrease quicker than on the front.

At the opposite with a frequency-dependent delay it is possible to find some values of d which give almost a constant pressure at $\theta = 180°$, for example $d = 1.3d_{f_{Max}}$ when $f = 100Hz$ and $d = 1.5d_{f_{Max}}$ when $f = 75Hz$ (see figures 7.3 and 7.4). These delays $d = 1.3d_{f_{Max}}$, $d = 1.5d_{f_{Max}}$ produce higher pressure level on the front of the system for $f = 100Hz$ and $f = 75Hz$ respectively. They also keep the shape of the directivity pattern identical to the one obtained for the perfect cardioid behavior with $f = f_{max}$.

Mathematical relation and performances

With the empirical approach described above, the following mathematical relation 7.3 is established. This relation appears appears to be the one which gives the best results over a wide frequency range.

$$d = \frac{c}{4f_{max}} + (1 - \frac{f}{f_{max}}) \times \frac{c}{4f_{max}} \tag{7.3}$$

with

- d: delay in meter
- c: celerity of the sound in $m.s^{-1}$
- f_{max}: the maximum frequency of interest produced by the subwoofer. The frequency that gives the ideal cardioid behavior.
- f: the frequency in Hz

In appendix D.1 one compares the directivities obtained with and without the frequency-dependent delay at different discrete frequencies. To help understanding the advantages of this delay function, the results of appendix D.1 are summarized in figures 7.5, 7.6, 7.7 and 7.8.

On figures 7.5 and 7.6 one can see that when the frequency decreases and becomes farer from the frequency of the perfect cardioid behavior, the pressure difference between the setup with a frequency-dependent delay and the setup with a fixed delay tends to increase in the front ($\theta = 0°$) and in the side ($\theta = 90°$) of the system. Between 2 and 3 dB of difference can be observed at 30 Hz in the front of the system and up to 4 dB of difference at 30 Hz on the side of the system.

Figure 7.8 shows one of the main advantage of the frequency-dependent delay. One can observe on this figure that along the frequency range considered here, the difference of pressure between the front and the side of the system varies only of 0.5 dB in the case of the frequency-dependent delay, whereas it changes of more than 3 dB in the case of a fixed-delay. This means that with the delay function proposed in this chapter the shape of the directivity is kept nearly constant on the front of the system and along the studied bandwidth.

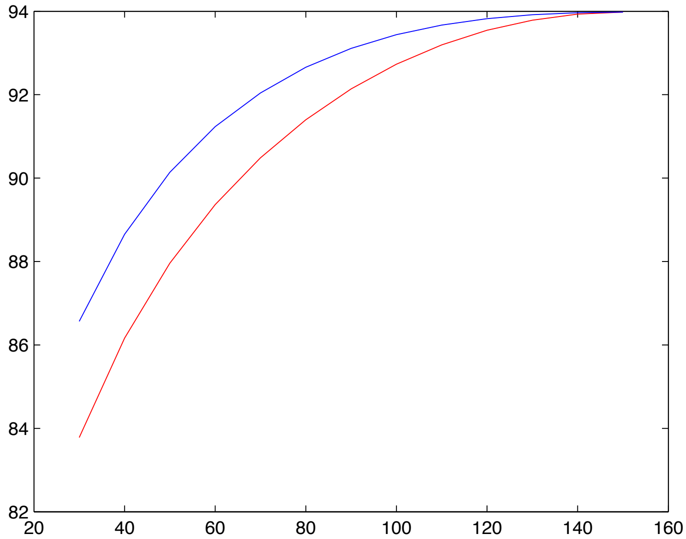

Figure 7.5: Pressure in dB SPL in function of the frequency at $\theta = 0°$ for a first-order gradient speaker-unidirectional, with a fixed delay (red curve) and with a frequency-dependent delay (blue curve)

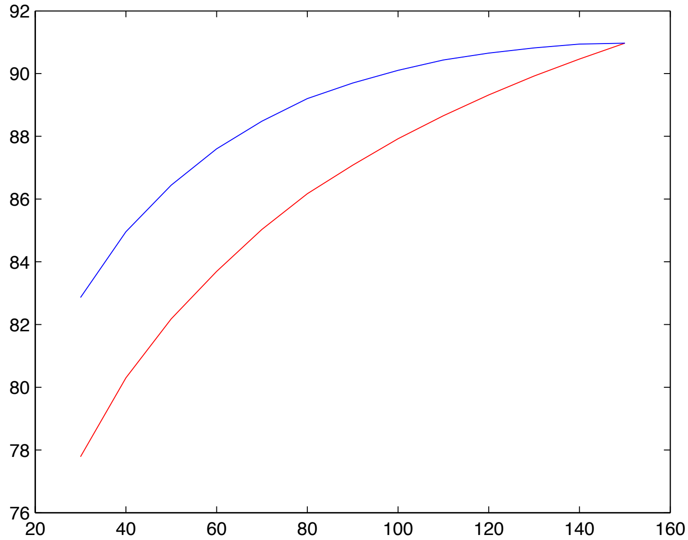

Figure 7.6: Pressure in dB SPL in function of the frequency at $\theta = 90°$ for a first-order gradient speaker-unidirectional, with a fixed delay (red curve) and with a frequency-dependent delay (blue curve)

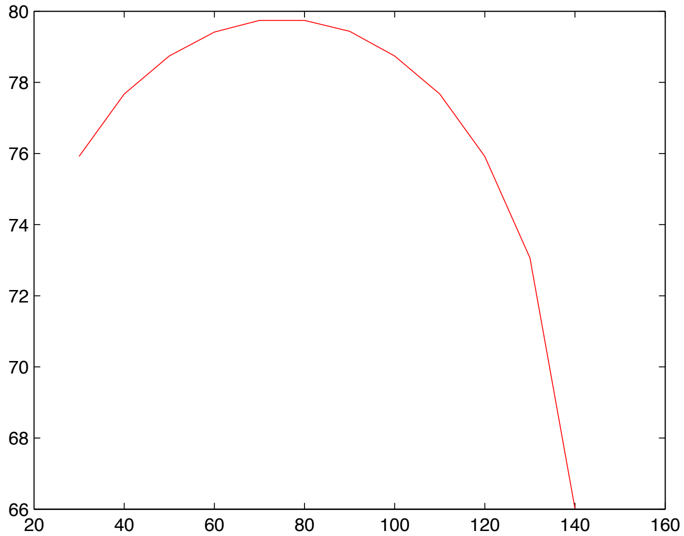

Figure 7.7: Pressure in dB SPL in function of the frequency at $\theta = 180°$ for a first-order gradient speaker-unidirectional with a frequency-dependent delay

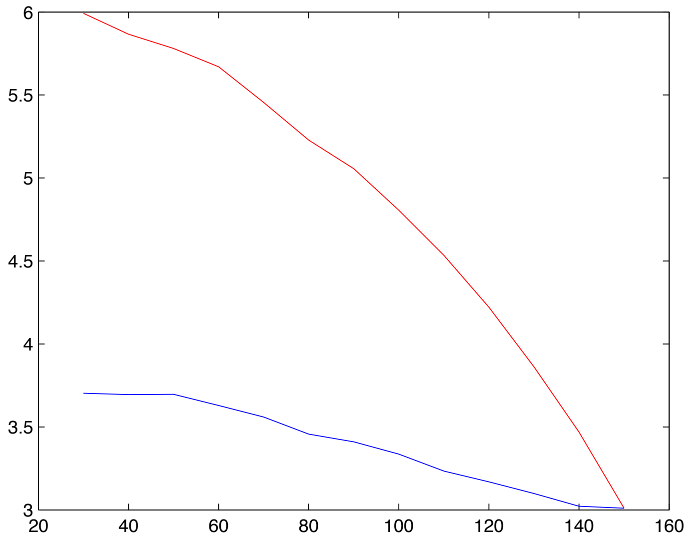

Figure 7.8: Difference of pressure between the front $\theta = 0°$ and the side $\theta = 90°$ of a first-order gradient speaker-unidirectional, with a fixed delay (red curve) and with a frequency-dependent delay (blue curve). The results are dB SPL in function of the frequency.

7.3 FDTD simulations

Earlier in this project, it has been remarked that some differences could exist between the directivity pattern obtained analytically and the one obtained for real and simulated more accurately with the FDTD method. Therefore, the effects of the floating delay described by equation 7.3 are tested with the FDTD method. The details concerning the parameters of the simulations as well as the complete results are shown in appendix D.2.

On these simulations the differences between the setup with a fixed delay and the setup with the floating delay appears quickly. At 30 Hz from the frequency of the perfect cardioid behavior a small rejection starts to appear on the back of the setup with the fixed delay whereas the setup with the floating delay is almost unchanged. At 50 Hz from the frequency of the ideal behavior the differences between both setups are obvious. A higher rejection appears on the back of the system with the fixed delay. On the front of the system with the floating delay the pressure keeps a shape comparable to the one of the ideal behavior whereas it becomes narrower with the fixed delay. These differences are going to increase as long as the frequency decrease. At the low frequencies of the bandwidth, the setup with a frequency-dependent delay seems better for projecting the sound forward and keeping the back rejection lower.

7.4 Conclusions

In this chapter the work has been focused on improving the control of the directivity of a first-order gradient sound source-unidirectional and more specifically, on trying to keep the directivity pattern constant over a wide frequency range.

This has led to find a relation between the frequency and the delay applied on the back subwoofer of a first-order gradient setup.

This frequency-dependent delay has been tested both analytically and with the FDTD simulation. The results appeared to be encouraging. So this floating delay should then be tested on a setup using real subwoofers.

8

Design of an all-pass filter with specified group-delay

8.1 Introduction

Spectral delay filtering is an audio processing method in which different frequencies of a signal are delayed by different amounts. Different methods can be implemented to achieve such results. One of the recently introduced method consists in utilizing a cascade of first order all-pass filters.

Usually, filtering an audio signal with a time-invariant all-pass filter does not have a major effect on the timbre because it does not change the magnitude of the signal. Moreover the group delay of a first order all-pass filter is almost constant for all the frequencies. So no noticeable change would be heard if an audio signal was processed with a first order all-pass filter.

At the contrary if a high-order all-pass filter is constructed by cascading several low-order all-pass filters, each introducing a mild phase shift, the overall filter has a phase shift that is the sum of the phase shifts of the individual low-order filters. In that case, impressive audible changes maybe obtained if an audio signal is processed by a such filter. The reason is that the low and the high frequencies become separated in the output signal and a chirp like effect can be heard.

Therefore, all-pass filters are commonly used in audio and music processing. Their applications go from effect processing (simulation of reverberation, digital phase, shelving filter, distortion effect) to fractional delay or inharmonic synthesis of piano tones. More generally in lot of different fields all pass filters are used to compensate for phase non-linearity of linear systems or for group-delay equalization.

In this project an all-pass filter is used to obtain a frequency dependent delay on the back subwoofer of a first-order gradient setup.

This chapter aims to design an all-pass filter whose group-delay closely approximates the ideal group-delay function previously defined in chapter 7 by equation 7.3.

8.2 Properties of all-pass filters

As its name indicates an all-pass filter has an unity magnitude response in the whole frequency band. Thus, when designing an all-pass filter one can concentrate on the approximation of a desired phase or on the group-delay.

The z-transfer function of a N^{th}-order all-pass filter is:

$A(z) = \frac{a_N + a_{N-1}z^{-1} + a_{N-2}z^{-2} + ... + a_1 z^{-(N-1)} + z^{-N}}{1 + a_1 z^{-1} + ... + a_{N-1}z^{-(N-1)} + a_N z^{-N}}$

The numerator polynomial is a mirrored version of the denominator. One of the main disadvantage of this filter is the possible instability. So it has to be aware that the poles remain within the unit circle when designing such filter. In this project the coefficients are assumed to be real values to allowed an eventual implementation.

According to [17] The phase response of the all pass filter can be expressed as:

$$\theta_A(\omega) = arg(A(e^{j\omega})) = -N\omega + \arctan \frac{\sum_{k=0}^{N} a_k sin(k\omega)}{\sum_{k=0}^{N} a_k cos(k\omega)}$$

where N is the order of the all-pass filter, ω is the radial frequency and a_k are the coefficients of the filter.

The group delay is defined as:

$$\tau_A = -\frac{d\theta_A(\omega)}{d\omega} = N - 2\frac{\mathbf{a}^T G \Lambda \mathbf{a}}{\mathbf{a}^T G \mathbf{a}} \tag{8.1}$$

with

- $\mathbf{a} = [a_0 \, a_1 \, a_2 \, ... \, a_N]^T$
- $G = cc^T + ss^T$
- $c = [1 \cos(\omega) \cos(2\omega) ... \cos(N\omega)]^T$
- $s = [1 \sin(\omega) \sin(2\omega) ... \sin(N\omega)]^T$
- $\Lambda = diag(0 \, 1 \, 2 \, ... \, N)$
- T is the matrix operator transpose

It can be noticed that the group delay is related to the filter coefficients in a nonlinear manner. Therefore it is not possible to have simple design formulas for the all-pass filter coefficients. Instead an iterative optimization techniques that minimize the traditional error criteria can be used. The next section describes a method to find the coefficients of an all-pass filter having a desired group delay based on the minimization of the error criteria.

8.3 Filter coefficient determination

8.3.1 Error minimization

Whatever the algorithm used for the determination of the filter coefficients **a** they are all based on the minimization of the error function $\varepsilon(\omega)$ over the band of interest $[\omega_1\, \omega_2]$.

$$\varepsilon(\omega) = \tau_{id}(\omega) - [\tau(\omega) + \tau_A(\omega)] \tag{8.2}$$

with

- $\tau_{id}(\omega)$: the ideal or desired group delay
- $\tau(\omega)$: the initial group delay of the system
- $\tau_A(\omega)$: the group delay of the all pass filter one wants to design
- $\omega \in [\omega_1\, \omega_2]$

In this project the ideal group delay τ_{id} is defined by equation 7.3. The group delay of the filter one wants to design is defined by equation 8.1. The initial group delay of the system $\tau(\omega)$ is set to zero.

A way to find out **a** is to minimize the mean squared value of the error function $\varepsilon(\omega)$ over the band of interest. This is equivalent to solve the non-linear equation 8.3.

$$\zeta = \int_{\omega_1}^{\omega_2} \varepsilon^2(\omega)d\omega = \int_{\omega_1}^{\omega_2} (\tau_{id}(\omega) - \tau_A(\omega))^2 d\omega \tag{8.3}$$

ω_1 and ω_2 define the frequency interval where one wants to design the desired filter. The best realizable filter $\tau_A(\omega)$ is the one that minimizes the integral ζ of equation 8.3. Different methods can be used to solve this nonlinear minimization problem. An overview of them is made in the next subsection.

8.3.2 Overview of the algorithms

Several different algorithms that minimize the integral of equation 8.3 and help to determine the coefficients **a** have been developed in the past decades. It is not possible to study the advantages and disadvantages of all of them in this report. Only a brief overview of the most famous and the most relevant algorithms is made. This will end by the choice of one of them for this project.

In the sixties and the seventies the minimization of equation 8.3 has been studied by Fletcher and Powell and by Deczky. They have left famous algorithms still considered as references today but whose applications are mainly focused on group delay equalization. In [2] the design of the IIR filter uses a constrained gradient algorithm for group delay equalization.

A new approach based on matrix operation is introduced by Laakso and al in [17]. This study was reused later by Tapia and al in [7] specifically for the design of allpass filter respecting a desired group delay. According to the expressions of $\tau_{id}(\omega)$ and $\tau_A(\omega)$ defined by equations 7.3 and 8.1

respectively, the error $\varepsilon(\omega)$ can be expressed as a multiplication of several matrix as shown in equation 8.4.

$$\varepsilon(\omega) = \frac{\mathbf{a}^T G((\tau_{id}(\omega) - N)Id + 2\Lambda)\mathbf{a}}{\mathbf{a}^T G\mathbf{a}} \tag{8.4}$$

In equation 8.4 Id designates the identity matrix. The integral 8.3 that needs to be minimized can then be written as in equation

$$\zeta = \int_{\omega_1}^{\omega_2} \left[\frac{\mathbf{a}^T GK\mathbf{a}}{\mathbf{a}^T G\mathbf{a}}\right]^2 d\omega \tag{8.5}$$

with

$$K = (\tau_{id}(\omega) - N)Id + 2\Lambda \tag{8.6}$$

To minimize the error ζ Tapia constrains K to be positive in order to remove the squared function. The error becomes

$$\zeta = \mathbf{a}^T R\mathbf{a} \tag{8.7}$$

with

$$R = \int_{\omega_1}^{\omega_2} \frac{GK}{\mathbf{a}^T G\mathbf{a}} d\omega \tag{8.8}$$

The minimum error ζ is then obtained after few iteration steps by finding the eigen vector **a** corresponding to the smallest eigen value of R. This method has the advantage that it can be quickly coded and simulated. It also gives good results with few iteration steps. But the constrain of K positive is a limiting factor of this method. In [8] Tapia proposes another method minimizing the error with an iterative quadratic maximum likelihood algorithm. Facing the complexity of this method, especially on a mathematical point of view, it has been decided to not simulate this method.

Different algorithms for the design of recursive filters using optimization methods have been proposed by Antoniou in [4]. Starting with the Newton algorithms to minimizes the integral of equation 8.3, Antoniou proposes several improvements leading to new classes of algorithms called quasi-Newton algorithm and Minimax algorithm. The detailed theory describing these algorithms are presented pages 496-515 in [4]. The works of Antoniou are the basis of a Matlab function called *iirgrpdelay*. This Matlab function allows to design all pass IIR filters that have group delay characteristics defined by the user.

Thereby, this Matlab function will be used unchanged to find the coefficients of the all pass filter that fits the best with the desired delay needed in this project and defined earlier by equation 7.3. In the next subsection 8.3.3 the Matlab function *iirgrpdelay* is used to design the filter needed in this project. The results obtained are presented.

8.3.3 Design of the desired group delay

This subsection 8.3.3 aims to design the all pass filter needed in this project using the Matlab function *iirgrpdelay*. The inputs and outputs of this function are presented and the corresponding values used in the case of this project are detailed.

The *iirgrpdelay* function can be used with different numbers of input and outputs depending on the needs of the user (see Matlab help). In this project a version with 6 inputs and 3 outputs is used.

Inputs

The six inputs of the *iirgrpdelay* are the order N, the frequency F, the band-edges, the vector defining the desired group delay Gd, the vector to weight the error W and the maximum pole radius.

- N: This first entry gives the order of the all pass filter. After several tries it appears that increasing the order was not giving results significantly better. The only constrain imposed by Matlab on this input is that it must be an even number. Thus, it is decided to take $N = 8$.
- F: This entry is a vector containing the frequencies used to defined the shape of the desired group delay. Frequencies have to be normalized between 0 and 1. The frequency-dependent delay function defined by equation 7.3 is a linear function. So it is graphically represented by a straight. Therefore only two points are needed in the frequency vector and in the Gd vector. One chooses arbitrarily both extreme frequencies of the bandwidth of interest. Regarding the bandwidth of the subwoofer used before one takes $f_1 = 30Hz$ and $f_2 = 150Hz$. So expressed in normalized frequency $F = \left[\frac{30}{f_s}\,\frac{150}{f_s}\right]$ with f_s the sampling frequency.
- Edges: This vector specifies the band-edge where one wants to design the desired group delay. The values of this vector are also normalized. As the frequency vector defined just before contains only two frequencies which are the lower and upper limits of the bandwidth the edge vector is equal to vector F.
- Gd: This entry is the vector whose elements are the desired group delay at frequencies specified in F. Its values are expressed in samples. An important remark is that the desired group delay defined in this vector is relative. This point will be rediscussed later. From a practical point of view, according to equation 7.3 which is the group delay one wants to design, if the maximum frequency where the cardioid mode is desired is equal to 150 Hz (see chapter 7) and the sampling frequency is equal to 8000 Hz (for the reasons previously discussed in chapter 6), one obtains a desired group delay of 24 samples for $f = 30Hz$ and 13 samples for $f = 150Hz$. So $Gd = [24\,13]$.
- W: This vector aims to weight the error. It must have the same size than F. Here one sets it equal to $[11]$.
- radius: This number limits the maximum pole radius. It is a number between 0 and 1 (excluded). Its default value is 0.9999. In the design of this project the default value is conserved.

Outputs

The three outputs generated by the function *iirgrpdelay* are the coefficients of the numerator *b*, the coefficients of the denominator *a* and the offset tau. If the meaning of vectors *b* and *a* are obvious, the role of tau needs some explanations. Few lines before, one has said that the desired

group delay defined in Gd was relative. The filters created by *iirgrpdelay* have a group delay that approximates $(Gd + tau)$. So the values of the group delay obtained through this design are not the ones expected on an absolute point of view. But the shape of the desired group delay is the same at a factor tau near.
Practically in this project, a delay equal to tau will be applied on the front subwoofer so that the relative delay between the front and the back subwoofer is still corresponding to the desired delay of equation 7.3.

Results

Respecting the specifications given for the inputs of the *iirgrpdelay* function, the group delay represented by the blue curve on figure 8.1 is obtained. The green curve corresponds to the group delay desired for this project and defined by the vector Gd. The red curve corresponds to the desired delay shifted with the offset return buy the Matlab function. This offset is equal to 53 samples.

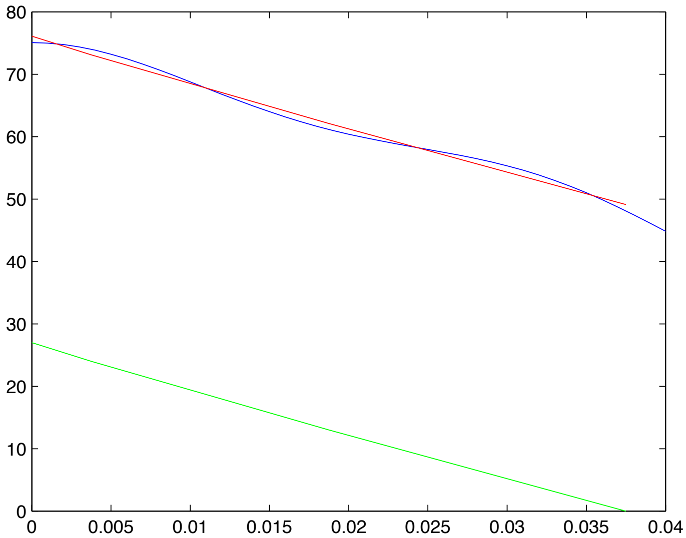

Figure 8.1: Group delay of the filter designed by the Matlab function *iirgrpdelay* (blue curve). Desired group delay (green curve). Desired group delay shifted by the offset (red curve). The x-axis represents the normalized frequencies. The y-axis represents the group delay expressed in samples

Regarding figure 8.1 the result obtained fulfill the conditions needed for this project. In the next subsection 8.4 the iir filter one has designed is going to be tested in the FDTD simulation of a first order gradient source-unidirectional using the impulse response of a real subwoofer.

8.4 FDTD simulations with an all pass filter of desired group delay

The frequency-dependent delay function defined in chapter 7 is now realized with the IIR all pass filter designed in section 8.3.3. Its performances are going to be evaluated with a FDTD simulation.

The aim of this section 8.4 is to simulate the behavior of a first order gradient source-unidirectional that uses the impulse response of a real subwoofer and whose back subwoofer is filtered by the all pass filter designed in 8.3.3.

The signal path of both subwoofers for a such setup is shown on figure 8.2. On this figure, the ***IIR** all pass filter* block filters the signal going to the back subwoofer introducing a delay dependent of the frequency with respect to equation 7.3. This IIR filter introducing also an offset as previously discussed in 8.3.3 the front subwoofer needs to be delayed by a number of samples equal to the offset introduced by the all pass filter. This explains the block $Z^{-offset}$ in the block diagram of figure 8.2.

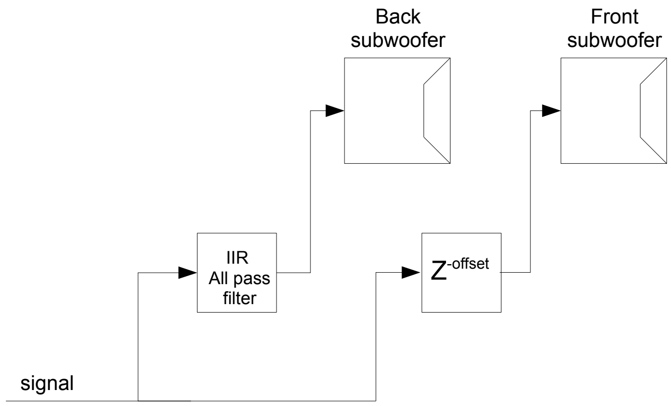

Figure 8.2: Signal path of a first order gradient setup with an IIR filter on the back subwoofer

In the simulations presented in this section, one uses the same subwoofer and simulation parameters than in the simulations of chapter 6 so that a direct comparison between both can be made.

To avoid the formation of notches in the front of the system the cardioid frequency is chosen equal to the maximum frequency produced by the subwoofer. So $f_{max} = 150Hz$. To justify this choice one can refer to sections 6.3 and 7.2. For a cardioid frequency equal to 150 Hz the distance between both subwoofers must be $D = \frac{c}{4f_{max}} = 0.57$m (with $c = 343m.s^{-1}$).

The results of the FDTD simulation can be seen in appendix E. Some examples are showed bellow on figure 8.3. The pressure field obtained at different discrete frequencies is plotted with the same method than in 6.3. To facilitate comparisons between a setup having the all pass filter and a setup without this all pass filter, one shows in parallel the results obtained when the designed all pass filter is applie on the back subwoofer and the results previously obtained in the *case 1* simulated in 6.3.

Observing the results one can see the influence of the all pass filter on the pressure field at different discrete frequencies.
The differences between both setups (with and without the all pass filter) seems more obvious in the front of the system than in the back. Indeed, on the front of the system the designed all pass filter seems to help the sound pressure going forward and keeping the shape of the directivity constant (with respect to the original variations of the magnitude of the measured subwoofer). Without the filter the directivity of the system seems becoming more narrow as long as the frequency decreases.
On the back of the system the results obtained are not as good as expected. The back rejection has not exactly the same shape in both setups but a detailed observation shows that the pressure in the back-axis of the subwoofer is almost identical and this for all the frequencies.

Different hypothesis could explain these disappointing results in the back of the system, starting by a possible wrong choice in the desired group delay found in chapter 7 and used in these simulations. Nevertheless, through the experience acquired in the different FDTD simulations, one has already

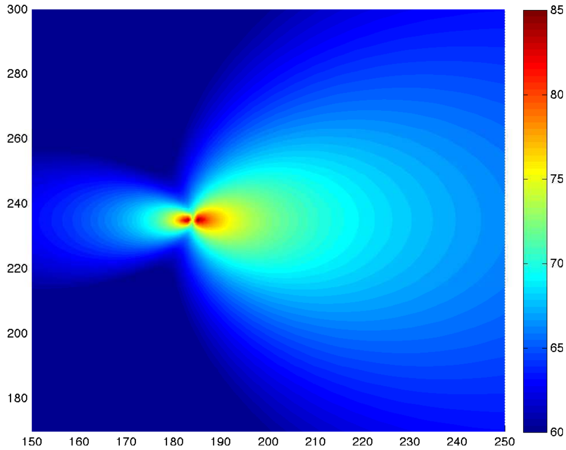

(a) $f = 50Hz$

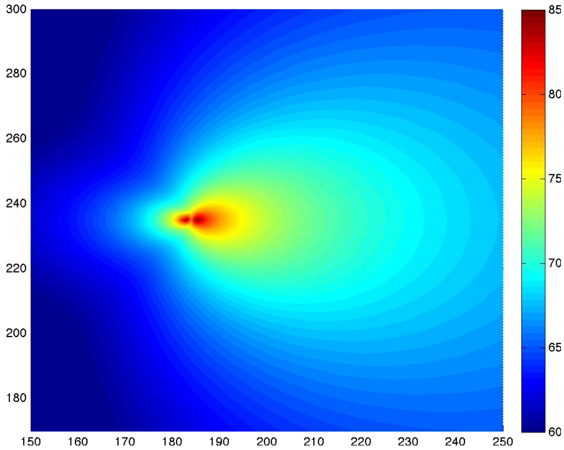

(b) $f = 50Hz$

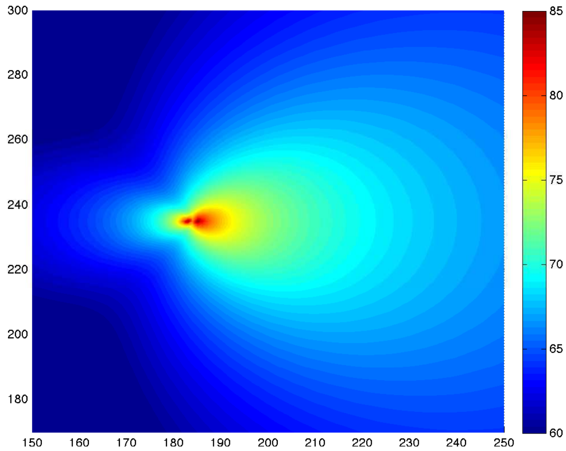

(c) 100

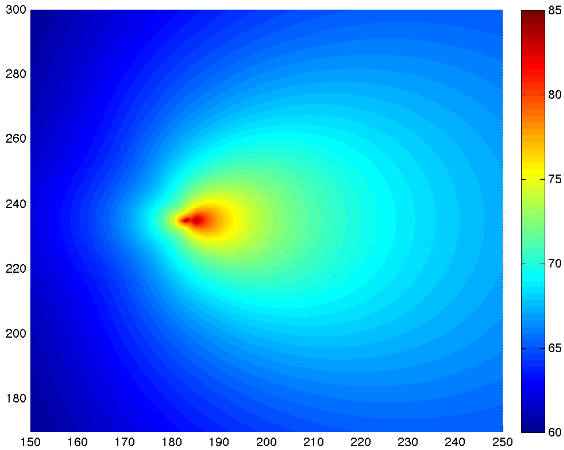

(d) $f = 100Hz$

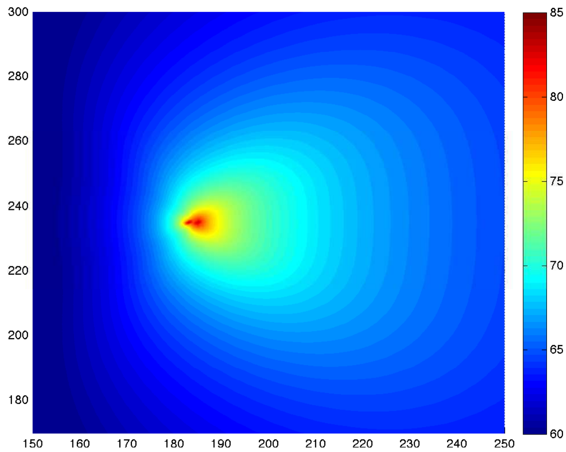

(e) $f = 150Hz$

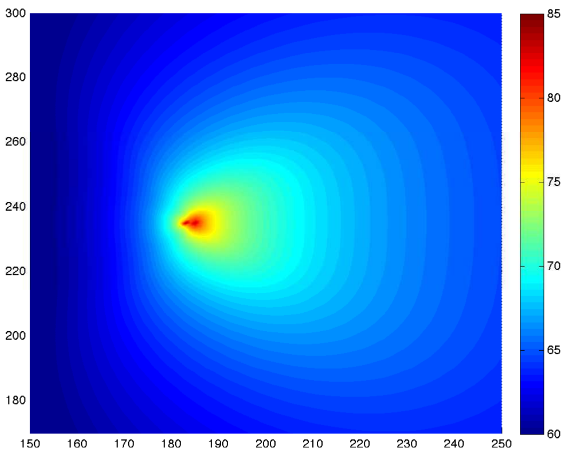

(f) $f = 150Hz$

Figure 8.3: Pressure in dB SPL for a first order gradient sound source-unidirectional setup simulated with a FDTD method fed by the impulse response of a subwoofer. In the left column the delay on the back subwoofer is fixed and equal to $\frac{c}{4f_{max}}$ with $f_{max} = 150Hz$. In the right column the back subwoofer is filtered with the IIR all pass filter designed in chapter 8.4

evoked that the direct vibrations coming from the back subwoofer could explain this rejection present on the back of the system. In all the simulations run till now, both subwoofers had the same input gain. One makes now the hypothesis that using a different gain on the front subwoofer and on the back subwoofer can help improving the control of the directivity of the system. This hypothesis is studied in the next chapter.

9

Influence of the gain on the directivity

9.1 Introduction

This chapter aims to study the possible influence of the gains of the front and back subwoofers on the directivity of the system. Until now, the simulations were conducted with a same gain for both subwoofers. But in [14], Mogale presents some simulation results where the number of subwoofers destined to produce the sound for the audience is higher than the number of subwoofers used to cancel the back-wave. This kind of setup is well known from the sound engineers. Changing the gain on the front and the back subwoofer could help to increase the front to back rejection. After an analytical description, FDTD simulations will be made to see which enhancement can bring a gain variation between the front and the back subwoofer.

9.2 Analysis

9.2.1 Equations

Starting with the first order gradient sound source-unidirectional setup shown on figures 2.7 and 2.8, one adds a gain G in the expression of the pressure generated by the front subwoofer originally defined by equation 2.34. This leads to a new equation for the pressure of the front subwoofer 9.1:

$$p_1(r) = -\frac{jG\rho_0 U_0 Skc}{4\pi(r+\Delta r_1)} \exp j(\omega t - k(r - \Delta r_1 - \frac{d}{4})) \tag{9.1}$$

Following the same procedure than in section 2.4 to find the pressure generated by the system in far field one gets equation 9.2 as final result.

$$p(r) = -\frac{j\rho_0 U_0 Skc}{4\pi r} \exp j(\omega t - kr)\Big[G \exp jk(\Delta r + \frac{d}{4}) - \exp -jk(\Delta r + \frac{d}{4})\Big] \tag{9.2}$$

The expression of the directivity pattern generated by this system is contained in the last term of the equation 9.2. Taking its absolute value gives

$$R(\theta) = \sqrt{1 + G^2 - 2G\cos\left(2k(\Delta r + \frac{d}{4})\right)} \tag{9.3}$$

Expressing the directivity pattern in function of the ratio $\frac{D}{\lambda}$ as previously done in chapter 2 gives a new expression 9.4 for the directivity pattern:

$$R(\theta) = \sqrt{1 + G^2 - 2G\cos\left(\frac{\pi D}{\lambda}cos\theta + \frac{\pi d}{\lambda}\right)} \tag{9.4}$$

It is important to notice that if G is taken equal to 1, meaning equal to the gain of the back subwoofer, equation 9.3 becomes equal to the expression of the directivity pattern 2.38 previously found in section 2.4.

9.2.2 Simulations

In this subsection 9.2.2 equation 9.3 is simulated for different values of gain G and ratio $\frac{D}{\lambda}$.

One makes varying the gain G from 1 to 2 by step of 0.1. Two different values of $\frac{D}{\lambda}$ are chosen. $\frac{D}{\lambda} = 0.25$ corresponds to the ideal cardioid behavior, and $\frac{D}{\lambda} = 0.125$ chosen arbitrarily, corresponds to the behavior at the frequency equal to half the cardioid frequency. Figures 9.1 and 9.2 show some of the results obtained. The whole results can be seen in appendix F.1.1 and F.1.2.

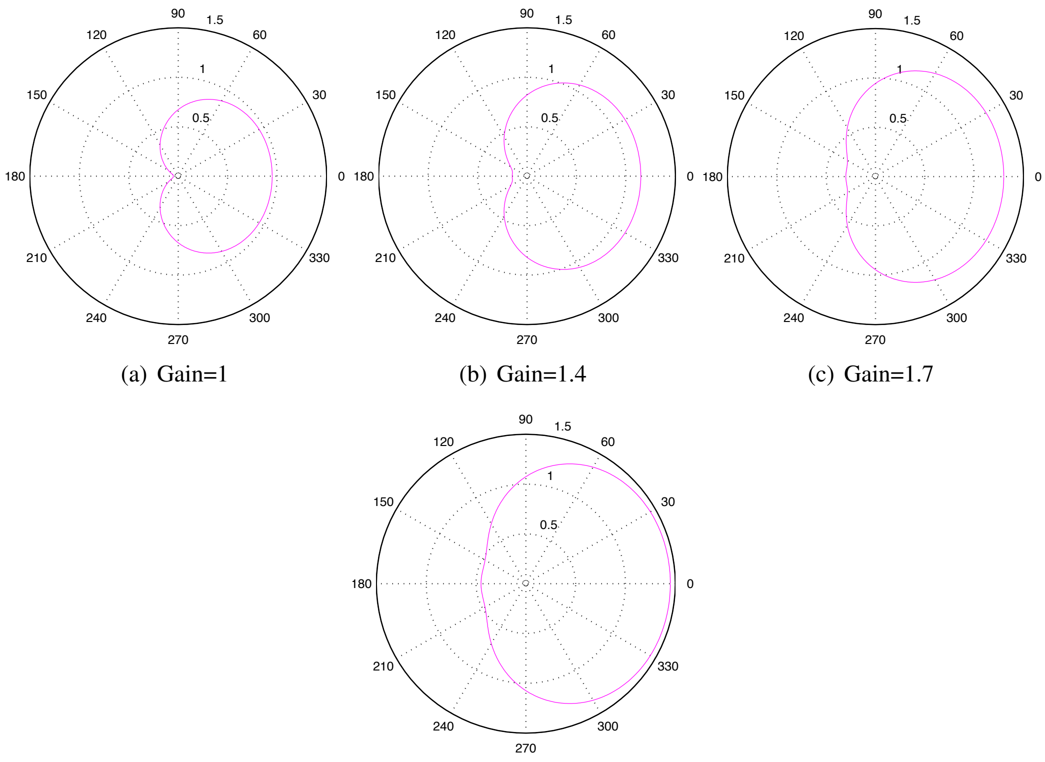

(a) Gain=1 (b) Gain=1.4 (c) Gain=1.7

(d) Gain=2

Figure 9.1: Directivity pattern of a first order gradient sound source-unidirectional for different values of gain applied on the front subwoofer. The results are expressed in pascal. The ratio $\frac{D}{\lambda}$ and $\frac{d}{\lambda}$ in equation 9.4 are equal to 0.25.

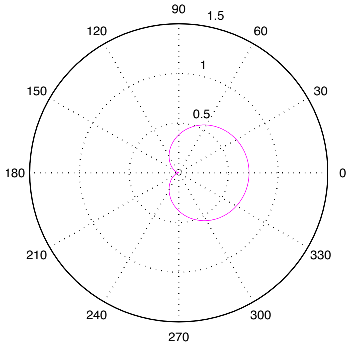

(a) Gain=1

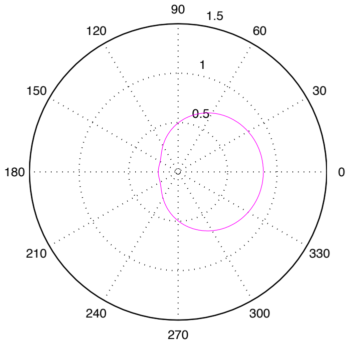

(b) Gain=1.4

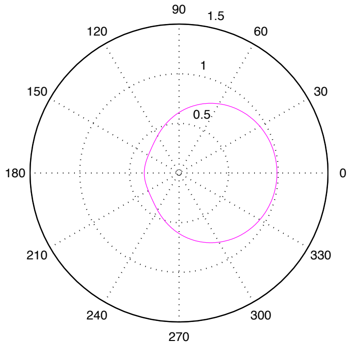

(c) Gain=1.7

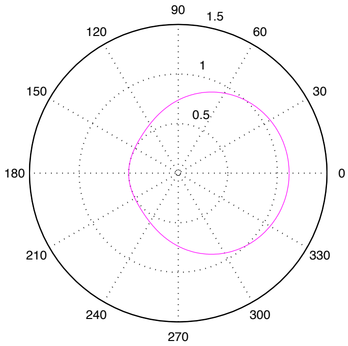

(d) Gain=2

Figure 9.2: Directivity pattern of a first order gradient sound source-unidirectional for different values of gain applied on the front subwoofer. The results are expressed in pascal. The ratio $\frac{D}{\lambda}$ and $\frac{d}{\lambda}$ in equation 9.4 are equal to 0.125.

From these results, different observations can be made. Whatever the value of $\frac{D}{\lambda}$, increasing the gain of the front subwoofer produce a higher pressure in the front of the system. But at contrary it also tends to increase the rejection in the back of the system. Therefore a trade-of should be found to produce higher SPL in the front of the system without increasing it much in the back. Nevertheless it has been shown in chapters 5 and 7 that some deviations were existing between the analytical models and the FDTD methods. So FDTD simulations are needed to to complete the observations.

It has already been noticed in chapters 2 and 7 that when the value of $\frac{D}{\lambda}$ decreases the pressure generated by the system decreases as well. So a frequency-dependent gain might helps to keep the pressure produce by the system and its directivity pattern nearly constant along a given frequency band. For a question of time this point will not be developed in this project.

9.3 FDTD simulations

In this section two different kinds of FDTD simulations are made. In the first one, a mono-frequency sinusoidal signal is used and the distance D between the sources as well as the delay d applied on the back source are kept constant. These first FDTD simulations aims to make comparisons with the analytical results of subsection 9.2.2.

In the second kind of simulation one uses a real subwoofer impulse response and the back-subwoofer is filtered with the IIR filter designed in chapter 8.4.

9.3.1 FDTD simulation: Sinusoidal signals

This subsection aims to simulate with a FDTD method a first order gradient source-unidirectional for two values of ratio $\frac{D}{\lambda}$ equal to 0.125 and 0.25 and different values of gain for the front subwoofer as previously made in subsection 9.2.2. Details about the parameters of the FDTD simulation as well as the whole results can be seen in appendix F.2. One presents only few examples in this subsection. On figures 9.3, 9.4, 9.5, 9.6 one shows four examples of gain when $\frac{D}{\lambda} = 0.25$. On figures 9.7, 9.8, 9.9, 9.10 one shows four examples of gain when $\frac{D}{\lambda} = 0.125$.

Case 1: $\frac{D}{\lambda} = \frac{d}{\lambda} = 0.25$

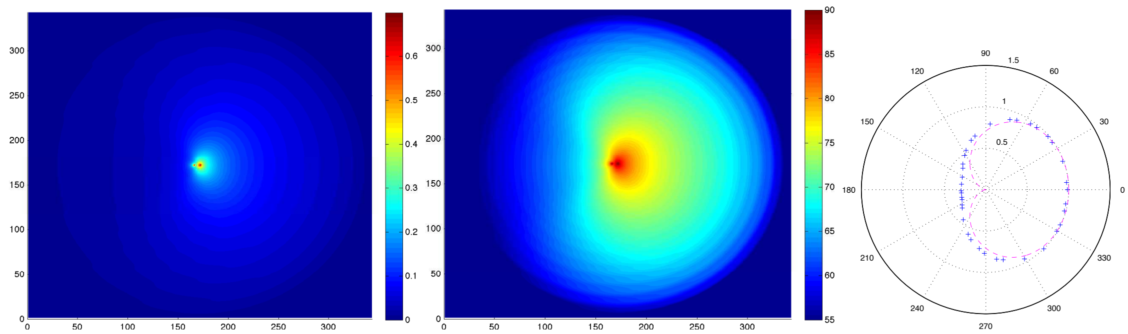

(a) RMS pressure field in pascal (b) RMS pressure field in dB SPL (c) Polar pattern at 10 m in pascal.

Figure 9.3: FDTD simulation for a gain equal to 1

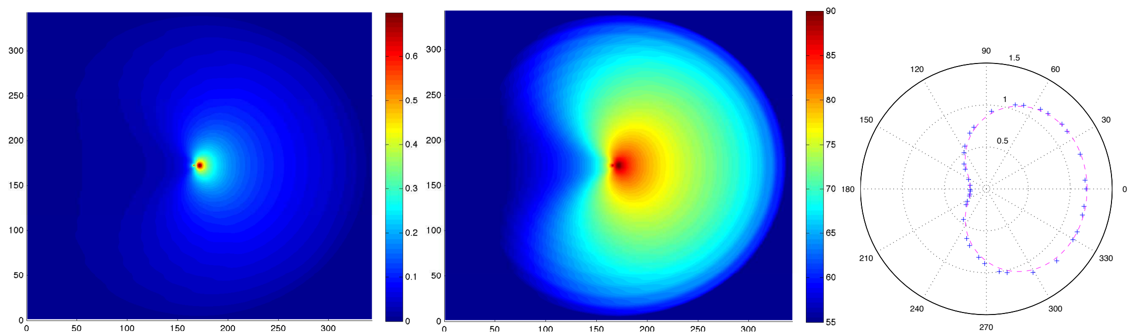

(a) RMS pressure field in pascal (b) RMS pressure field in dB SPL (c) Polar pattern at 10 m in pascal.

Figure 9.4: FDTD simulation for a gain equal to 1.4

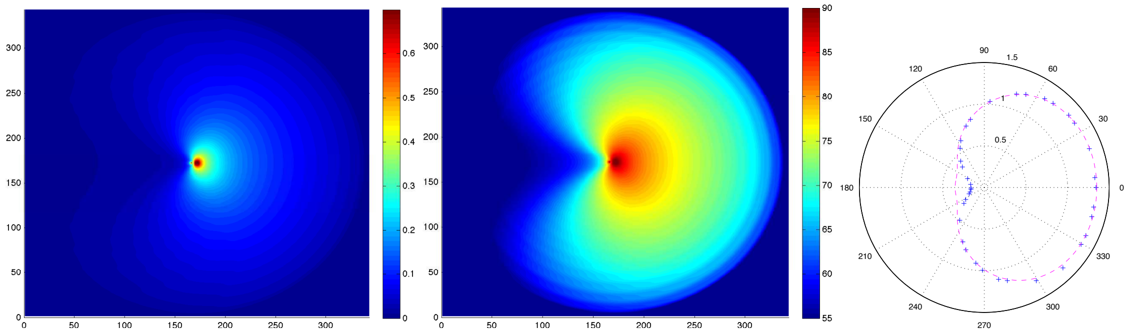

(a) RMS pressure field in pascal

(b) RMS pressure field in dB SPL

(c) Polar pattern at 10 m in pascal.

Figure 9.5: FDTD simulation for a gain equal to 1.7

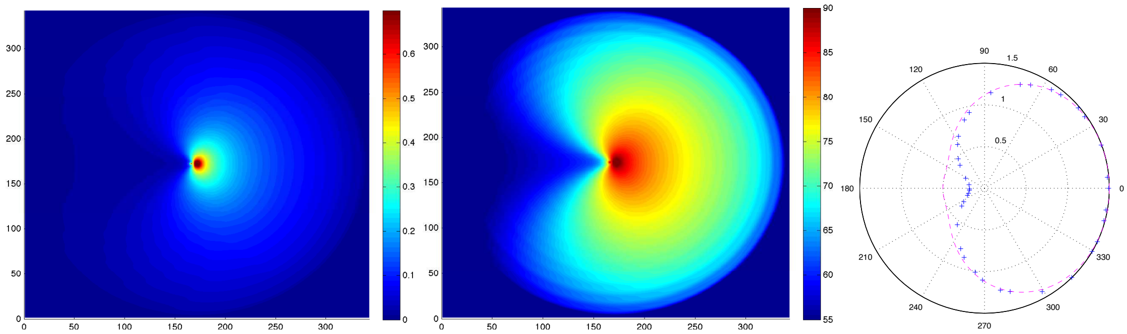

(a) RMS pressure field in pascal

(b) RMS pressure field in dB SPL

(c) Polar pattern at 10 m in pascal.

Figure 9.6: FDTD simulation for a gain equal to 2

Case 2: $\frac{D}{\lambda} = \frac{d}{\lambda} = 0.125$

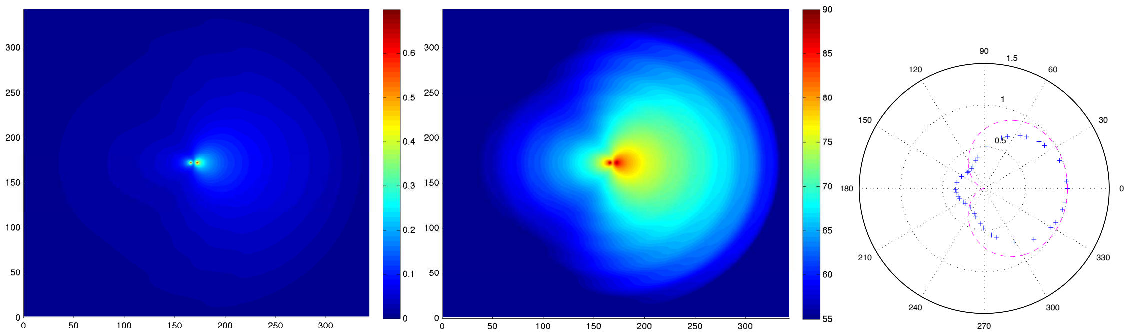

(a) RMS pressure field in pascal

(b) RMS pressure field in dB SPL

(c) Polar pattern at 10 m in pascal.

Figure 9.7: FDTD simulation for a gain equal to 1

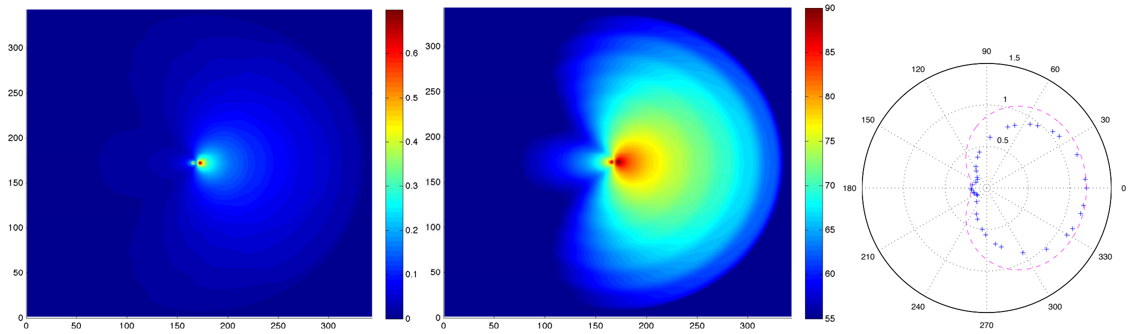

(a) RMS pressure field in pascal (b) RMS pressure field in dB SPL (c) Polar pattern at 10 m in pascal.

Figure 9.8: FDTD simulation for a gain equal to 1.4

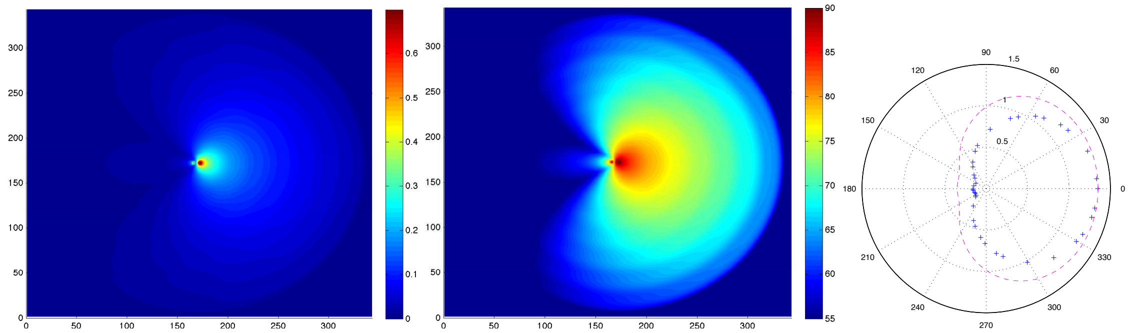

(a) RMS pressure field in pascal (b) RMS pressure field in dB SPL (c) Polar pattern at 10 m in pascal.

Figure 9.9: FDTD simulation for a gain equal to 1.7

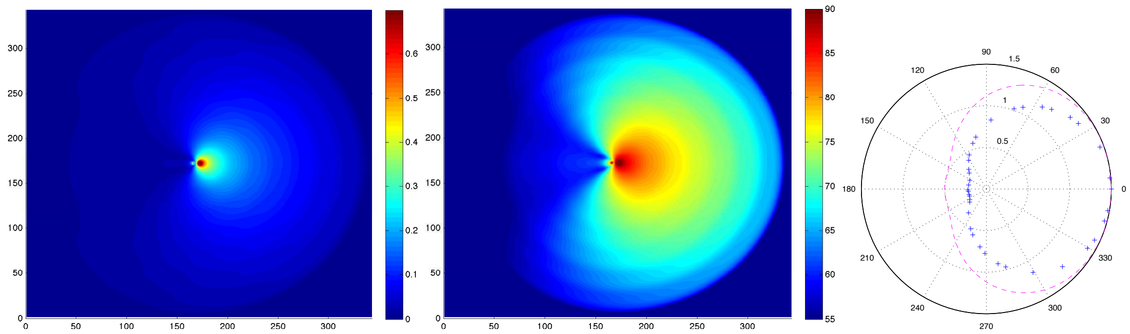

(a) RMS pressure field in pascal (b) RMS pressure field in dB SPL (c) Polar pattern at 10 m in pascal.

Figure 9.10: FDTD simulation for a gain equal to 2

The analysis of the results from the FDTD simulations show that when increasing the gain of the front subwoofer one tends to send more energy to the front of the system and creating a pressure field that has a cardioid shape. The front to back rejection increases as described by Mogale in []. Higher rejections seems nevertheless obtained on the side.

When comparing the analytic polar pattern with the polar pattern extracted from the FDTD simulations one can notice that when the gain of the front subwoofer is close to 1 the analytic simulations predicts better results than the FDTD simulations. Especially the direct radiations coming from the back subwoofer are inexistent in the analytic simulations. When the gain get closer to 2, the FDTD simulations seems more optimistic than the analytical results in term of reduction of the back rejection while keeping identical results in the front of the system.

Therefore these simulations shows that increasing the gain of the front subwoofer can be benefit for a higher control of the low frequency directivity.

9.3.2 FDTD simulation: Real subwoofer impulse response

Now that some observations have been made with pure sinusoid, one realizes different FDTD simulations using the impulse response of a real subwoofer. This impulse response is the same than described in subsection 6.2.1 and already used during previous simulations.

As the gain difference method studied in this chapter 9.3.2 is used as a complement of the IIR filter designed in chapter 8.4 to improve the control of the directivity of the subwoofers, the simulations will be made with the back subwoofer filtered by the all-pass filter of frequency-dependent delay designed previously.

Testing the influence of the gain would take lot of time if one would like to make as many simulations as in subsection 9.3.1 and check the results at several frequencies. Therefore one limits the simulations to two different values of gain. Many loudspeaker manufacturers of the professional audio industry recommends a ratio of two subwoofers in the front and one in the back or three in the front and one in the back to obtain the cardioid behavior. Starting from these recommendations one will do one FDTD simulation with a difference of +3 dB between the front-subwoofer and the back-subwoofer and another simulation with a difference of +4.7 dB. The first case is equivalent to have two sources in the front and one in the back (when doubling the number of sources in the front one earns 3 dB) and the second case is equivalent to three sources in the front and one in the back.

The parameters of the FDTD simulations and the whole results are visible in appendix F.3. One only presents few examples on figures 9.11, 9.12 and 9.13in this subsection. To facilitate the comparisons one plots in parallel the pressure field obtained at different frequencies when:

- The front subwoofer and the back subwoofer have the same gain.
- The front subwoofer produce 3 dB more than the back subwoofer
- The front subwoofer produces 4.7 dB more than the back subwoofer

Regarding the results presented on figures 9.11, 9.12 and 9.13 one can see that for all the frequencies an improvement could be noticed when the gain of the front subwoofer becomes higher than the gain of the back subwoofer. The cardioid pattern is more pronounced as the back rejection decreases significantly. It seems also that one loses some pressure in the front when the gain increases compared to the case of identical gain but the shape stays nearly constant at all the frequencies.

Therefore a combination of both frequency-dependent delay and gain-difference between the front

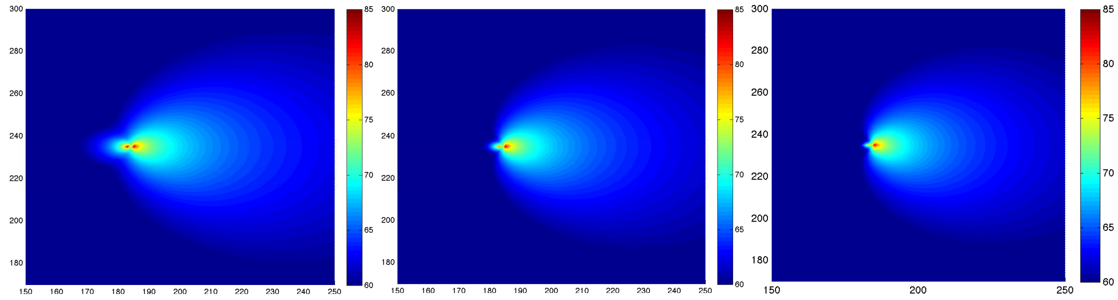

(a) Same gain on both subwoofers (b) 3 dB gain difference (c) 4.7 dB gain difference

Figure 9.11: Pressure field at 40 Hz for three different values of gain-difference between the front and the back subwoofer. The results are expressed in dB SPL

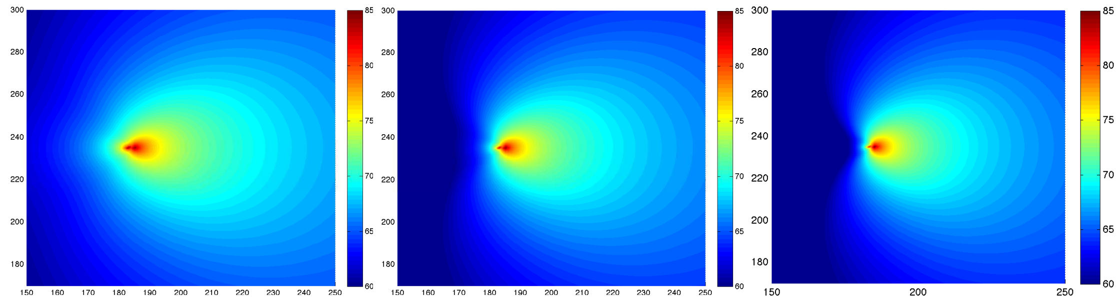

(a) Same gain on both subwoofers (b) 3 dB gain difference (c) 4.7 dB gain difference

Figure 9.12: Pressure field at 100 Hz for three different values of gain-difference between the front and the back subwoofer. The results are expressed in dB SPL

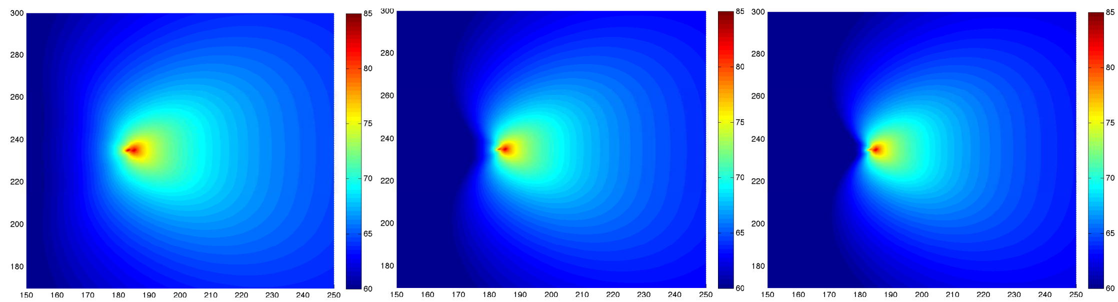

(a) Same gain on both subwoofers (b) 3 dB gain difference (c) 4.7 dB gain difference

Figure 9.13: Pressure field at 150 Hz for three different values of gain-difference between the front and the back subwoofer. The results are expressed in dB SPL

and the back subwoofer could give a good directivity control of low frequencies. The measurements of next chapter 10 will help to validate this hypothesis.

10

Measurements of real setups

10.1 Introduction

In the previous chapters, the subwoofer directivity has been studied on an analytical point of view and through simulations modeling the pressure field produced by different setups of subwoofers. Analytical studies and simulations introduce always approximations simplifying the models and thus giving results different from the reality. Therefore this chapter aims to present the results of measurements conducted on a real subwoofer setup with the different working conditions simulated in chapters 6, 8 and 9.3.2. The working conditions are:

- Subwoofer alone: omnidirectional behavior
- First order gradient source-unidirectional: Initial setup with the distance between the source and the delay kept constant for all the frequencies.
- First order gradient source-unidirectional: Setup with the back subwoofer filtered with the IIR filter designed in chapter 8.
- First order gradient source-unidirectional: Setup with the back subwoofer filtered with the IIR filter and different values of gains.

The results of these measurements are compared with the results of the simulations in order to validate the conclusions made in the previous chapters.

10.2 Measurement conditions

10.2.1 Choice of the method

All the simulations previously made in this project were under the assumption of a free-field behavior. Thus, to compare the simulations and the measurements one should also make these last ones in free field environment. The problem is that measuring low-frequencies in free field conditions has always presented some limitations.

Measuring loudspeakers in free field conditions is very often associated with measurements is anechoic chambers. But when dealing with low-frequencies the free field connections are not mer anymore in anechoic chambers. The reason is that the wavelength at low-frequencies is higher than the size of the chamber. Therefore researchers have tried to find other methods to evaluate the response of loudspeakers at low-frequencies.

In [13], Melon and al compare four different techniques of measurements of subwoofers:

- In anechoic chamber
- Outside in pseudo free field
- In small non-symmetrical room ($2m^2$)
- With a field separation techniques

Regarding the conclusions of [13] and for practical reasons the measurements done in this project will be realized outside. Indeed, measurements in anechoic room are not appropriated if a reference source is not available. Moreover it would require more processing to split the impulse response of the sound system from those of the anechoic room. In small non symmetrical room one can not measure the directivity which is a problem here as one wants to measure the pressure field around the source at different distances. At last the field separation, despite she gives reliable results, seems difficult to perform practically. At the opposite outdoor measurements, despite some constraints that will be described later in 10.2.2, is simple to realize and does not need much post-processing.

[13] presents two different setups for outdoor measurements.

- Subwoofer stacked on the ground
- Subwoofer lifts up far from the ground

Lifting up the subwoofer and the microphone from the ground presents the problem of measuring also the reflections coming from the ground. These reflections can affect a lot the measures. Thus the measurements will be performed with the subwoofers and microphone on the floor. With a such setup the effects introduced by the floor are limited. Nevertheless the floor has still a role in this kind of setup. As it can be considered as a perfect rigid boundary it reflects the sound almost perfectly creating an image-source as shown on figure 10.1.

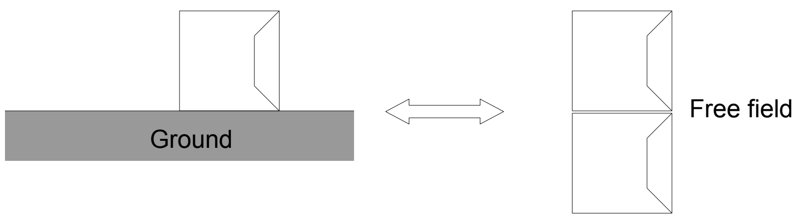

Figure 10.1: Equivalence between a loudspeaker staked on a rigid boundary and its behavior in free-field

So a ground stacked setup is equivalent to use two sources in free field conditions. The same remark could be done for the microphone.

10.2.2 Setup recommendations

According to [13] some parameters need to be carefully controlled or at least considered when doing measurements outside.

- Weather forecast: For outside measurements very kind weather is needed. Especially it must be windless because wind generates mostly low frequencies.

- Background Noise: The background noise should be as low as possible. Indeed if an anechoic room is used its background noise is inaudible and do not affect the measures. At the opposite, outside, the background noise can be high and come from different kind of sources: wind, road traffic or other transportation facilities (train, plane), people, etc... Therefore, the place where the measurements will be conducted should have a limited background noise especially a low-frequencies.

- Distances from the walls: In the case of a place surrounded by walls, a minimum distance between the subwoofer and the wall should be respected. This distance should be higher than the biggest wavelength in order to limit the effect of the reflections and the creation of interference between the direct wave and the reflected wave. On a practical point of view, a long distance between the subwoofer and the walls delay the arrival time of the first reflections in the measured impulse response as shown on figure 10.2. So it does not affect much the direct impulse response measured leaving enough samples to have a good accuracy in the FFT at the lower frequencies of the bandwidth. In [13] a minimum distance of 10 meters between the subwoofer and the wall is considered as acceptable.

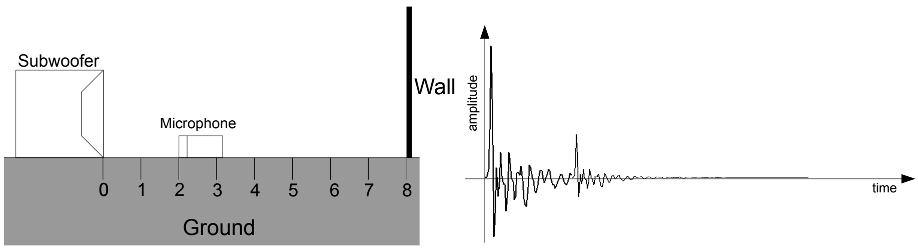

(a) Subwoofer positioned at 8 m from a wall (b) Impulse response corresponding to subfigure 10.2(a)

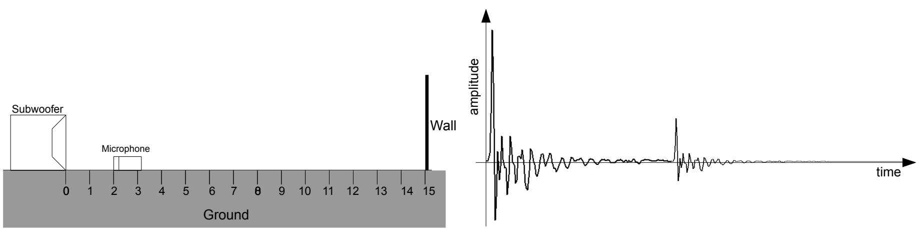

(c) Subwoofer positioned at 15 m from a wall (d) Impulse response corresponding to subfigure 10.2(c)

Figure 10.2: Theoretical impulse response measured for two different distances between the subwoofer and the wall

10.3 Measurement Setup

To facilitate the comparison between the simulation results from the FDTD method and the measurements it is decided to measure the pressure field around the subwoofer in many points positioned on a pre-determined grid that looks like the grid used for the FDTD simulation. This choice will allow to obtain the pressure-map generated by the different subwoofer setups at different discrete frequencies similarly than in the previous simulations. But choosing a such measurement setup can be time consuming as the number of point to measure can increase quickly. Therefore, the distance between the measured points will be higher than the grid size of the FDTD simulations and the size of the space one wants to measure will be smaller. In the FDTD simulations the grid size was varying between 0.1 m and 0.3 m depending on the simulations and the space where simulations were conducted spread between around 600 m^2 (square of 25 m by 25m) and 1200 m^2 (square of 35 m by 35 m). For the real measurements the grid size is arbitrarily chosen equal to 1 m and the space to measure has a surface of 200 m^2 (rectangle of 10 m by 20 m). In regard to the directivity pattern of the subwoofer previously measured in appendix (see figure) one can also consider that the radiation of the subwoofer is symmetric and so reduce the number of points to measure. Thus the measurements are only performed on one side of the subwoofer setup and deduced by symmetry on the other side. Figure 10.3 shows the position of the subwoofers in the grid of measurement and the microphones positions.

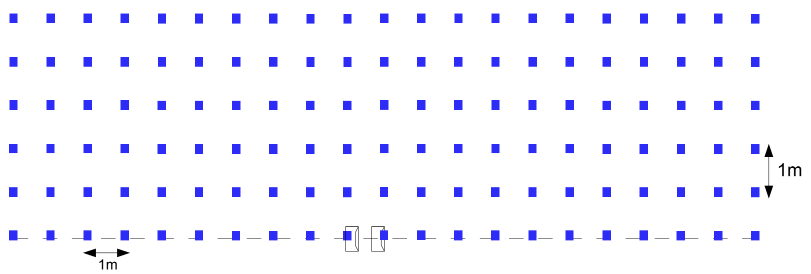

Figure 10.3: Grid for the measurements. Each blue point represents a microphone position. The dashed line represents the symmetry axis.

The journal of measurements with the information relative to the equipment, the signal, the positions of the subwoofers and the microphone as well as the weather conditions is presented in appendix G.3.5.

10.4 Measurement results

The results of the measurements are displayed in appendix G.3.

Different observations can be made. For the measurements with only one subwoofer playing alone, one can see that the omnidirectional behavior is met at all the frequencies from 50 to 150 Hz. This observation confirms the assumption that a subwoofer can be modeled as a point source with omnidirectional directivity pattern.

In the case of a cardioid setup with a fixed distance between the subwoofers and a fixed delay applied on the back subwoofer the results are similar to those of the FDTD simulations. One can especially observe the small rejection generated by the back subwoofer on the back of the system and a reduction of the pressure produced in the front when the frequency decreases.

The configuration with the back subwoofer filtered by the designed all pass filter do not give the expected results. If a cardioid behavior seems to exist from 40 to 80 Hz, the measurements show a quasi omnidirectional radiation at higher frequencies. Different hypothesis could explain these results. It can be a problem with the filtering function used within Matlab that would affect a lot the results. It can also be a behavior that has not been modeled properly during the FDTD simulations. One remark that can be done is that a clear difference could be heard at the back of the system when playing the cardioid configuration without extra processing and the cardioid configuration with the IIR filter. The first of both seemed working better.

For the two last configurations one can observe that the back rejection produced by the back subwoofer has disappeared as expected after the FDTD simulations. The pressure in the front seems a bit lower than in the case of a cardioid setup with fixed delay, but the shape of the directivity seems more constant especially in width. In the case of a gain difference of 4.7 dB between the subwoofers and unexpected high pressure peak is visible on each side of the source at 5 m distance. That might be due to reflections measured at this point that affect the results.

Part V

Conclusion and future studies

11

Conclusion

The purpose of the project documented in this report was to study different methods that could provide a control of the directivity pattern of loudspeakers at low frequency and to propose new solutions to improve the existing methods.

After an analytical study of basic subwoofer setups, helped by FDTD simulations, one has seen that the traditional methods used in the audio industry for controlling the directivity of subwoofers was frequency dependent.

Two solutions have been proposed to counter this frequency dependence. The first one is based on a IIR all pass filter that delays the signal by different amounts depending on the frequency. The second one studied the influence of the gain-difference between the front and the back subwoofer on the directivity control at low frequency.

FDTD simulations showed that each method was providing improvements in term of directivity control and frequency-dependence and that combining both solutions together was giving the best results. These improvements were less significative in the measurement of a real setup. Different explanations could explain these differences between the simulations and the measuremetns. The simulations made with the FDTD method might not be a good representations of what is really happening in the reality, despite some similarities appear in the simulations and in the real setup. Another explanation is that one of the proposed solution, and more particularly the designed IIR filter, do not give the expected results. Maybe that the model of the target filter is not the one which improves the most the directivity control. At last one explanation could be that filtering the signal in Matlab is not as good as implementing the designed filter on a real DSP card.

Therefore, one of the future study could be to implement the proposed solution on a DSP card working in real time to redo the measurements. As some of the solutions developed in this project have been done empirically, the development of advanced mathematical models may lead to a better solution for the target filter to design. Finally using more sound sources like for the second order gradient sound source proposed by Olson in [16] could help to generate more different directivity pattern and help to earn in efficiency.

Bibliography

[1] S.B. Nielsen A. Celestinos. Low-frequency loudspeaker-room simulation using finite difference in the time domain-part 1: Analysis. *Journal of the Audio Engineering Society.*, 56: 772–785, October 2008.

[2] R W. Schafer A V. Oppenheim. *Discrete-time signal processing*. Prentice-Hall, Inc, 1999. ISBN 0-13-754920-2.

[3] MOJ Hawksford AJ Hill. Seeing through the darkness: visualizing low frequency behavior in small rooms. *Proceedings of the Institute of Acoustics*, 31, 2009.

[4] Andreas Antoniou. *Digital filters: analysis, design and applications*. McGraw-Hill, 1993. ISBN 0-07-002121-X.

[5] D. Botteldooren. Finite-difference time-domain simulation of low frequency room acoustic problems. *Journal of the Acoustical society of America*, 98 (6):3302–3308, December 1995.

[6] Malcolm J. Crocker. *Handbook of acoustics*. John Wiley and Sons, Inc, 1998. ISBN 0-471-25293-X.

[7] J L. LoCicero J J. Tapia, G E. Atkin. Digital all-pass filter phase compensation with an enhanced eigenfilter algorithm. *Proceedings IEEE 42nd Midwest Symposium on circuits and systems*, vol 1, 1999.

[8] J L. LoCicero J J. Tapia, G E. Atkin. All-pass filter design in the frequency delay domain using the iterative quadratic maximum likelihood algorithm. *Acoustics, speech and signal processing. IEEE International conference*, vol 6, 2001.

[9] Lawrence E. Kinsler and al. *Fundamentals of acoustics*. John Wiley and Sons, Inc, 2000.

[10] R.J. Luebbers K.S. Kunz. *The finite difference time domain method for electromagnetics*. CRC press LLC, 1993. ISBN 0-8493-8657-8.

[11] H. Kuttruff. *Room acoustics*. Spon press, 5 edition, 2009. ISBN 0-203-87637-7.

[12] U. Kempe L. Ferekidis. The beneficial coupling of cardioid low frequency sources to the acoustic of small rooms. *Audio Engineering Society*, 116 convention, May 2004.

[13] D. Rousseau P. Herzog M. Melon, C. Langrenne. Comparison of four subwoofer measurement techniques. *Journal of the Audio Engineering Society*, 55, 2007.

[14] Rog Mogale. A practical guide to bass arrays, part 1. *Void acoustics LTD*, 2008.

[15] S.K. Olesen. Low frequency room simulation using finite difference equations. *Audio Engineering Society.*, 102 convention, March 1997.

[16] Harry F. Olson. Gradient loudspeakers. *Journal of the Audio Engineering Society*, 21:86–93, 1973.

[17] M Karjalainen U K. Laine T I. Laakso, V Valimaki. Splitting the unit delay. *ieee signal processing magazine*, vol 13, No 1, January 1996.

List of Figures

List of Tables

Part VI

Appendix

A

FDTD method: Figures of the simulations

In all the following sections, the sound sources are defined as a pressure sources fed by a sinusoidal signal varying between -1 and 1.

A.1 First Order Gradient sound source: Bidirectional

In these simulations, the distance between the sources is kept constant $D = 1.14m$, which corresponds to the wavelength of 300 Hz. Then the frequency of the sinusoidal signal is changed in order to obtain the different values of ratio $\frac{D}{\lambda}$.

The graduations on the x and y axis of figures *a* and *b* represent the indexes in the FDTD grid used to calculate the pressure. As the cell size has been chosen equal to 0.1 meter, it is possible to switch directly from indexes to distance (expressed in meter) by multiplying the index by 0.1.

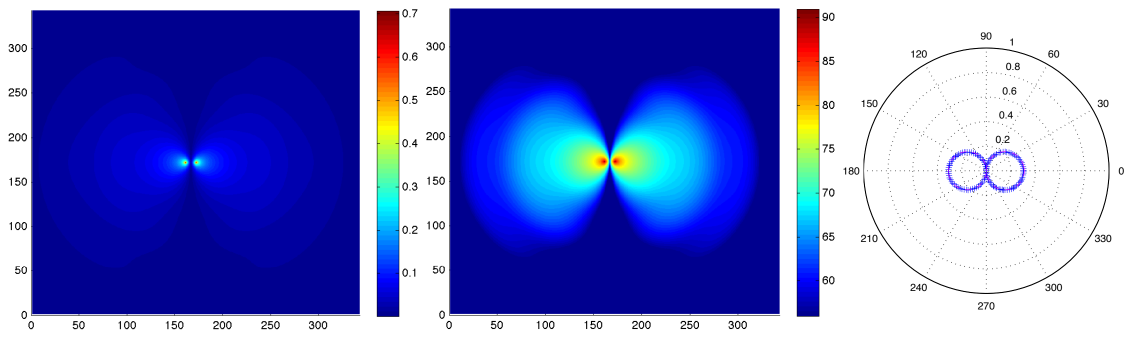

(a) RMS pressure field in pascal

(b) RMS pressure field in dB SPL

(c) Polar pattern at 10 m in pascal

Figure A.1: FDTD simulation for $\frac{D}{\lambda}$=0.1, f=30 Hz

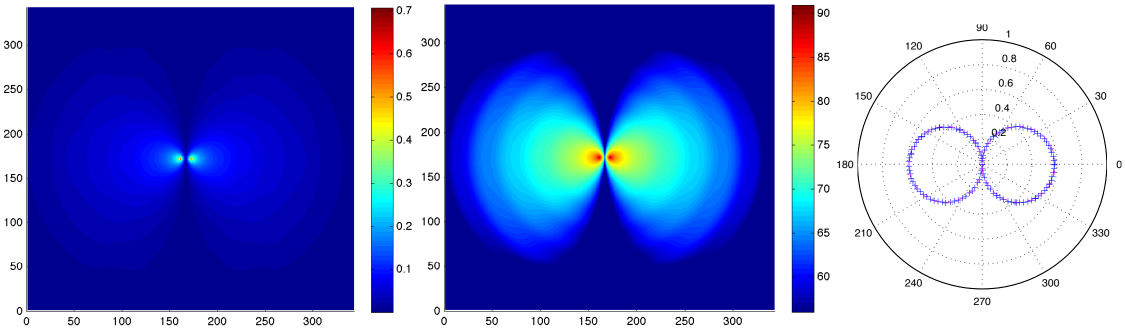

(a) RMS pressure field in pascal (b) RMS pressure field in dB SPL (c) Polar pattern at 10 m in pascal

Figure A.2: FDTD simulation for $\frac{D}{\lambda}$=0.2, f=60 Hz

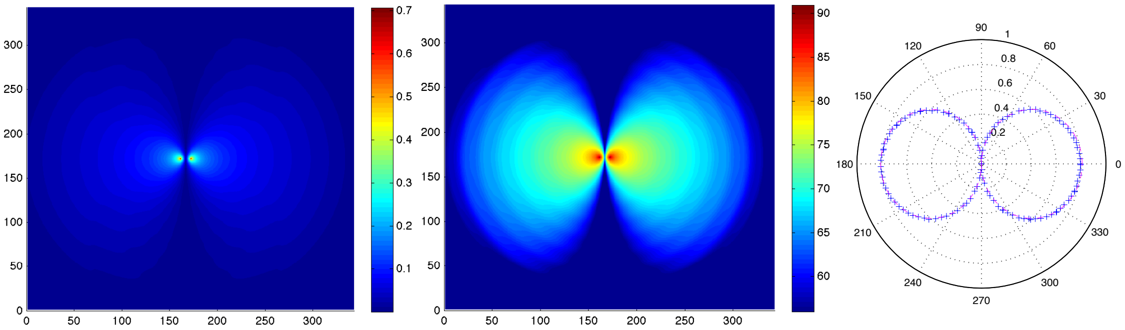

(a) RMS pressure field in pascal (b) RMS pressure field in dB SPL (c) Polar pattern at 10 m in pascal

Figure A.3: FDTD simulation for $\frac{D}{\lambda}$=0.3, f=90 Hz

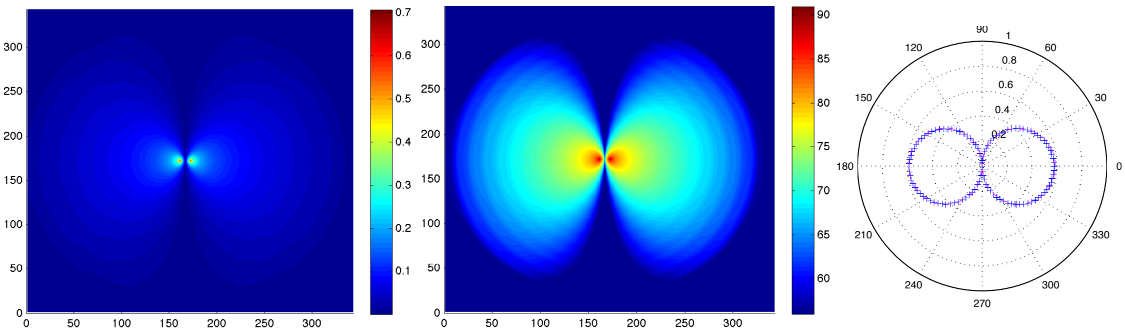

(a) RMS pressure field in pascal (b) RMS pressure field in dB SPL (c) Polar pattern at 10 m in pascal

Figure A.4: FDTD simulation for $\frac{D}{\lambda}$=0.4, f=120 Hz

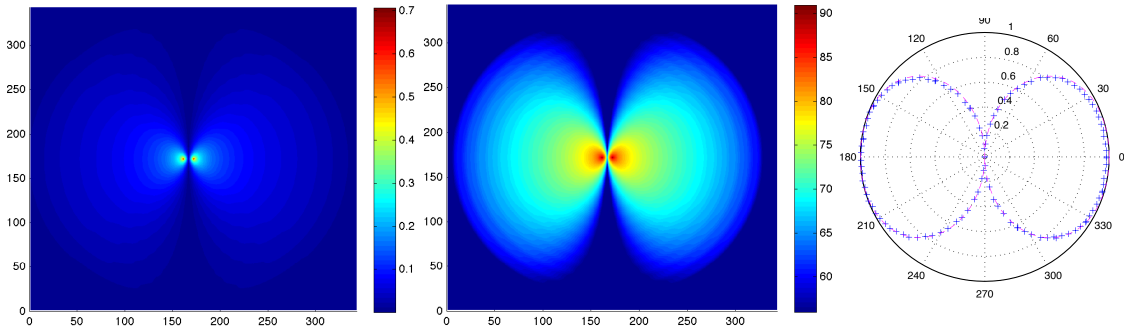

(a) RMS pressure field in pascal

(b) RMS pressure field in dB SPL

(c) Polar pattern at 10 m in pascal

Figure A.5: FDTD simulation for $\frac{D}{\lambda}$=0.5, f=150 Hz

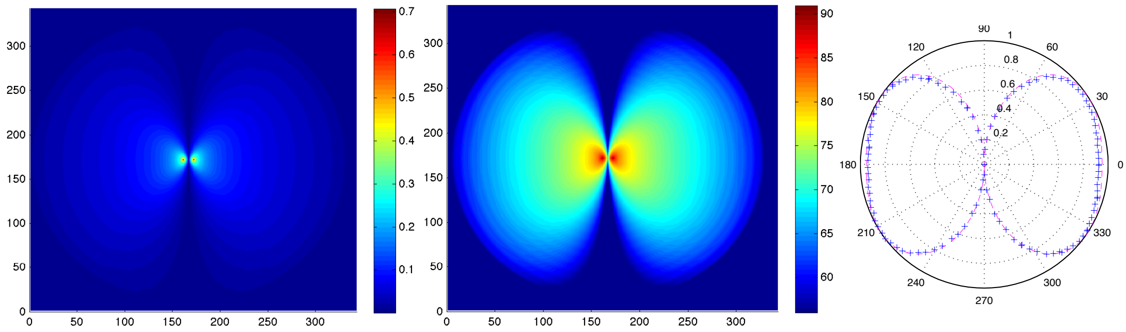

(a) RMS pressure field in pascal

(b) RMS pressure field in dB SPL

(c) Polar pattern at 10 m in pascal

Figure A.6: FDTD simulation for $\frac{D}{\lambda}$=0.6, f=180 Hz

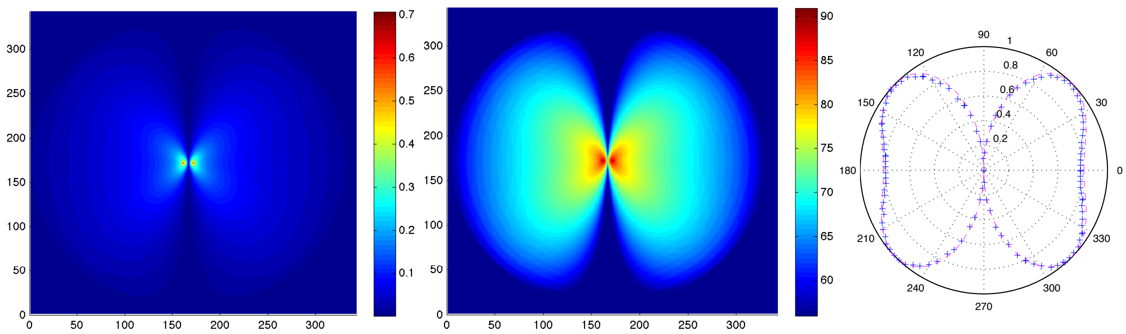

(a) RMS pressure field in pascal

(b) RMS pressure field in dB SPL

(c) Polar pattern at 10 m in pascal

Figure A.7: FDTD simulation for $\frac{D}{\lambda}$=0.7, f=210 Hz

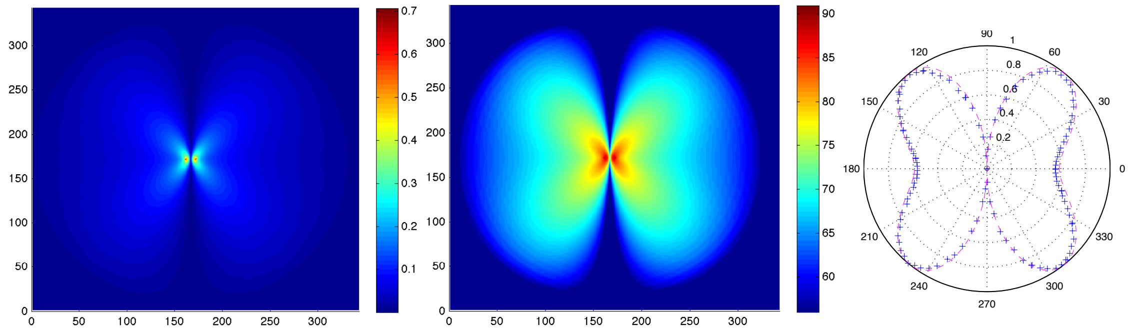

(a) RMS pressure field in pascal (b) RMS pressure field in dB SPL (c) Polar pattern at 10 m in pascal

Figure A.8: FDTD simulation for $\frac{D}{\lambda}$=0.8, f=240 Hz

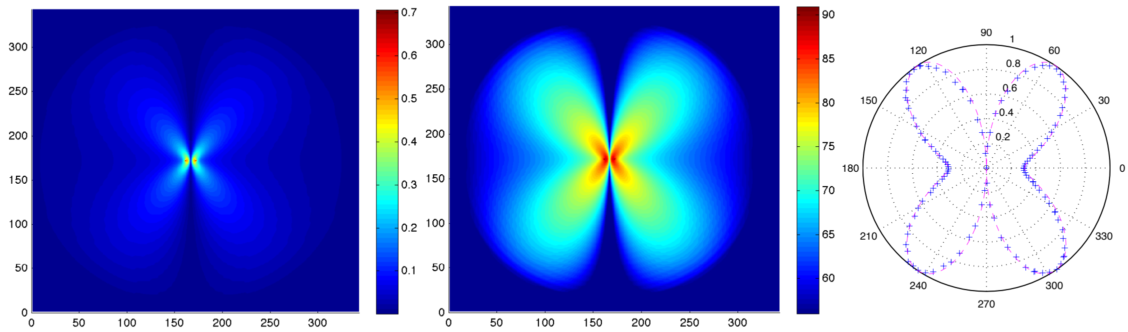

(a) RMS pressure field in pascal (b) RMS pressure field in dB SPL (c) Polar pattern at 10 m in pascal

Figure A.9: FDTD simulation for $\frac{D}{\lambda}$=0.9, f=270 Hz

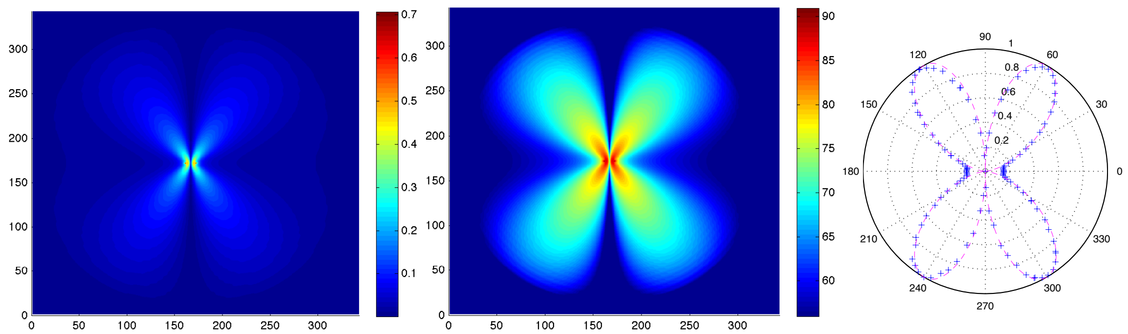

(a) RMS pressure field in pascal (b) RMS pressure field in dB SPL (c) Polar pattern at 10 m in pascal

Figure A.10: FDTD simulation for $\frac{D}{\lambda}$=1, f=300 Hz

A.2 First Order Gradient sound source: Unidirectional

A.2.1 Case 1: $D = d$

The graduations on the x-axis and y-axis of figures *a* and *b* represent the indexes in the FDTD grid used to calculate the pressure. As the cell size has been chosen equal to 0.1 meter (see section 5.1), it is possible to switch directly from index to distance (expressed in meter) by multiplying the index-scale of the figures by 0.1.

In these simulations $D = d = 1.14m$ which corresponds to the wavelength of 300 Hz. In order to respect the analytical study of chapter 2 and the works of Olson [16] the distance between the sources as well as the numerical delay applied on the back-source are kept constant and equal to $\frac{d}{2} = \frac{D}{2} = 0.57m$ in accordance to figure 2.8. Then the frequency of the sinusoidal signal is changed in order to obtain the different values $\frac{D}{\lambda}$ and $\frac{d}{\lambda}$.

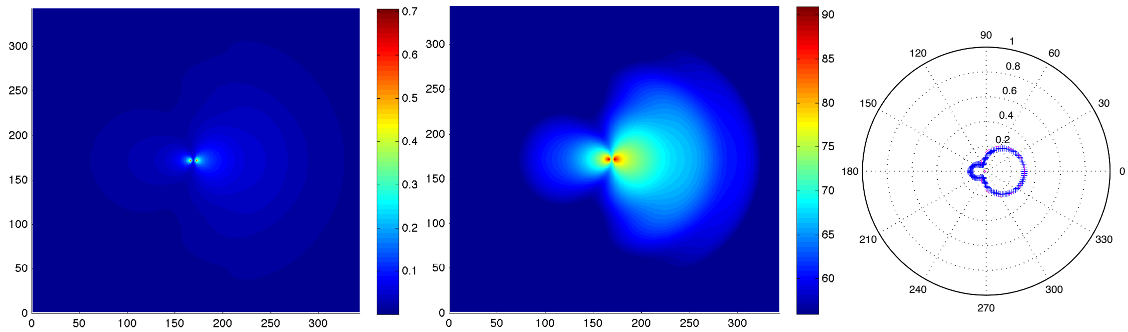

(a) RMS pressure field in pascal (b) RMS pressure field in dB SPL (c) Polar pattern at 10 m in pascal

Figure A.11: FDTD simulation for $\frac{D}{\lambda} = \frac{d}{\lambda}$=0.1, f=30 Hz

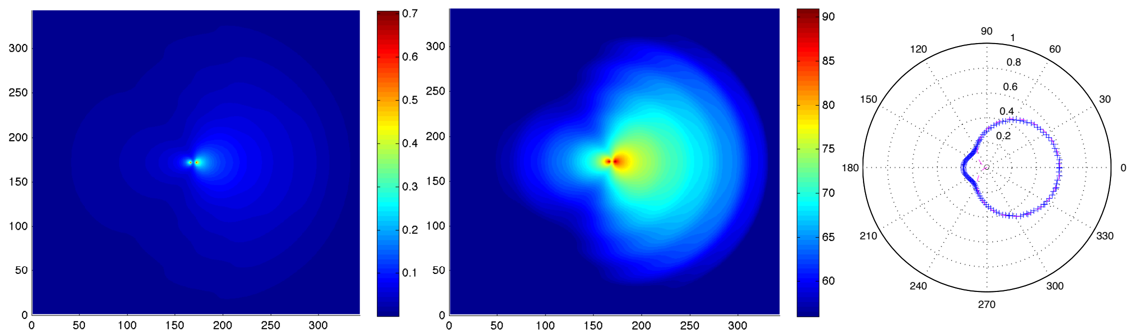

(a) RMS pressure field in pascal (b) RMS pressure field in dB SPL (c) Polar pattern at 10 m in pascal

Figure A.12: FDTD simulation for $\frac{D}{\lambda} = \frac{d}{\lambda}$=0.2, f=60 Hz

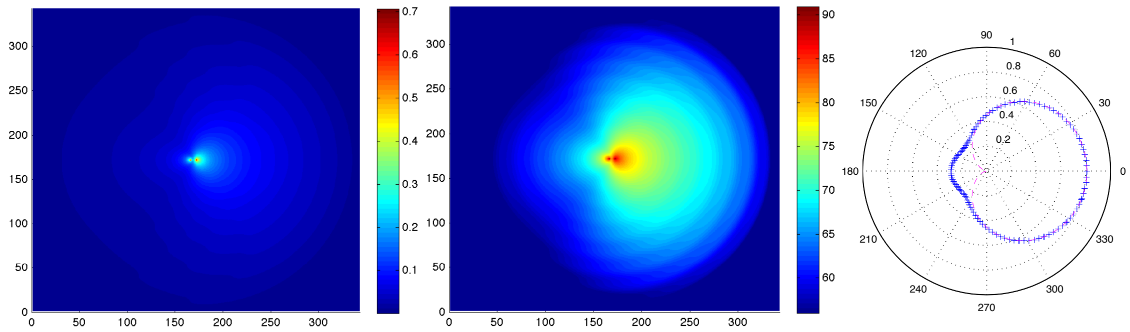

(a) RMS pressure field in pascal (b) RMS pressure field in dB SPL (c) Polar pattern at 10 m in pascal

Figure A.13: FDTD simulation for $\frac{D}{\lambda} = \frac{d}{\lambda}$=0.3, f=90 Hz

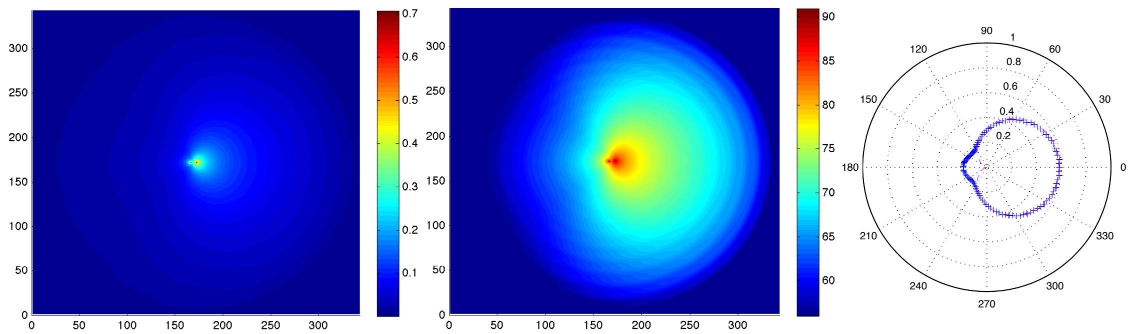

(a) RMS pressure field in pascal (b) RMS pressure field in dB SPL (c) Polar pattern at 10 m in pascal

Figure A.14: FDTD simulation for $\frac{D}{\lambda} = \frac{d}{\lambda}$=0.4, f=120 Hz

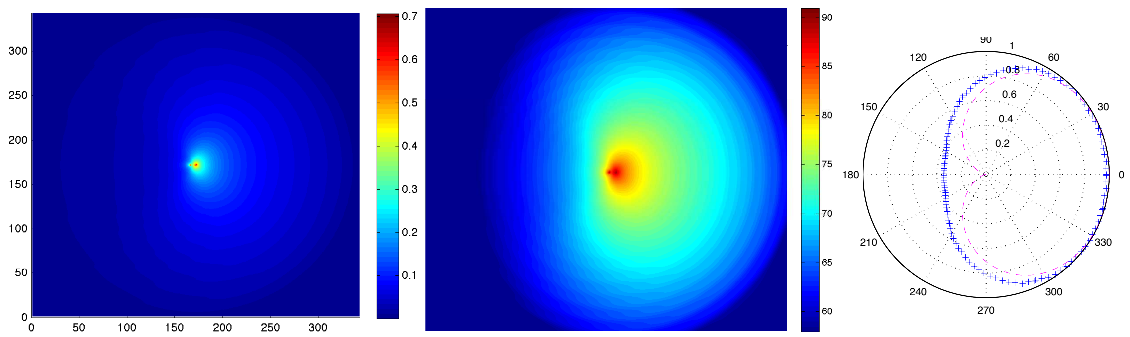

(a) RMS pressure field in pascal (b) RMS pressure field in dB SPL (c) Polar pattern at 10 m in pascal

Figure A.15: FDTD simulation for $\frac{D}{\lambda} = \frac{d}{\lambda}$=0.5, f=150 Hz

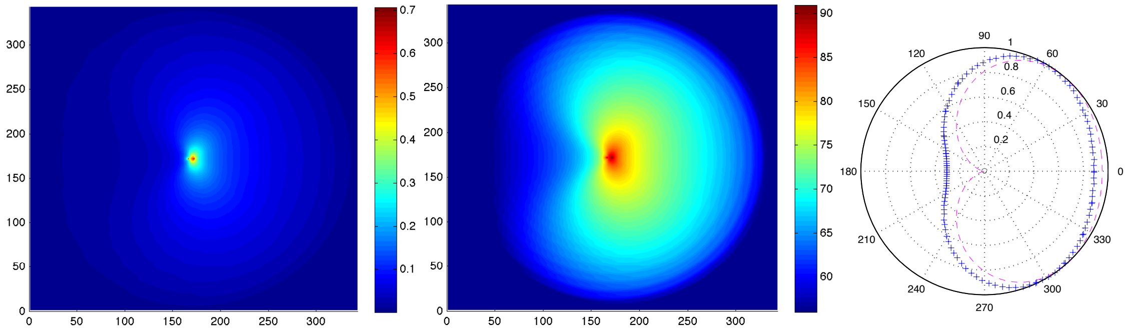

(a) RMS pressure field in pascal (b) RMS pressure field in dB SPL (c) Polar pattern at 10 m in pascal

Figure A.16: FDTD simulation for $\frac{D}{\lambda}=\frac{d}{\lambda}$=0.6, f=180 Hz

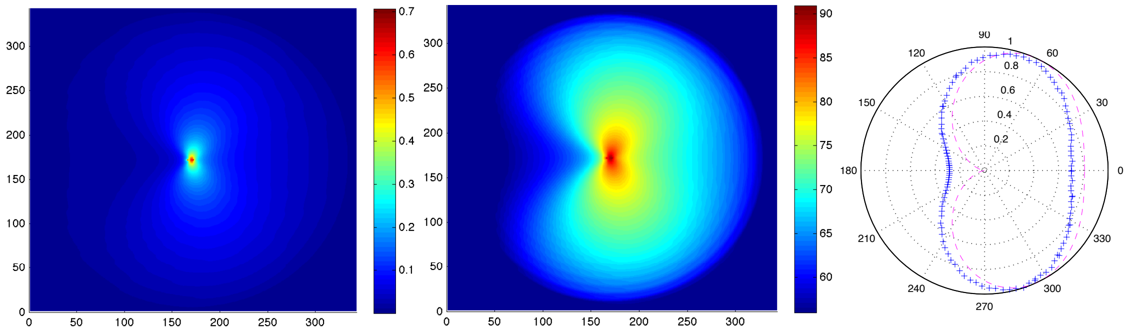

(a) RMS pressure field in pascal (b) RMS pressure field in dB SPL (c) Polar pattern at 10 m in pascal

Figure A.17: FDTD simulation for $\frac{D}{\lambda}=\frac{d}{\lambda}$=0.7, f=210 Hz

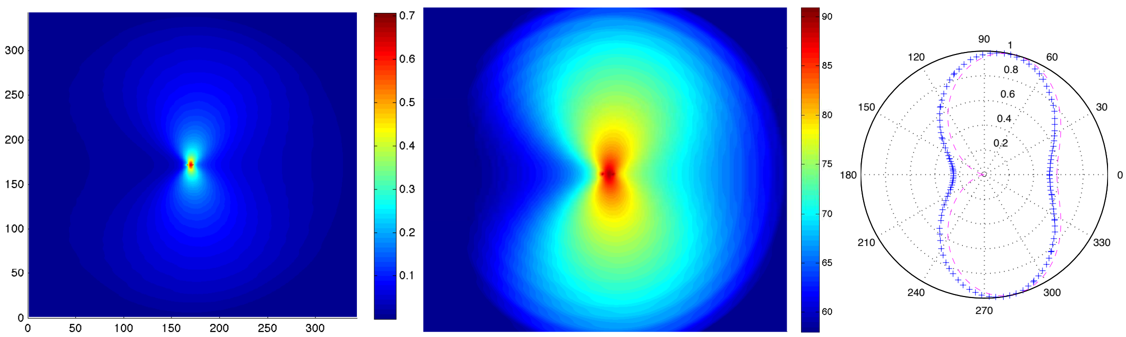

(a) RMS pressure field in pascal (b) RMS pressure field in dB SPL (c) Polar pattern at 10 m in pascal

Figure A.18: FDTD simulation for $\frac{D}{\lambda}=\frac{d}{\lambda}$=0.8, f=240 Hz

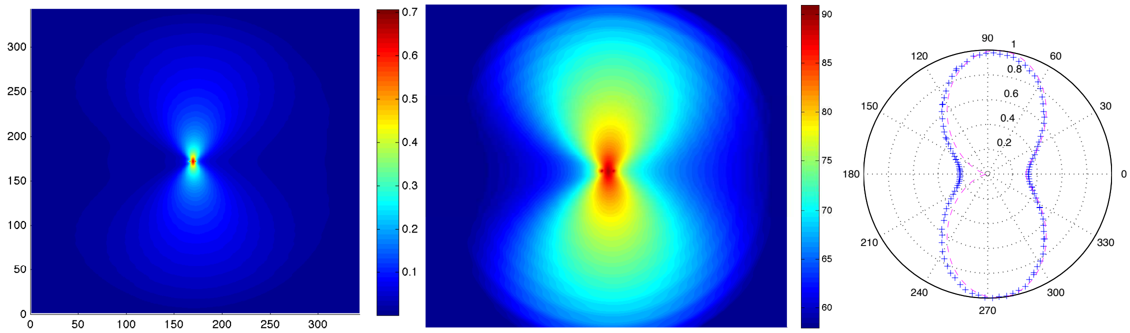

(a) RMS pressure field in pascal

(b) RMS pressure field in dB SPL

(c) Polar pattern at 10 m in pascal

Figure A.19: FDTD simulation for $\frac{D}{\lambda} = \frac{d}{\lambda}$=0.9, f=270 Hz

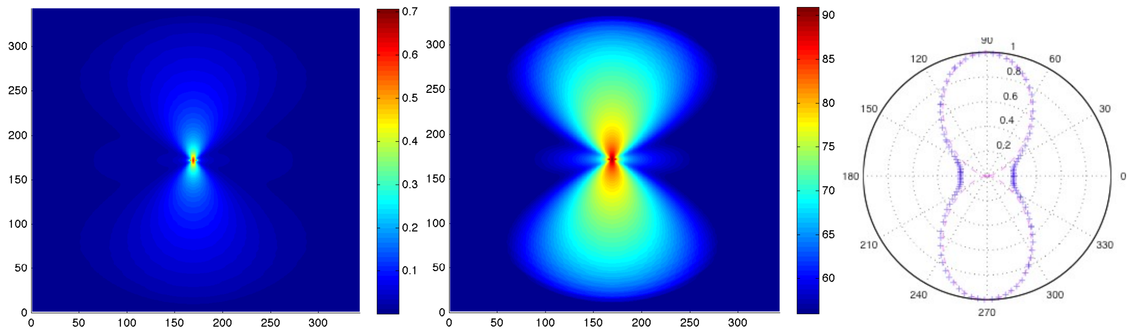

(a) RMS pressure field in pascal

(b) RMS pressure field in dB SPL

(c) Polar pattern at 10 m in pascal

Figure A.20: FDTD simulation for $\frac{D}{\lambda} = \frac{d}{\lambda}$=1, f= 300 Hz

A.2.2 Case 2: $\frac{D}{\lambda}$=0.25 and $\frac{d}{\lambda}$ varies from 0.1 to 1

The graduations on the x-axis and y-axis of figures *a* and *b* represent the indexes in the FDTD grid used to calculate the pressure. As the cell size has been chosen equal to 0.1 meter (see section 5.1), it is possible to switch directly from index to distance (expressed in meter) by multiplying the index-scale of the figures by 0.1.

In these simulations $d = 1.14m$ which corresponds to the wavelength of 300 Hz. The numerical delay d is constant during all these simulations such that when the frequency of the signal changes the ratio $\frac{d}{\lambda}$ changes as well. The distance between the sources D changes in function of the frequency such that whatever the frequency of the signal, the ratio $\frac{D}{\lambda}$ is always equal to 0.25.

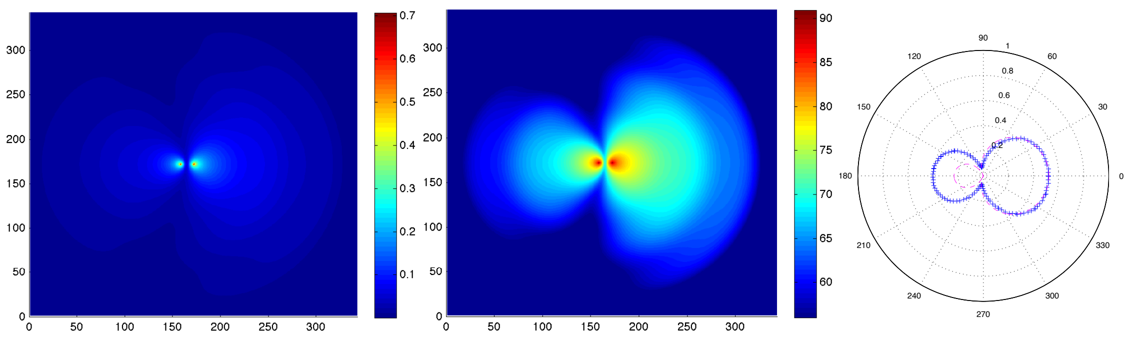

(a) RMS pressure field in pascal (b) RMS pressure field in dB SPL (c) Polar pattern at 10 m in pascal

Figure A.21: FDTD simulation for $\frac{D}{\lambda}$=0.25 and $\frac{d}{\lambda}$=0.1, f=30 Hz

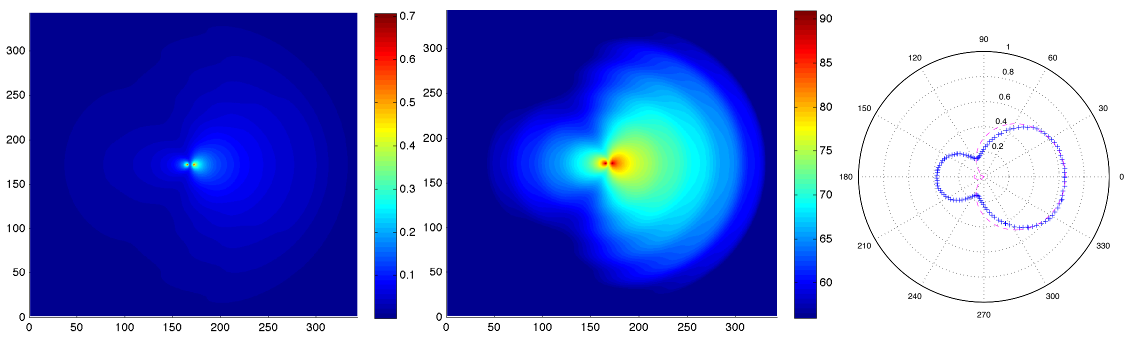

(a) RMS pressure field in pascal (b) RMS pressure field in dB SPL (c) Polar pattern at 10 m in pascal

Figure A.22: FDTD simulation for $\frac{D}{\lambda}$=0.25 and $\frac{d}{\lambda}$=0.2, f=60 Hz

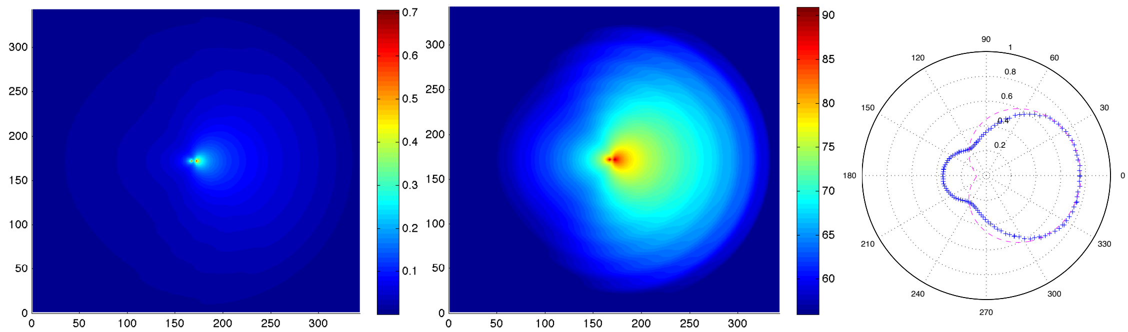

(a) RMS pressure field in pascal (b) RMS pressure field in dB SPL (c) Polar pattern at 10 m in pascal

Figure A.23: FDTD simulation for $\frac{D}{\lambda}$=0.25 and $\frac{d}{\lambda}$=0.3, f=90 Hz

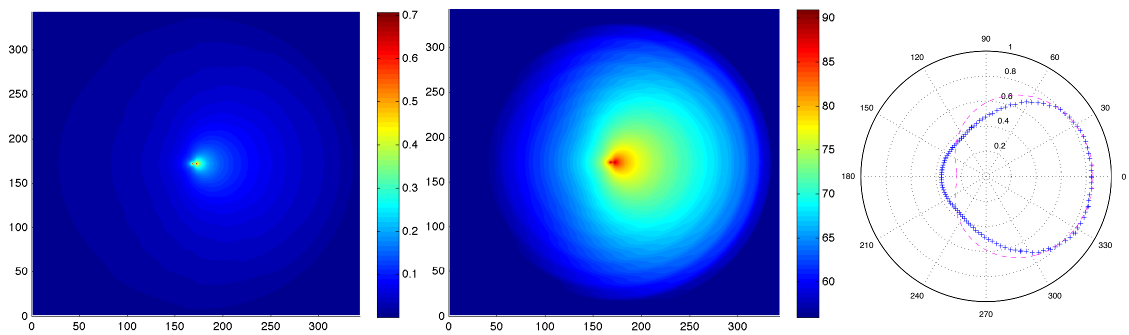

(a) RMS pressure field in pascal (b) RMS pressure field in dB SPL (c) Polar pattern at 10 m in pascal

Figure A.24: FDTD simulation for $\frac{D}{\lambda}$=0.25 and $\frac{d}{\lambda}$=0.4, f=120 Hz

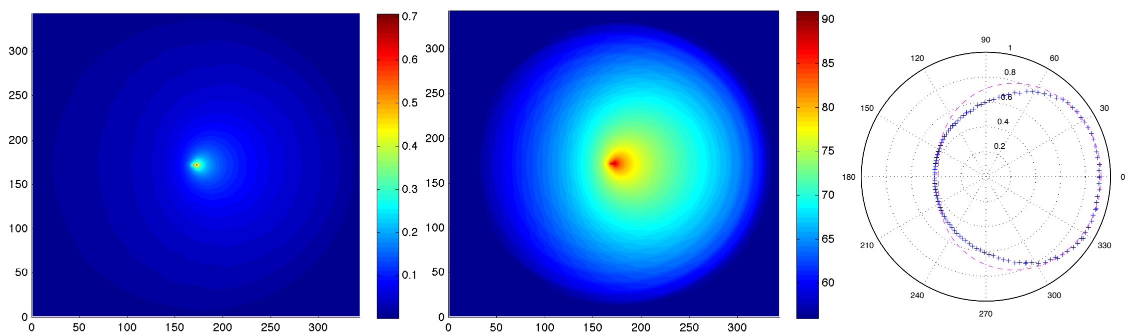

(a) RMS pressure field in pascal (b) RMS pressure field in dB SPL (c) Polar pattern at 10 m in pascal

Figure A.25: FDTD simulation for $\frac{D}{\lambda}$=0.25 and $\frac{d}{\lambda}$=0.5, f=150 Hz

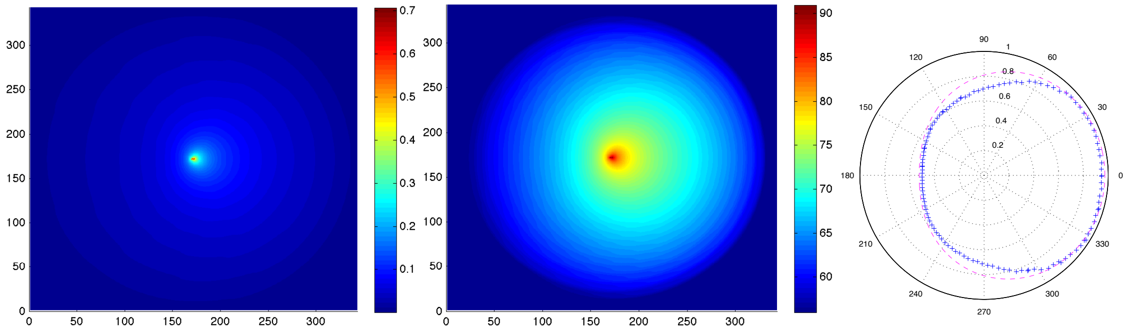

(a) RMS pressure field in pascal (b) RMS pressure field in dB SPL (c) Polar pattern at 10 m in pascal

Figure A.26: FDTD simulation for $\frac{D}{\lambda}$=0.25 and $\frac{d}{\lambda}$=0.6, f=180 Hz

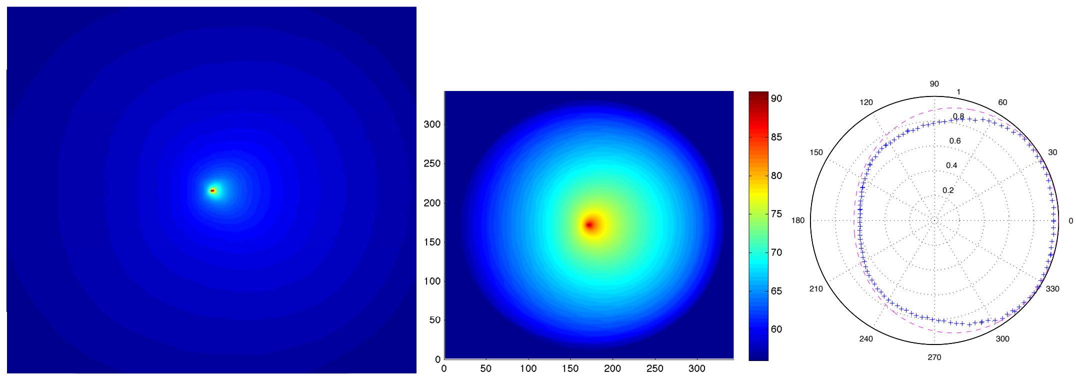

(a) RMS pressure field in pascal (b) RMS pressure field in dB SPL (c) Polar pattern at 10 m in pascal

Figure A.27: FDTD simulation for $\frac{D}{\lambda}$=0.25 and $\frac{d}{\lambda}$=0.7, f=210 Hz

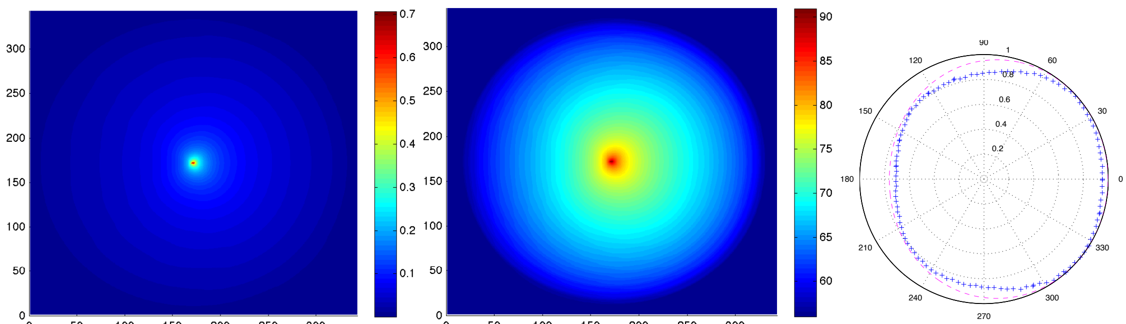

(a) RMS pressure field in pascal (b) RMS pressure field in dB SPL (c) Polar pattern at 10 m in pascal

Figure A.28: FDTD simulation for $\frac{D}{\lambda}$=0.25 and $\frac{d}{\lambda}$=0.8, f=240 Hz

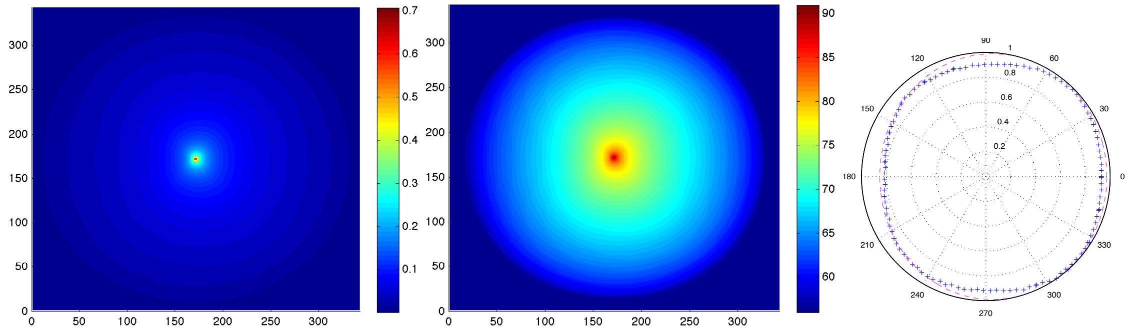

(a) RMS pressure field in pascal

(b) RMS pressure field in dB SPL

(c) Polar pattern at 10 m in pascal

Figure A.29: FDTD simulation for $\frac{D}{\lambda}$=0.25 and $\frac{d}{\lambda}$=0.9, f=270 Hz

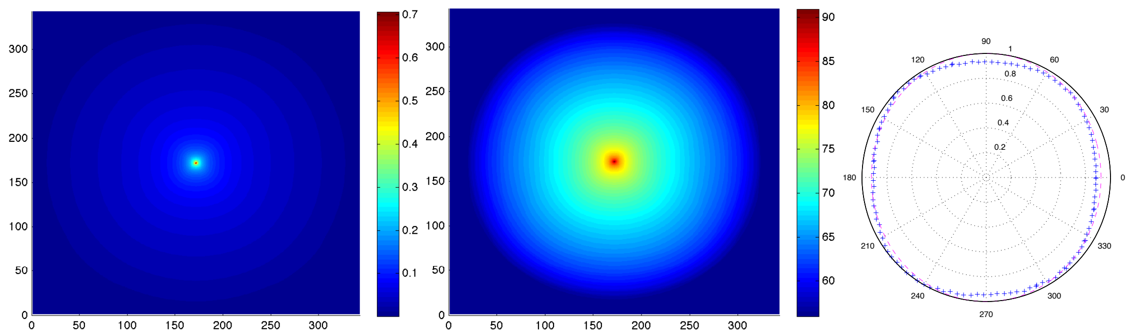

(a) RMS pressure field in pascal

(b) RMS pressure field in dB SPL

(c) Polar pattern at 10 m in pascal

Figure A.30: FDTD simulation for $\frac{D}{\lambda}$=0.25 and $\frac{d}{\lambda}$=1, f=300 Hz

A.2.3 Case 3: $\frac{d}{\lambda}$=0.25 and $\frac{D}{\lambda}$ varies from 0.1 to 1

The graduations on the x-axis and y-axis of figures *a* and *b* represent the indexes in the FDTD grid used to calculate the pressure. As the cell size has been chosen equal to 0.1 meter (see section 5.1), it is possible to switch directly from index to distance (expressed in meter) by multiplying the index-scale of the figures by 0.1.

In these simulations $D = 1.14m$ which corresponds to the wavelength of 300 Hz. The distance between the sources D is constant during all these simulations such that when the frequency of the signal changes the ratio $\frac{d}{\lambda}$ changes as well. The numerical delay d changes in function of the frequency such that whatever the frequency of the signal, the ratio $\frac{d}{\lambda}$ is always equal to 0.25.

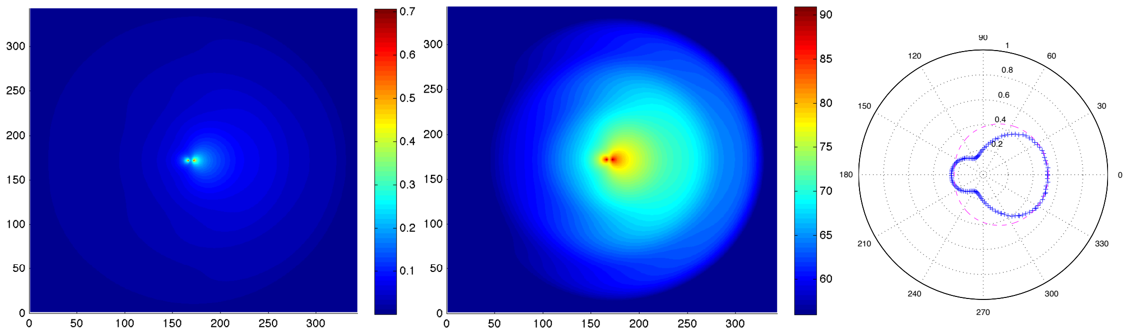

(a) RMS pressure field in pascal

(b) RMS pressure field in dB SPL

(c) Polar pattern at 10 m in pascal

Figure A.31: FDTD simulation for $\frac{d}{\lambda}$=0.25 and $\frac{D}{\lambda}$=0.1, f=30 Hz

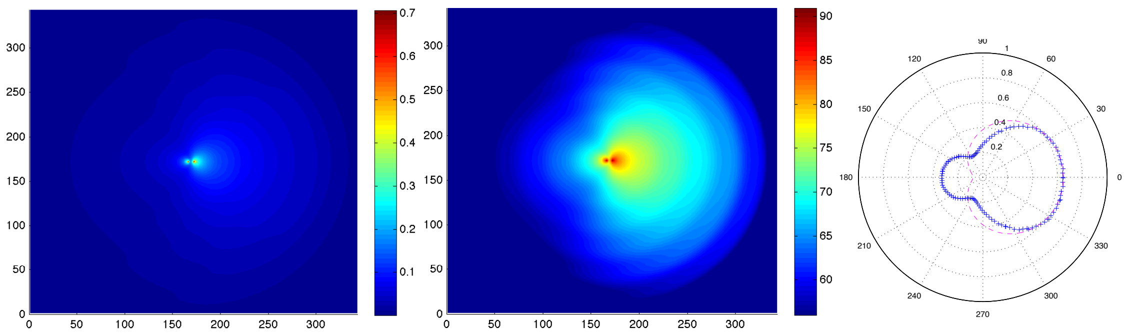

(a) RMS pressure field in pascal

(b) RMS pressure field in dB SPL

(c) Polar pattern at 10 m in pascal

Figure A.32: FDTD simulation for $\frac{d}{\lambda}$=0.25 and $\frac{D}{\lambda}$=0.2, f=60 Hz

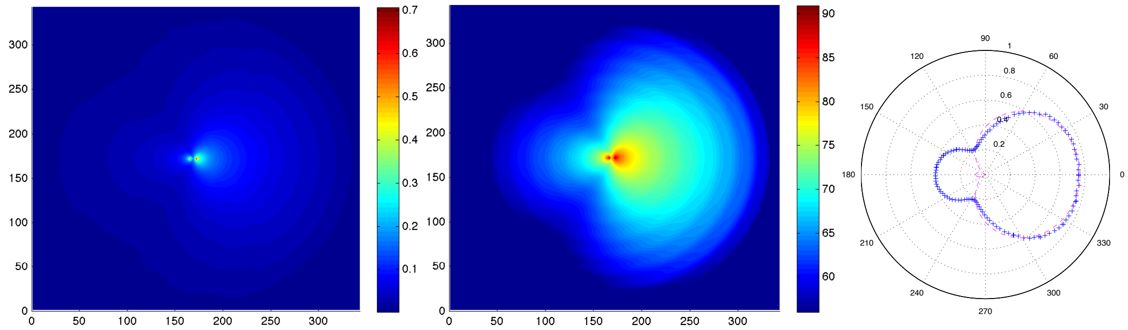

(a) RMS pressure field in pascal (b) RMS pressure field in dB SPL (c) Polar pattern at 10 m in pascal

Figure A.33: FDTD simulation for $\frac{d}{\lambda}$=0.25 and $\frac{D}{\lambda}$=0.3, f=90 Hz

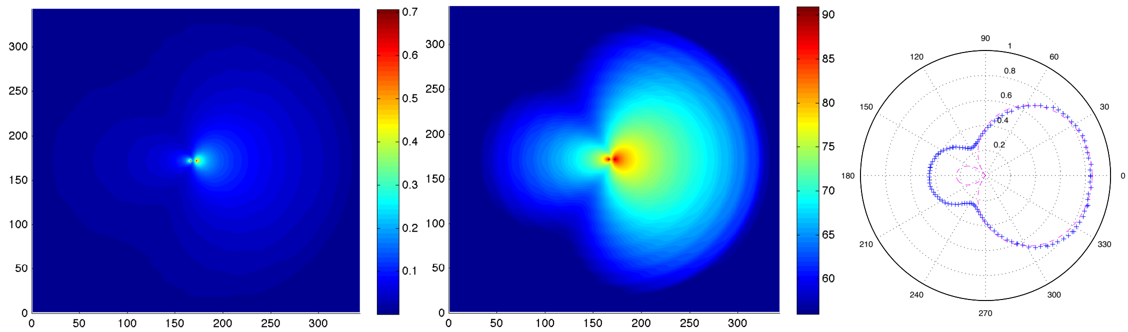

(a) RMS pressure field in pascal (b) RMS pressure field in dB SPL (c) Polar pattern at 10 m in pascal

Figure A.34: FDTD simulation for $\frac{d}{\lambda}$=0.25 and $\frac{D}{\lambda}$=0.4, f=120 Hz

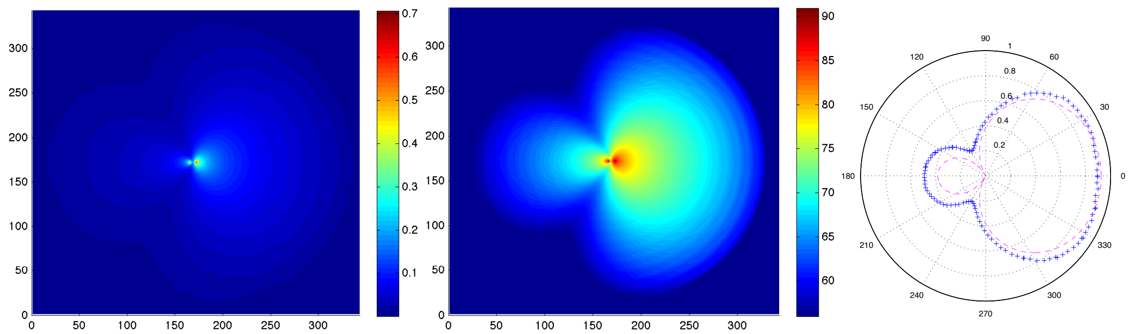

(a) RMS pressure field in pascal (b) RMS pressure field in dB SPL (c) Polar pattern at 10 m in pascal

Figure A.35: FDTD simulation for $\frac{d}{\lambda}$=0.25 and $\frac{D}{\lambda}$=0.5, f=150 Hz

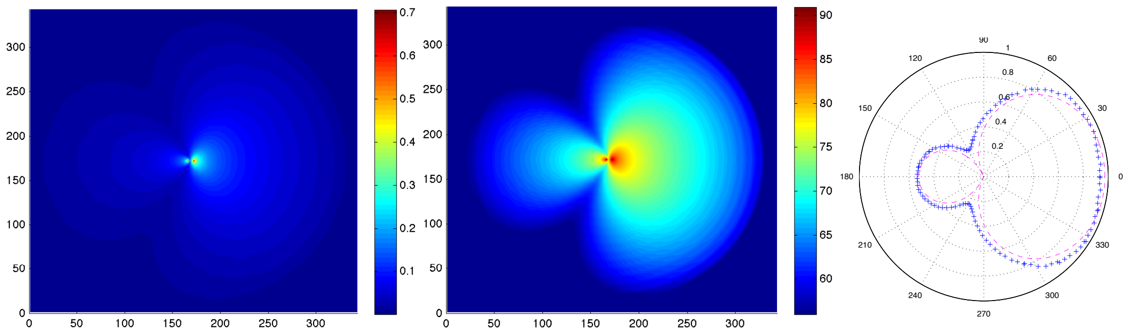

(a) RMS pressure field in pascal (b) RMS pressure field in dB SPL (c) Polar pattern at 10 m in pascal

Figure A.36: FDTD simulation for $\frac{d}{\lambda}$=0.25 and $\frac{D}{\lambda}$=0.6, f=180 Hz

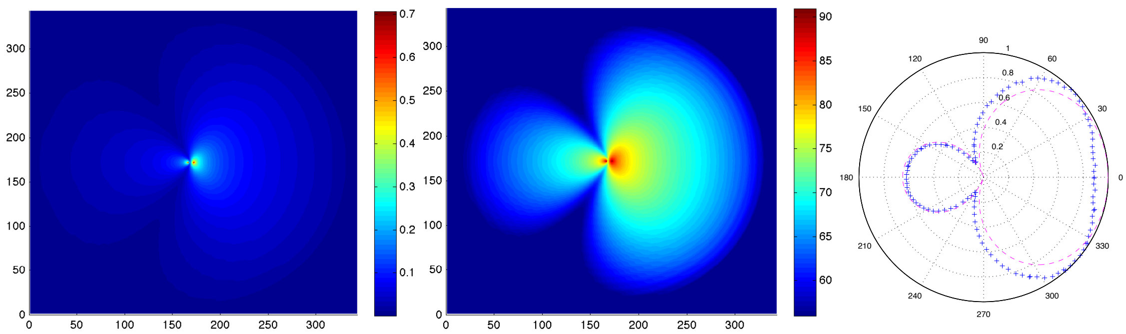

(a) RMS pressure field in pascal (b) RMS pressure field in dB SPL (c) Polar pattern at 10 m in pascal

Figure A.37: FDTD simulation for $\frac{d}{\lambda}$=0.25 and $\frac{D}{\lambda}$=0.7, f=210 Hz

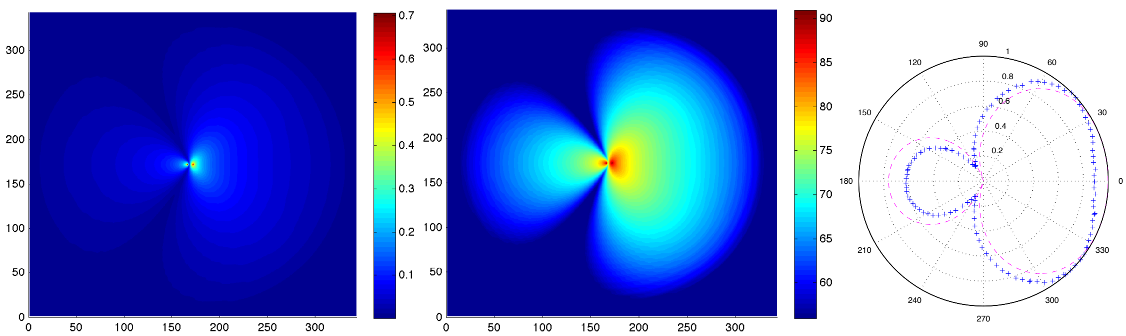

(a) RMS pressure field in pascal (b) RMS pressure field in dB SPL (c) Polar pattern at 10 m in pascal

Figure A.38: FDTD simulation for $\frac{d}{\lambda}$=0.25 and $\frac{D}{\lambda}$=0.8, f=240 Hz

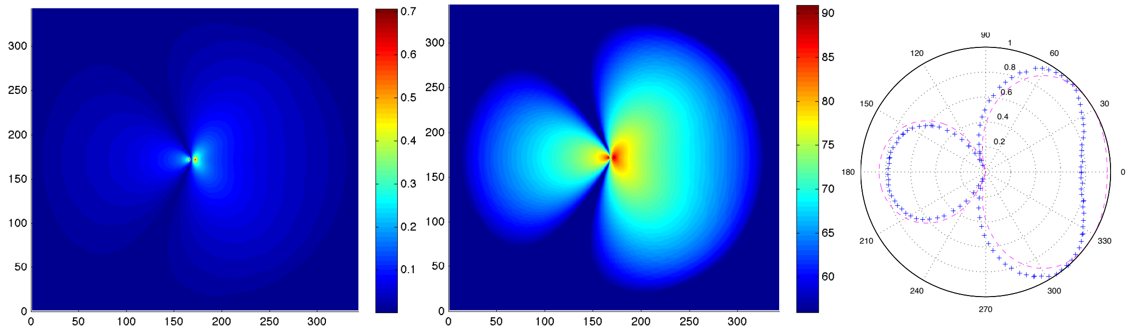

(a) RMS pressure field in pascal

(b) RMS pressure field in dB SPL

(c) Polar pattern at 10 m in pascal

Figure A.39: FDTD simulation for $\frac{d}{\lambda}$=0.25 and $\frac{D}{\lambda}$=0.9, f=270 Hz

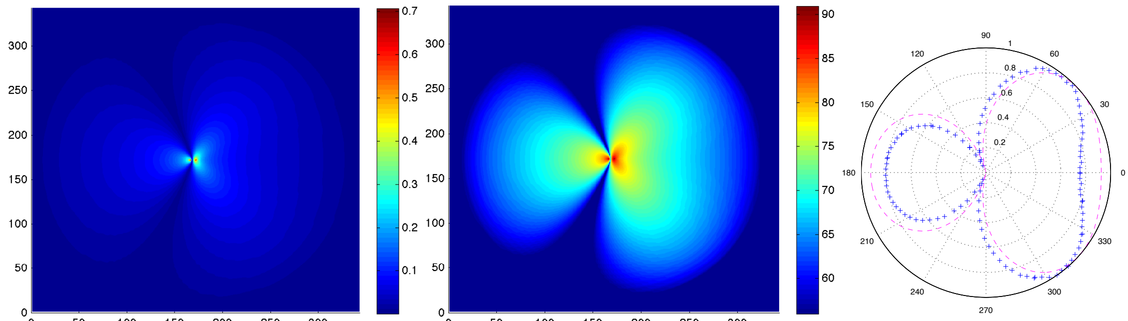

(a) RMS pressure field in pascal

(b) RMS pressure field in dB SPL

(c) Polar pattern at 10 m in pascal

Figure A.40: FDTD simulation for $\frac{d}{\lambda}$=0.25 and $\frac{D}{\lambda}$=1, f=300 Hz

A.3 Second-Order gradient sound source-Unidirectional

The graduations on the x-axis and y-axis of figures *a* and *b* represent the indexes in the FDTD grid used to calculate the pressure. As the cell size has been chosen equal to 0.1 meter (see section 5.1), it is possible to switch directly from index to distance (expressed in meter) by multiplying the index-scale of the figures by 0.1.

In these simulations $D = d = 1.14m$ which corresponds to the wavelength of 300 Hz. The distances between the sources and the delays are kept constant in accordance to figure 2.10. Then the frequency of the sinusoidal signal is changed in order to obtain the different values $\frac{D}{\lambda}$ and $\frac{d}{\lambda}$.

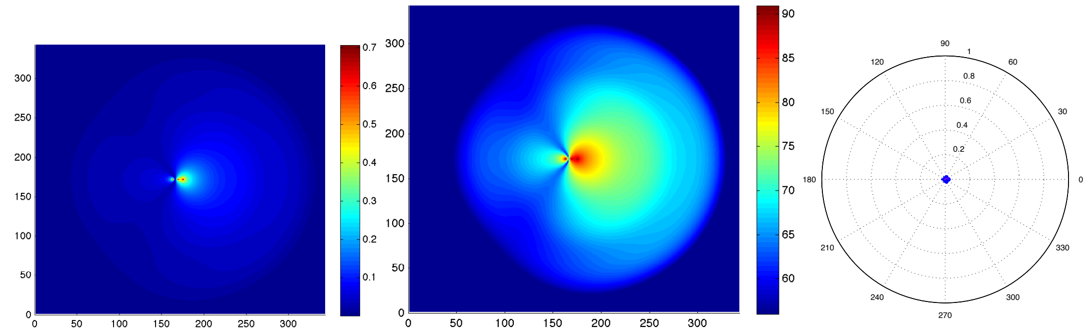

(a) RMS pressure field in pascal

(b) RMS pressure field in dB SPL

(c) Polar pattern at 10 m in pascal

Figure A.41: FDTD simulation for $\frac{d}{\lambda}$=$\frac{D}{\lambda}$=0.1, f=30 Hz

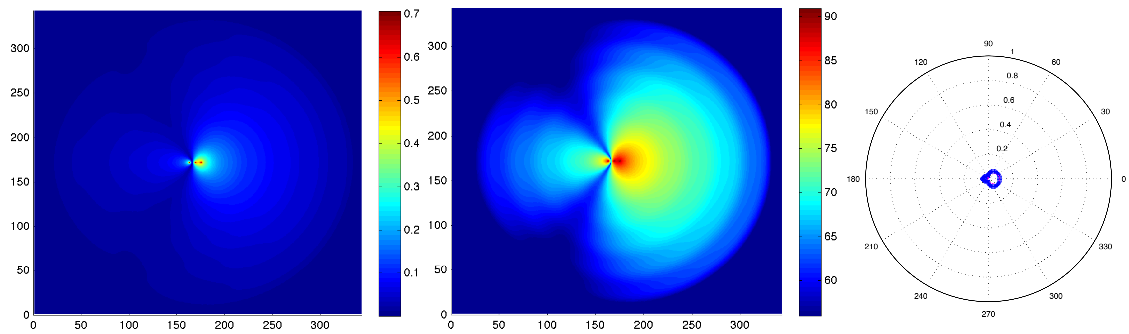

(a) RMS pressure field in pascal

(b) RMS pressure field in dB SPL

(c) Polar pattern at 10 m in pascal

Figure A.42: FDTD simulation for $\frac{d}{\lambda}$=$\frac{D}{\lambda}$=0.2, f=60 Hz

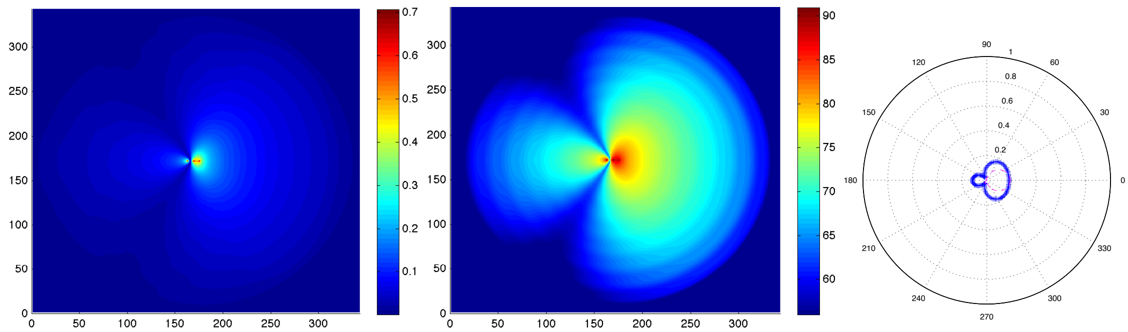

(a) RMS pressure field in pascal (b) RMS pressure field in dB SPL (c) Polar pattern at 10 m in pascal

Figure A.43: FDTD simulation for $\frac{d}{\lambda}=\frac{D}{\lambda}$=0.3, f= 90 Hz

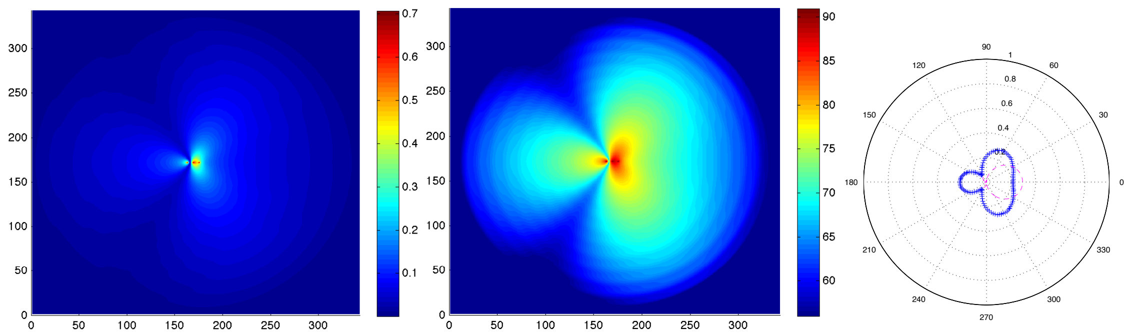

(a) RMS pressure field in pascal (b) RMS pressure field in dB SPL (c) Polar pattern at 10 m in pascal

Figure A.44: FDTD simulation for $\frac{d}{\lambda}=\frac{D}{\lambda}$=0.4, f=120 Hz

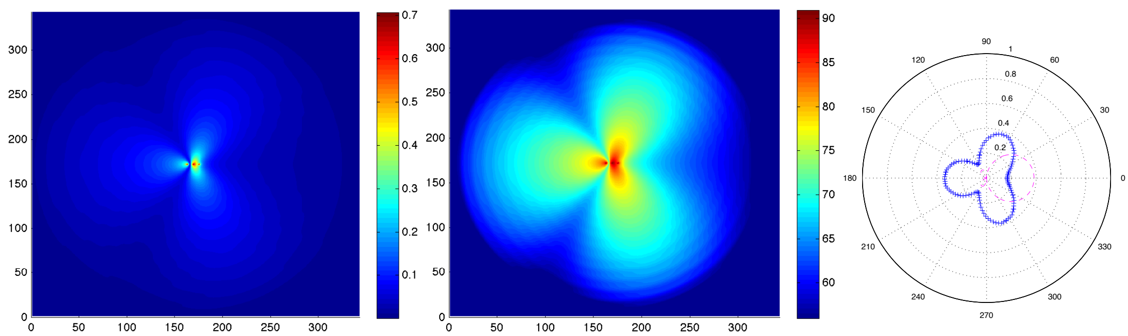

(a) RMS pressure field in pascal (b) RMS pressure field in dB SPL (c) Polar pattern at 10 m in pascal

Figure A.45: FDTD simulation for $\frac{d}{\lambda}=\frac{D}{\lambda}$=0.5, f=150 Hz

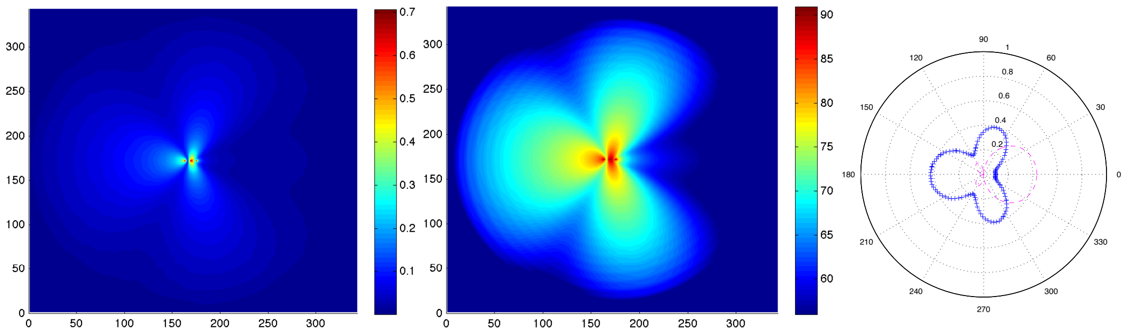

(a) RMS pressure field in pascal (b) RMS pressure field in dB SPL (c) Polar pattern at 10 m in pascal

Figure A.46: FDTD simulation for $\frac{d}{\lambda}=\frac{D}{\lambda}$=0.6, f=180 Hz

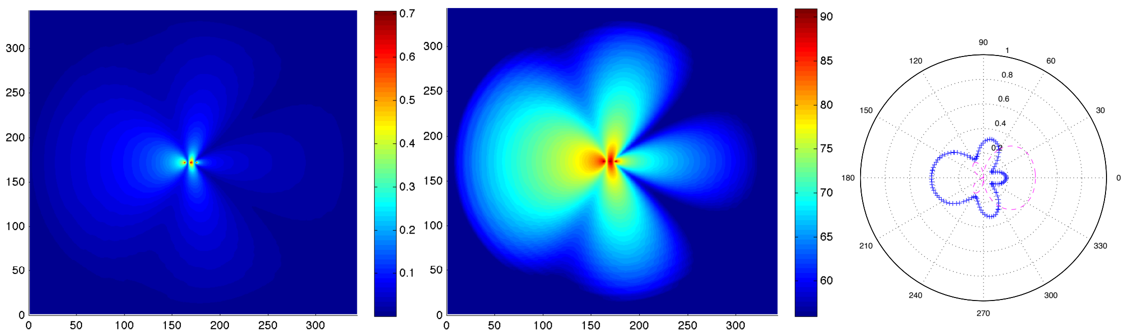

(a) RMS pressure field in pascal (b) RMS pressure field in dB SPL (c) Polar pattern at 10 m in pascal

Figure A.47: FDTD simulation for $\frac{d}{\lambda}=\frac{D}{\lambda}$=0.7, f=210 Hz

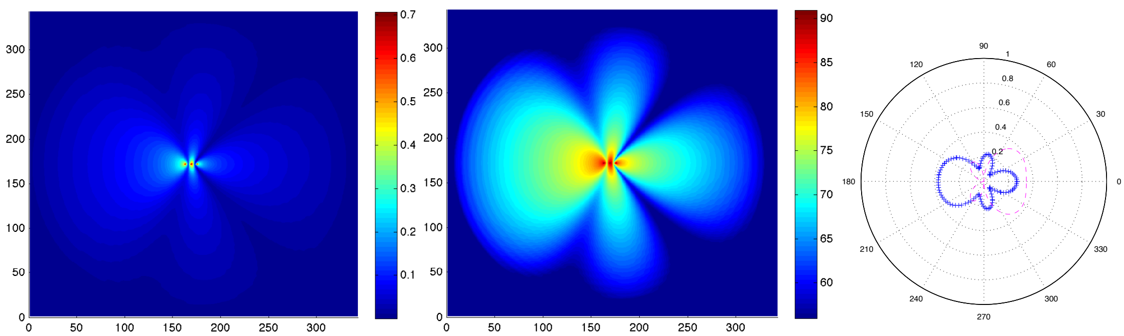

(a) RMS pressure field in pascal (b) RMS pressure field in dB SPL (c) Polar pattern at 10 m in pascal

Figure A.48: FDTD simulation for $\frac{d}{\lambda}=\frac{D}{\lambda}$=0.8, f=240 Hz

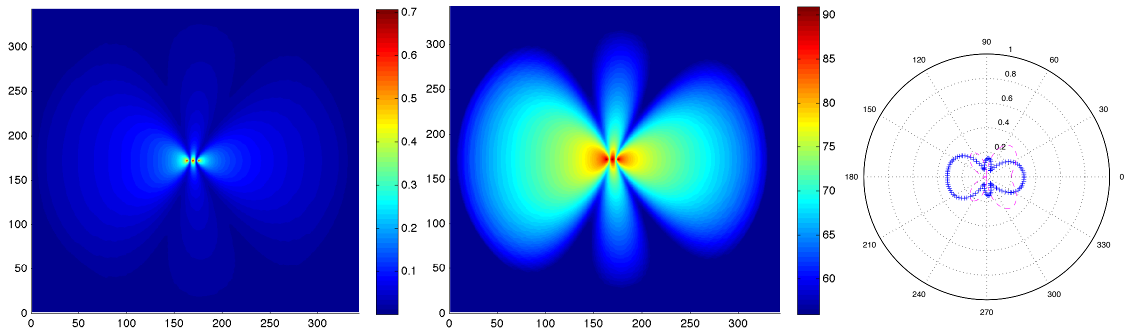

(a) RMS pressure field in pascal

(b) RMS pressure field in dB

(c) Polar pattern at 10 m in pascal

Figure A.49: FDTD simulation for $\frac{d}{\lambda}=\frac{D}{\lambda}$=0.9, f=270 Hz

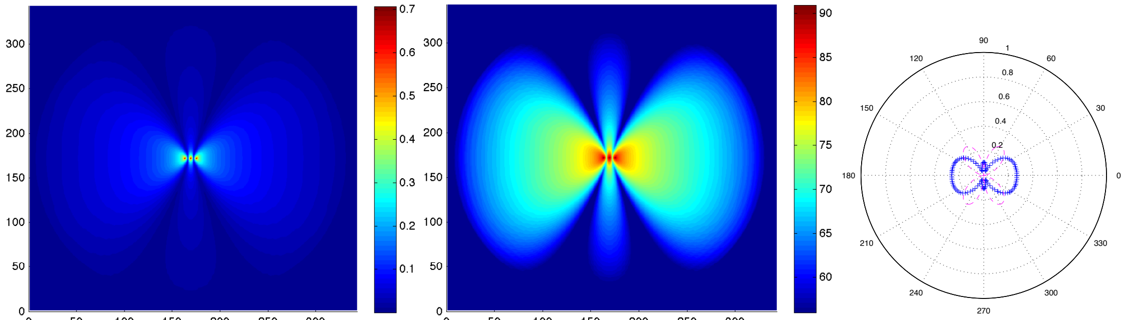

(a) RMS pressure field in pascal

(b) RMS pressure field in dB SPL

(c) Polar pattern at 10 m in pascal

Figure A.50: FDTD simulation for $\frac{d}{\lambda}=\frac{D}{\lambda}=1$, f=300 Hz

B

Measurement of the impulse response of a subwoofer

In this appendix the measurement of the impulse response of a subwoofer in the horizontal plane is documented

B.1 Equipment used

Item	Type	AAU LBNR/SN
Loudspeaker	DALI SWA-8 Active subwoofer	261413
Microphone	BK 4133	06548
Preamplifier	BK 2619	07797
Measuring amplifier	BK 2636	08451
Analyzer	MLSSA	26827

B.2 Purpose

The purpose of this appendix is to obtain an impulse response who is an average in the frequency domain of measurements of the response of a subwoofer in the horizontal plane at 1.15 meter from the membrane with a resolution of 30 °.

B.3 Setup

The setup used to measure the impulse response of a subwoofer is presented in figure B.1. The measurements are conducted in the large anechoic room of the Acoustic department of Aalborg University.

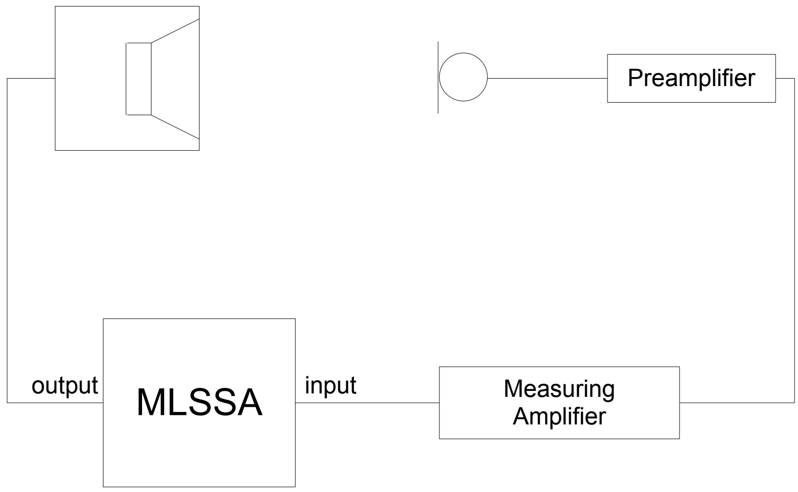

Figure B.1: Setup for the measurement of the impulse response in the anechoic chamber

Loudspeaker

The subwoofer used for this project is a closed-box type with a 8" woofer driver and an integrated amplifier. This subwoofer has an embedded active low-pass filter whose cutoff frequency can vary from 50 to 150 Hz. For the measurements realized in this part the low pass filter is set to 150 Hz. Despite the anechoic chamber has a cut-off frequency of around 63 Hz the subwoofer is left in a full-range configuration with a low cutoff frequency of 30 Hz according to the manufacturer data-sheet. The gain potentiometer of the amplifier is set to the medium position. The subwoofer is positioned on a stand so that its gravity center is on the rotation-axis used for the 30 ° rotations. The subwoofer is symmetric so the impulse responses are only measured between $\theta = 0°$ and $\theta = 180°$.

Microphone

The microphone used for the measurements is a B&K 4133 free-field microphone. It is positioned at 1,15 m from the membrane of the subwoofer and at the same height than the center of the woofer. The microphone stays at the same position for all the measurements, it is the loudspeaker which turns on its stand.

MLSSA configuration

The MLSSA system was used with the following parameters:

- **Stimulus:** Burst MLS was chosen as stimulus signal with an amplitude of 0.3 volts. A MLS sequence of 16th order was chosen leading to a period of 65535 samples.
- **Acquisition:** Cross-correlation mode was chosen to obtain the impulse response of the subwoofer. The acquisition length was set to 65536 samples and sample rate set to 8kHz. This clock was generated internally by MLSSA.
- **Aniti-aliasing filter:** The anti-aliasing filter is a Butterworth with a cutting frequency of 2 kHz.

- **Pre-average cycle:** To increase the SNR 16 pre-average cycles are run.

B.4 Results

B.4.1 Results of the seven measurements

Figure B.2 shows the magnitude of the impulse responses of the subwoofer for θ varying from 0 to 180 degree with a resolution of 30 degree. These magnitudes have been obtained using the first 3276 points of the impulse response and a FFT of 4096 points. From the results displayed

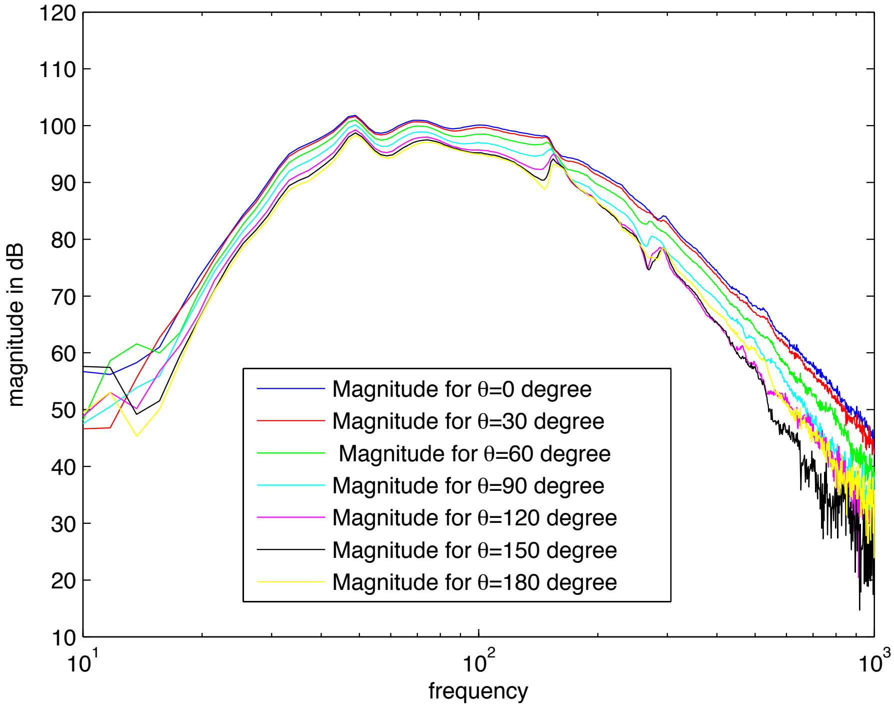

Figure B.2: Magnitude of the impulse responses obtained for different positions around the subwoofer

on figure B.2 it is possible to deduce the polar directivity for several discrete frequencies. These discrete polar patterns are showed on figure B.3.

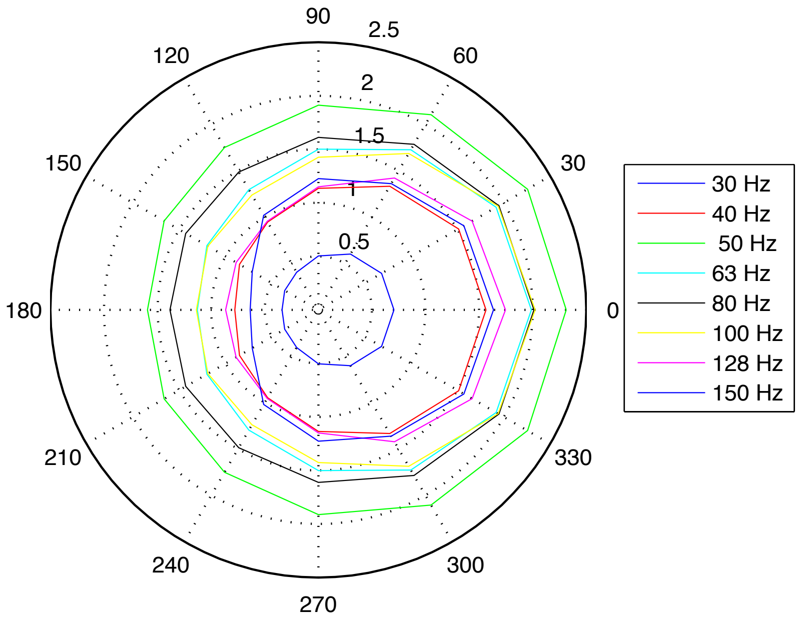

Figure B.3: Polar directivity of the DALI subwoofer expressed in pascal

Regarding this polar plot the subwoofer seems almost perfectly omnidirectional for all the frequencies. It can be seen that for all the frequencies there is few pascals of difference between the front and the back of the subwoofer. When expressed in dB SPL this difference is by mean of around 4 dB SPL. Nevertheless, it confirms that in a FDTD simulation a subwoofer could be modeled with a good accuracy by an omnidirectional point source characterized by the subwoofer impulse response.

B.5 Average impulse response

Instead of feeding the FDTD simulation with the subwoofer impulse response corresponding to only one position of the microphone it is decided to use an average of all the impulse responses obtained around the subwoofer. This section deals with the method to obtain this average impulse response.

It is not possible to average directly the impulse responses in time domain. An average in the frequency domain followed by an inverse FFT is more practical. But when proceeding to this kind of average it has to be aware that the average impulse response should be minimum phase. Thus the determination of the average impulse response is based on the Matlab function *rceps*. It calculates the real cepstrum and a minimum phase reconstructed version of a real impulse response.

So after the impulse response has been measured at seven different positions around the subwoofer their respecting magnitudes are calculated according to equation B.1.

$$Y = |fft(y)| \tag{B.1}$$

The mathematical operator | . | defines the absolute value.

When the magnitude at the seven positions $(y_1, y_2, ..., y_7)$ are obtained they are averaged together

B.2:

$$\bar{Y} = \frac{\sum_{i=1}^{7} |fft(y_i)|}{7} \tag{B.2}$$

Then the cepstrum of this average magnitude is determined with equation B.3:

$$\bar{Y}_{cepstrum} = real(ifft(log(\bar{Y}))) \tag{B.3}$$

A rectangular window is then applied on this cepstrum to give the reconstructed minimum phase signal. This window is defind in Matlab by the following equation B.4:

$$w = [1; 2 * ones(n/2 - 1, 1); ones(1 - rem(n, 2), 1); zeros(n/2 - 1, 1)] \tag{B.4}$$

with n the number of points composing the impulse response of y_i. Finally it has to go back from the cepstrum domain to the time domain with equation B.5 (In Matlab language):

$$\bar{y} = real(ifft(exp(fft(w. * \bar{Y}_{cepstrum})))) \tag{B.5}$$

C

FDTD method: Simulation of a real subwoofer

In the following sections the simulation results of a first order gradient source-unidirectional fed with the impulse response of a subwoofer are presented. Different distances and delays between the sources are tested. Information relative to the input signal, the cell size and the step size are discussed in subsections 6.2.1, 6.2.2 and 6.2.3 respectively. The method to obtain the pressure fields at different discrete frequencies is explained in section 6.3.

C.1 Case 1: $f_{cardioid} = 150Hz$

In this first case, the frequency giving the ideal cardioid directivity is $f_{cardioid}$=150 Hz. For a such frequency, the distance between the sources is $D = \frac{\lambda_{f_{cardioid}}}{4} = 0.6m$ and the delay applied on the back subwoofer is $d = \frac{\lambda_{f_{cardioid}}}{4} = 0.6m$.

The results are expressed in dB SPL. The scales on the x-axis and y-axis represent the indexes in the FDTD grid and can be converted into meter by multiplying them by 0.2 (the grid size).

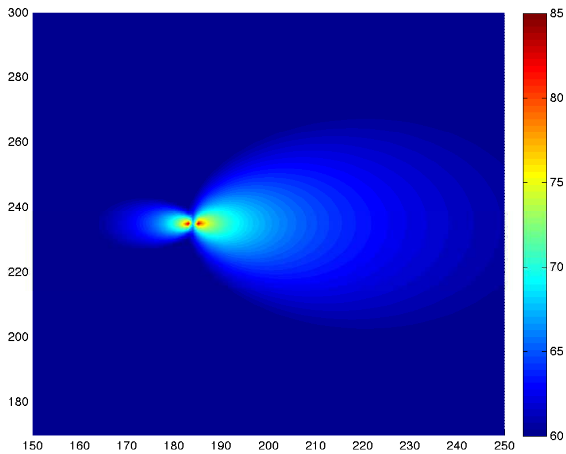

(a) $f = 40Hz$

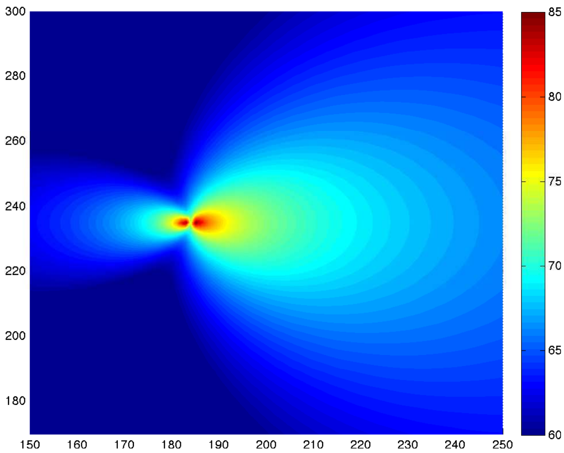

(b) $f = 50Hz$

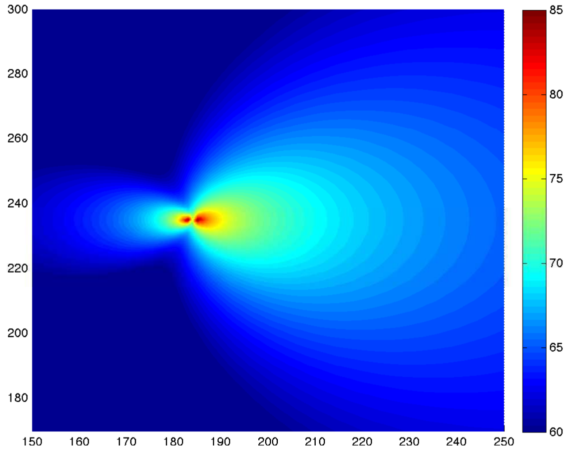

(c) $f = 60Hz$

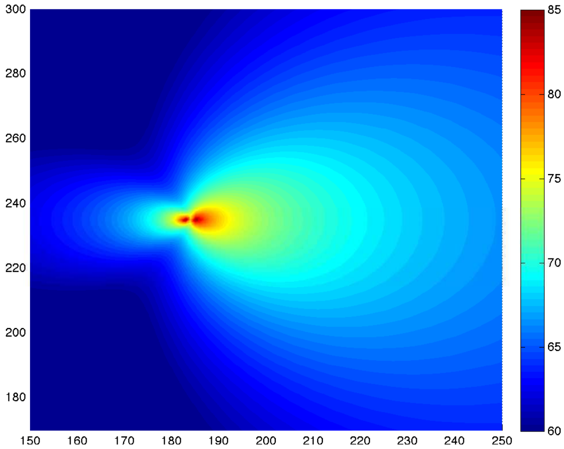

(d) $f = 80Hz$

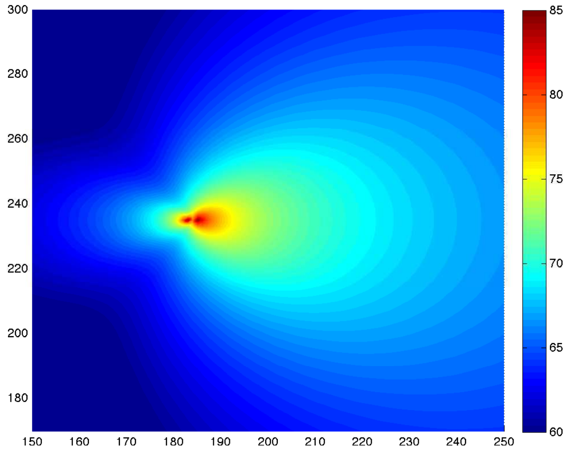

(e) 100

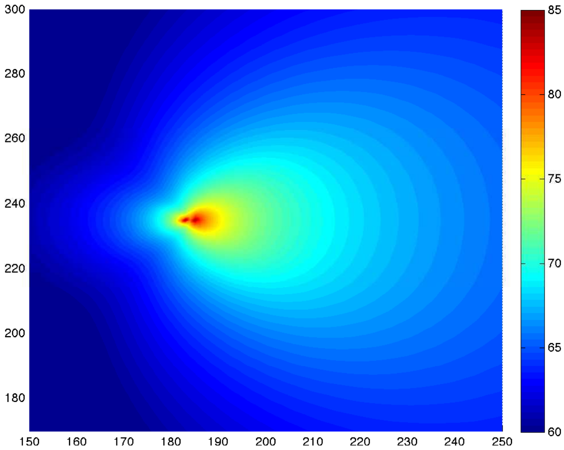

(f) $f = 120Hz$

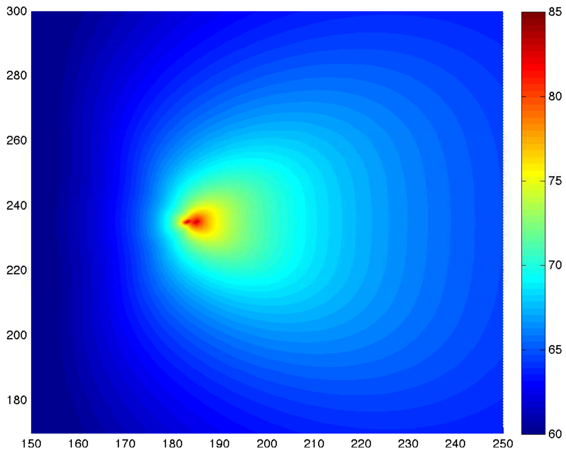

(g) $f = 150Hz$

Figure C.1: Pressure in dB SPL for a first order gradient sound source-unidirectional setup simulated with a FDTD method and the impulse response of a sub-woofer

C.2 Case 2: $f_{cardioid} = 100Hz$

In case 2, the frequency giving the ideal cardioid directivity is $f_{cardioid}$=100 Hz. For a such frequency, the distance between the sources is $D = \frac{\lambda_{f_{cardioid}}}{4} = 0.85m$ and the delay applied on the back subwoofer is $d = \frac{\lambda_{f_{cardioid}}}{4} = 0.85m$.

The results are expressed in dB SPL. The scales on the x-axis and y-axis represent the indexes in the FDTD grid and can be converted into meter by multiplying them by 0.2 (the grid size).

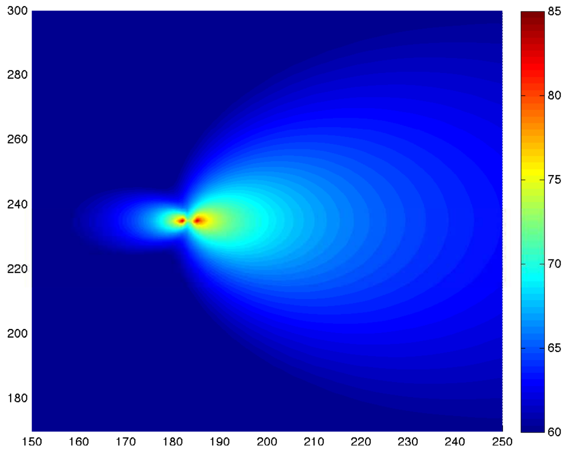

(a) $f = 40Hz$

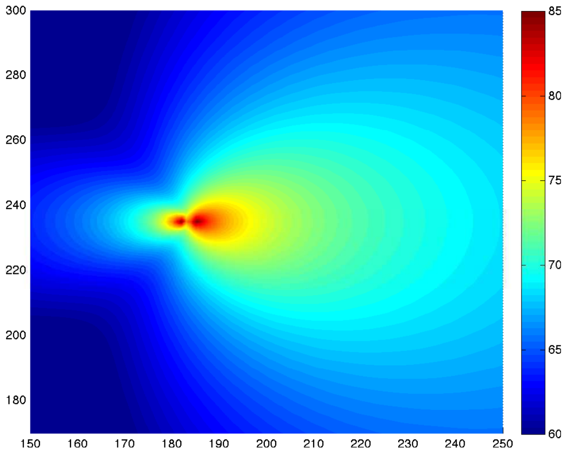

(b) $f = 50Hz$

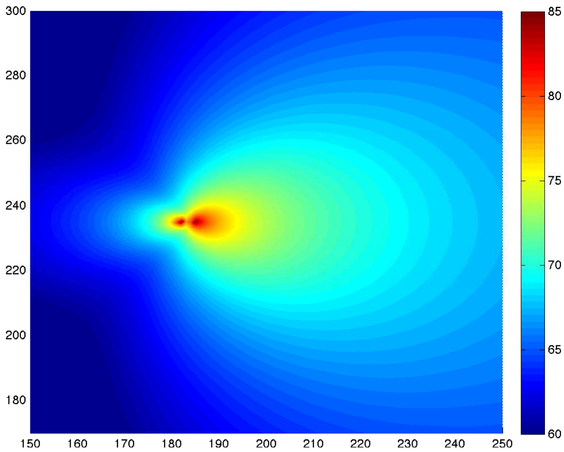

(c) $f = 60Hz$

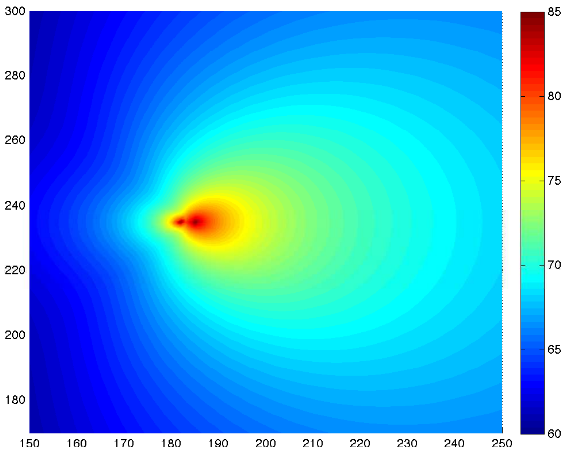

(d) $f = 80Hz$

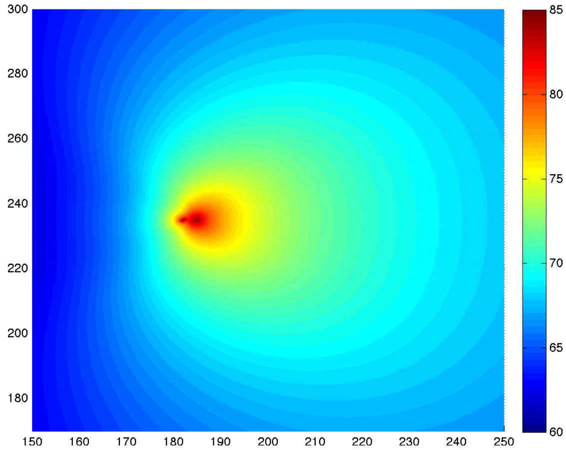

(e) 100

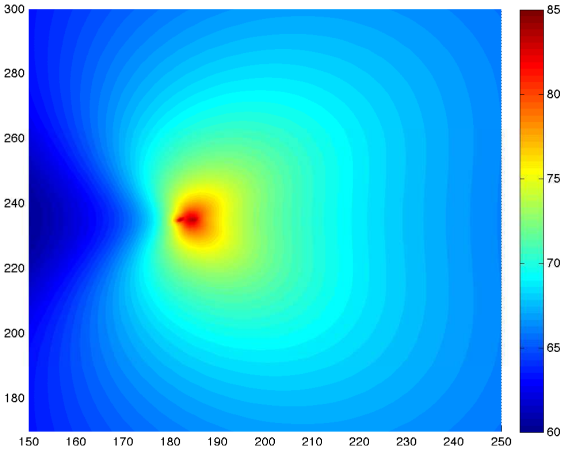

(f) $f = 120Hz$

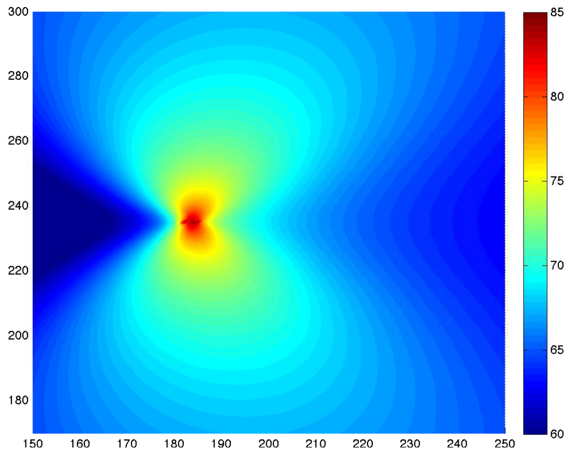

(g) $f = 150Hz$

Figure C.2: Pressure in dB SPL for a first order gradient sound source-unidirectional setup simulated with a FDTD method and the impulse response of a subwoofer

C.3 Case 3: $f_{cardioid} = 80Hz$

In the third case, the frequency giving the ideal cardioid directivity is $f_{cardioid}$=80 Hz. For a such frequency, the distance between the sources is $D = \frac{\lambda_{f_{cardioid}}}{4} = 1.1m$ and the delay applied on the back subwoofer is $d = \frac{\lambda_{f_{cardioid}}}{4} = 1.1m$.

The results are expressed in dB SPL. The scales on the x-axis and y-axis represent the indexes in the FDTD grid and can be converted into meter by multiplying them by 0.2 (the grid size).

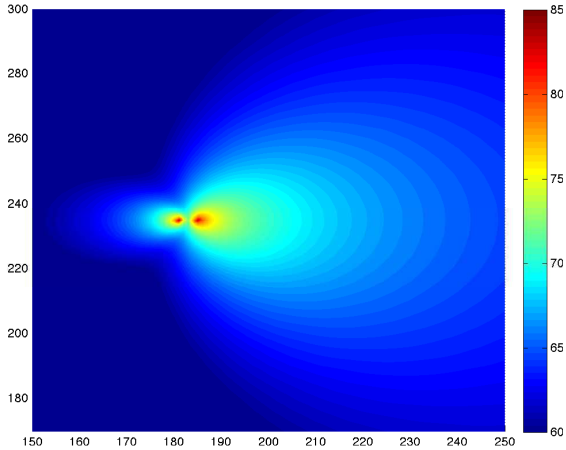

(a) $f = 40Hz$

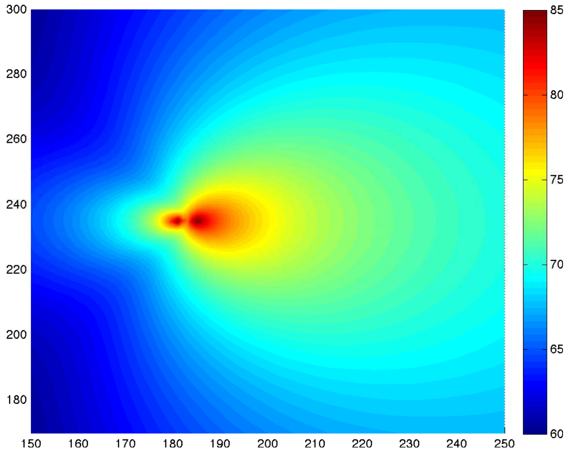

(b) $f = 50Hz$

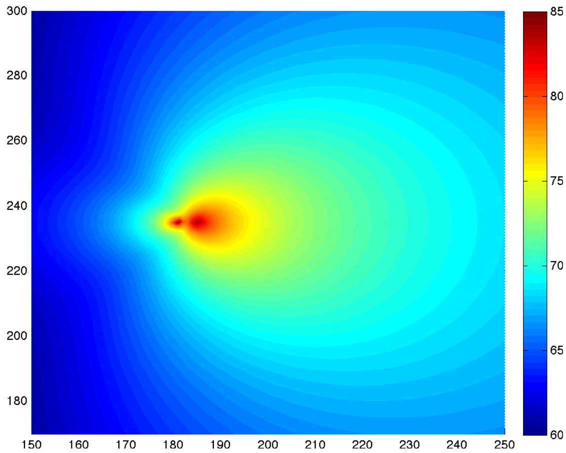

(c) $f = 60Hz$

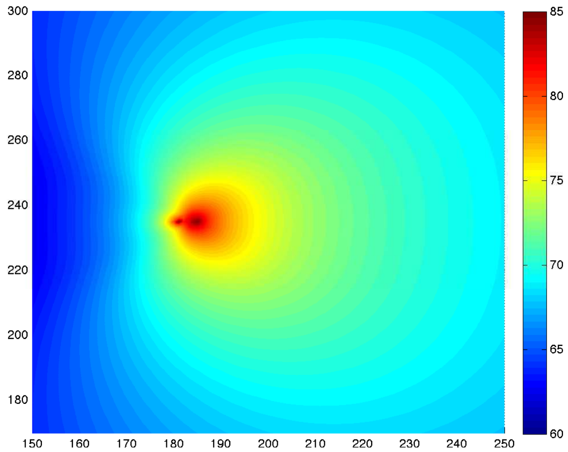

(d) $f = 80Hz$

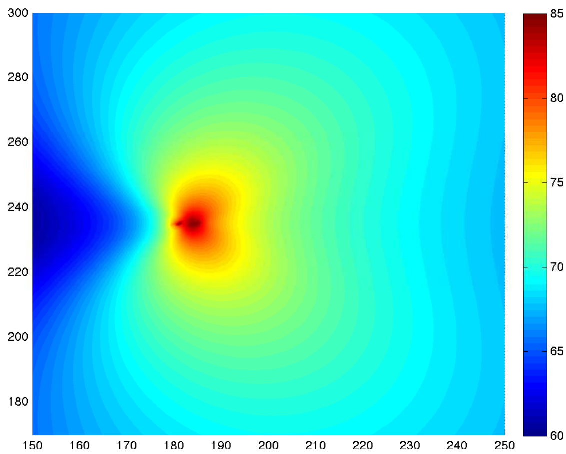

(e) 100

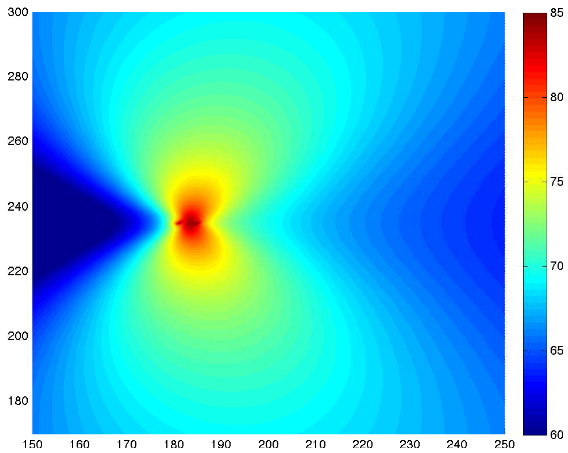

(f) $f = 120Hz$

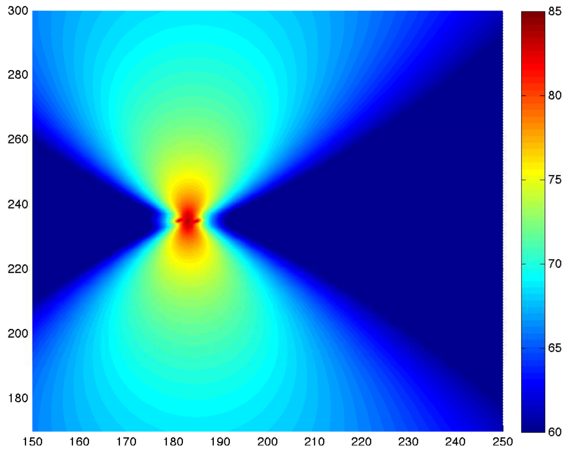

(g) $f = 150Hz$

Figure C.3: Pressure in dB SPL for a first order gradient sound source-unidirectional setup simulated with a FDTD method and the impulse response of a subwoofer

C.4 Case 4: $f_{cardioid} = 50Hz$

In the fourth case, the frequency giving the ideal cardioid directivity is $f_{cardioid}$=50 Hz. For a such frequency, the distance between the sources is $D = \frac{\lambda_{f_{cardioid}}}{4} = 1.7m$ and the delay applied on the back subwoofer is $d = \frac{\lambda_{f_{cardioid}}}{4} = 1.7m$.

The results are expressed in dB SPL. The scales on the x-axis and y-axis represent the indexes in the FDTD grid and can be converted into meter by multiplying them by 0.2 (the grid size).

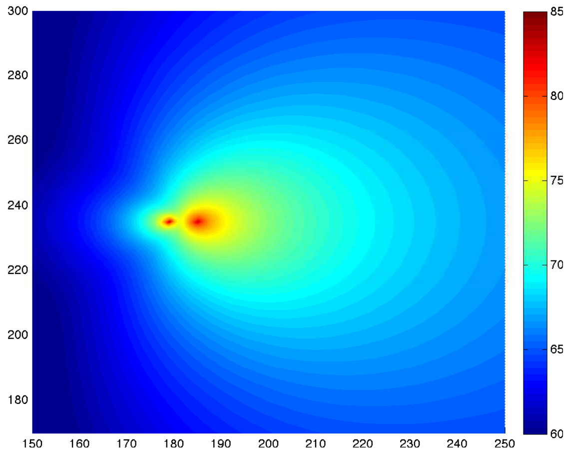

(a) $f = 40Hz$

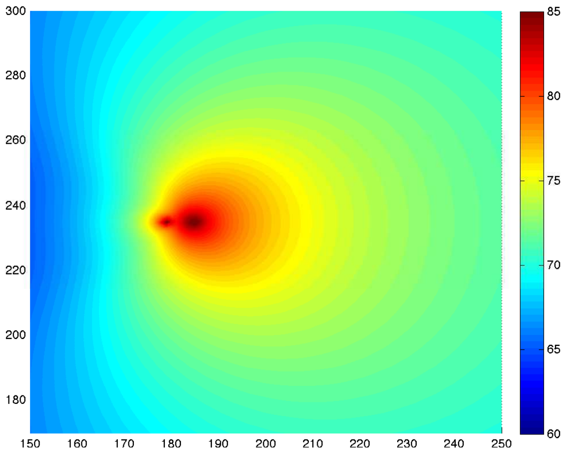

(b) $f = 50Hz$

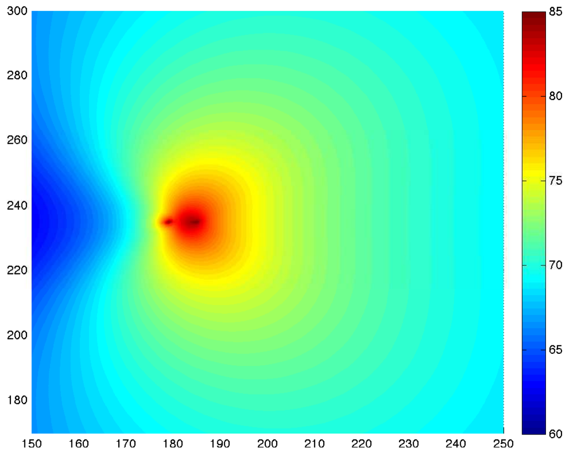

(c) $f = 60Hz$

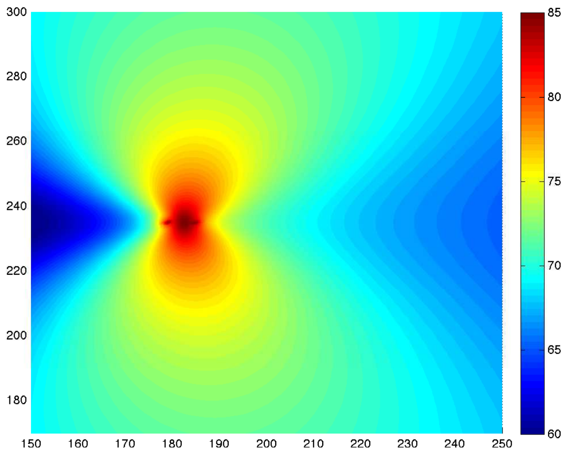

(d) $f = 80Hz$

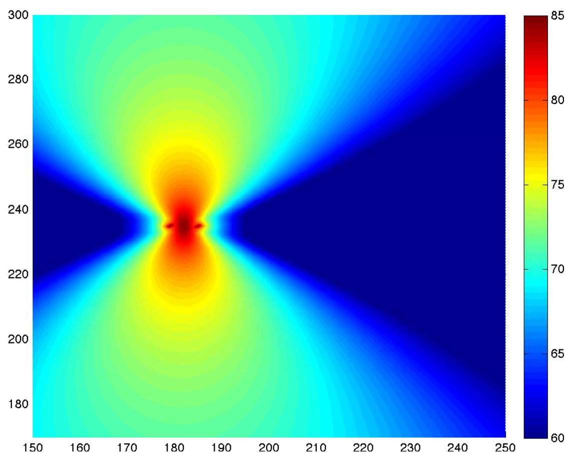

(e) 100

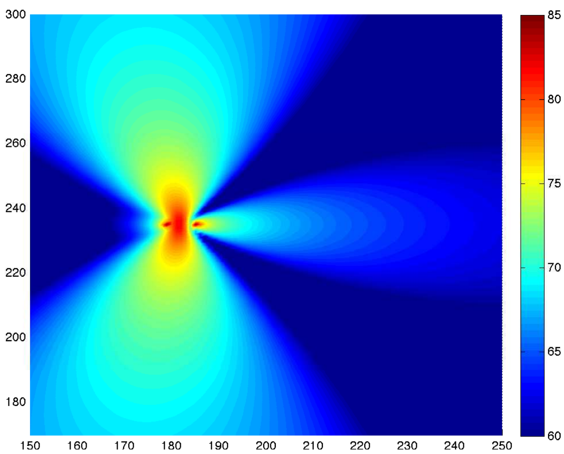

(f) $f = 120Hz$

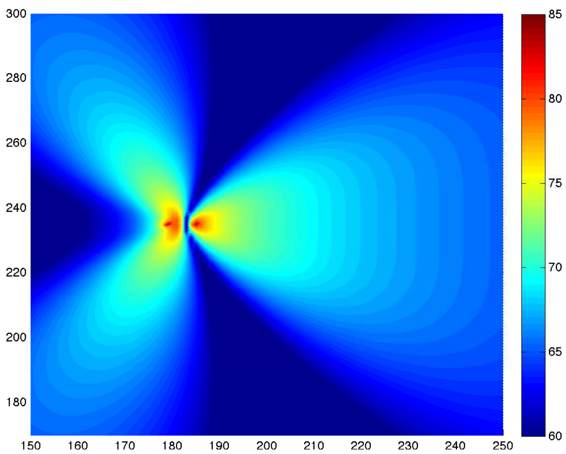

(g) $f = 150Hz$

Figure C.4: Pressure in dB SPL for a first order gradient sound source-unidirectional setup simulated with a FDTD method and the impulse response of a subwoofer

D

Frequency-dependent delay

This appendix shows the analytical polar directivity and the FDTD simulations of a first order gradient sound source-unidirectional with a frequency-dependent delay on the back subwoofer.

D.1 Analytical polar directivity of a first order gradient sound source-unidirectional with a frequency dependent delay

On figure D.1 the polar patterns of a first-order gradient sound source-unidirectional with and without a frequency-dependent delay are plotted at different discrete frequencies.

The red plots correspond to the case where the delay d is kept constant for all the frequencies, $D = d = \frac{\lambda_{f_{max}}}{4}$ and the directivity pattern is defined by equation D.1.

$$R_\theta = \sin\left(\pi \frac{d_{f_{max}}}{\lambda} + \pi \frac{D_{f_{max}}}{\lambda} \cos\theta\right) \tag{D.1}$$

The blue plots correspond to the case where $D = \frac{\lambda_{f_{max}}}{4}$, d follow the relation D.3 and the directivity pattern is defined by equation D.2.

$$R_\theta = \sin\left(\pi \frac{d}{\lambda} + \pi \frac{D_{f_{max}}}{\lambda} \cos\theta\right) \tag{D.2}$$

$$d = \frac{c}{4 f_{max}} + \left(1 - \frac{f}{f_{max}}\right) \times \frac{c}{4 f_{max}} \tag{D.3}$$

The maximum frequency of interest f_{max}, which gives the perfect cardioid behavior, is chosen arbitrarily equal to 150 Hz. The reasons of this choice are that it allows to see the performances of the frequency-dependent delay on a wide frequency range (120 Hz), it is a good trade-off between the cutting frequency of the subwoofer used in home-cinema (maximum fc $\approx$ 200 Hz) and the ones used in the concert industry (fc $\approx$ 85 Hz) and finally because it corresponds to the cutting frequency of the real subwoofer used in this project, which can be useful for future comparisons.

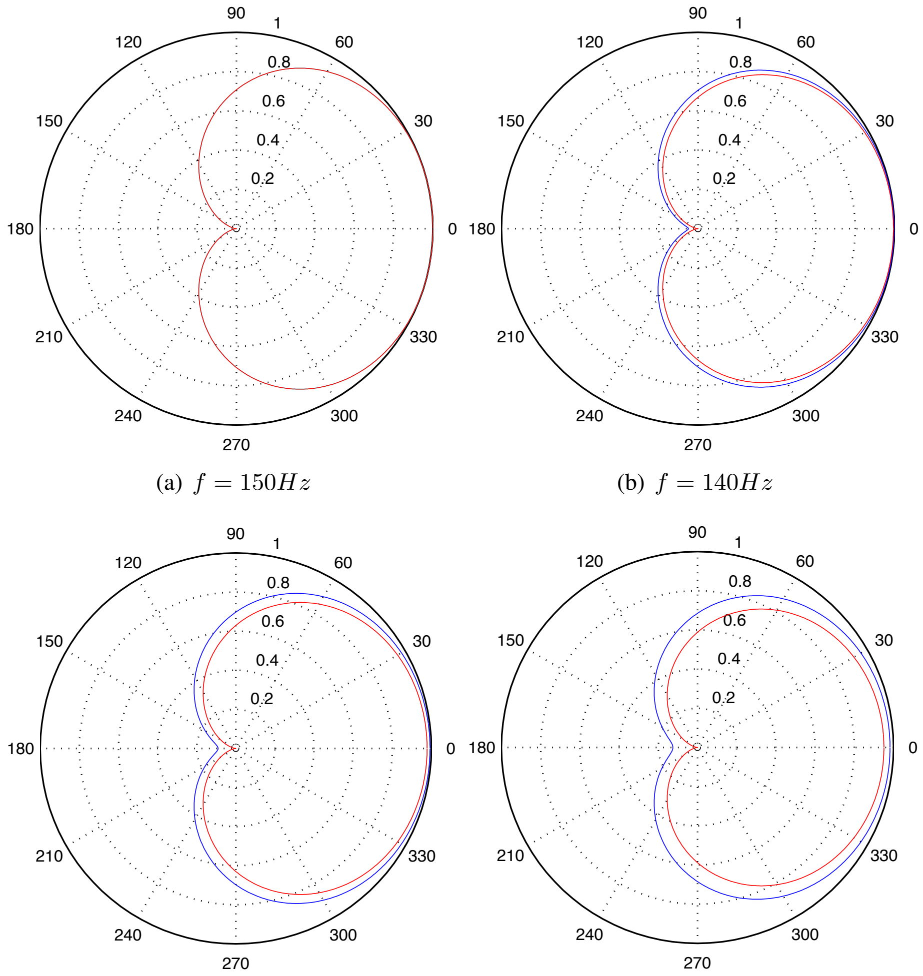

(a) $f = 150Hz$

(b) $f = 140Hz$

(c) $f = 130Hz$

(d) $f = 120Hz$

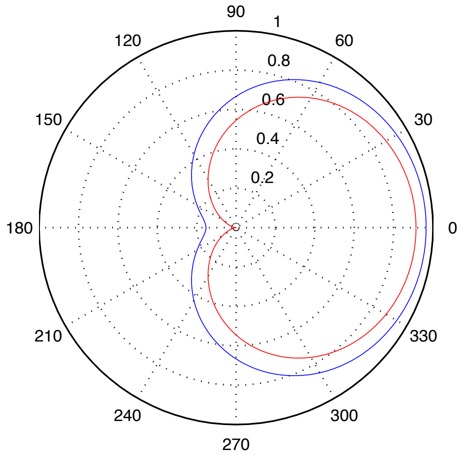

(e) $f = 110Hz$

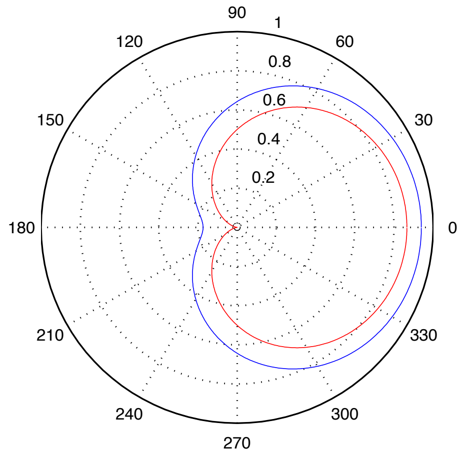

(f) $f = 100Hz$

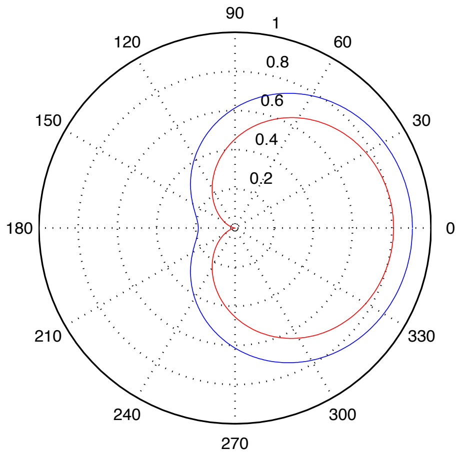

(g) $f = 90Hz$

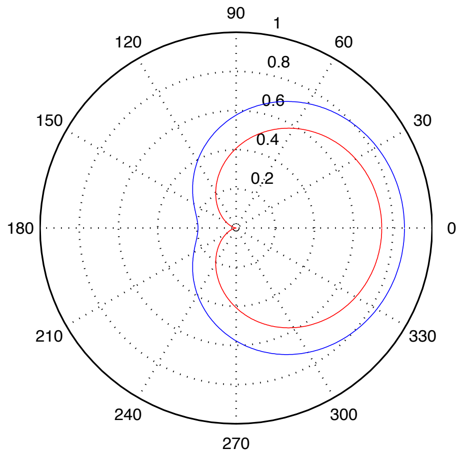

(h) $f = 80Hz$

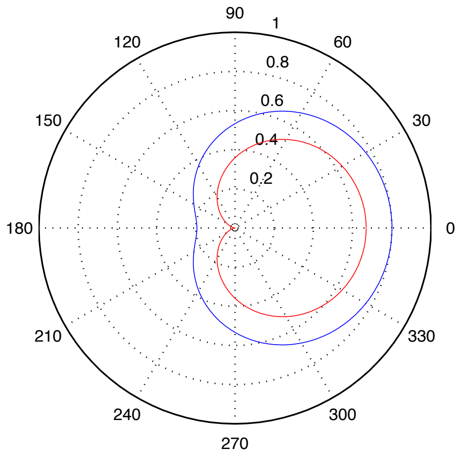

(i) $f = 70Hz$

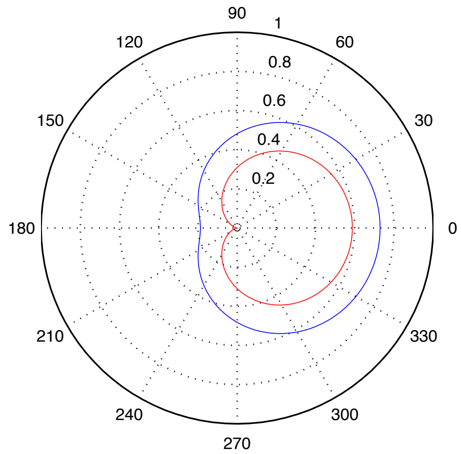

(j) $f = 60Hz$

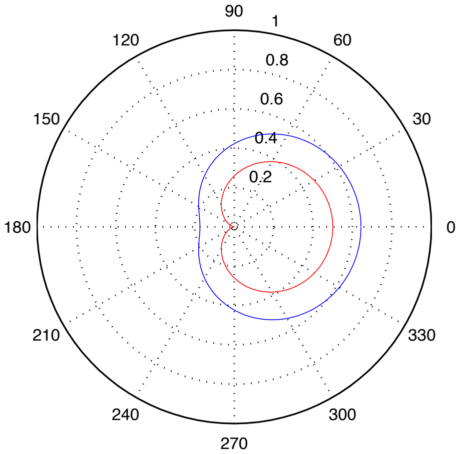

(k) $f = 50Hz$

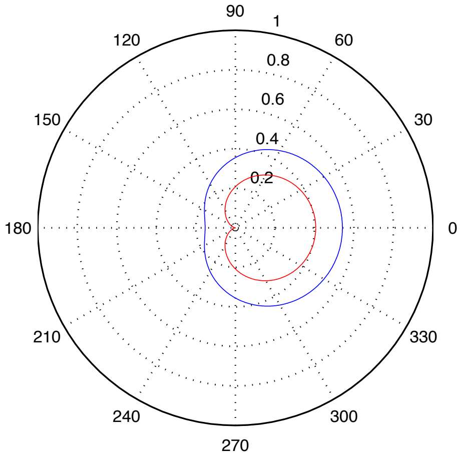

(l) $f = 40Hz$

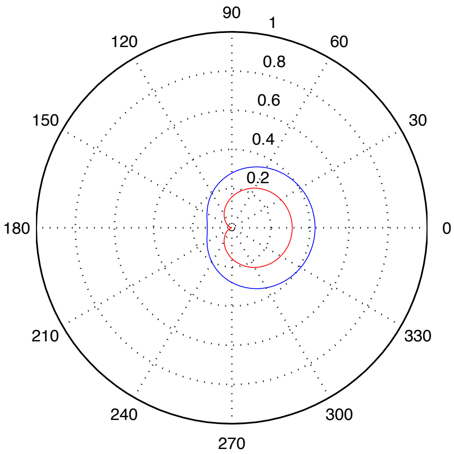

(m) $f = 30Hz$

Figure D.1

D.2 FDTD simulations

In this section the FDTD method is used to simulate the behavior of a first order gradient sound source-unidirectional with a fixed delay and with a frequency-dependent delay.

These simulation have been run over a time of 0.05 sec corresponding to the period of the lowest frequency produced. The grid size is 0.1 m and the sampling frequency is 8000 Hz, so the stability conditions in the space and time domains are fulfilled.

The signal used in these simulations is a sinusoid of mono-frequency f. The distance between the sources is $D = \frac{\lambda_{f_{max}}}{4}$ with $f_{max} = 150Hz$ and stays unchanged during all the simulations. In the case of the setup with a fixed delay, the delay is chosen to be $d = \frac{\lambda_{f_{max}}}{4}$ (in meter). Therefore the perfect cardioid behavior is expected for $f_{max} = 150Hz$. In the case of the frequency-dependent delay, the delay d changes with the frequency according to equation D.3.

The results of the simulations are presented on figure D.2. The figures represents the pressure in dB SPL at different discrete frequencies for both different setups. In the left column one displays the results for the first order gradient source with a fixed delay. In the right column one display the results obtained with the floating delay. The scales on the x-axis and y-axis represent the indexes in the FDTD grid.

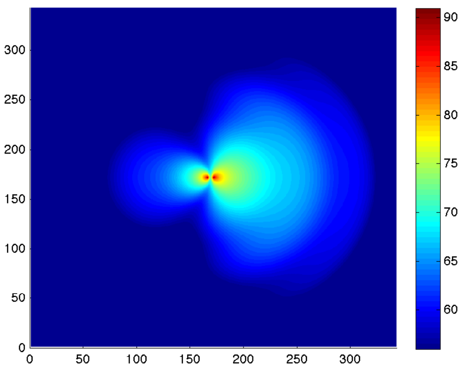

(a) $f = 30Hz, d = d_{f_{max}}$

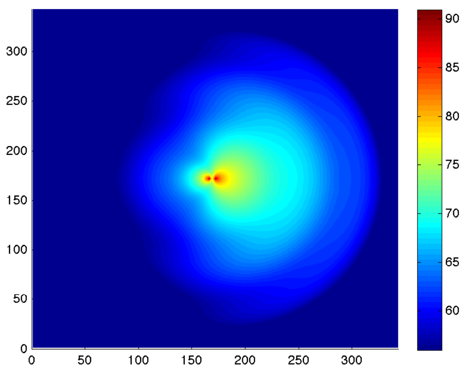

(b) $f = 30Hz, d = \frac{2c}{4f_{max}} - \frac{f}{f_{max}} \frac{c}{4f_{max}}$

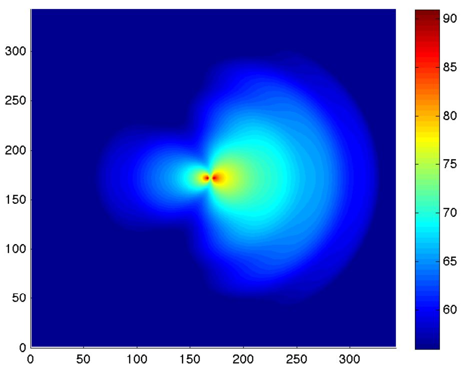

(c) $f = 40Hz, d = d_{f_{max}}$

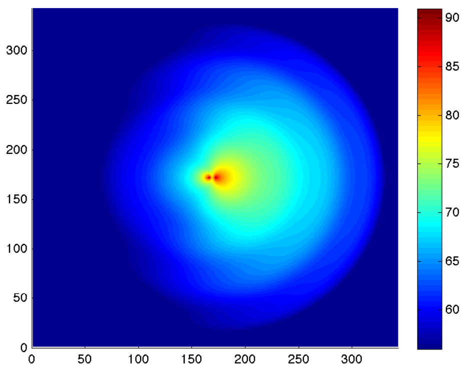

(d) $f = 40Hz, d = \frac{2c}{4f_{max}} - \frac{f}{f_{max}} \frac{c}{4f_{max}}$

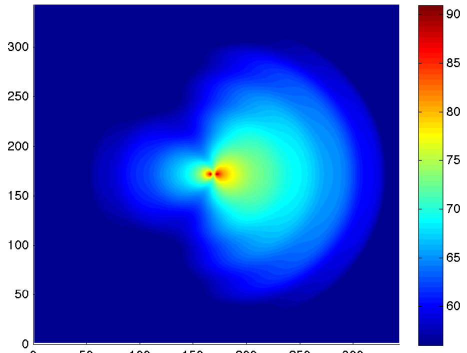

(e) $f = 50Hz, d = d_{f_{max}}$

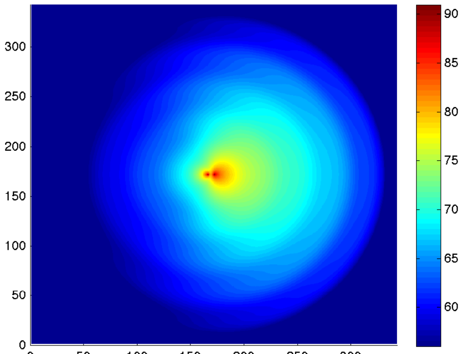

(f) $f = 50Hz, d = \frac{2c}{4f_{max}} - \frac{f}{f_{max}} \frac{c}{4f_{max}}$

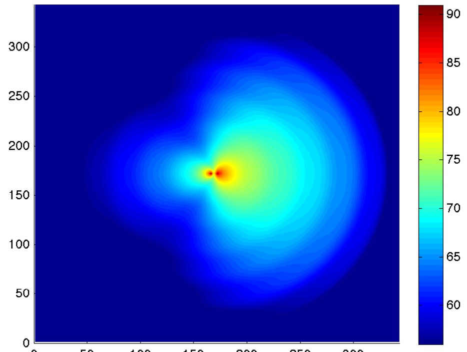

(g) $f = 60Hz, d = d_{f_{max}}$

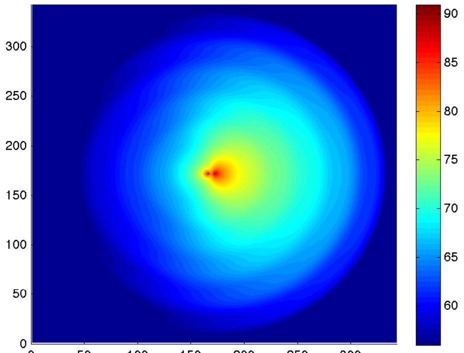

(h) $f = 60Hz, d = \frac{2c}{4f_{max}} - \frac{f}{f_{max}} \frac{c}{4f_{max}}$

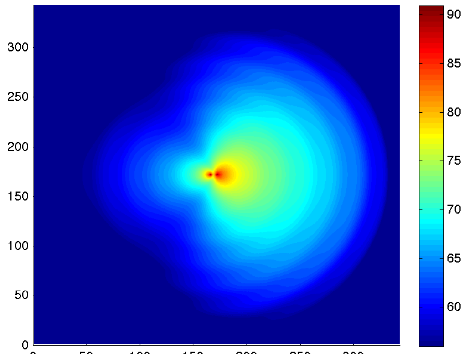

(i) $f = 70Hz, d = d_{f_{max}}$

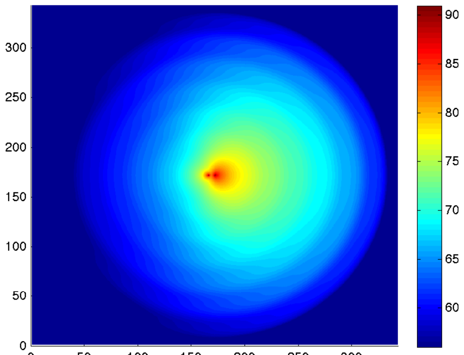

(j) $f = 70Hz, d = \frac{2c}{4f_{max}} - \frac{f}{f_{max}} \frac{c}{4f_{max}}$

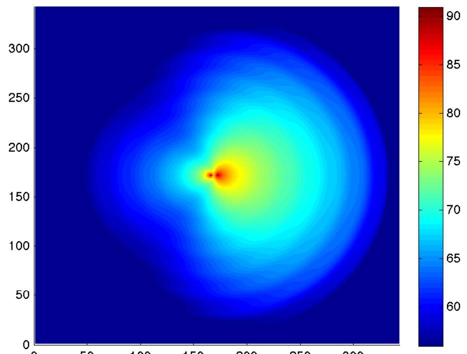

(k) $f = 80Hz, d = d_{f_{max}}$

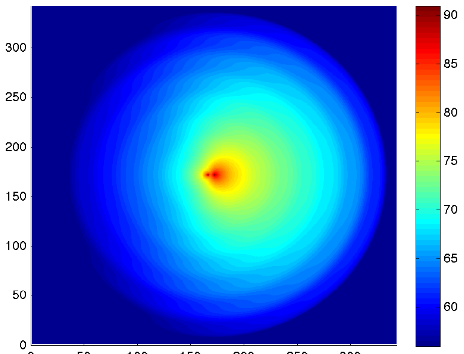

(l) $f = 80Hz, d = \frac{2c}{4f_{max}} - \frac{f}{f_{max}} \frac{c}{4f_{max}}$

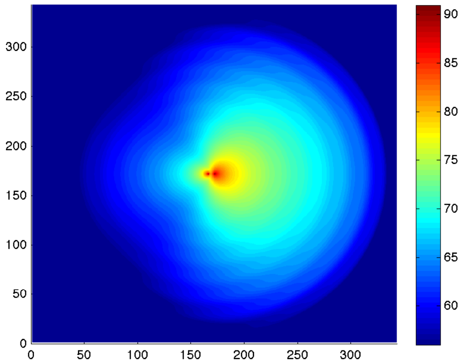

(m) $f = 90Hz, d = d_{f_{max}}$

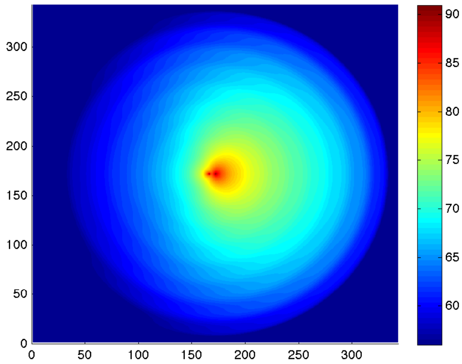

(n) $f = 90Hz, d = \frac{2c}{4f_{max}} - \frac{f}{f_{max}} \frac{c}{4f_{max}}$

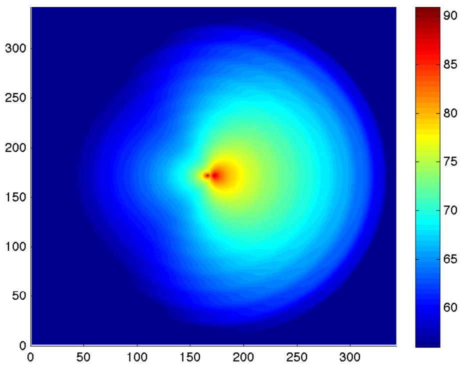

(o) $f = 100Hz, d = d_{f_{max}}$

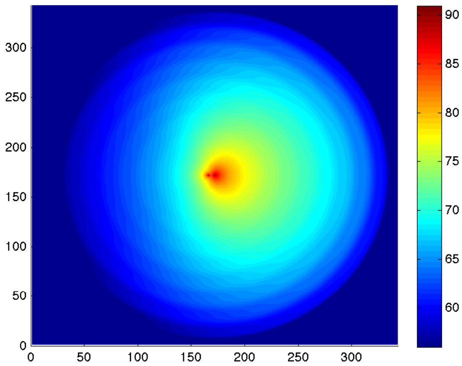

(p) $f = 100Hz, d = \frac{2c}{4f_{max}} - \frac{f}{f_{max}} \frac{c}{4f_{max}}$

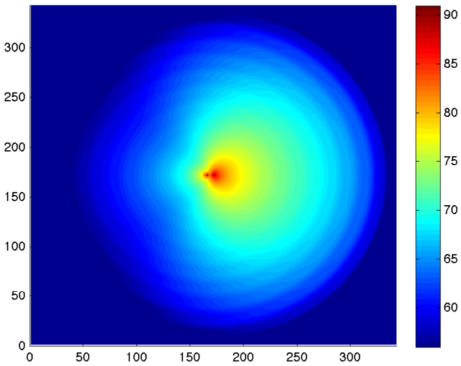

(q) $f = 110Hz, d = d_{f_{max}}$

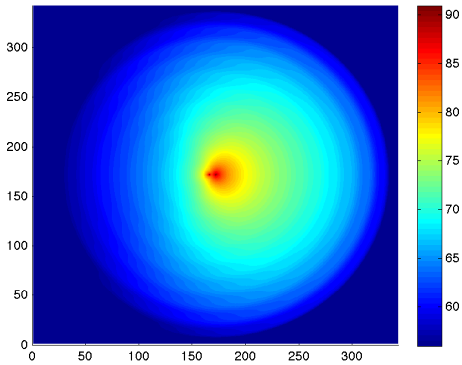

(r) $f = 110Hz, d = \frac{2c}{4f_{max}} - \frac{f}{f_{max}} \frac{c}{4f_{max}}$

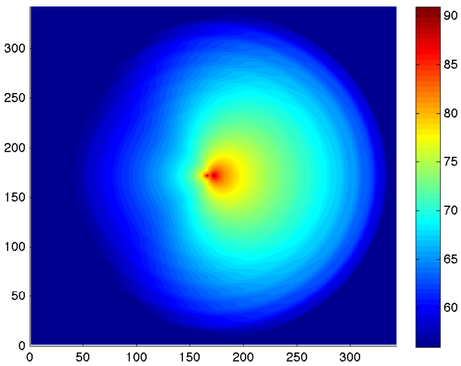

(s) $f = 120Hz, d = d_{f_{max}}$

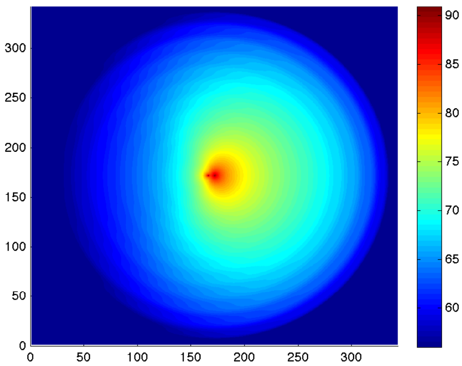

(t) $f = 120Hz, d = \frac{2c}{4f_{max}} - \frac{f}{f_{max}} \frac{c}{4f_{max}}$

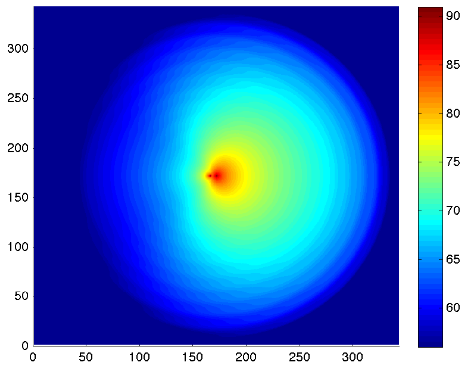

(u) $f = 130Hz, d = d_{f_{max}}$

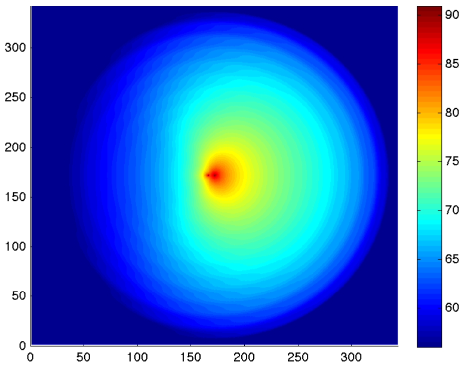

(v) $f = 130Hz, d = \frac{2c}{4f_{max}} - \frac{f}{f_{max}} \frac{c}{4f_{max}}$

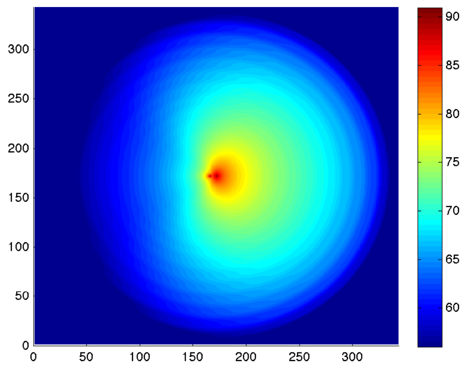

(w) $f = 140Hz, d = d_{f_{max}}$

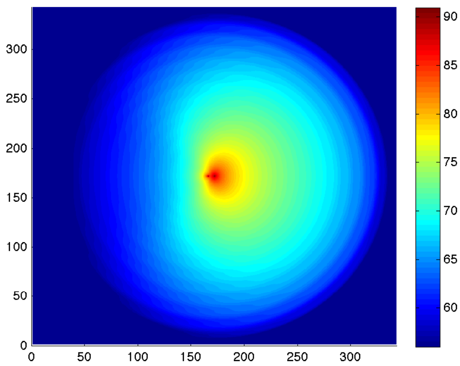

(x) $f = 140Hz, d = \frac{2c}{4f_{max}} - \frac{f}{f_{max}} \frac{c}{4f_{max}}$

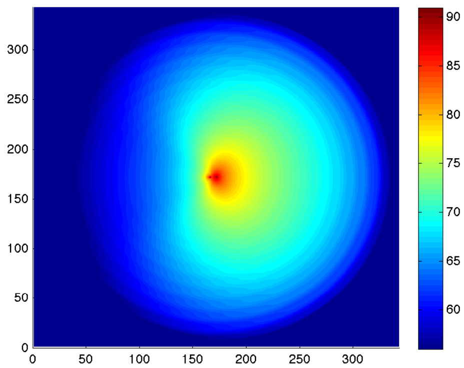

(y) $f = 150Hz, d = d_{f_{max}}$

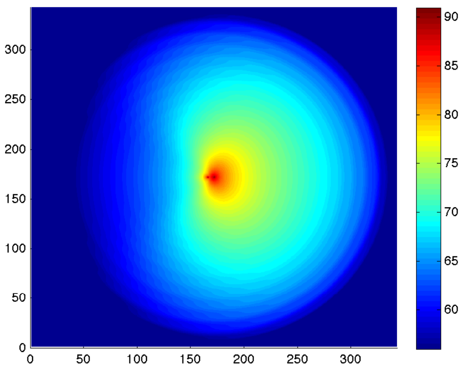

(z) $f = 150Hz, d = \frac{2c}{4f_{max}} - \frac{f}{f_{max}} \frac{c}{4f_{max}}$

Figure D.2: FDTD simulations of a first order gradient sound source with a fixed delay (left column) and with a frequency-dependent delay (right column) at different discrete frequencies f. Results are in dB SPL

E

FDTD method: Simulation of a real subwoofer filtered by an all pass filter having a desired group delay

In this appendix the FDTD method is used to simulate the behavior of a first order gradient sound source-unidirectional using the impulse response of a real subwoofer and whose back subwoofer is filtered by the IIR all pass filter designed in subsection 8.3.3. The results of these simulations are showed in parallel with the ones obtained in appendix C.1.

The characteristics of the subwoofer and particularly its impulse response are the same than in the subsection 6.2.1. The cell size and the time step size are also the same than for the simulations of chapter 6 with respect to the discussions of subsections 6.2.2 and 6.2.3. The cardioid frequency is equal to 150 Hz giving a distance between the subwoofers equal to $D = \frac{c}{4\times 150} = 0.57$ m (with $c = 343m.s^{-1}$).

Figure E.1 shows in parallel the pressure field at different discrete frequencies for the setup without the designed IIR filter (left column) and with the IIR filter (right column). These different pressure field are obtained in the same manner than in section 6.3.

Each subfigure represents the pressure in dB SPL. The scale on the x-axis and y-axis represents the indexes in the FDTD grid.

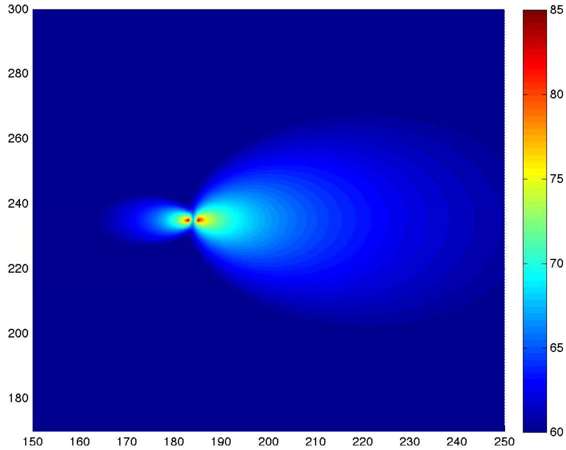

(a) $f = 40Hz$

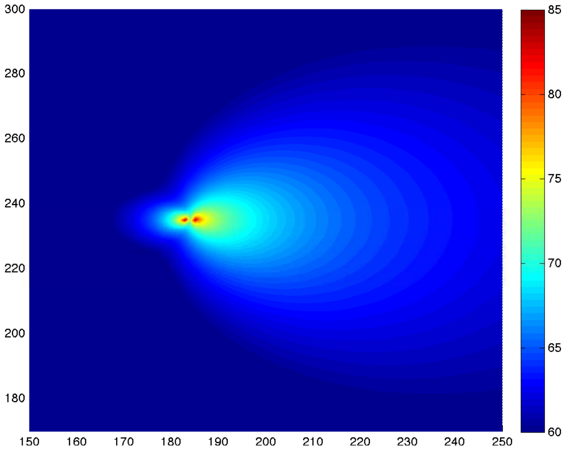

(b) $f = 40Hz$

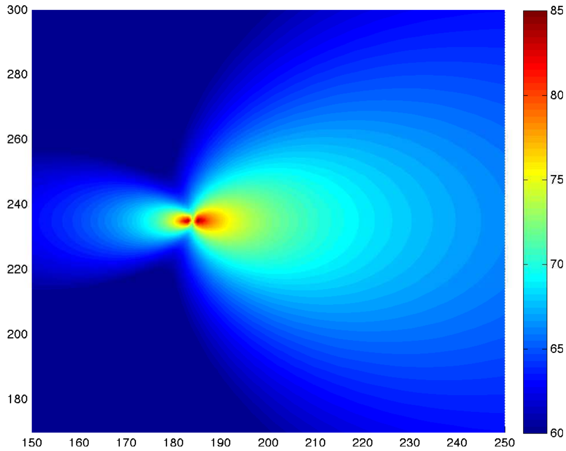

(c) $f = 50Hz$

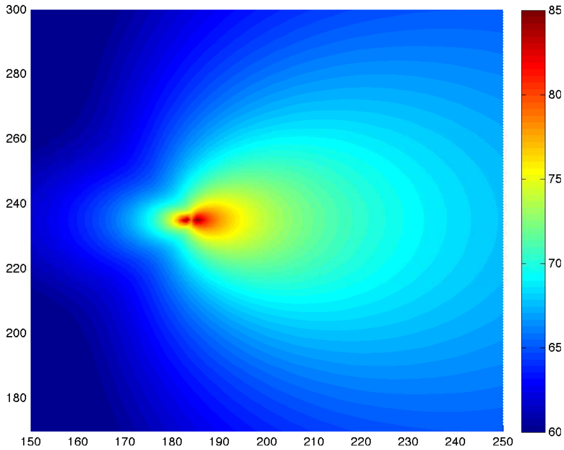

(d) $f = 50Hz$

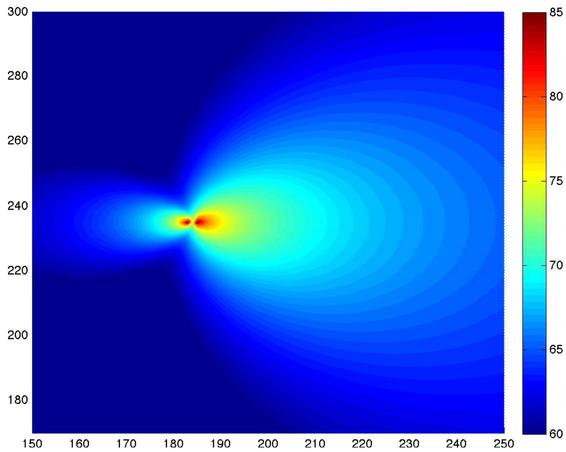

(e) $f = 60Hz$

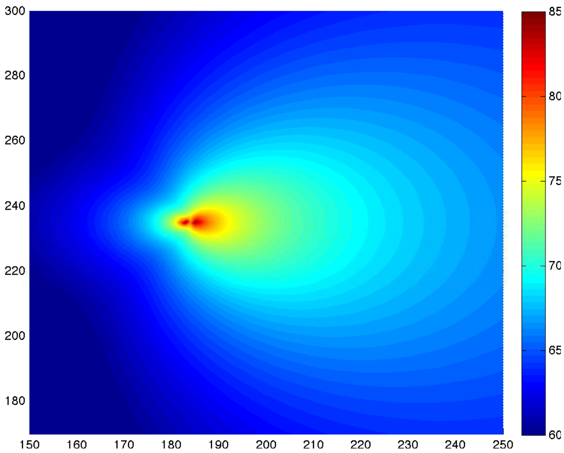

(f) $f = 60Hz$

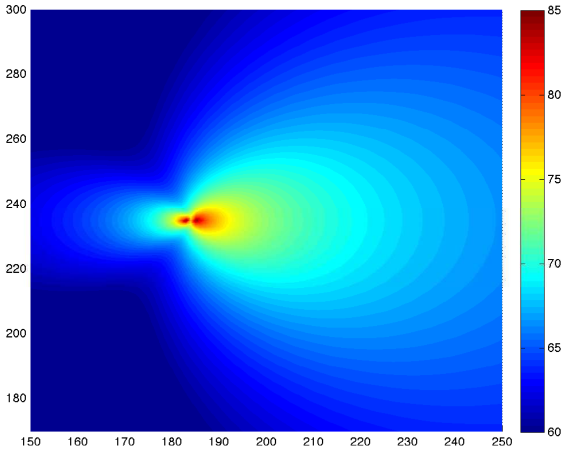

(g) $f = 80Hz$

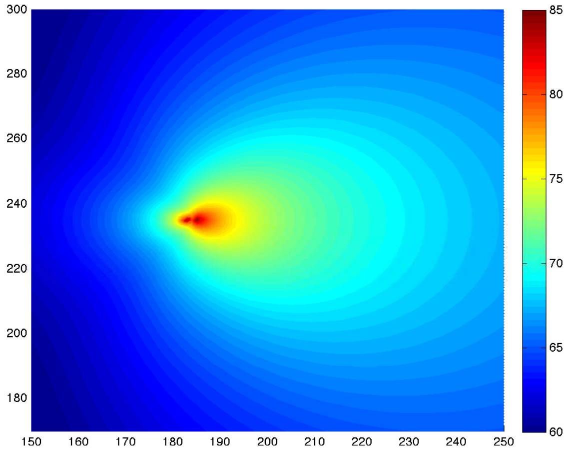

(h) $f = 80Hz$

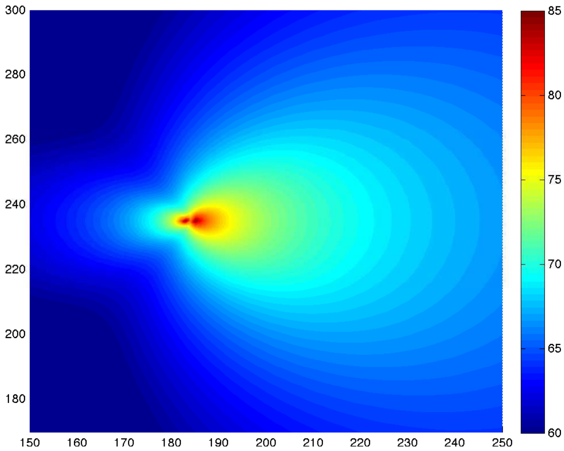

(i) 100

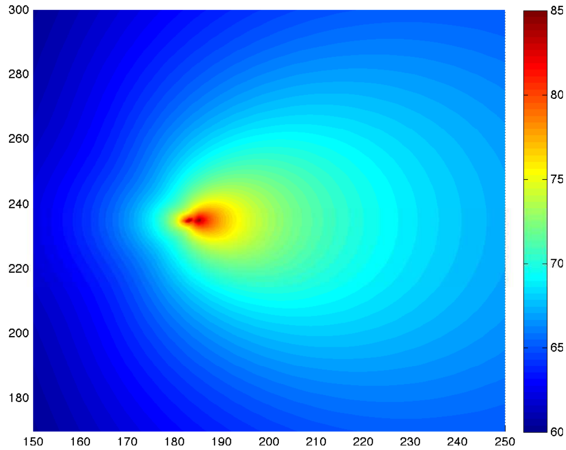

(j) $f = 100Hz$

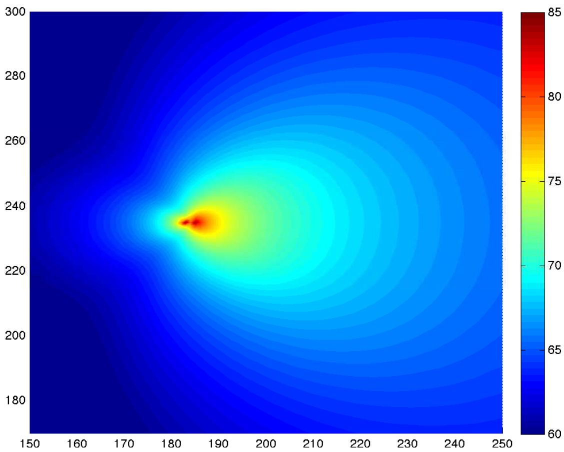

(k) $f = 120Hz$

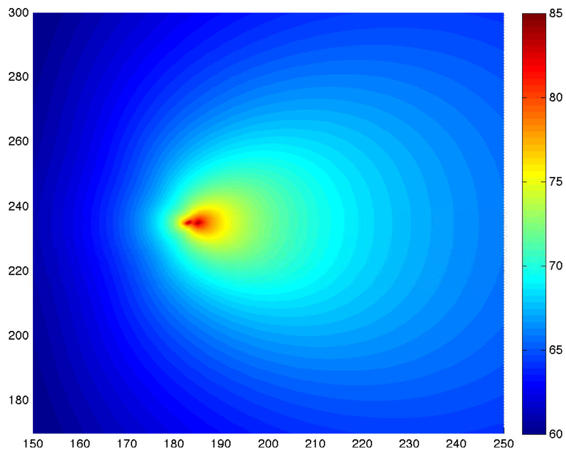

(l) $f = 120Hz$

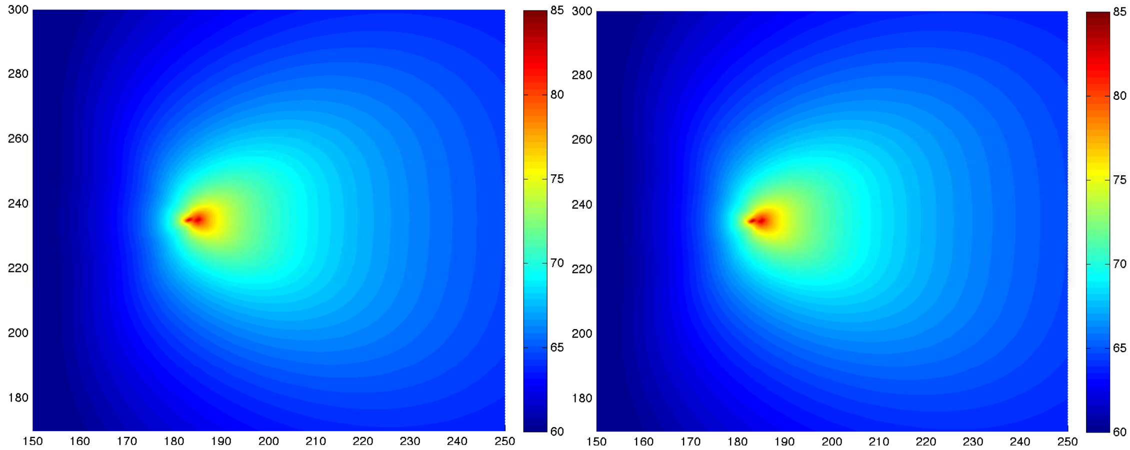

(m) $f = 150Hz$

(n) $f = 150Hz$

Figure E.1: Pressure in dB SPL for a first order gradient sound source-unidirectional setup simulated with a FDTD method fed by the impulse response of a subwoofer. In the left column the delay on the back subwoofer is fixed and equal to $\frac{c}{4f_{max}}$ with $f_{max} = 150Hz$. In the right column the back subwoofer is filtered with the IIR all pass filter designed in chapter 8.4

F

Simulation: Gain dependency

F.1 Simulation: Analytical part

Directivity pattern of a first order gradient source-unidirectional according to the analytical expression 9.4 for different values of gain G and two different ratio $\frac{D}{\lambda}$.

F.1.1 Simulations for $\frac{D}{\lambda} = 0.25$

F.1.2 Simulations for $\frac{D}{\lambda} = 0.125$

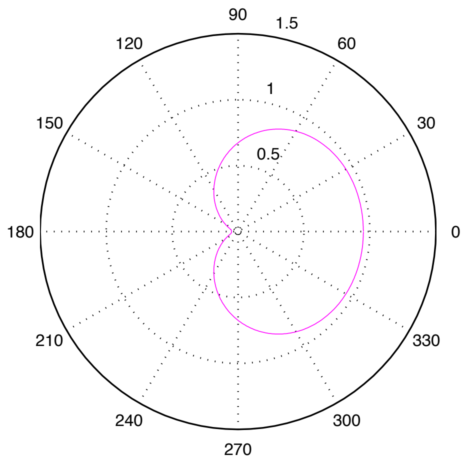

(a) Gain=1

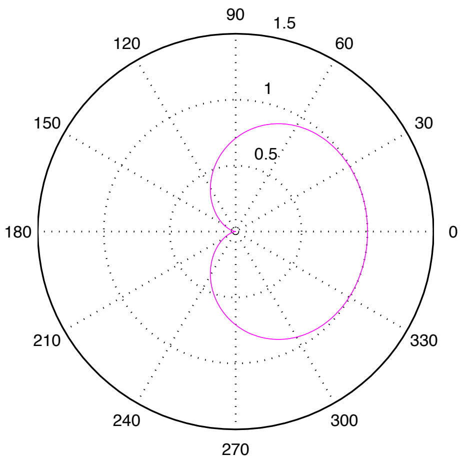

(b) Gain=1.1

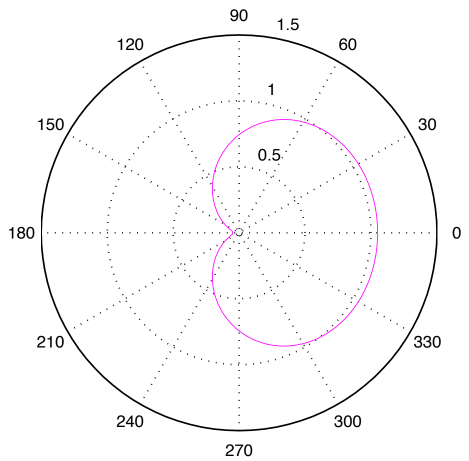

(c) Gain=1.2

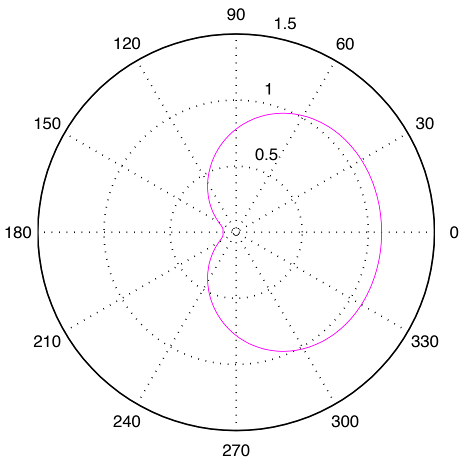

(d) Gain=1.3

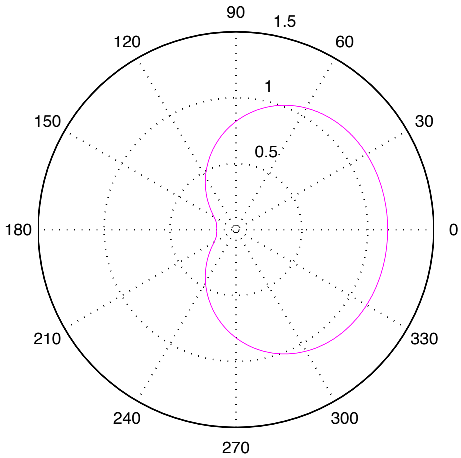

(e) Gain=1.4

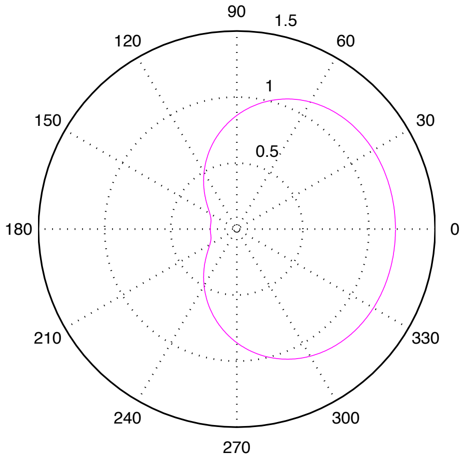

(f) Gain=1.5

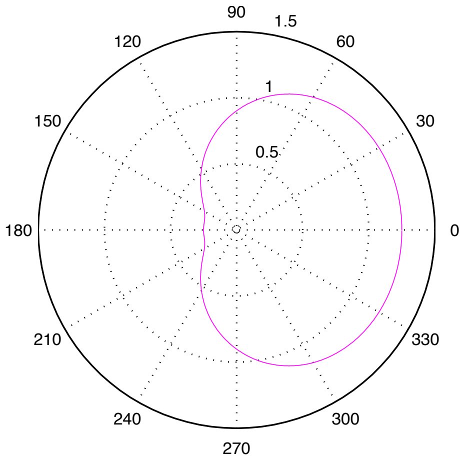

(g) Gain=1.6

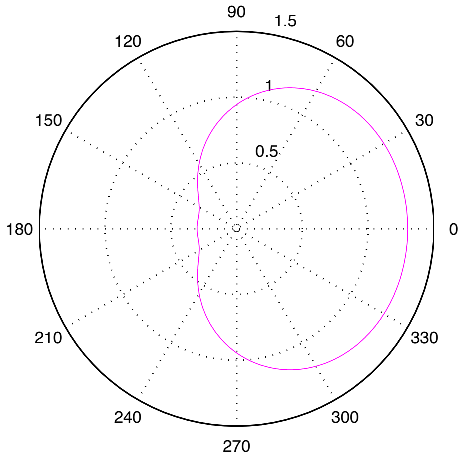

(h) Gain=1.7

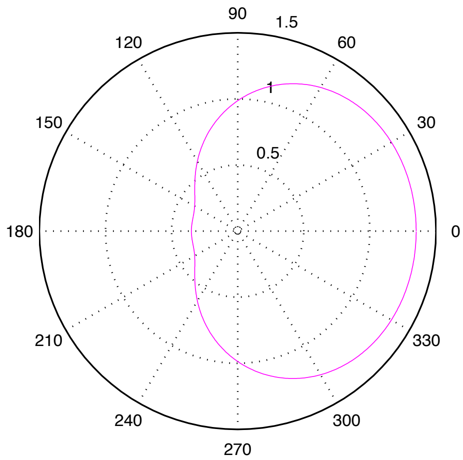

(i) Gain=1.8

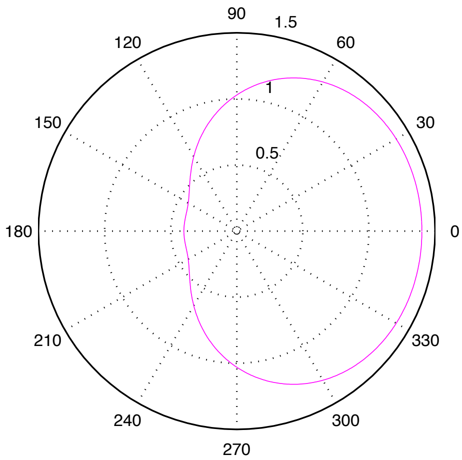

(j) Gain=1.9

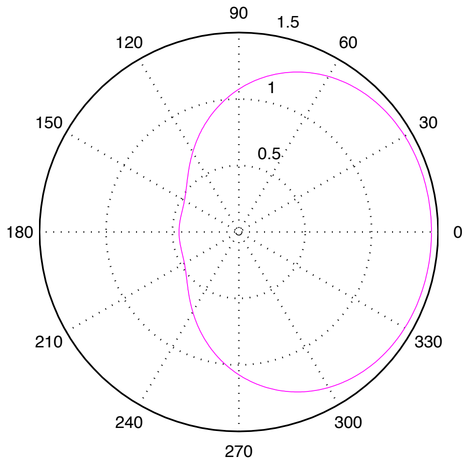

(k) Gain=2

Figure F.1: Directivity pattern of a first order gradient sound source-unidirectional for different values of gain applied on the front subwoofer. The results are expressed in pascal

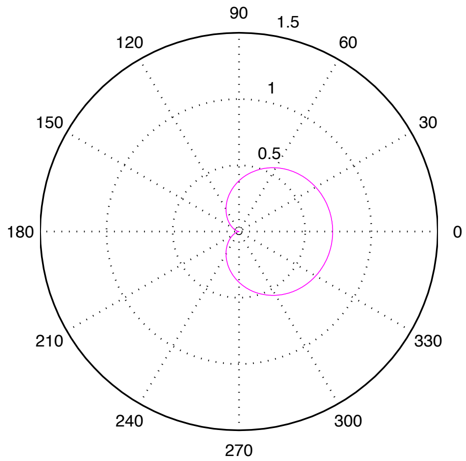

(a) Gain=1

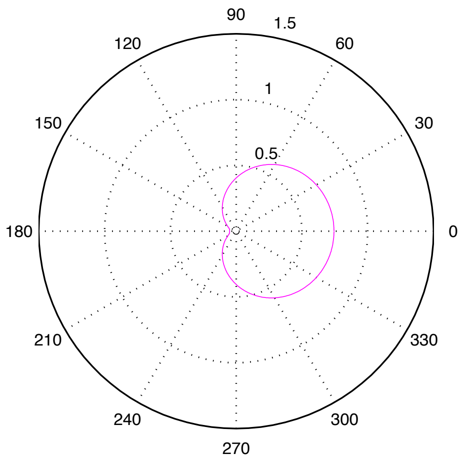

(b) Gain=1.1

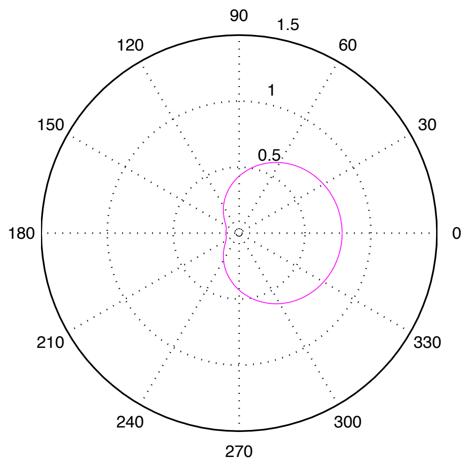

(c) Gain=1.2

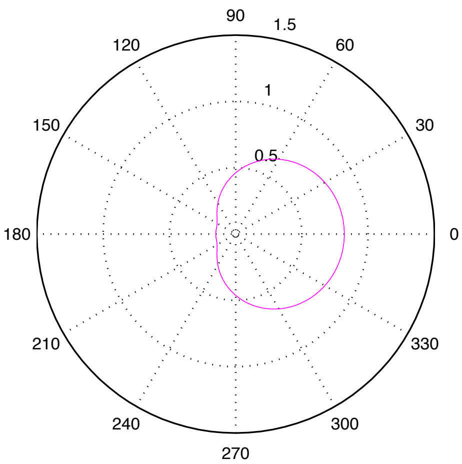

(d) Gain=1.3

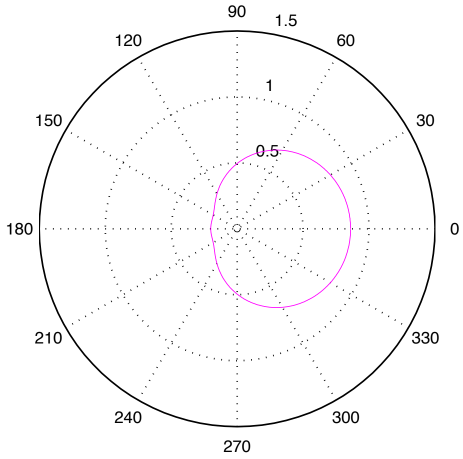

(e) Gain=1.4

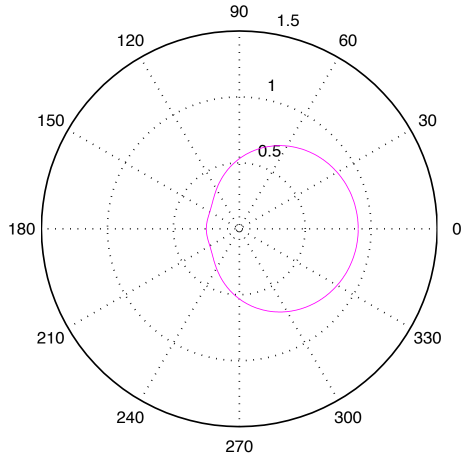

(f) Gain=1.5

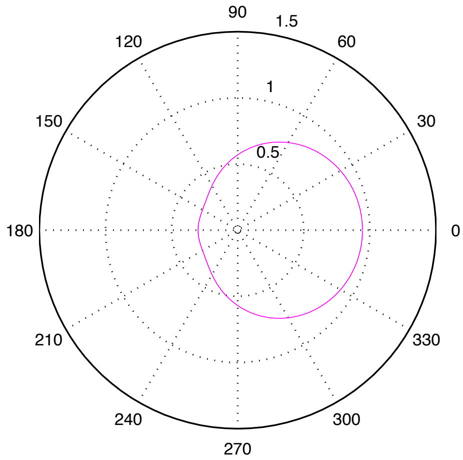

(g) Gain=1.6

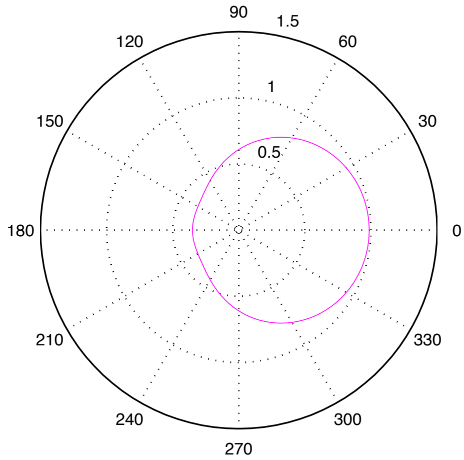

(h) Gain=1.7

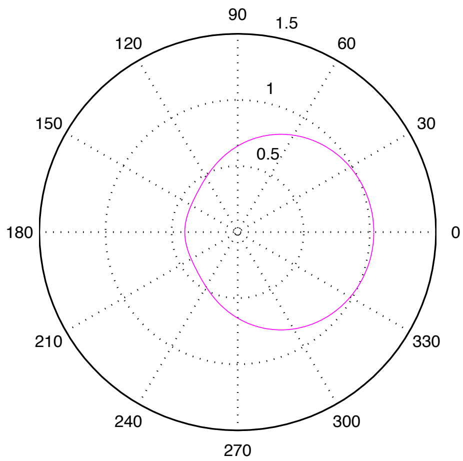

(i) Gain=1.8

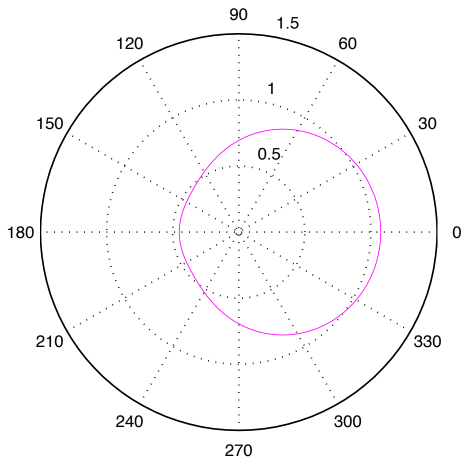

(j) Gain=1.9

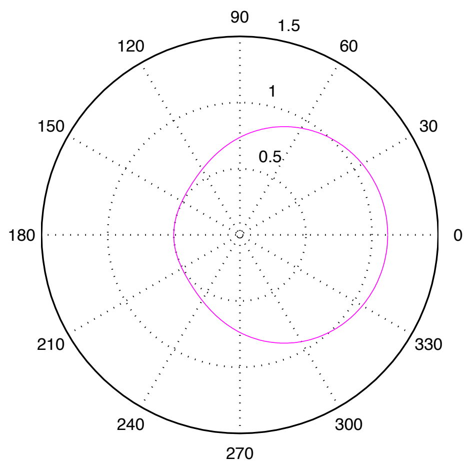

(k) Gain=2

Figure F.2: Directivity pattern of a first order gradient sound source-unidirectional for different values of gain applied on the front subwoofer. The results are expressed in pascal

F.2 FDTD simulation: Sinusoidal source

The graduations on the x and y axis of figures *a* and *b* represent the indexes in the FDTD grid used to calculate the pressure. As the cell size has been chosen equal to 0.1 meter, it is possible to switch directly from indexes to distance (expressed in meter) by multiplying the index by 0.1. The sampling frequency used in these FDTD simulations is 8000 Hz.

F.2.1 Case 1: $\frac{D}{\lambda} = \frac{d}{\lambda} = 0.25$

In these simulations, the distance between the sources is kept constant $D = 0.57m$, which corresponds to one fourth of the wavelength of 150 Hz. The delay applied on the back source is also $d = 0.57m$. The sound sources are defined as a pressure sources fed by a sinusoidal signal of frequency 150 Hz. The magnitude of the back subwoofer varies between -1 and 1. The magnitude of the front subwoofer varies from -1 to 1 times the value of the gain. One runs the FDTD simulations for different values of gain. For each simulation one plots three figures: the RMS pressure in pascal, the RMS pressure in dB SPL and the the polar pattern extracted from the FDTD simulation following to the explanations of subsection 5.6.1. On this last one the dashed line represents the analytical result of subsection 9.2.2 and the blue cross the polar pattern extracted from the FDTD simulation

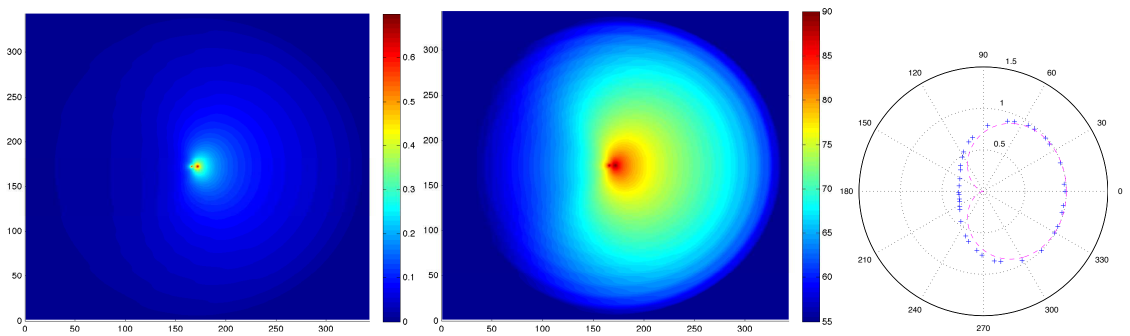

(a) RMS pressure field in pascal

(b) RMS pressure field in dB SPL

(c) Polar pattern at 10 m in pascal.

Figure F.3: FDTD simulation for a gain equal to 1

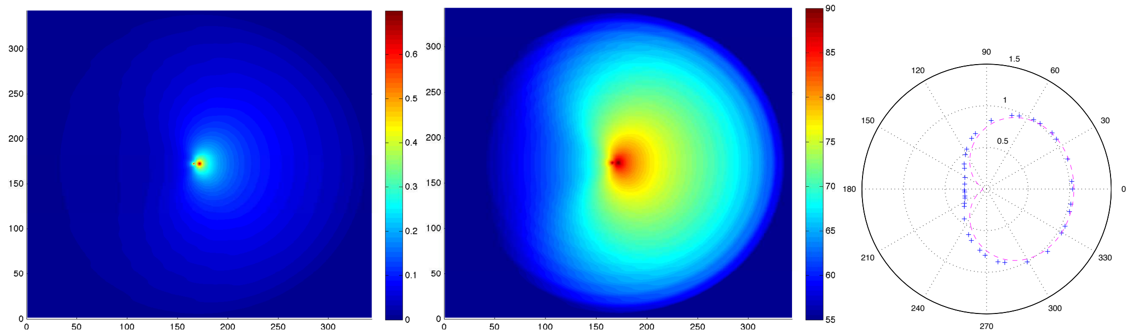

(a) RMS pressure field in pascal (b) RMS pressure field in dB SPL (c) Polar pattern at 10 m in pascal.

Figure F.4: FDTD simulation for a gain equal to 1.1

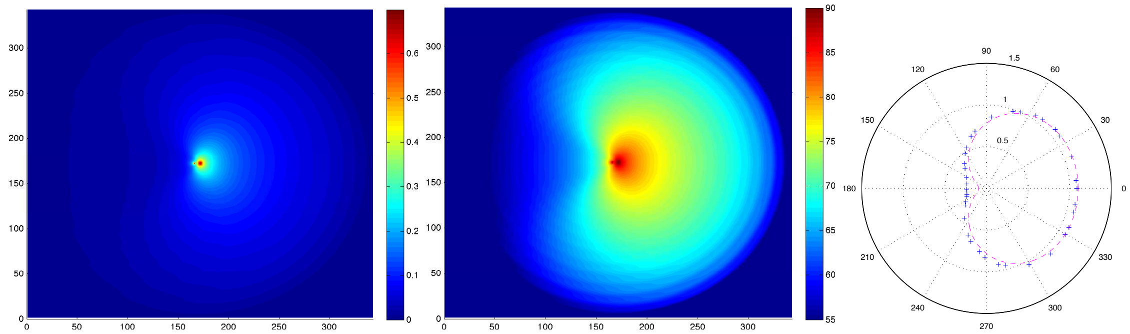

(a) RMS pressure field in pascal (b) RMS pressure field in dB SPL (c) Polar pattern at 10 m in pascal.

Figure F.5: FDTD simulation for a gain equal to 1.2

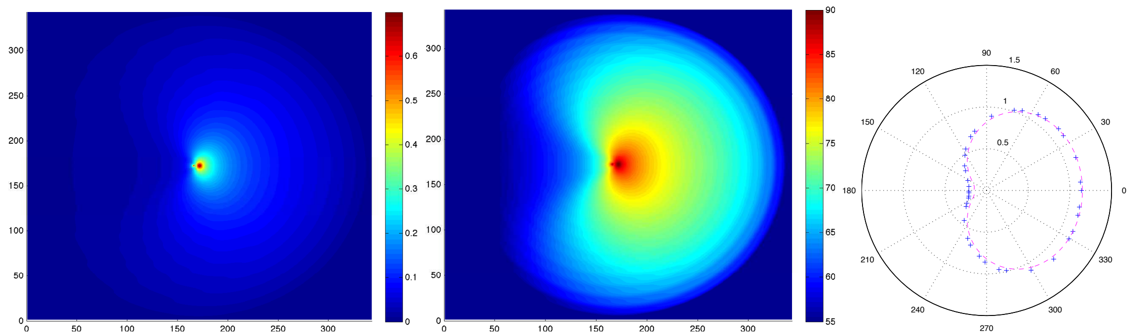

(a) RMS pressure field in pascal (b) RMS pressure field in dB SPL (c) Polar pattern at 10 m in pascal.

Figure F.6: FDTD simulation for a gain equal to 1.3

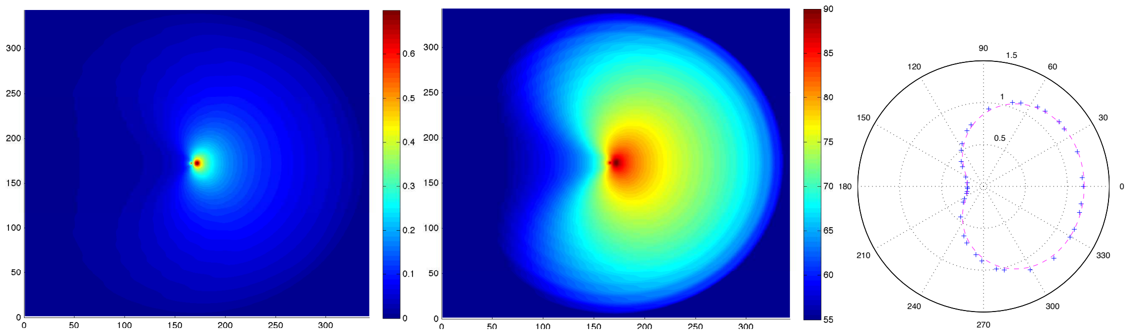

(a) RMS pressure field in pascal (b) RMS pressure field in dB SPL (c) Polar pattern at 10 m in pascal.

Figure F.7: FDTD simulation for a gain equal to 1.4

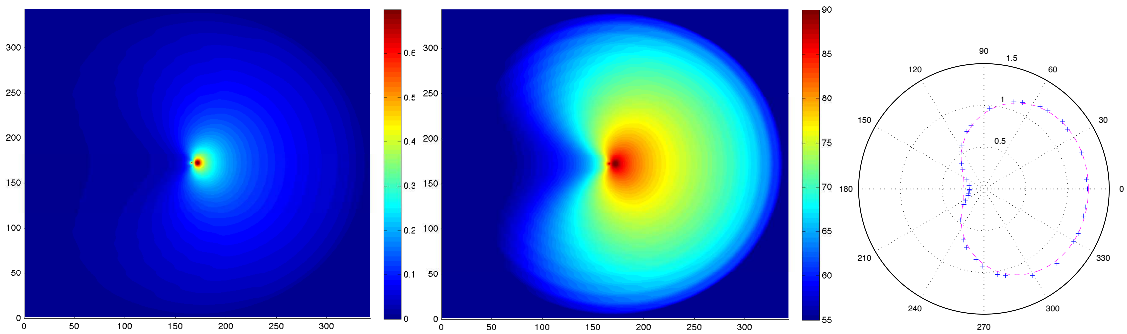

(a) RMS pressure field in pascal (b) RMS pressure field in dB SPL (c) Polar pattern at 10 m in pascal.

Figure F.8: FDTD simulation for a gain equal to 1.5

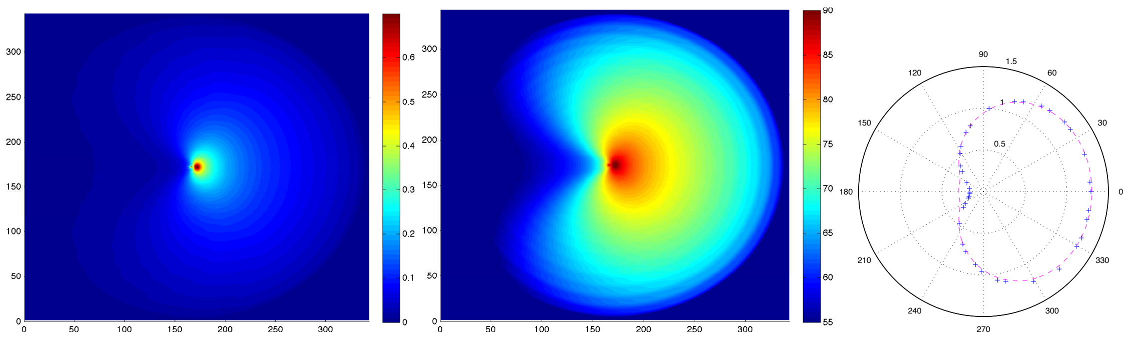

(a) RMS pressure field in pascal (b) RMS pressure field in dB SPL (c) Polar pattern at 10 m in pascal.

Figure F.9: FDTD simulation for a gain equal to 1.6

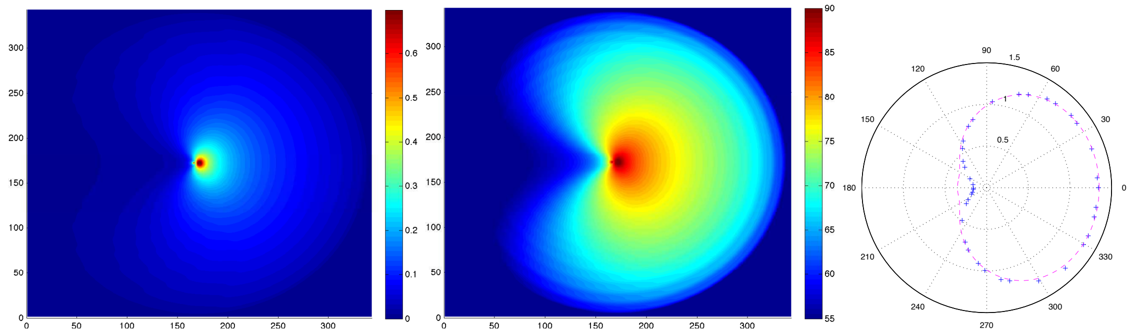

(a) RMS pressure field in pascal (b) RMS pressure field in dB SPL (c) Polar pattern at 10 m in pascal.

Figure F.10: FDTD simulation for a gain equal to 1.7

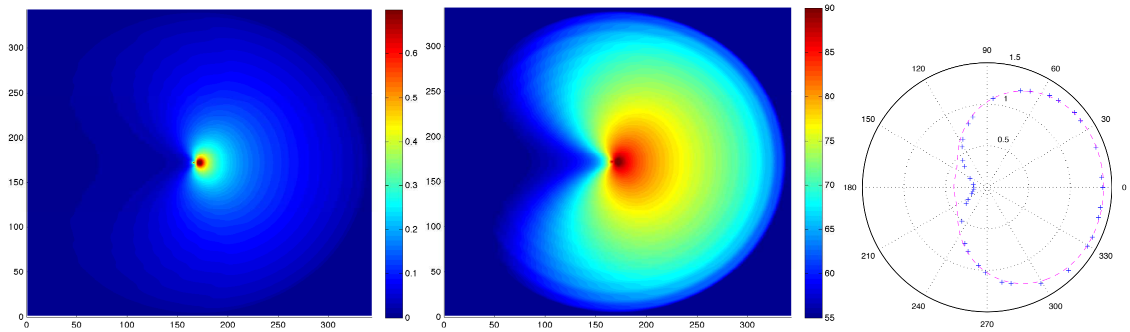

(a) RMS pressure field in pascal (b) RMS pressure field in dB SPL (c) Polar pattern at 10 m in pascal.

Figure F.11: FDTD simulation for a gain equal to 1.8

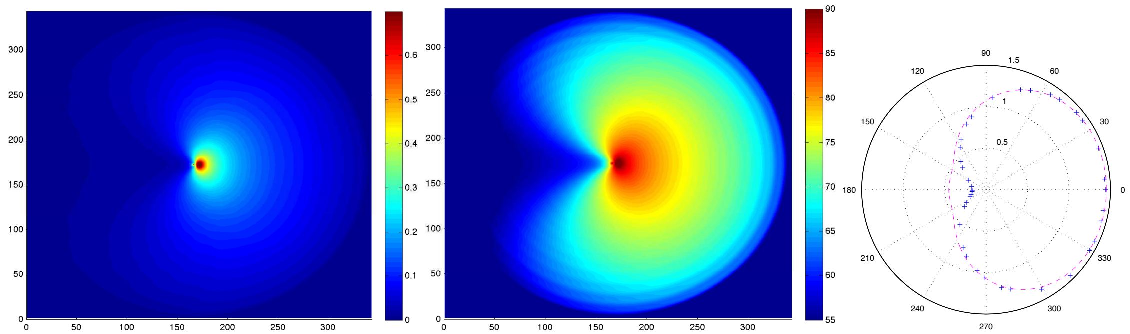

(a) RMS pressure field in pascal (b) RMS pressure field in dB SPL (c) Polar pattern at 10 m in pascal.

Figure F.12: FDTD simulation for a gain equal to 1.9

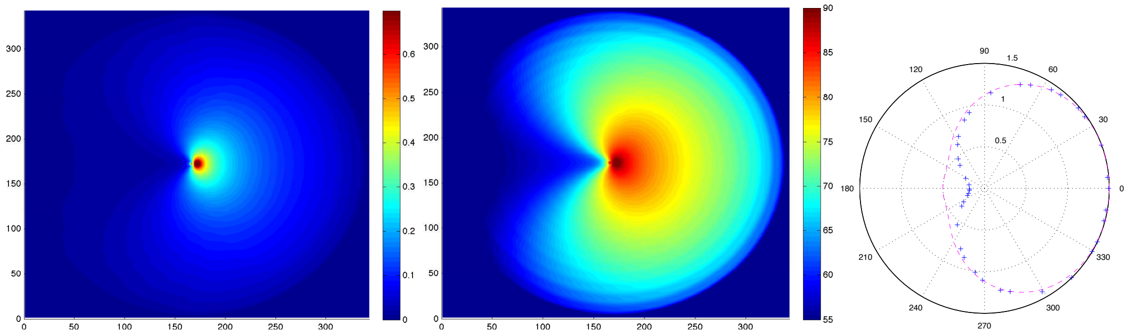

(a) RMS pressure field in pascal

(b) RMS pressure field in dB SPL

(c) Polar pattern at 10 m in pascal.

Figure F.13: FDTD simulation for a gain equal to 2

F.2.2 Case 2: $\frac{D}{\lambda} = \frac{d}{\lambda} = 0.125$

In these simulations, the distance between the sources is kept constant $D = 0.57m$, which corresponds to one fourth of the wavelength of 150 Hz. The delay applied on the back source is also $d = 0.57m$. The sound sources are defined as a pressure sources fed by a sinusoidal signal of frequency 75 Hz. The magnitude of the back subwoofer varies between -1 and 1. The magnitude of the front subwoofer varies from -1 to 1 times the value of the gain. One runs the FDTD simulations for different values of gain. For each simulation one plots three figures: the RMS pressure in pascal, the RMS pressure in dB SPL and the the polar pattern extracted from the FDTD simulation following to the explanations of subsection 5.6.1. On this last one the dashed line represents the analytical result of subsection 9.2.2 and the blue cross the polar pattern extracted from the FDTD simulation

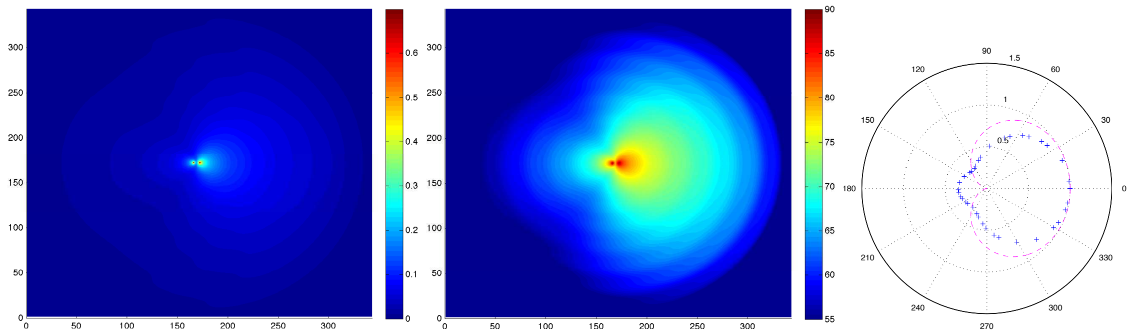

(a) RMS pressure field in pascal (b) RMS pressure field in dB SPL (c) Polar pattern at 10 m in pascal.

Figure F.14: FDTD simulation for a gain equal to 1

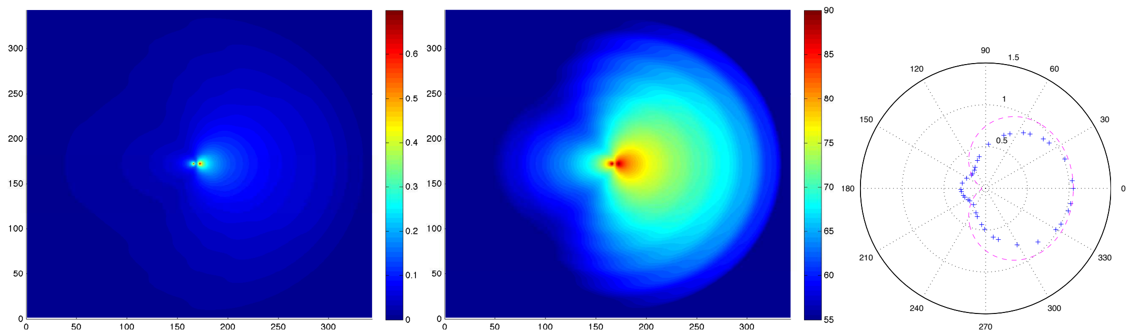

(a) RMS pressure field in pascal (b) RMS pressure field in dB SPL (c) Polar pattern at 10 m in pascal.

Figure F.15: FDTD simulation for a gain equal to 1.1

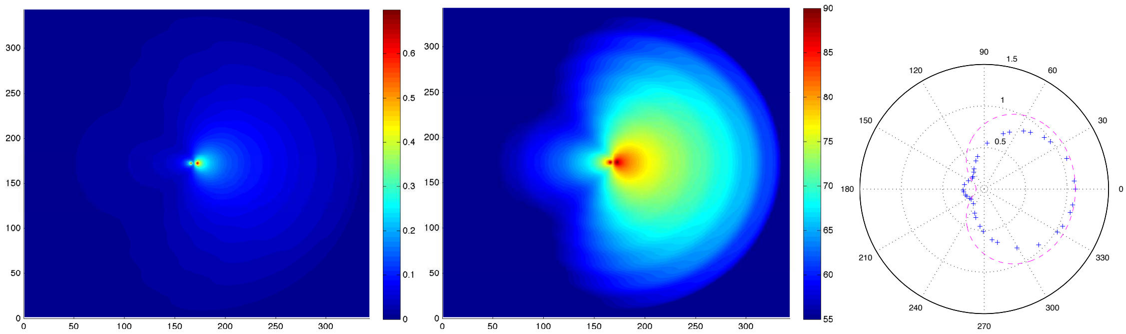

(a) RMS pressure field in pascal

(b) RMS pressure field in dB SPL

(c) Polar pattern at 10 m in pascal.

Figure F.16: FDTD simulation for a gain equal to 1.2

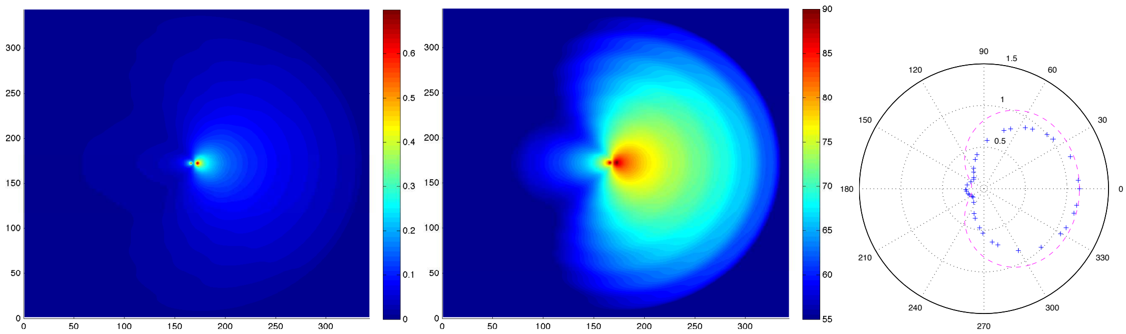

(a) RMS pressure field in pascal

(b) RMS pressure field in dB SPL

(c) Polar pattern at 10 m in pascal.

Figure F.17: FDTD simulation for a gain equal to 1.3

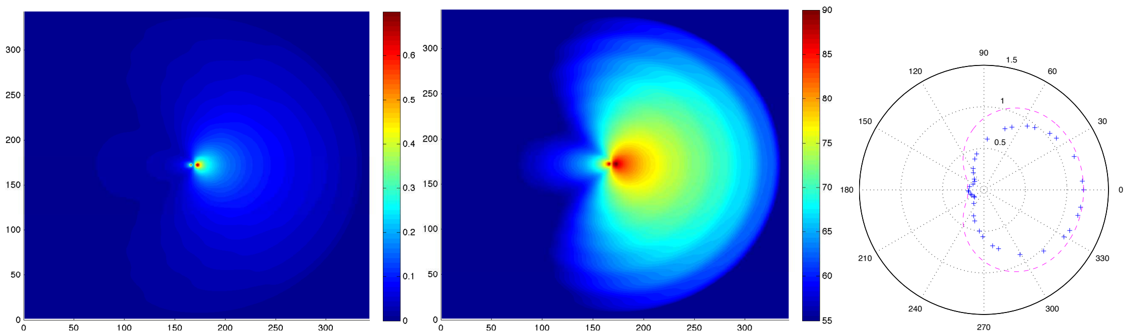

(a) RMS pressure field in pascal

(b) RMS pressure field in dB SPL

(c) Polar pattern at 10 m in pascal.

Figure F.18: FDTD simulation for a gain equal to 1.4

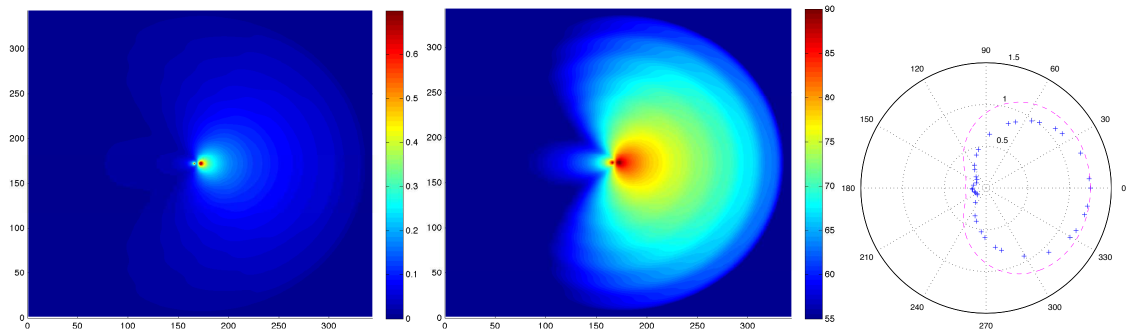

(a) RMS pressure field in pascal

(b) RMS pressure field in dB SPL

(c) Polar pattern at 10 m in pascal.

Figure F.19: FDTD simulation for a gain equal to 1.5

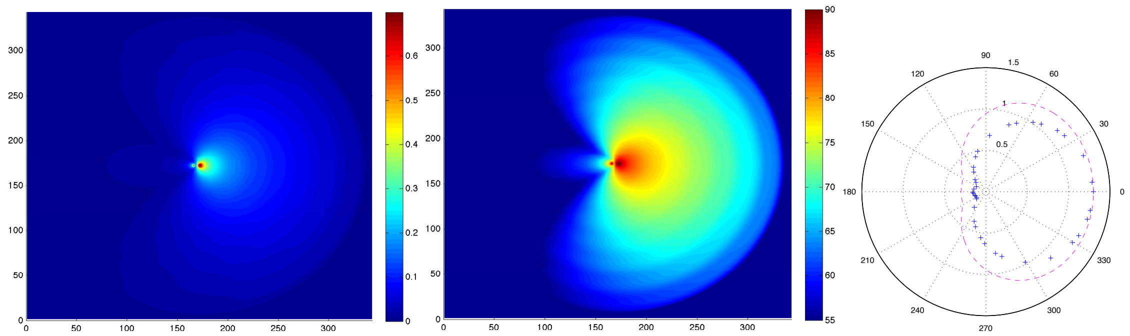

(a) RMS pressure field in pascal

(b) RMS pressure field in dB SPL

(c) Polar pattern at 10 m in pascal.

Figure F.20: FDTD simulation for a gain equal to 1.6

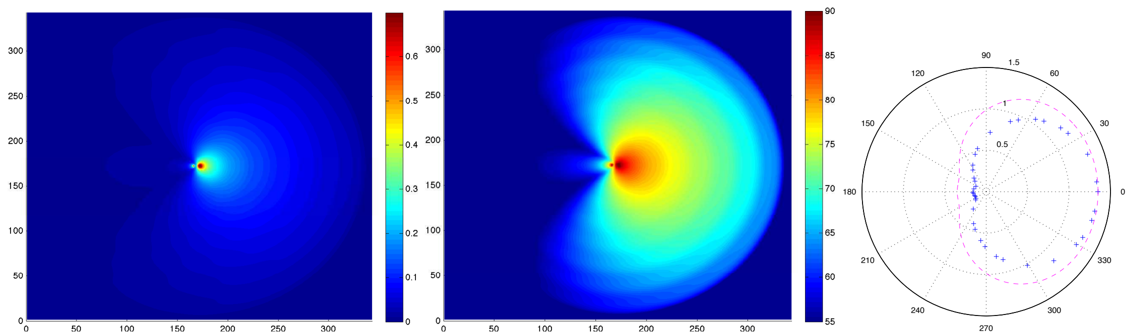

(a) RMS pressure field in pascal

(b) RMS pressure field in dB SPL

(c) Polar pattern at 10 m in pascal.

Figure F.21: FDTD simulation for a gain equal to 1.7

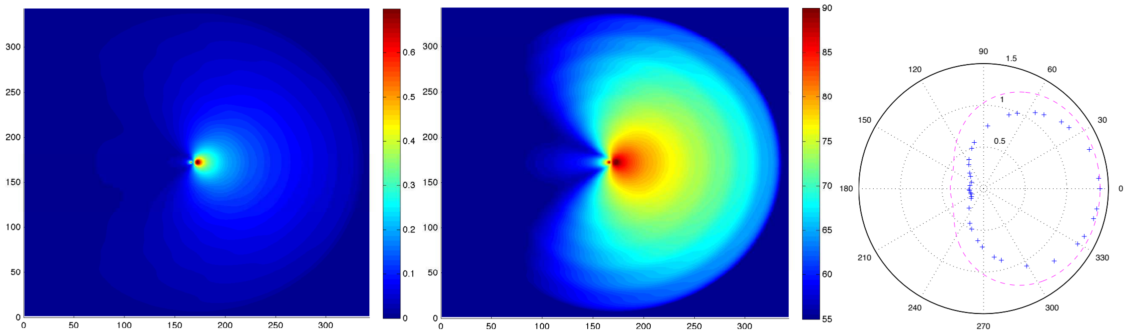

(a) RMS pressure field in pascal (b) RMS pressure field in dB SPL (c) Polar pattern at 10 m in pascal.

Figure F.22: FDTD simulation for a gain equal to 1.8

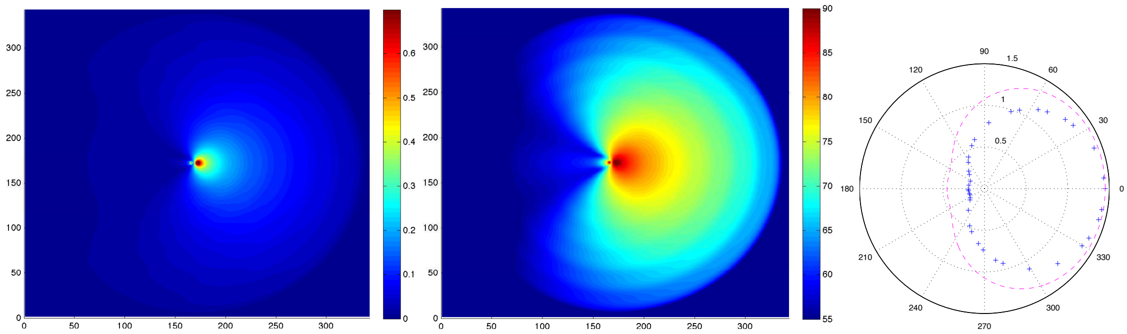

(a) RMS pressure field in pascal (b) RMS pressure field in dB SPL (c) Polar pattern at 10 m in pascal.

Figure F.23: FDTD simulation for a gain equal to 1.9

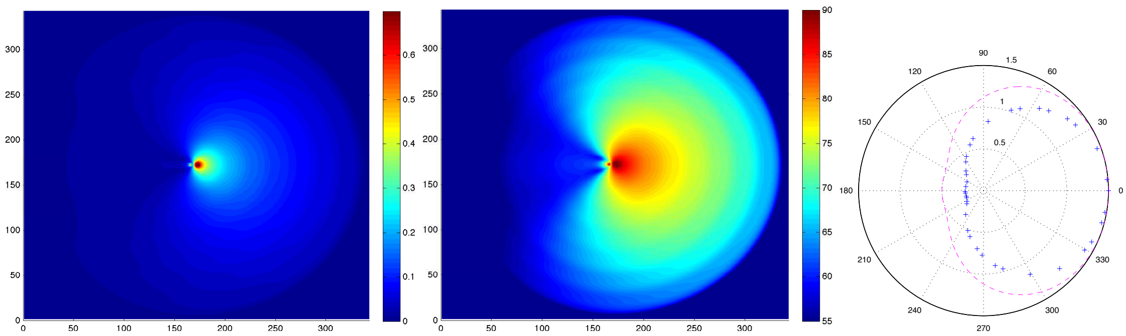

(a) RMS pressure field in pascal (b) RMS pressure field in dB SPL (c) Polar pattern at 10 m in pascal.

Figure F.24: FDTD simulation for a gain equal to 2

F.3 Simulation: FDTD simulations

In this section the FDTD method is used to simulate the behavior of a first order gradient sound source-unidirectional using the impulse response of a real subwoofer with the frequency dependent delay filter designed in chapter applied on the back subwoofer and three different values of gain-difference applied between the front and back subwoofer.

The characteristics of the subwoofer and particularly its impulse response are the same than in the subsection 6.2.1.

The cell size and the time step size are also the same than for the simulations of chapter 6 with respect to the discussions of subsections 6.2.2 and 6.2.3. So it gives a cell size of 0.2 m and a sampling frequency of 8000 Hz. The cardioid frequency is equal to 150 Hz giving a distance between the subwoofers equal to $D = \frac{c}{4 \times 150} = 0.57$ m (with $c = 343 m.s^{-1}$).

Figures F.25 to F.25 show in parallel the pressure field at different discrete frequencies:

- For a setup where both subwoofer have the same gain (left column)
- For a setup where the front subwoofer is 3 dB louder than the back subwoofer (middle column)
- For a setup where the front subwoofer is 4.7 dB louder than the back subwoofer (right column)

Each subfigure represents the pressure in dB SPL. The scale on the x-axis and y-axis represents the indexes in the FDTD grid.

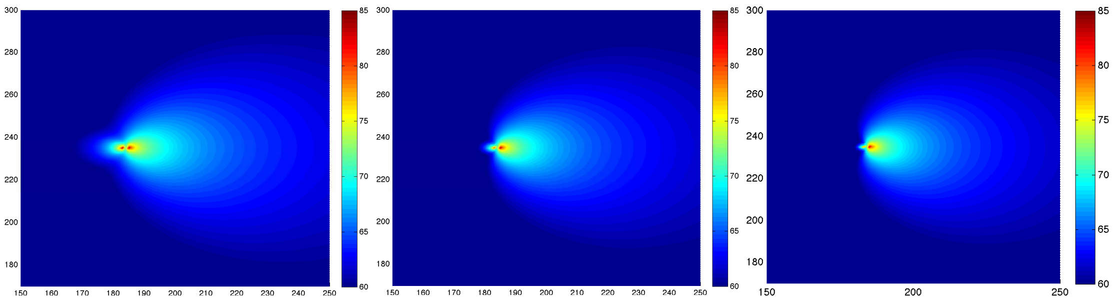

(a) Same gain on both subwoofers (b) 3 dB gain difference (c) 4.7 dB gain difference

Figure F.25: Pressure field at 40 Hz for three different values of gain-difference between the front and the back subwoofer. The results are expressed in dB SPL

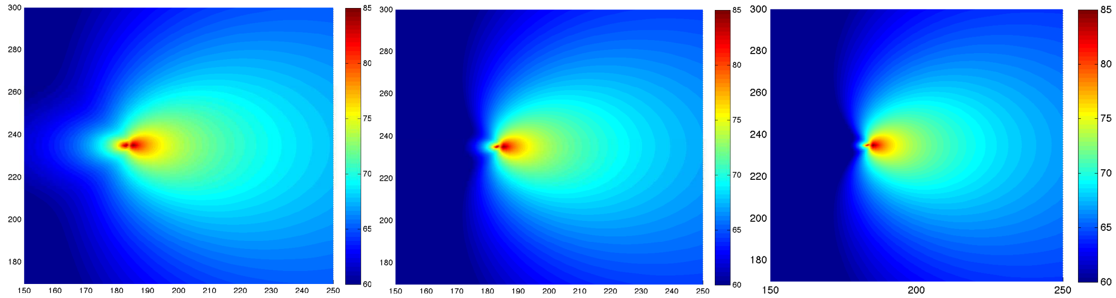

(a) Same gain on both subwoofers (b) 3 dB gain difference (c) 4.7 dB gain difference.

Figure F.26: Pressure field at 50 Hz for three different values of gain-difference between the front and the back subwoofer. The results are expressed in dB SPL

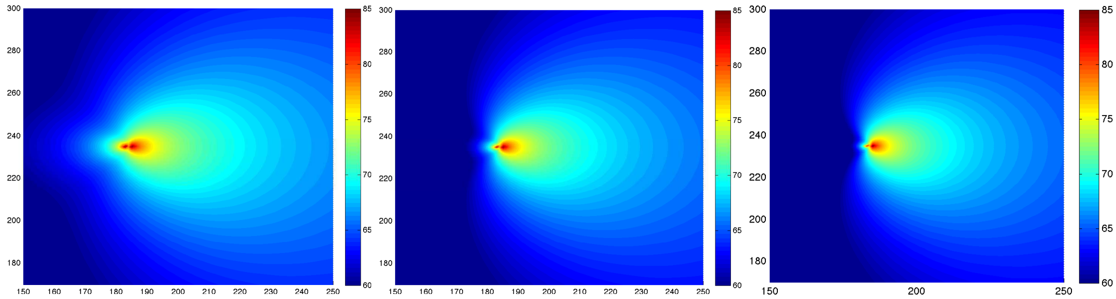

(a) Same gain on both subwoofers (b) 3 dB gain difference (c) 4.7 dB gain difference

Figure F.27: Pressure field at 60 Hz for three different values of gain-difference between the front and the back subwoofer. The results are expressed in dB SPL

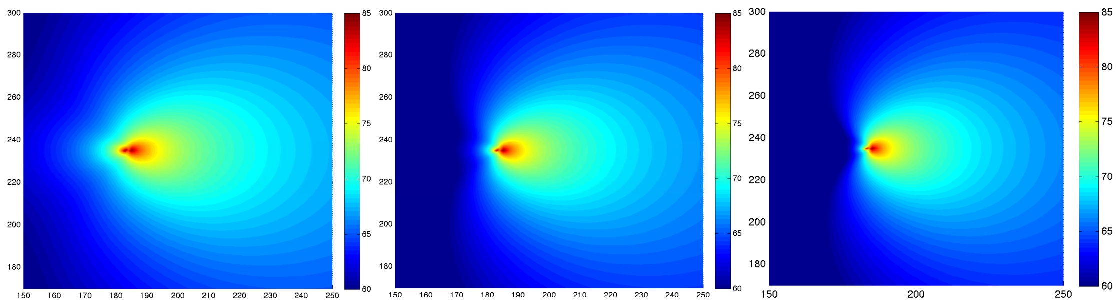

(a) Same gain on both subwoofers (b) 3 dB gain difference (c) 4.7 dB gain difference

Figure F.28: Pressure field at 80 Hz for three different values of gain-difference between the front and the back subwoofer. The results are expressed in dB SPL

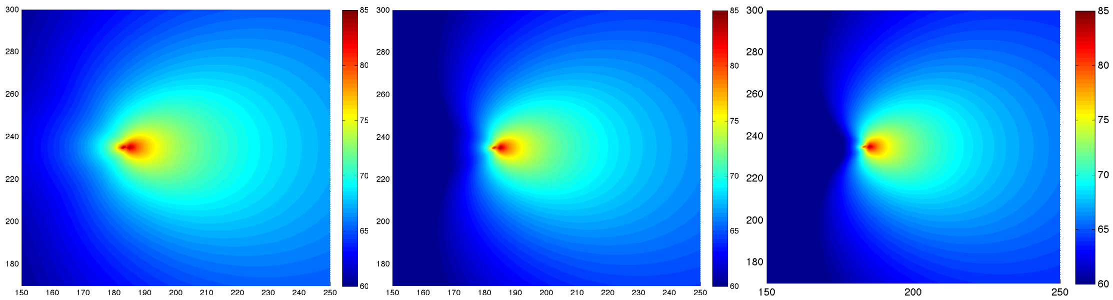

(a) Same gain on both subwoofers (b) 3 dB gain difference (c) 4.7 dB gain difference

Figure F.29: Pressure field at 100 Hz for three different values of gain-difference between the front and the back subwoofer. The results are expressed in dB SPL

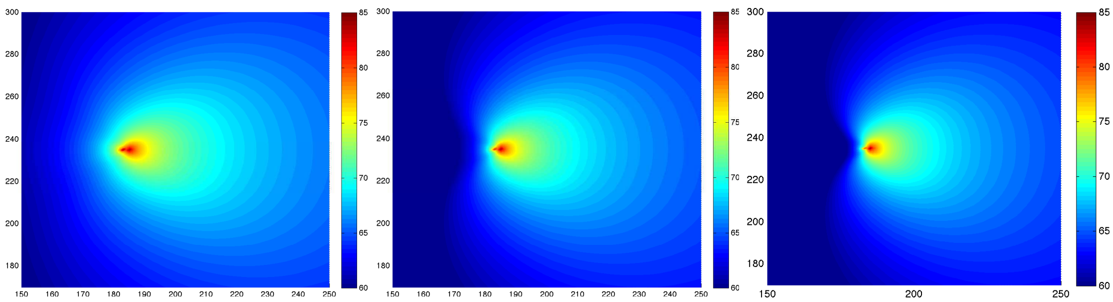

(a) Same gain on both subwoofers (b) 3 dB gain difference (c) 4.7 dB gain difference

Figure F.30: Pressure field at 120 Hz for three different values of gain-difference between the front and the back subwoofer. The results are expressed in dB SPL

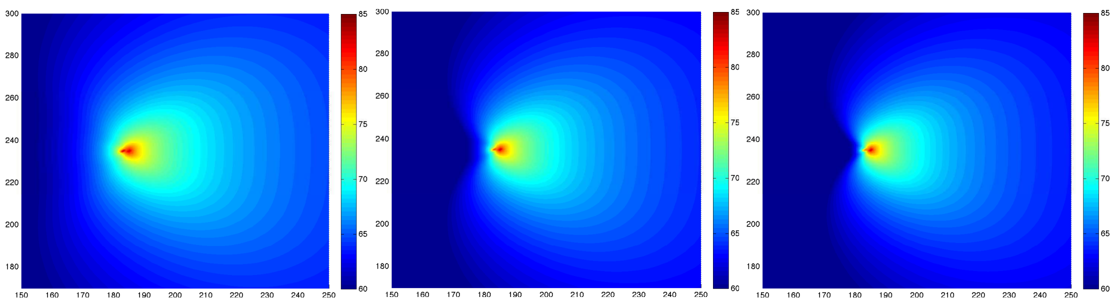

(a) Same gain on both subwoofers (b) 3 dB gain difference (c) 4.7 dB gain difference

Figure F.31: Pressure field at 150 Hz for three different values of gain-difference between the front and the back subwoofer. The results are expressed in dB SPL

G

Pressure field measurement

In this appendix the procedure for measuring the impulse response generated by different setups of subwoofers in a pseudo free field is described.

G.1 Equipment

Item	Type	AAU LBNR/SN
Loudspeaker 1	DALI SWA-8 Active subwoofer	61415
Loudspeaker 2	DALI SWA-8 Active subwoofer	61416
Microphone	BK 4133	06548
Preamplifier	BK 2619	07798
Measuring amplifier	BK 2636	08415
Sound card	M-Audio Fast Track Pro	257Z07300038D3

G.2 Setup

G.2.1 Block Diagram

The setup used to measure the impulse response of the different subwoofer configurations is presented in figure G.1.

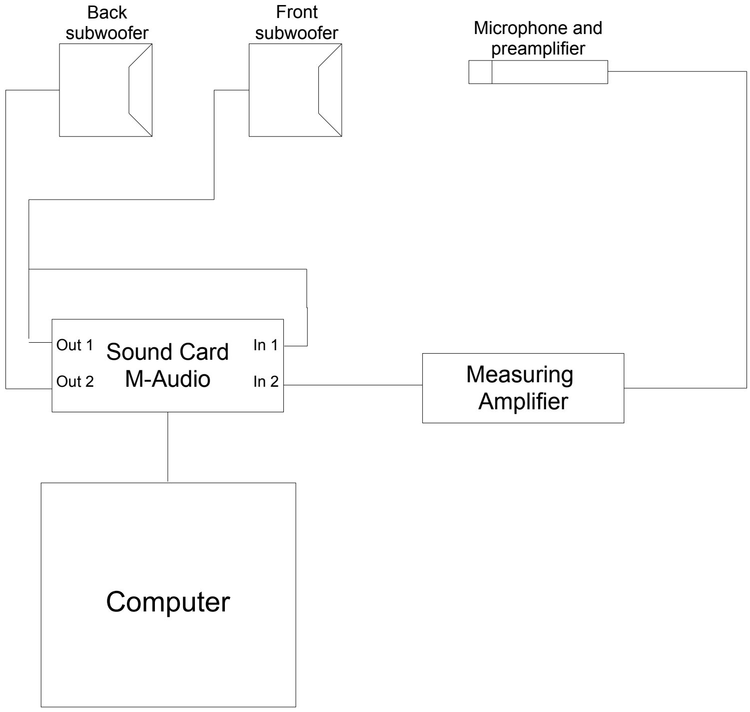

Figure G.1: Block diagram of the setup used for measuring the impulse response of the different subwoofer setups

G.2.2 Microphone positions

The microphone is positioned on the ground in order to limit the reflection effects of the floor. 126 microphone positions are defined to measure the impulse response of the subwoofer setups as shown on figure G.2. These positions formed a grid whose cell size is 1 meter (with an approximation of ± 3 cm). The grid has been drawn previously on the floor.

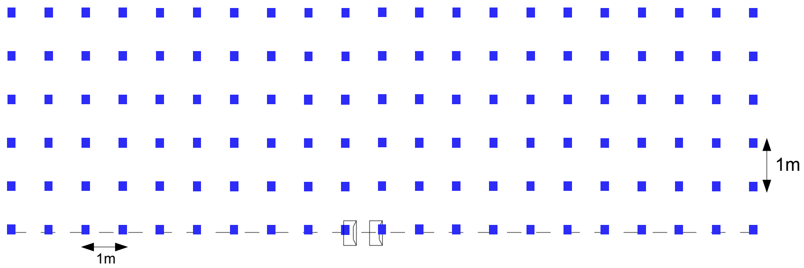

Figure G.2: Grid for the measurements. Each blue point represents a microphone position.

Starting on the axis formed by both subwoofers, the first microphone position is at 20 cm from the membrane of the front subwoofer. Then, from this first microphone position one defines 10 positions in the front of the subwoofers setup and 10 positions in the back with 1 meter difference between each position. When these first 21 microphone positions are defined, one translates them ten times by step of one meter on the side of the subwoofers to finally obtain the microphone grid of figure G.2.

G.2.3 Subwoofer position

According to the recommendations previously discussed in subsection 10.2.2 the subwoofers are kept on the ground. To fit with the simulations made in chapters 6 8.4, 9.3.2 and the characteristics of the filter designed in chapter 8.4, the frequency of 150 Hz is chosen as the cardioid frequency. Therefore the distance between both subwoofer is $D = \frac{\lambda_{150Hz}}{4} = 0.57\text{m}$. Figure G.3 shows a picture of the subwoofer setup.

Figure G.3: Subwoofer setup during the measurements with the microphone at the closest position (20 cm).

G.2.4 Equipments parameters

Subwoofers

The DALI subwoofers have three buttons for changing the gain, the cutting frequency of the embedded low pass filter and the phase (shift from 0° to 180°).

The gain potentiometer is set to the maximum value on both subwoofers. The frequency potentiometer that changes the cutting frequency of the embedded low pass filter is set to 150 Hz on both subwoofers so that they play with the widest bandwidth allowed. The measured setup is based on a first order gradient source-unidirectional. For such setup the back subwoofer has its polarity inverted compared to the front subwoofer. Therefore the polarity switch on the front subwoofer is set to 0° and the one of the back subwoofer is set to 180°

Matlab signal

For the measurements Matlab is used to generate the signals that are played in the subwoofers and to record the signal measured by the microphone for finally obtain the impulse response at the different positions.

Signal: The signal for all the measurements of this project is a Maximum Length Sequence (MLS) signal of order 16th giving 65535 samples. The sampling frequency is chosen equal to 48000 Hz so it produces a signal of 1.36 seconds. As the measurements are conducted outside they could be affected by different punctual noises that would modify the results from one position to another. Indeed the techniques consisting of using MLS signal and cross-correlation to obtain the impulse response of a system is very sensitive to non-stationary process. Therefore it is decided to repeat this MLS signal 15 times for each of the five subwoofer configurations introduced in section 10.1. Repeating 15 times this MLS sequence gives measurements over a time of 20 seconds. So the impulse response obtained is equal to the mean of the 15 impulse responses. This number of 15 repetitions has been chosen arbitrarily and is a trade-off between measuring the MLS response of the system over a long period and having a computational time when calculating the cross-correlation in Matlab which is reasonable.

The MLS signal is then used as a base to obtain the different filtered and delayed signals applied on the front and back subwoofers.

Input signal: Two input signals are recorded with Matlab during the measurements.

As shown on figure G.1 the input 1 is directly linked with the output feeding the front subwoofer. The purpose of this connection is to remove the nonlinearities of the AD and DA convertors of the sound card. Indeed the signal feeding this input will be then considered as the reference MLS signal for the cross-correlation with the signal measured by the microphone. A such loop is allowed because the signal send to the front subwoofer corresponds to the original MLS signal.

The second input of the sound card receives the signal measured by the microphone.

Cross-correlation: To obtain the impulse response of the different subwoofer configurations one computes the the cross-correlation between the reference MLS signal recorded on the first input of the sound card and the MLS signal measured by the microphone. The cross-correlation is performed with the 9830 25 samples recorded by both inputs. This number of samples corresponds to the length of a MLS signal of 16th order multiplied by 15. The results obtained after the cross-correlation contains the main impulse response of the system and all the reflections coming from the walls around. Therefore one must extract the main impulse response before applying more signal processing tools.

Measuring Amplifier

The measuring amplifier B&K 2636 has some embedded high pass and low pass filter that can be commuted or bypassed depending on the application. In the case of the measurements conducted in this project, it is decided to apply the high pass filter of 22.1 Hz is order to limit the amount of low frequency background noise, especially wind, measured. The low pass filter (22.1 kHz) of the measuring amplifier is also applied to avoid any aliasing. One reminds that the sampling frequency of the signal is 48000 so applying this low pass filter let to respect the theorem of Nyquist.

The input gain and output gain of the measuring amplifier are set to 10 dB and 10 dB respectively.

G.2.5 Method

When the subwoofers have been positioned on the floor and all the microphone positions indicated on the floor as well, one measures for each microphone position the pressure field generated when five different kind of signals feed the subwoofers. In the order these signals are:

- Front subwoofer fed with the original MLS signal and back subwoofer muted.
- Front subwoofer fed with the original MLS signal and back subwoofer fed by the original MLS signal delayed and inverted in polarity. The delay applied is equal to 80 samples, which corresponds to 0.0017 sec or 0.57 m (one fourth of the wavelength of 150 Hz) with a sampling frequency of 48000 Hz.
- Front subwoofer fed with the original MLS signal and back subwoofer fed with the MLS signal filtered by the filter designed in chapter 8.4 and with inverted polarity.
- Front subwoofer fed with the original MLS signal and back subwoofer fed with the MLS signal filtered by the filter designed in chapter 8.4, inverted polarity and with a gain reduction of 3 dB.
- Front subwoofer fed with the original MLS signal and back subwoofer fed with the MLS signal filtered by the filter designed in chapter 8.4, inverted polarity and with a gain reduction of 4.5 dB.

These 5 configurations are measured in row without moving the microphone. The microphone is only moved to another position when the five measurements have been completed.

G.3 Results

In this section one displays the results obtained for the five different configurations previously quoted. The impulse responses used to make the FFT and obtain figures G.4, G.5, G.6, G.7 and G.8 have 16000 points and their sampling frequency is 48000 Hz. The results are expressed in dB. The scales of the x and y axis are in meter. One will be aware in the comments that the plot obtained with matlab are represented in a square whereas the measurement area is rectangular. So the results are compressed along the x-axis.

G.3.1 Front subwoofer playing alone

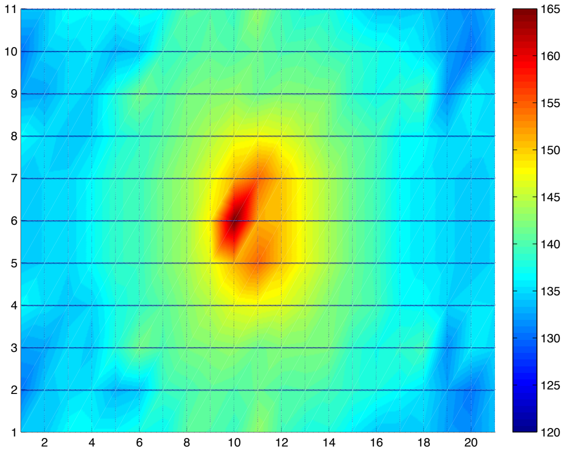

(a) $f = 40Hz$

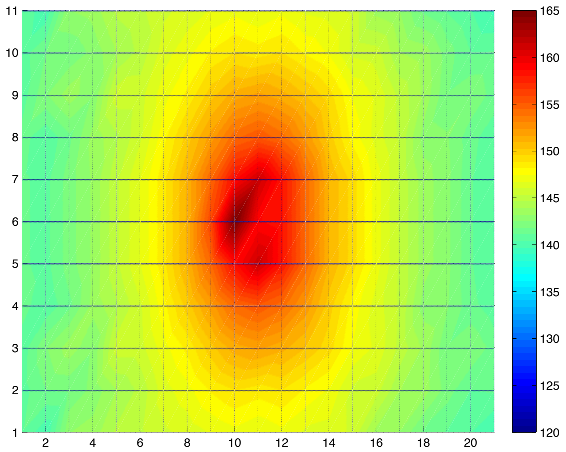

(b) $f = 50Hz$

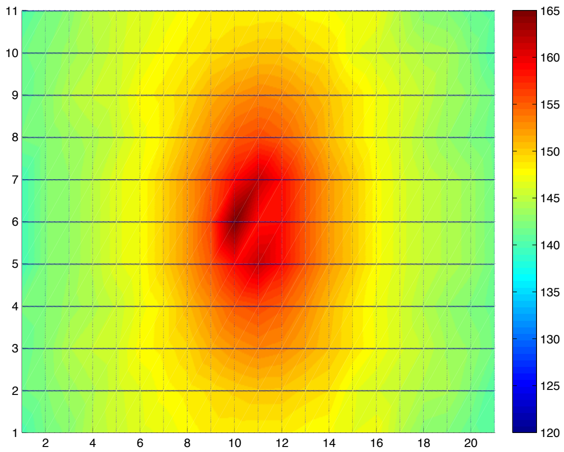

(c) $f = 60Hz$

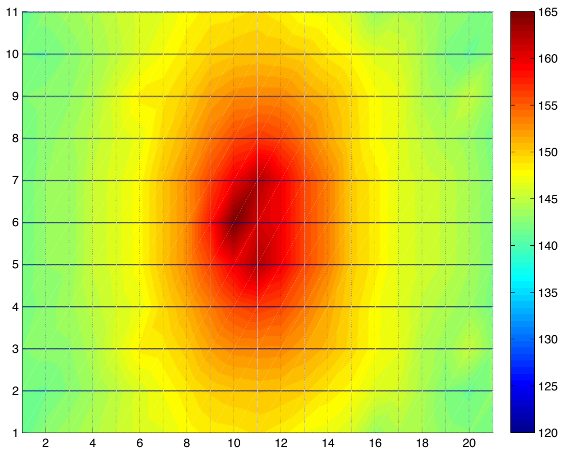

(d) $f = 80Hz$

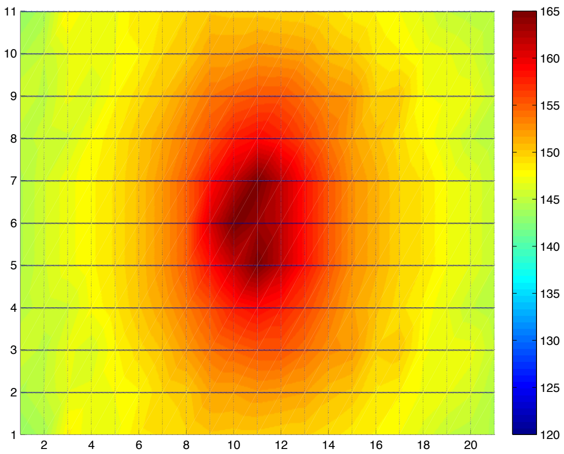

(e) $f = 100Hz$

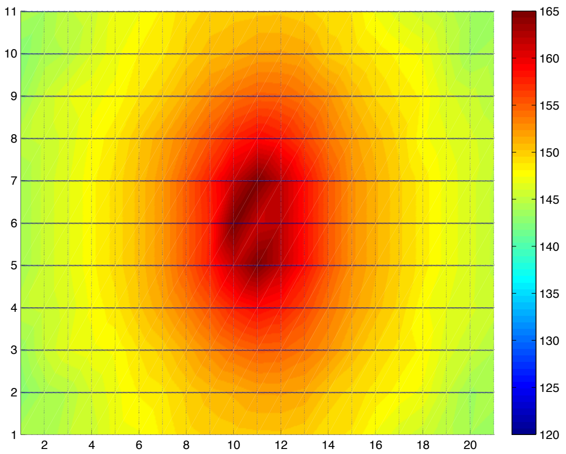

(f) $f = 120Hz$

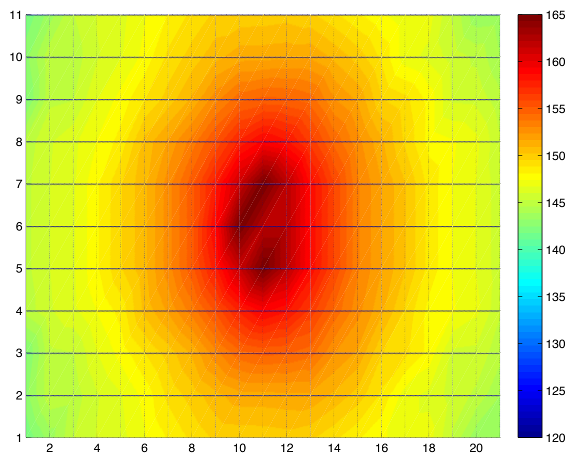

(g) $f = 150Hz$

Figure G.4: Measured pressure field at different discrete frequencies

G.3.2 Cardioid subwoofer without extra processing

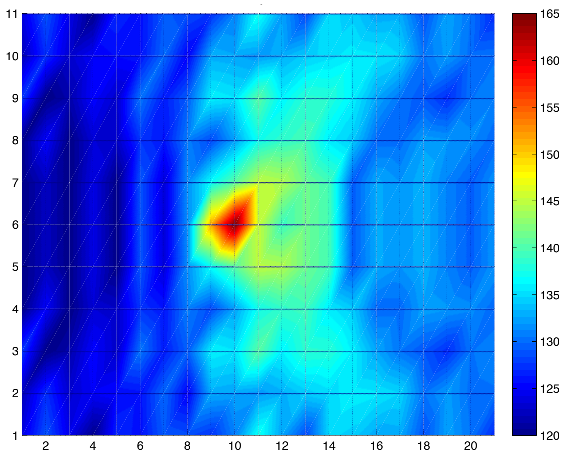

(a) $f = 40Hz$

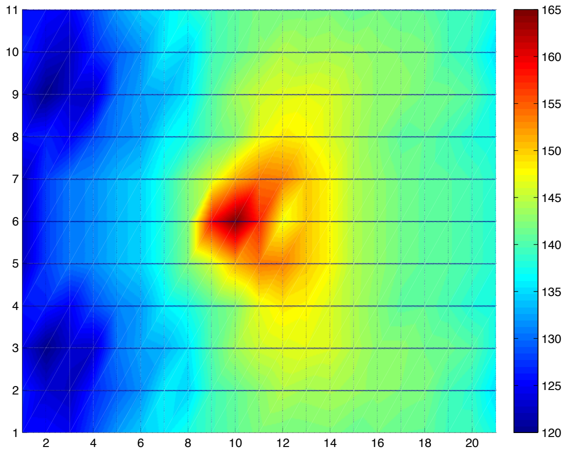

(b) $f = 50Hz$

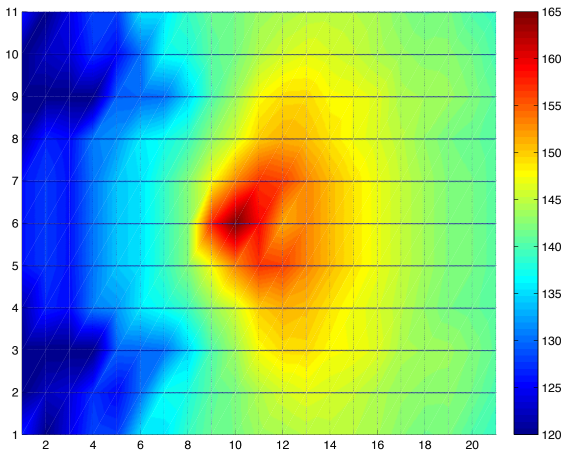

(c) $f = 60Hz$

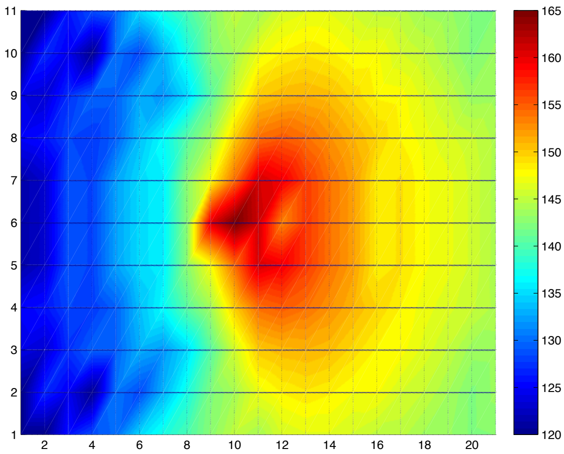

(d) $f = 80Hz$

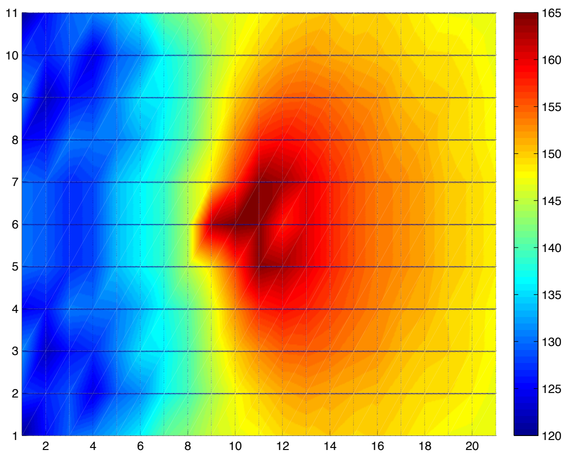

(e) $f = 100Hz$

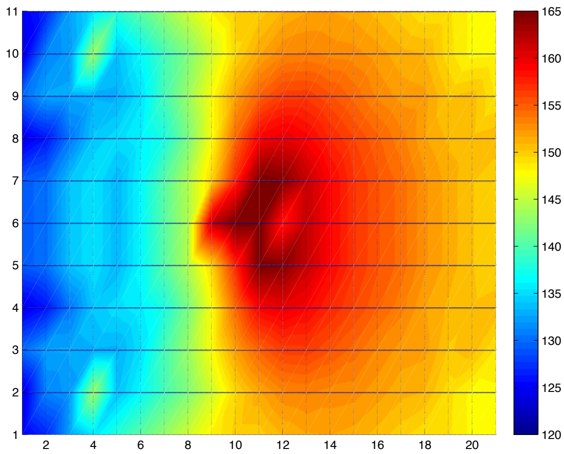

(f) $f = 120Hz$

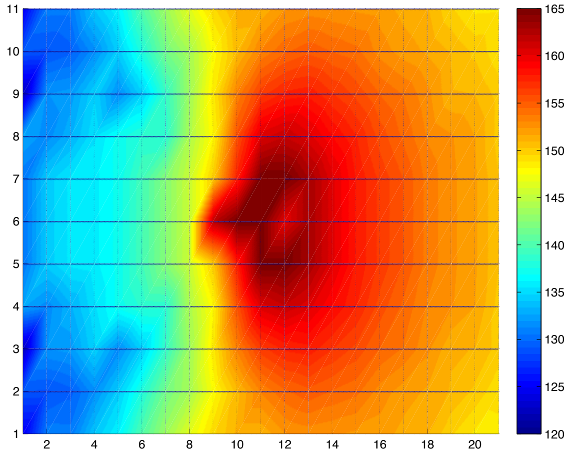

(g) $f = 150Hz$

Figure G.5: Measured pressure field at different discrete frequencies

G.3.3 Cardioid subwoofer with IIR all pass filter on the back subwoofer

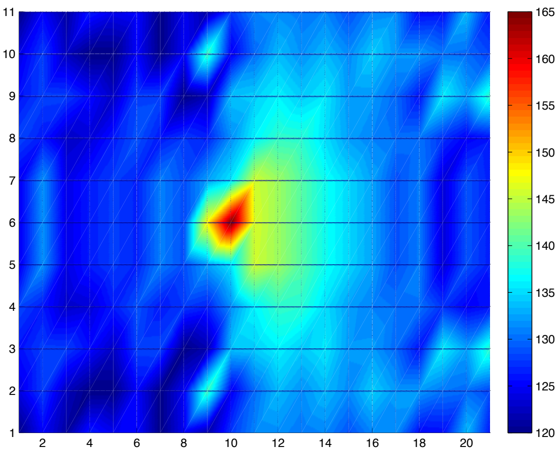

(a) $f = 40Hz$

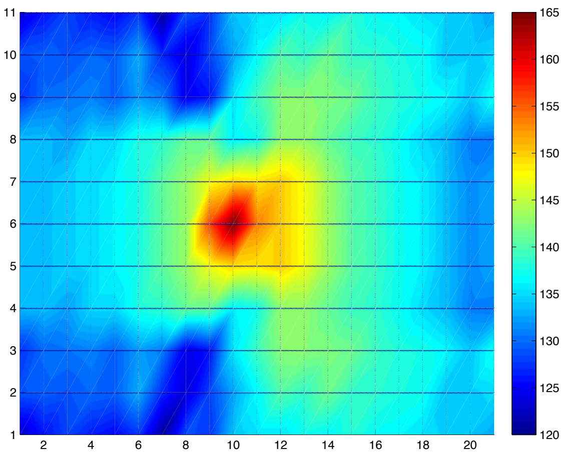

(b) $f = 50Hz$

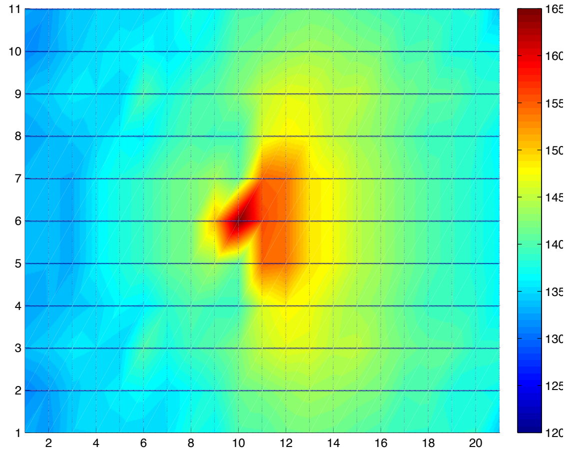

(c) $f = 60Hz$

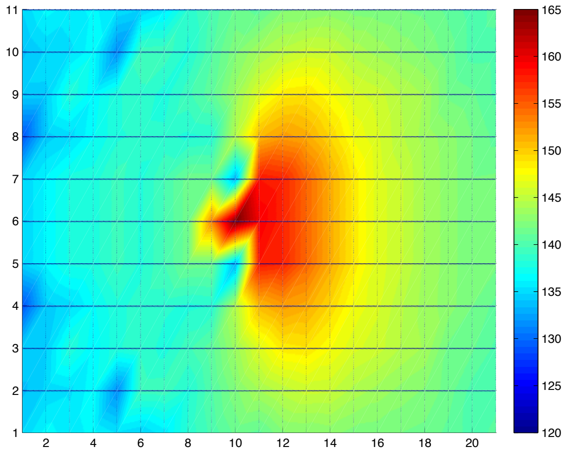

(d) $f = 80Hz$

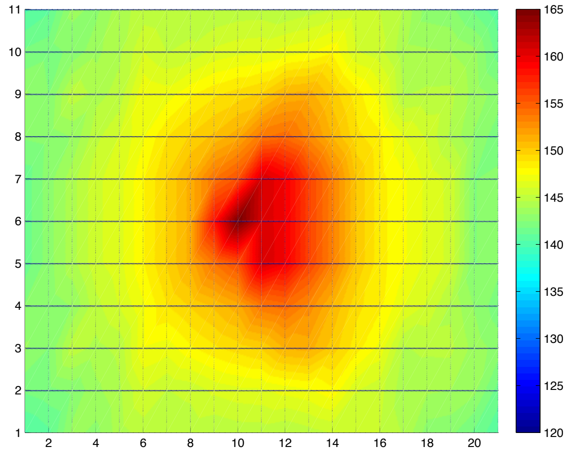

(e) $f = 100Hz$

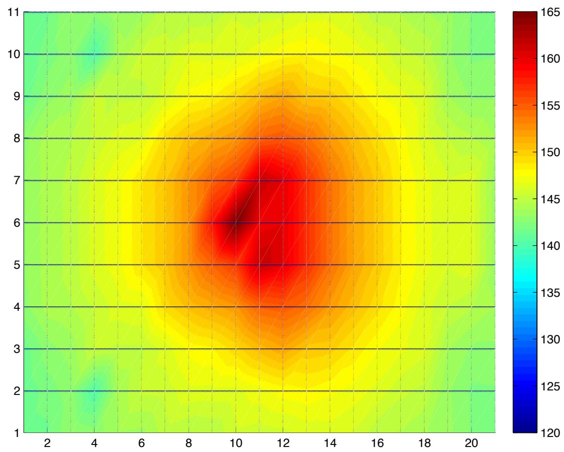

(f) $f = 120Hz$

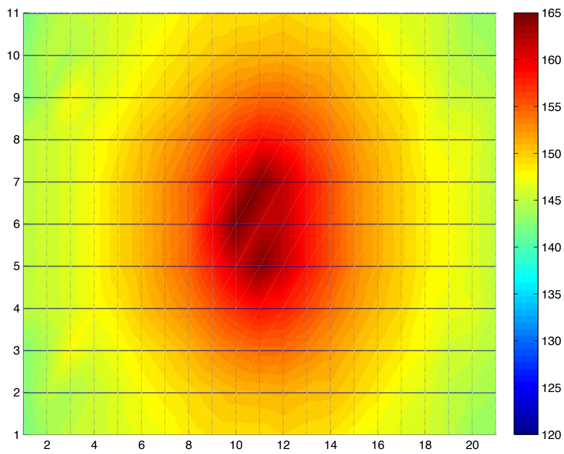

(g) $f = 150Hz$

Figure G.6: Measured pressure field at different discrete frequencies

G.3.4 Cardioid subwoofer with IIR all pass filter on the back subwoofer and a difference of 3 dB between both subwoofers

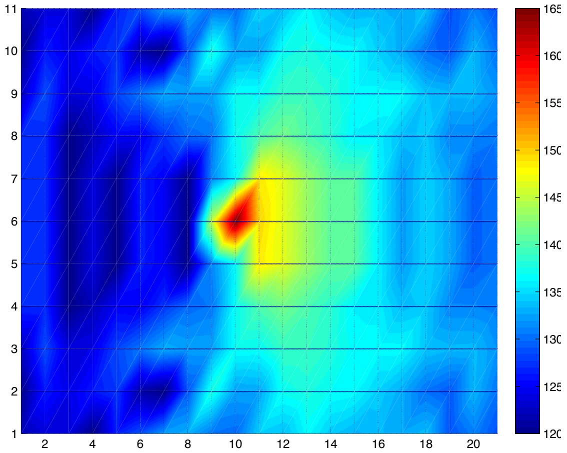

(a) $f = 40Hz$

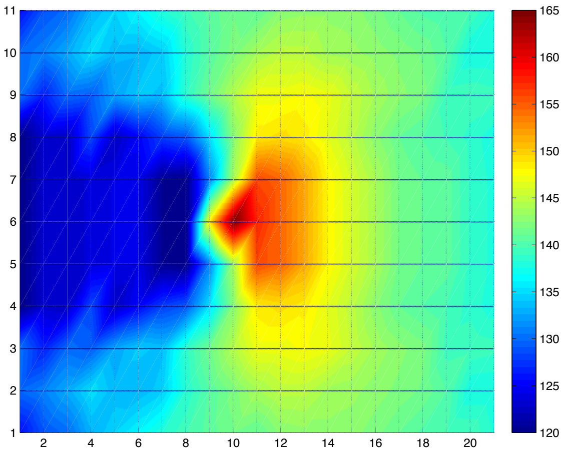

(b) $f = 50Hz$

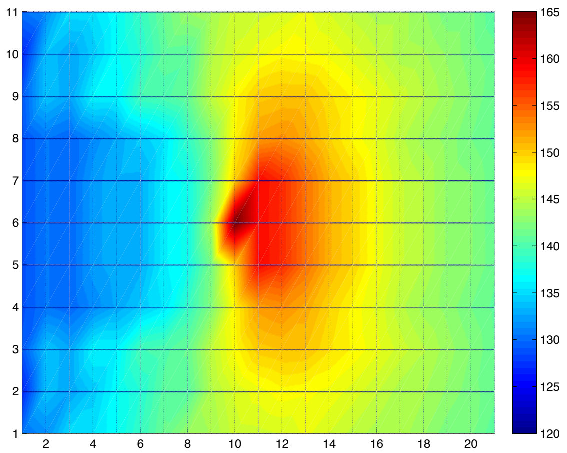

(c) $f = 60Hz$

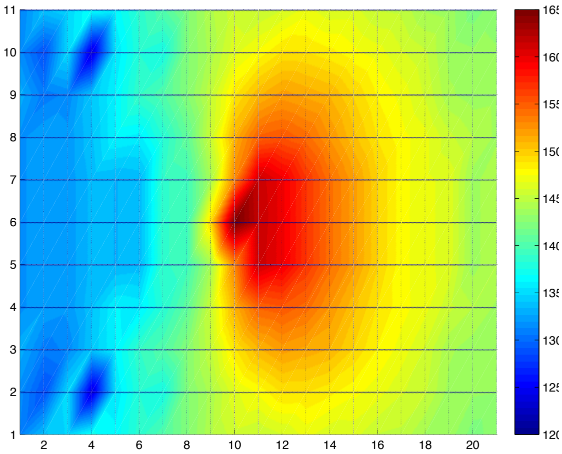

(d) $f = 80Hz$

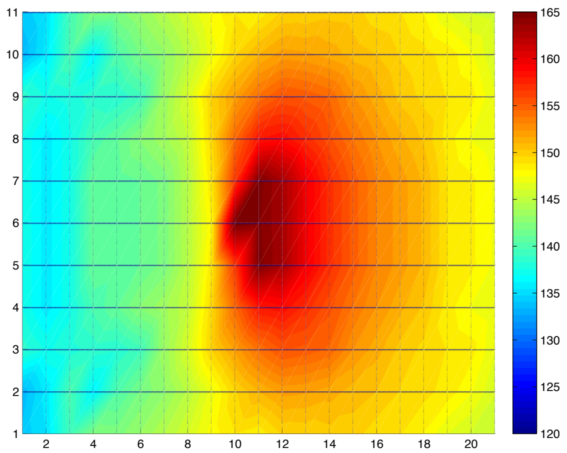

(e) $f = 100Hz$

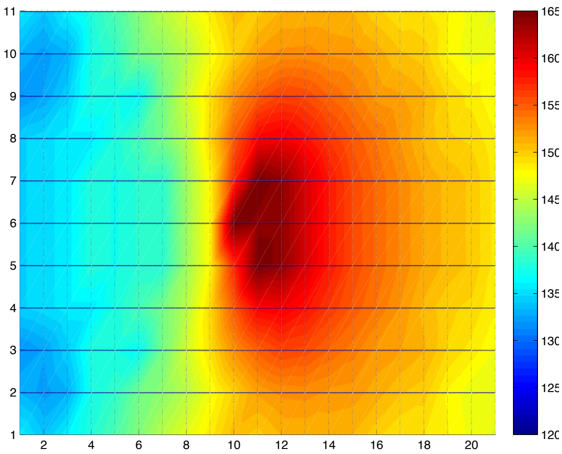

(f) $f = 120Hz$

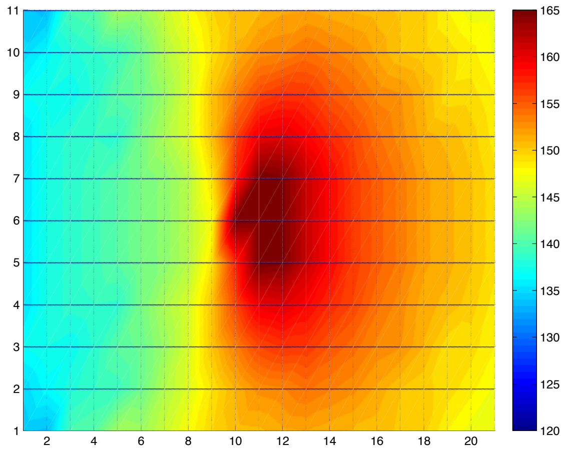

(g) $f = 150Hz$

Figure G.7: Measured pressure field at different discrete frequencies

G.3.5 Cardioid subwoofer with IIR all pass filter on the back subwoofer and a difference of 4.7 dB between both subwoofers

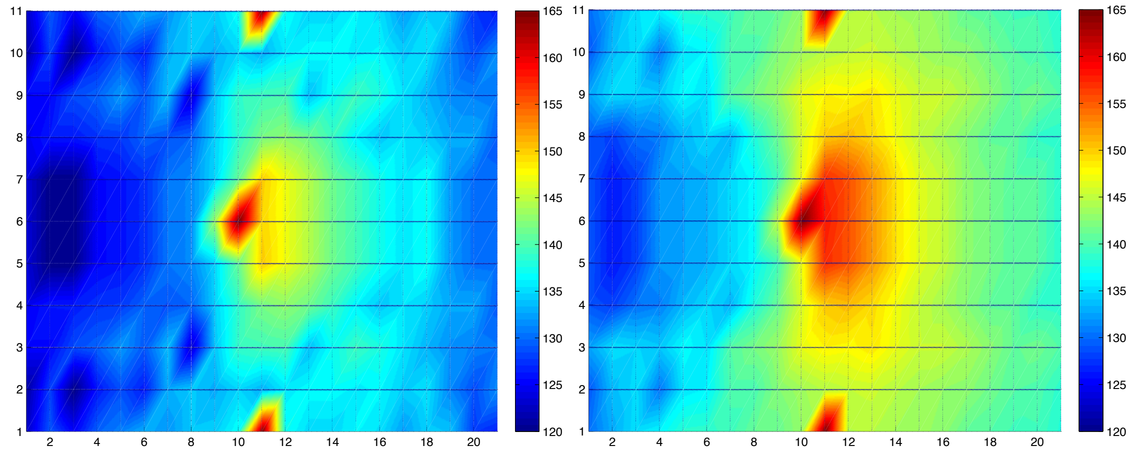

(a) $f = 40Hz$ (b) $f = 50Hz$

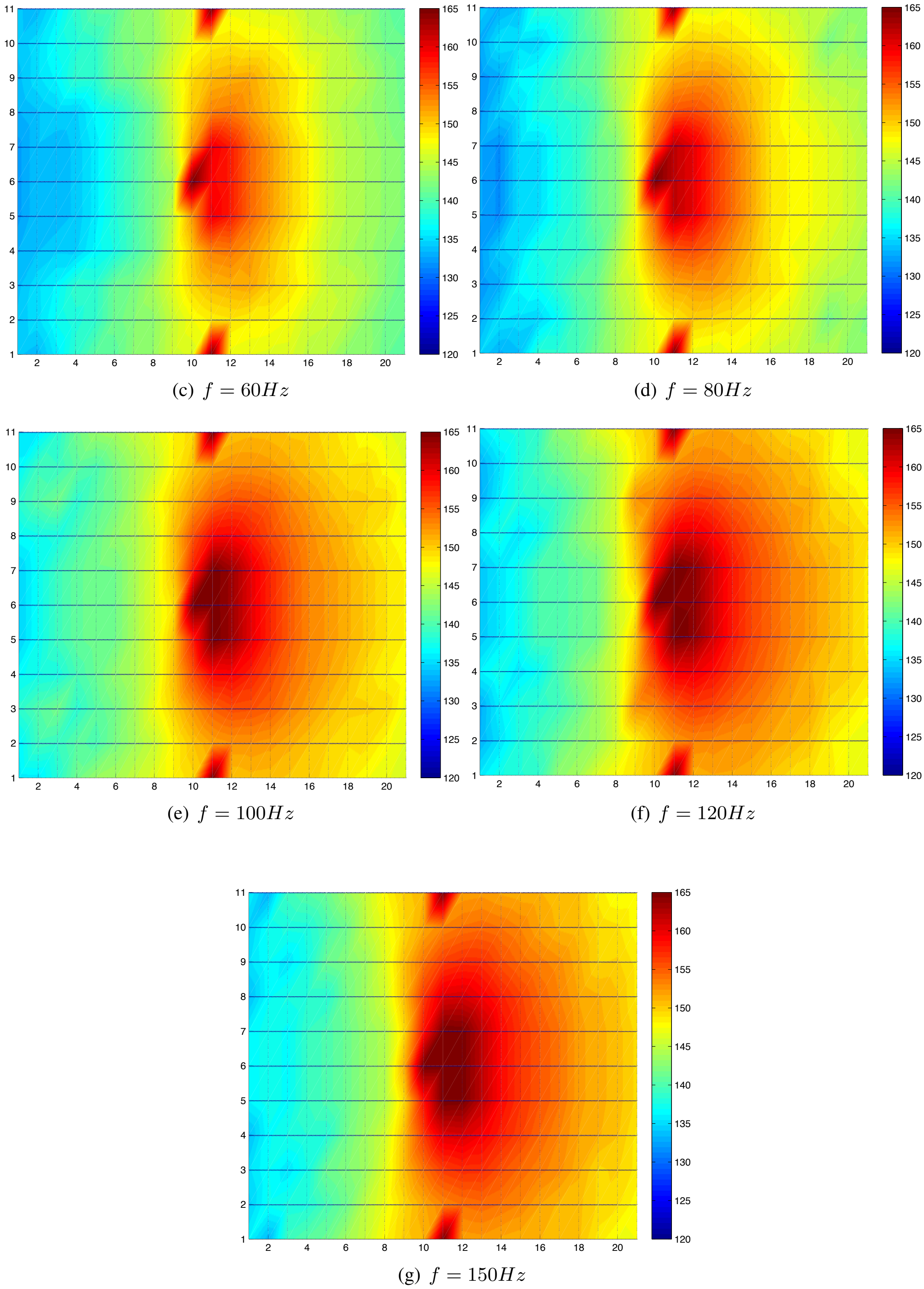

Figure G.8: Measured pressure field at different discrete frequencies